CRAS 2016

6th Joint Workshop on New Technologies for Computer/Robot Assisted Surgery

SEPTEMBER 12-14, 2016 - Scuola Superiore Sant'Anna, PISA, Italy

6th Joint Workshop on New Technologies for Computer/Robot Assisted Surgery, CRAS2016

September 12-14, 2016 in Pisa

Proceedings 2016

https://www.cras-eu.org/cras-2016

ISBN 9791220014779

Joining Efforts – Progressing Faster

Robotic surgery is one of the most appealing fields of modern robotics. With over 2 decades history, more than 2.000 systems installed worldwide and over 200.000 interventions conducted per year, the field of robotic surgery is considered well-established. Despite these impressive figures and increasing popularity in research labs all over the world, the list of technological advances that made it into the operating room during this last decade is fairly limited. Long expected techniques such as 3D reconstruction, motion compensation, virtual guidance, haptic feedback, under study in many labs all over the planet did not make their appearance into the market yet.

CRAS seeks to give a clear view on the status and recent trends of assistive surgical robotic technologies. It aims to support and propose concrete measures to accelerate research and innovation in this field. CRAS originates from efforts to collaborate among European groups to achieve a critical mass in surgical robotics. As such the workshop continues on discussions started at ERF in Lyon and at ICRA in Karlsruhe, and previous meetings at Verona, Genoa and Brussels. More in particular CRAS attempts to identify the steps necessary to stimulate cooperation between research and industry, across national borders and different surgical robotic projects to take advantage of the growing attention and support for research and exploitation in this interesting and growing field.

This year, CRAS will be linked also to the Summer School on Control of Surgical Robots (COSUR 2016, Verona) and will collect also the European users of the same teleoperated surgical platform, i.e. the Da Vinci Research Kit.

Arianna Menciassi
Scuola Superiore Sant'Anna, Pisa, Italy

Leonardo De Mattos
Italian Institute of Technology, Genova, Italy

Paolo Fiorini
University of Verona, Italy

Emmanuel Vander Poorten
Katholieke Universiteit Leuven, Belgium

Editors: Selene Tognarelli, Arianna Menciassi, Leonardo De Mattos, Paolo Fiorini, Emmanuel Vander Poorten.

This workshop is supported by the following sponsors:

BBZ Srl is a spin off of the University of Verona. The main field of operation of the company is the development of hardware and software tools for medicine and surgery. The expertise of its founders ranges from the development and certification of surgical robots, to the interactive simulation of realistic environments on parallel architectures.
BBZ Srl is developing different systems for the training in laparoscopy, robotic surgery and endoscopy in general.

Born as a university spin-off founded by two research associates, CAMELOT is a provider of advanced software solutions for the biomedical industry since 2010. In this context, the company has accumulated considerable expertise in the processing, analysis and display of diagnostic images, skills that have been applied in recent years to the Image-Guided Therapy applications. Since 2014 the company adopted an ISO-13485-certified quality management system, and a software development life cycle that is compliant with the technical standard IEC 62304. From early on our company has always invested in R&D, and is currently participating to three European research projects, all started in 2013: TheraGlio (www.theraglio.eu), FUTURA (www.futuraproject.eu) and Nano2fun (www.nano2fun.eu).

A spin-off of CEA (French Nuclear Research Agency), HAPTION benefits from results and know-how developed in more than 30 years of research. HAPTION designs, manufactures and sells haptic devices with professional quality, suited to the needs of its customers, both industrial and academic. For the medical sector, our haptic devices can be used for different purposes, from learning manual skills by rehearsing them on virtual patients, to using the device as a robotic co-manipulator in surgery, a teleoperation system or a rehabilitation robot.

S.M. Scienzia Machinale s.r.l. (SM) is a SME Italian R&D company (25 employees) operating in R&D contract design in the fields of mechatronics and robotic engineering (from the idea to the design and the manufacture of prototypes up to the small-series production) with 25 years experience in the fields of robotics (including rehabilitative and surgical), marble and plastic processing and robotic welding and sanding through the use of industrial robots or special machines made under customer specification. SM operates in several scientific and industrial areas, crosswise applying established technologies, dealing with all the principal design steps: mechanical, electronic and software. SM also develops robot control and CNC machine control SW. Since 1991 SM joined several European and Italian R&D projects also regarding surgical robotics. SM is currently a member of the USA Company Group "Epica International, Inc.".

The following EU funded projects on surgical robotics supported CRAS:

and also with the support of Regione Toscana

CRAS Committee (Not limited to the mentioned EU projects and in alphabetical order)

Kaspar Althoefer (QMUL)
Peter Brett (Brunel)
Alicia Casals (IBEC)
Brian Davies (ICL, IIT)
Nikhil Deshpande (IIT)
Paolo Fiorini (Univ. Verona)
Edward Grant (NCSU, IIT)
Benoit Herman (UCLouvain)
Leonardo Mattos (IIT)
Sarthak Misra (Univ Twente)
George Mylonas (ICL)
Philippe Poignet (LIRRM)
Benoit Rosa (Harvard Med)
Bruno Siciliano (Univ Napoli)
E. Vander Poorten (KUL)
Tom Vercauteren (UCL)
Stefan Weber (U. Bern)
Gianni Borghesan (KUL)
Marta Capiluppi (Univ. Verona)
Gastone Ciuti (SSSA)
Elena De Momi (POLIMI)
Giancarlo Ferrigno (POLIMI)
Stamatia Giannarou (ICL)
Tamas Haidegger (Obuda Univ)
Lüder A. Kahrs (LUH)
Arianna Menciassi (SSSA)
Guillaume Morel (ISIR)
Angelika Peer (UWE)
F Rodriguez Y Baena (ICL)
Ulrich Seibold (DLR)
Danail Stoyanov (UCL)
Augusta Van Poelgeest (IPA)
Valentina Vitiello (ICL)
Helge Wurdemann (UCL)

CRAS 2016 Local Organizing Committee

Selene Tognarelli (SSSA)
Federica Radici (SSSA)
Marta Capiluppi (Univ. Verona)

Program Overview

September 12		September 13		September 14	
9.00	*Workshop start*	8.30	*Start day 2*	8.30	*Start day 3*
9.15	Keynote **Paolo Dario** Scuola Superiore Sant'Anna	8.45	Keynote **Brain Davies** Imperial College London	8.45	Keynote **Franca Melfi** University Hospital of Pisa
10.00	Session 1 Microsurgery	9.30	Session 4 Novel robotic hardware	9.30	Session 7 Safety and novel applications
11.30	Session 2 Endoscopy	11.00	Session 5 Sensing & Classification	11.00	First European meeting of the DVRK community
12.30	Poster Session 1	12.00	Poster session 3	12.00	Closing remarks and awards
13.00	*Lunch break*	12.30	*Lunch break*	13.00	End of the workshop
14.30	Keynote **Joel Burdick** California institute of technologies	14.00	Keynote **Michel Brochard** EU commission		
15.15	Poster session 2	14.45	Round table		
16.15	Session 3 Training, interfaces and tools	16.30	Session 6 Segmentation and algorithms		
17.15	COSUR event	17.30	Poster view and exhibition		
17.45	Poster view and exhibition	18.30	*Closure of 2nd day*		
18.30	*Closure of 1st day*				
		20.00	***Social Dinner***		

Keynote speech

Paolo Dario
The BioRobotics Institute, Scuola Superiore Sant'Anna

The Saga of Capsule Endoscopy: from Science Fiction to Clinics and Beyond

Paolo Dario is Full Professor of Biomedical Robotics and Director of The BioRobotics Institute of SSSA. He has been Visiting Professor in several institutions worldwide. His main research interests are in the fields of medical robotics, bio-robotics, mechatronics and micro/nano engineering, and specifically in sensors and actuators in robotics. He is the coordinator of many national and European projects, the editor of two books on the subject of robotics, and the author of more than 700 scientific papers (more than 300 on ISI journals). He has a H-index of 52 and a total of 10,836 citations according to the Scopus source.

He has been and is Editor-in-Chief, Associate Editor and member of the Editorial Board of many international journals. He has been program chair and plenary invited speaker in many international conferences. He served as President of the IEEE Robotics and Automation Society in the years 2002-2003, and as Chair of many Technical Committees of the same Society. He is an IEEE Fellow, a Fellow of the European Society on Medical and Biological Engineering, and a recipient of many honors and awards, such as the Joseph Engelberger Award. He is also a member of the Board of the International Foundation of Robotics Research (IFRR) and a Fellow of the School of Engineering, University of Tokyo. He serves in several Boards and Committees. He was recently appointed with the IEEE RAS George Saridis Leadership Award in Robotics and Automation for 2014, with the following motivation "*For pioneering and consolidating robotics as pervasive technology, with interdisciplinary and visionary ideas, extending RAS leadership through inclusiveness towards other communities*". In March 2015 Prof. Paolo Dario was identified by the IEEE Robotics and Automation Magazine as the second most influent scientist in robotics worldwide according to *degree centrality and betweenness bibliometric criteria*.

Joel. W. Burdick

California Institute of Technologies

Spinal Stimulation, Machine Learning, and Robotics to enable recovery after severe spinal cord injury

Professor **Joel Burdick** activities focus on robotics, kinematics, mechanical systems and control. Joel Burdick obtained the B.S in Mechanical Engineering from the Duke University in 1981, the M.S. and the Ph.D from the Stanford University, respectively in 1982 and 1988. He started his career at the California Institute of Technology (CalTech) in 1988, as assistant professor, where he is now Richard and Dorothy Hayman Professor. During his career he obtained many awards and honors, such as the Richard Feyman-Hughes Followship, Office of Naval Research Young Investigator Award, GSU Excellence in Graduate Teaching Award, Popular Mechanics Breakthrough award, in addition to many awards for contributions to ICRA.

Active research areas include: robotic locomotion, sensor-based motion planning algorithms, multi-fingered robotic manipulation, applied nonlinear control theory, neural prosthetics, and medical applications of robotics.

Brian Davies
Imperial College London

Hands-On Robotics: is there further to go in CRAS?

Brian Davies is an Emeritus Professor of Medical Robotics at Imperial College London, where he has been since 1983, and is also a senior research investigator there. He has a PhD in Medical Robotics and was awarded a DSc. in 2001 for his international contribution to Robotic and Computer Aided Surgery systems. He has over 250 refereed papers. He was made a Fellow of the Royal Academy of Engineering in 2005 and serves on their Community of Practice Committee in Biomedical Engineering. He developed the world's first special-purpose surgical robot called PROBOT, to remove quantities of prostatic tissue from a human patient in a clinical trial in April 1991. He subsequently developed the concept of Active Constraints particularly applied to orthopaedic robots and in 1999 he was a co-founder of the spin-off company ACROBOT limited, who developed robots for MIS hip and knee joint replacement and he was their Technical Director. Eventually the company was acquired by Stryker Ltd in 2013. He was a founder of the new "Technologies in Medicine" section of the Royal Society of Medicine. He is on the Board of the IMechE Engineering in Medicine & Health Division. 2001-2014 he has been program chair for the annual conference of the International Society for Computer Aided Orthopaedic Surgery (CAOS) and is on their Executive Board. 2000-2013 he has chaired the Scientific Advisory Board for the Co-Me Swiss research organisation, and since 2006 he has been a consultant advising on Medical Robots for the Advanced Robotics Group of the Italian Institute of technology in Genoa. He has participated in a number of EU medical robotics projects and is a regular reviewer for EU FP7 projects. From 2013-2016 he Chairs the Strategic Advisory Board for the Leeds HTC in Colorectal Cancer group. In 2015 he was awarded the International Society of Technology in Arthroplasty (ISTA) life-time achievement award for research into the use of Robots in Surgery.

Michel Brochard
European Commission

H2020 & CRAS: from results to expectations, which path for the future?

Dr. **Michel Brochard** is an electronic engineer from ULB (Belgium) and worked 9 years in the telecommunications sector at Alcatel Bell in Belgium before joining the European Commission in 1995. Since then, he worked for DG Connect (former DG XIII and DG INFSO) as Project Officer, supervising research and non-research projects co-financed by the European Union in different areas such as electronic publishing, HRI, language technologies, eLearning and robotics.

However since many years he is following more specifically robotics developments in the medical sector (surgery, exoskeleton, robotics assistance in hospitals, teleoperation and assistive living).

Franca Melfi
Robotic Multispeciality Center for Surgery,
University Hospital of Pisa

Robotic Thoracic Surgery: evolution in technique and technology

Dr. **Franca Melfi** is Chief Robotic Multispeciality Center for Surgery, Robotic and Minimally invasive Thoracic Surgery of University Hospital of Pisa. She is Professor of Thoracic Residency courses at the University of Pisa in the field of Minimally Invasive Thoracic surgery courses, Tutorship of Robotic procedures for lung cancer and authorized Surgeons for Intuitive and University Hospital of Pisa.

Dr. Melfi is currently involved in research projects at the University of Pisa, in cooperation with other clinical Institutions. Presently, she is carrying out research on the application of high-technology in surgery (Robotic Surgery), focusing on robotic surgery for the standardization of procedures and clinical application in the field of Thoracic Surgery. She started to work in this field in 2001 with a consistent activity from 2004 to date with over 1400 thoracic procedures.

CRAS2016 Workshop Program

CRAS 2016

6th Joint Workshop on New Technologies for Computer/Robot Assisted Surgery

SEPTEMBER 12-14, 2016 - Scuola Superiore Sant'Anna, PISA, Italy

MONDAY, SEPTEMBER 12TH, 2016

8.00-9.00	REGISTRATION
9.00-9.15	WORKSHOP START - WELCOME BY *PROF. PIERDOMENICO PERATA*, RECTOR OF SCUOLA SUPERIORE SANT'ANNA AND *PROF. MARIO ENRICO PÈ*, DEAN OF THE FACULTY OF EXPERIMENTAL SCIENCES
9.15-10.00	KEYNOTE - **PAOLO DARIO** (CHAIR: ARIANNA MENCIASSI) THE SAGA OF CAPSULE ENDOSCOPY: FROM SCIENCE FICTION TO CLINICS AND BEYOND

10.00-11.00 SESSION 1 - *MICROSURGERY*

SESSION CHAIRS: LEONARDO DE MATTOS AND DANAIL STOYANOV

10.00-10.15	*T.O. VRIELINK, A. DARZI AND G. MYLONAS* MICROCYCLOPS: A ROBOTIC SYSTEM FOR MICROSURGICAL APPLICATIONS
10.15-10.30	*M. CHAUHAN, N. DESHPANDE, D.G. CALDWELL AND L. MATTOS* DESIGN OF ROBOT ASSISTED MICROSURGICAL FORCEPS FOR TRANSORAL LASER MICROSURGERY
10.30-10.45	*L. VANTHOURNHOUT, B. HERMAN, J. SZEWCZYK, B. LENGELÉ AND B. RAUCENT* DESIGN AND PROTOTYPING OF A ROBOTIC ASSISTANT FOR MICROSURGERY
10.45-11.00	*G. DWYER, C. BERGELES, F. CHADEBECQ, V. PAWAR, E. VANDER POORTEN, S. OURSELIN, P. DE COPPI, T. VERCAUTEREN AND D. STOYANOV* COOPERATIVE CONTROL WITH DISTAL MANIPULATION FOR FETOSCOPIC LASER PHOTOCOAGULATION
11.00-11.30	*COFFEE BREAK, POSTER VIEW AND EXHIBITION*

11.30-12.30 SESSION 2 - *ENDOSCOPY*

SESSION CHAIRS: PAOLO DARIO AND GEORGE MYLONAS

11.30-11.45	*F.B. AVILA-RENCORET, D.S. ELSON AND G. MYLONAS* A ROBOTIC HYPERSPECTRAL SCANNING FRAMEWORK FOR ENDOSCOPY
11.45-12.00	*G. LUCARINI, G. TORTORA, C. QUAGLIA, G. CIUTI AND A. MENCIASSI* A NOVEL MAGNETIC PLATFORM FOR ACTIVE ENDOSCOPIC INVESTIGATIONS
12.00-12.15	*G. CUMMINS, H. LAY, B. COX, V. SEETOHUL, Y. QIU, F. STEWART, J. FAERBER, V. MITRAKOS, M. AL-RAWHANI, J. BEELEY, D. WATSON, R. POLTARJONOKS, I. NATHKE, C. DEMORE, D. CUMMING, M. DESMULLIEZ AND S. COCHRAN* SONOPILL: A PLATFORM FOR GASTROINTESTINAL DISEASE DIAGNOSIS AND THERAPEUTICS
12.15-12.30	*G. CIUTI, D. STOYANOV, A. AREZZO, A. KOULAOUZIDIS, S. SCHOSTEK, M.O SCHURR, B. MAGNANI, C.M. ODDO, A. MENCIASSI AND P. DARIO* ENDOVESPA: A COMPUTER-INTEGRATED ROBOTIC PLATFORM FOR MAGNETICALLY-DRIVEN SOFT-TETHERED COLONOSCOPY

12.30-13.00 - *POSTER SESSION 1* (POSTER CHAIR: ARIANNA MENCIASSI)

12.30-12.33	*S. GUPTA, S. MACHERI RAVISHANKAR, M. GRIFFIOEN, R. BABUSKA AND T. KLEM* - HIP FRACTURE REDUCTION ROBOT
12.33-12.36	*J. BACK, G. ZHANG, S. WANG AND H. LIU* - SURGICAL GRIPPER WITH EMBEDDED SOFT TACTILE ARRAY FOR NOTES
12.36-12.39	*A. FARAGASSO, A. STILLI, J. BIMBO, H. WURDEMANN AND K. ALTHOEFER* - CLIP-ON STIFFNESS SENSOR FOR ENDOSCOPIC CAMERAS RETRIEVING SENSE OF TOUCH IN MINIMALLY INVASIVE INTERVENTION
12.39-12.42	*C. GIRERD, K. RABENOROSOA AND P. RENAUD* - SYNTHESIS OF A NEW CONCENTRIC TUBE ROBOT FOR OLFACTORY CELLS EXPLORATION
12.42-12.45	*L. PATERNÒ, G. TORTORA AND A. MENCIASSI* - PRELIMINARY DESIGN OF HYBRID SOFT RIGID ACTUATORS FOR MIS
12.45-12.48	*G. BORGHESAN, D. BOUGET, E. LANKENAU, R. NEFFIN, P. KOCH, K. WILLEKENS, P. STALMANS, D. REYNAERTS AND E. VANDER POORTEN*-SINGLE FIBER OCT - BASED VESSEL DETECTION FOR ROBOT-ASSISTED RETINAL VEIN CANNULATION
12.48-12.51	*A. ACEMOGLU AND L. MATTOS* - MAGNETICALLY ACTUATED SURGICAL LASER SCANNER FOR ENDOSCOPIC APPLICATIONS
12.51-12.54	*L. MASSARI, P. SACCOMANDI, F. SORGINI, E. SINIBALDI, G. CIUTI, A. MENCIASSI, P. CAPPA, E. SCHENA AND C.M ODDO* - TACTILE SENSOR ARRAY INTEGRATING FIBER BRAGG GRATING TRANSDUCERS FOR BIOMECHANICAL MEASUREMENT
12.54-12.57	*A. STILLI, H.A. WURDEMANN AND K. ALTHOEFER* - A NOVEL INFLATABLE AND FLEXIBLE ENDOSCOPE FOR INHERENTLY SAFE MINIMALLY INVASIVE EXAMINATION

CRAS 2016

6th Joint Workshop on New Technologies for Computer/Robot Assisted Surgery

SEPTEMBER 12-14, 2016 - Scuola Superiore Sant'Anna, PISA, Italy

12.57-13.00	*S. Nisar, T. Endo and .F. Matsuno* - A 2 degrees-of-freedom planar remote center of motion mechanism for minimally invasive surgery manipulators
13.00-14.30	*Free Lunch Break*
14.30-15.15	Keynote – **Joel. W. Burdick** (chair: Paolo Fiorini) Spinal Stimulation, Machine Learning, and Robotics to enable Recovery After Severe Spinal Cord Injury

15.15-15.45 - *Poster Session 2* (Poster Chair: Arianna Menciassi)

15.15-15.18	*U. Seibold, B. Kuebler and M. Groeger*- An innovative method of cooperative research – Introduction of the DLR-Miro Innovation Lab
15.18-15.21	*C. Tarola, P. Perona, Y. Yue, J. Gabany and M. Zenati* - Teamwork Monitoring in Robotic Surgery: A Role for Computer Vision and Machine Learning?
15.21-15.24	*M. Tenucci, S. Mazzoleni, M. Galgani, G. Ciuti, G. Calvosa and P. Dario* - Spine surgery and biorobotics: clinical experience and research challenges
15.24-15.27	*V. Ferrari, F. Cutolo and M. Ferrari* - Wearable augmented reality displays for image guided surgery
15.27-15.30	*M. Brancadoro, S. Tognarelli, I. Scarcella and A. Menciassi* - High-fidelity simulation in newborns therapy through an active soft pulmonary simulator
15.30-15.33	*A. Kogkas, A. Darzi and G. Mylonas* - Gaze-Driven Human-Robot Interaction in the Operating Theatre
15.33-15.36	*F. Visentin and P. Fiorini* - Angle Detection and Measurement on Continuous and Deformable Medical Tools
15.36-15.39	*S. Sadati, S. Elnaz Naghibi and A. Shiva* - Continuum manipulators mechanics, a comparative study of three methods for surgery applications
15.39-15.42	*C. Gruijthuijsen, A. Javaux, A. Devreker, T. Vercauteren, S. Ourselin, D. Stoyanov, J.Deprest, D. Reynaerts and E. Vander Poorten* - Haptic guidance schemes for robot-assisted minimal invasive fetal surgery
15.42-15.45	*Y. Chen, S.A Bowyer and J.W Giles* - Development of a haptic Simulator for the training of surgeons in knee physical exam skills
15.45-16.15	*Coffee Break, poster view and exhibition*

16.15-17.15 Session 3 – *Training, Interfaces and Tools*

Session Chairs: Marco Zenati and Vincenzo Ferrari

16.15-16.30	*C. Schlenk, T. Bahls, S. Tarassenko, J. Klodmann and T. Wüsthoff* - Real-time-capable robot integrated buttons for direct user interaction in versatile medical procedures
16.30-16.55	*R.M Viglialoro, S. Condino, S. Fani, M. Bianchi, A. Bicchi, M. Ferrari and V. Ferrari* – Augmented reality in surgical training
16.45-17.00	*K. Yoshida, W. Jensen, S. Micera and P.N. Sergi* - Failure of surgical insertion of tungsten needles into in vivo suine peripheral nerves: a hybrid procedure to assess the influence of biotic factors
17.00-17.15	*Y. Noh, A. Shiva, E. Hamid, H. Liu, K. Althoefer and K. Rhode* – Light intensity based optical force/torque sensor for robotic manipulators

17.15-17.45 COSUR event
chairs: Marta Capiluppi and Riccardo Muradore

17.45-18.30	*Poster View and Exhibition*

18.30 End of the First day

CRAS 2016

6th Joint Workshop on New Technologies for Computer/Robot Assisted Surgery

SEPTEMBER 12-14, 2016 - Scuola Superiore Sant'Anna, PISA, Italy

TUESDAY, SEPTEMBER 13TH, 2016

8.30-8.45	WELCOME
8.45-9.30	KEYNOTE – **BRIAN DAVIES** (CHAIR: LEONARDO DE MATTOS) HANDS-ON ROBOTICS: IS THERE FURTHER TO GO IN CRAS?

9.30-10.30 SESSION 4 – *NOVEL ROBOTIC HARDWARE*

SESSION CHAIRS: BRUNO SICILIANO AND ULRICH SEIBOLD

9.30-9.45	*A. DIODATO, A. CAFARELLI, A. SCHIAPPACASSE, L.A. CHANEL, S. TOGNARELLI, G. CIUTI AND A. MENCIASSI* – COMPUTER-ASSISTED ROBOTIC PLATFORM FOR USGFUS TREATMENT
9.45-10.00	*N. KALAVAKONDA, N. AGHDASI AND B. HANNAFORD* - SURGEON'S ASSISTANT: A TOUCH-FREE NAVIGATION SYSTEM
10.00-10.15	*P. PHILIPP, L. SCHREITER, J. GIEHL, Y. FISCHER, J. RACZKOWSKY, M. SCHWARZ, H. WÖRN AND J. BEYERER* - SITUATION DETECTION FOR AN INTERACTIVE ASSISTANCE IN SURGICAL INTERVENTIONS BASED ON DYNAMIC BAYESIAN NETWORKS
10.15-10.30	*B. VÉRON, N. HUNGR AND J. TROCCAZ*- MAKING A CLINICAL DEVICE FROM A LABORATORY PROTOTYPE: FROM PROSPER TO PROSPER OR
10.30-11.00	*COFFEE BREAK, POSTER VIEW AND EXHIBITION*

11.00-12.00 SESSION 5 – *SENSING & CLASSIFICATION*

SESSION CHAIRS: EDWARD GRANT AND EMMANUEL VANDER POORTEN

11.00-11.15	*M. DE PICCOLI, M. CAPILUPPI AND P. FIORINI* - A SHAPE SIMILARITY FRAMEWORK FOR BRAIN FIBERS CLASSIFICATION BASED ON FRÉNET FRAME
11.15-11.30	*Z. CHENG, B.L. DAVIES, D.G. CALDWELL AND L. MATTOS* - A NOVEL VENIPUNCTURE DETECTION SYSTEM BASED ON ELECTRICAL IMPEDANCE MEASUREMENT
11.30-11.45	*V. VIRDYAWAN, M. OLDFIELD AND F. RODRIGUEZ Y BAENA* - LASER DOPPLER BASED SENSING FOR BLOOD VESSEL DETECTION WITH A STEERABLE NEEDLE
11.45-12.00	*A. JAVAUX, M. DENHAEN, Y. HAGENIMANA, A. DEVREKER, C. GRUIJTHUIJSEN, T. VERCAUTEREN, S. OURSELIN, D. STOYANOV, J. DEPREST, D. REYNAERTS, E. VANDER POORTEN AND K. DENIS* - ESTIMATING THE INTERACTION FORCES ON THE BODY WALL DURING MINIMAL INVASIVE FETAL SURGERY

12.00-12.30 – *POSTER SESSION 3* (POSTER CHAIR: ARIANNA MENCIASSI)

12.00-12.03	*M. HAVLENA, K.K MANINIS, D. BOUGET, E. VANDER POORTEN AND L. VAN GOOL* - 3D RECONSTRUCTION OF THE RETINAL SURFACE FOR ROBOT-ASSISTED EYE SURGERY
12.03-12.06	*F. FAZIOLI, F. FICUCIELLO, A. FONTANELLI, B. SICILIANO AND L. VILLANI* - IMPLEMENTATION OF A SOFT-RIGID COLLISION ALGORITHM IN AN OPEN-SOURCE ENGINE FOR SURGERY REALISTIC SIMULATION
12.06-12.09	*D. EVANGELISTA, F. IODICE, A. PERICA, M. CEFALO, E. MAGRINI, M. ANZIDEI AND M. VENDITTELLI* - RESIDUAL-BASED INTERACTION FORCE ESTIMATION FOR HAPTIC FEEDBACK IN TELEOPERATED NEEDLE INSERTION
12.09-12.12	*G. LUCARINI, V. IACOVACCI, L. RICOTTI AND A. MENCIASSI* - CONTROL OF MAGNETIC MILLIROBOTS FOR TARGETED DRUG DELIVERY: FEASIBILITY STUDY
12.12-12.15	*K. MEISWINKEL, T. HORN, S. ZANI, T. PAPPAS, E. GRANT AND E. KLANG* - A MONOLITHIC UNDERACTUATED AND COMPLIANT ENDOSCOPIC TOOL DESIGN
12.15-12.18	*A. KRACHT, F. LIVINGSTON, S. ZANI, T. PAPPAS AND E. GRANT* - A TELE-MANIPULATOR ROBOTIC ASSISTANT FOR ENDOSCOPIC SURGERY
12.18-12.21	*R. ELEK, D.A. NAGY, I. RUDAS AND T. HAIDEGGER* - FEATURE EXTRACTION-BASED AUTOMATED CAMERA MOTION FOR SURGICAL ENDOSCOPY SUPPORT
12.21-12.24	*E. SHOJAEI BARJUEI, J. LI, G. CIUTI, Y. HAO, P. ZHANG, Q. SHI, A. MENCIASSI, Q. HUANG AND P. DARIO* - IMPLEMENTATION OF AN ANALYTICAL MAGNETIC MODEL FOR MEDICAL ROBOTS DESIGN
12.24-12.27	*D.M. DE MICHELI, M. CURTI, A. DIODATO, G. CIUTI AND A. MENCIASSI*- A REAL-TIME COLLISION AVOIDANCE SIMULATION SOFTWARE TOOL FOR A MULTI-ROBOT, UNSTRUCTURED AND TIME-VARIANT SCENARIO

CRAS 2016

6th Joint Workshop on New Technologies for Computer/Robot Assisted Surgery

SEPTEMBER 12-14, 2016 - Scuola Superiore Sant'Anna, PISA, Italy

12.30-14.00	*Free Lunch Break*
14.00-14.45	Keynote : **Michel Brochard , European Commission** (chair: Paolo Fiorini) H2020 & CRAS: from results to expectations, which path for the future?
14.45-16.00	**Round table** : The Difficult Path from Research to Product: Many Obstacles and few Rewards Chair: Paolo Fiorini Participants: M. Brochard, G. Ferrigno, R. Fontanelli, G. Prisco, G. Turchetti, P. Dario
16.00-16.30	*Coffee Break, poster view and exhibition*

16.30-17.30 Session 6 – *Segmentation & Algorithms*

Session Chairs: Ferdinando Rodriguez y Baena and Cameron Riviere

16.30-16.45	*A.S. Ciullo, V. Penza, L. Mattos and E. De Momi* - Development of a surgical stereo endoscopic image dataset for validating 3D stereo reconstruction algorithms
16.45-17.00	*B. Maris, P. Fiorini and R. De Robertis Lombardi* - Segmentation of pancreatic solid tumors and texture analysis to discriminate pancreatic ductal adenocarcinomas from neuroendocrine neoplasms
17.00-17.15	*P. Brandao, E. Mazomenos, G. Ciuti, F. Bianchi, A. Menciassi, P. Dario, A. Koulaouzidis and D. Stoyanov* - Validating convolution neural networks for automatic polyp detection in robotic colonoscopy
17.15-17.30	*K. Pachtrachai, M. Allan, V. Pawar and D. Stoyanov* - Hand-eye calibration using instrument CAD models in robotics assisted minimally invasive surgery
17.30-18.30	*Poster View and Exhibition*

18.30 End of the Second Day

20.00 SOCIAL DINNER

Chiostro del Carmine, Corso Italia, 86 - Pisa

CRAS 2016

6th Joint Workshop on New Technologies for Computer/Robot Assisted Surgery

SEPTEMBER 12-14, 2016 - Scuola Superiore Sant'Anna, PISA, Italy

WEDNESDAY, SEPTEMBER 14TH, 2016

8.30-8.45	WELCOME
8.45-9.30	KEYNOTE: **FRANCA MELFI** (CHAIR: EMMANUEL VANDER POORTEN) ROBOTIC THORACIC SURGERY: EVOLUTION IN TECHNIQUE AND TECHNOLOGY

SESSION 7 – *SAFETY & NOVEL APPLICATIONS*

SESSION CHAIRS: HERMAN BENOIT AND ELENA DE MOMI

9.30-9.45	*A. SHAFTI, B.U LAZPITA, O. ELHAGE, H.A. WURDEMANN AND K. ALTHOEFER* - TOWARDS AN OBJECTIVE ASSESSMENT OF COMFORT AND ERGONOMICS DURING SURGERY
9.45-10.00	*S. MOCCIA, F. PRUDENTE, E. DE MOMI, C. RIVIERE, A. PERIN AND L. MATTOS* - SAFETY ENHANCEMENT IN ROBOTIC NEURO SURGERY THROUGH VESSEL TRACKING
10.00-10.15	*M. KOZLOVSZKY, K. BATBAYAR, G. KRONREIF AND E. JÓSVA I* -REQUIREMENT AND DESIGN OF SAFE MEDICAL DEVICE COMPONENT BASED SOFTWARE ARCHITECTURE
10.15-10.30	*S.H. JAWAD ABIDI, M. CIANCHETTI, M. BRANCADORO, A. DIODATO, G. DE ROSSI, D. DALL'ALBA, R. MURADORE, G. CIUTI, P. FIORINI AND A. MENCIASSI* - SOFT ENDOSCOPIC CAMERA SYSTEM FOR ROBOTIC SURGERY: A DVRK IMPLEMENTATION
10.30-11.00	*COFFEE BREAK, POSTER VIEW AND EXHIBITION*
11.00-12.00	FIRST EUROPEAN MEETING OF THE DVRK COMMUNITY (CHAIRS. **PAOLO FIORINI, ARIANNA MENCIASSI** AND **ELENA DE MOMI**)
12.00-13.00	CLOSING REMARKS AND BEST PAPER AND BEST POSTER AWARDS

13.00 END OF THE WORKSHOP

15.00 - 18.00	POSSIBLE VISITS/FREE TIME

CRAS2016 Workshop Proceedings

Table of Contents

An innovative method of cooperative research – Introduction of the DLR-Miro Innovation Lab

Ulrich Seibold, Bernhard Kuebler, Martin Groeger

German Aerospace Center (DLR), Institute of Robotics and Mechatronics, Wessling-Oberpfaffenhofen, Germany. E-Mail: Ulrich.Seibold@dlr.de

INTRODUCTION

In recent years funding agencies have attempted to integrate industrial and SME (small and medium-sized enterprise) partners closer into traditionally funded research efforts. The importance of not only disseminating scientific research results, but also looking for commercialization opportunities by establishing an exploitation plan together with the industrial partners early during the project was emphasized. With the Helmholtz Innovation Labs (HIL), the Helmholtz Association (HGF) has introduced a novel funding instrument. Funding is directed towards building long term, self sufficient innovation labs as enabling spaces for collaborative work between research and industrial or SME partners, modeled after examples of the Harvard Innovation Lab, the FabLab Berlin, and various other innovation lab and incubator initiatives. Initiatives in all levels of technology readiness, from early concept to late stage product development are supported.

The HGF is Germany's largest scientific organization, bringing together 18 scientific-technical and biological-medical research centers, one of them being the German Aerospace Center (DLR).

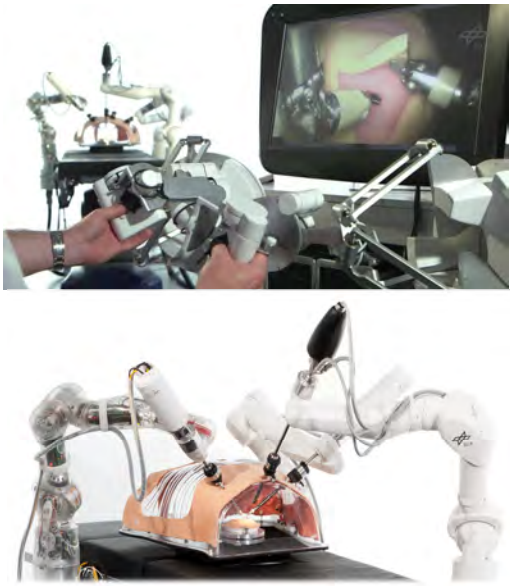

Fig. 1: Versatile DLR Miro robots, shown here using the example of minimally invasive surgery

Based on the MiroSurge robotic surgery demonstrator platform and building on the success of the MiroLab within the HGF Validation Fund, the DLR Institute of Robotics and Mechatronics (RM) proposed, and was granted, the „Miro Innovation Lab" (MIL) under the HGF Innovation Lab initiative [4]. The MIL is situated, embedded, and strongly supported by RM, whose expertise and facilities can be utilized in the lab. Core of the proposal is cooperative application development around an existing technology platform in the field of robot supported, interventional medicine (see Fig. 1). The current system has already been presented [1-3] and gained widespread acceptance in scientific and industrial circles. Although previously, the focus was mainly on minimally invasive surgery, the system is designed for versatility. This versatility can be leveraged in the Innovation Lab: A wide range of industrial partners and research institutions are invited to bring their respective expertise to the MIL, and together with the robotics expertise of RM cooperatively develop new robot supported applications. Developments may be directly connected to the MiroSurge system or only loosely linked to the existing robotic technology. The MIL is supported and upvalued by the close cooperation with a renowned clinical partner institution, MITI [5], located in close proximity to RM, providing services from medical consulting and problem analysis, clinical evaluation, workflow analysis and field tests, to animal experiments. The medium-term goal of the MIL is to open up access to the medical robotics market for small and medium-sized companies that do not have the chance to break into this highly complex and expensive but also potentially profitable sector due to a lack of robotic expertise. The second objective is to identify new applications that are useful in this context and, thereby, introduce a much broader range of technology in the medical robotics field. The third important aspect is creating partnerships and using synergies via the MIL and to disseminate medical robotics knowledge among interested parties and potential partners.

IMPLEMENTATION

The MIL concept specifies an 'Open Innovation Lab' targeting cooperative research and developments with an application readiness level (ARL) range of 2-5. Basic research, final product development, and preproduction remain the responsibility of the industrial partners.

If necessary and desired, office space can be made available for the partners, e.g. during longer-term activities in the MIL. The room concept offers the potential for an interactive process of innovation and development involving various areas of expertise.

The relevant fiscal and legal framework for cooperative research in an environment with variable partner constellations is being developed within the MIL project. Prior to the start of any project, an agreement containing the description of work, where possible in the form of a product requirements document (PRD), the time frame, and the financial resources needs to be executed. Furthermore, the involvement of other partners (if any), as well as the usage and exploitation of anticipated results have to be defined at the outset. Exploitation of jointly developed results needs to balance the expectations of all partners involved. Scientific partners (such as RM) are required to disseminate research results and expect to be able to build and expand on previous research. Industrial partners, who are funding cooperative research without HGF subsidy, might expect confidentiality and exclusive access to results, especially in the highly competitive and costly medical devices market. The funding agency sees the Innovation Lab as an innovation nucleus, benefitting from the cross-fertilization between the partners, allowing the identification of completely new research contents in cooperation with one or more partners, and bringing those ideas into a prototypical stage.
The HGF grant for the MIL will be available e.g. for the following areas: 1) Further improving robustness of the robot systems – which are presently available in a prototypic stage – so that system failures during experimental campaigns can be avoided and replacement systems are available. 2) A universal communication interface already in use by more than 10 renowned research institutions, including the Johns Hopkins University [6] will be integrated. 3) The formal legal bases for cooperation will be created, including e.g. a comprehensive contract which exemplarily governs relations between partners. 4) Gradually a lab infrastructure will be set up that creates an attractive environment for future projects. Equipment will be gradually expanded until the standard of a medical laboratory is met and various experimental campaigns can be conducted and documented. 5) Seminar-like training courses will be developed with focus-oriented lectures (e.g. “Joint control of manipulators”, “Design of highly integrated mechatronic systems”, “Fundamentals of ‘Human Factors’”) for potential project partners and interested experts, possibly with hands-on experiments and demonstrations.
Regular workshops will be offered on topics of robotic surgery and related disciplines. Potential partners can get to know the lab, capabilities and potential future opportunities during the workshops, as well as connect with partners of diverse expertise. This advertisement will be augmented by appearances at trade fairs and conferences to make the existence of the MIL known to a wider user base.
In addition, the MIL will offer added value through expertise in Human Factors analysis: In industrial psychological investigations mental, cognitive, and social driving forces in socio-technical systems and human-machine systems can be studied, since issues like human-computer interaction, usability, and cognitive ergonomics are often hardly quantifiable with classic engineering approaches. Optimizing performance and capacity limits with regard to cooperation with technical systems can be investigated on a scientific basis using these methods – especially with the help of the clinical partner institution [5] under realistic conditions, where appropriate and desired by the partners.

CONCLUSION AND INVITATION TO PARTNERS

To further the current efforts of transferring technology from research into (preferably small and medium) industry, and promote cooperation between various industrial partners, innovation labs are introduced as a pioneering strategy of governmental funding. This Abstract briefly introduced this new funding instrument from a research perspective, and highlighted the Miro Innovation Lab concept. We hereby invite and encourage interested parties to collaborate under this framework.

REFERENCES

[1] Hagn, U. et al.: DLR MiroSurge – A Versatile System for Research in Endoscopic Telesurgery. In: International Journal of Computer Assisted Radiology and Surgery, 2010;5(2):183-193.
[2] Hagn, U. et al.: Telemanipulator for Remote Minimally Invasive Surgery. In: IEEE Robotics and Automation Magazine, 2008;15(4):28-38.
[3] Hagn, U. et al.: The DLR MIRO: a versatile lightweight robot for surgical applications. Industrial Robot, 2008;35(4):324-336.
[4] Helmholtz fördert gemeinsame Innovationslabore mit Partnern aus der Wirtschaft. Press release of the Helmholtz Association, May 10, 2016. Website, 05/2016. https://www.helmholtz.de/aktuell/presseinformationen/artikel/artikeldetail/helmholtz_foerdert_gemeinsame_innovationslabore_mit_partnern_aus_der_wirtschaft/
[5] Minimally Invasive Interdisciplinary Therapeutical Intervention (MITI) research group, at the Klinikum rechts der Isar of the Technical University of Munich. Website, 05/2016. http://www.miti.med.tum.de
[6] Kazanzides, P.; Taylor, R.H.: An Open-Source Research Kit for the da Vinci® Surgical System. In: Proc. of the IEEE Int. Conf. on Robotics and Automation (ICRA), pp. 6434- 6439, Hong Kong, China, 2014.

Real-Time Capable Robot Integrated Buttons for Direct User Interaction in Versatile Medical Procedures

C. Schlenk, T. Bahls, S. Tarassenko, J. Klodmann, T. Wüsthoff

Institute of Robotics and Mechatronics, German Aerospace Center (DLR)

christopher.schlenk@dlr.de

INTRODUCTION

Lightweight robots with integrated torque sensors like the *DLR MIRO* [1, 2] or the *KUKA iiwa* allow a safe (cp. [3]) and intuitive interaction of robots and humans (hands-on robotics [2]). In the medical field, hands-on robotics is promising in both one-arm scenarios (e.g. robotic waterjet surgery [4]) and complex setups like minimally invasive robotic surgery (MIRS) [5]. In the first example it enables robot operation without external input devices and thus keeps the system setup simple. In the second example it allows not only the surgeon at the console but also the operating room (OR) staff at the OR table to interact directly with the robot. This disburdens the surgeon in routine procedures like instrument change and allows him to focus on his task. However, in complex procedures, where the desired robot behavior depends on the workflow step (e.g. in MIRS: hands-on robotics for inserting the instrument, teleoperation for the intervention), the users need input methods to navigate through the workflow.

This paper presents the subsequent integration of six programmable, real-time (RT) capable buttons in the *DLR MIRO* to realize a compact and flexible user interface for hands-on robotics.

MATERIALS AND METHODS

The versatile robotic research platform *DLR MIRO* has been used in various research projects within e.g. MIRS [2] or waterjet surgery [4]. Its low weight and integrated torque sensors allow a safe, direct user interaction.

The number and spatial arrangement of the buttons shown in Fig. 1 were derived from trials with OR staff.

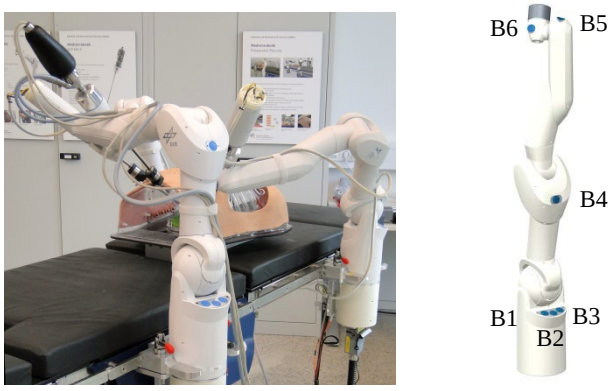

Figure 1 Left: *MiroSurge* demonstration setup for MIRS: The *DLR MIRO* in the foreground carries a stereo endoscope, the other two *MIROs* the robotic *MICA* instruments (see [2]). Right: Rendering of the *DLR MIRO* with its buttons (B1-B6).

The buttons are read in by a general purpose input output board (GPIO board). This 24 mm x 24 mm large board (see Fig. 2) provides nine single ended IOs, two galvanically insolated IOs and two power switches. Its FPGA technology enables real-time capability and easy adaption to various use cases. The integration into the real-time capable *SpaceWire* communication of the *DLR MIRO* [1] is achieved via a communication bridge to a proprietary protocol transmitted via three LVDS (Low Voltage Differential Signaling) lines. Alternatively any other communication protocol transmittable via three LVDS (e.g. BISS or 3-wire SPI) can be used provided that the FPGA firmware is adapted accordingly.

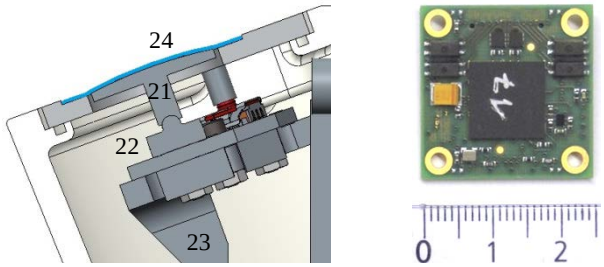

Figure 2 Left: Mechanical structure of B2: The tappet (21) transmits the finger pressure to switch (22), which is connected to the robot's mechanical structure by a RP part (23). A flexible membrane (24) covers the casing opening. Right: GPIO board with scale in real size.

The button design (see Fig. 2) provides distinct tactile feedback to the user, ensures mechanical robustness (all sensitive components are integrated into the casings) and simplifies the (dis)assembly (no disconnection of the cables is necessary to disassemble the casings).

Since the casings of the *DLR MIRO* are no integral part of the robot structure, rapid prototyping (RP) parts attach switch, tappet and GPIO board to the mechanical structure. The openings for the tappets in the casings are covered by a flexible membrane, which prevents the intrusion of dust or fluids and thereby allows the disinfection of the robot (when sterility is required, however, the robot must be wrapped in sterile drape).

As displayed in Fig. 3, the GPIO boards samples the electrical signal of one or more (in the present installation up to three) buttons and feeds it into the RT communication of the robot. The control software of the robotic system considers the digital button signals as additional sensor inputs from the robot arm.

Thanks to the modular software architecture only minor software changes are required to integrate the support of the buttons. The *MIRO Hardware Abstraction Layer* (HAL) [1] is extended to feature a button interface via

an additional *Inter Process Communication Channel (IPCC)*. To access the data from this *IPCC*, the software modules providing user interaction with buttons can use automatically generated functional stubs, e.g. a Simulink library or a pre-compiled C++ library.

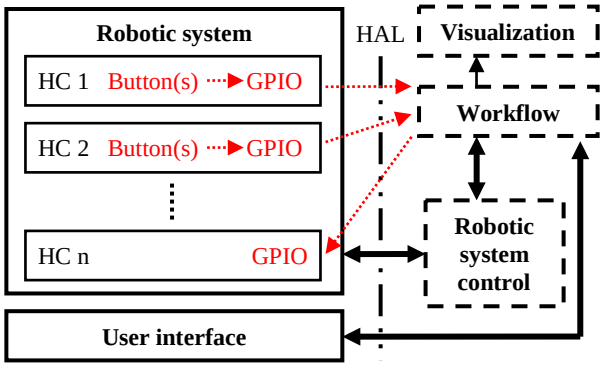

Figure 3 The button(s) and the GPIO board together form an input device, which can be attached to any hardware component HC x of the robotic system, e.g. the *DLR MIRO*. It enables the user to navigate through the workflow without an additional user interface like a tablet or a space mouse. Depending on the workflow step the robotic system control, the system state visualization and the behavior of the user interface can be adapted. On the other hand the GPIO board alone can serve as bridge between the software implemented workflow and a 3rd party hardware component HC n.

RESULTS

As example for the interaction possibilities offered by the buttons, the following workflow for MIRS was implemented for setting the trocar position in software [2] and inserting the instrument before the teleoperation:

- The user presses B1 (see Fig. 1) to move the robot to a predefined approach position.
- By holding B4 the user activates the hands-on mode to move the gravity compensated robot to the desired trocar position.
- Releasing B4 locks the robot's pose, allowing the user to check the correctness of the trocar position before confirming it via B2.
- To set the trocar, the user moves the robot in impedance control mode (activated by holding B5) away from the patient. In this mode virtual springs force the instrument axis to intersect the patient's body surface at the trocar point.
- To insert the instrument in the trocar, the user once more activates impedance control via B5.
- When B5 is released while the instrument tip is inside the patient, the robotic system automatically switches to teleoperation mode. In teleoperation mode pressing B4 activates the nullspace motion of the robot's elbow to gain better patient access.

In the described procedure a single person can set up all robots at the OR table without an external user interface. The described button functions are just exemplary and can easily be modified depending on the application.

Besides controlling the robot, the buttons can also control 3rd party devices (in MIRS e.g. the light source of an endoscope) connected to the same communication network. In this case the GPIO board can be used to connect the third party device (HC n in Fig. 3) with the communication network of the robotic system.

The RT capability of the GPIO board and its integration in the RT communication allows time-critical applications, e.g. sampling surfaces to build a 3D model, where button toggling and joint positions of the *DLR MIRO* must be registered synchronously with respect to time.

CONCLUSION AND DISCUSSION

The presented buttons offer the following advantages for the *robot developer*:

- *Low cost:* The GPIO board uses standard PCB technologies and electronic components. All other parts are commercially available or can be manufactured using RP processes.
- *Simple subsequent integration:* The required cabling is minimized by using the existing communication infrastructure of the robot.
- *Robust:* The membranes on the casing openings enable the disinfection of the robot. For easy maintenance, the casings can be disassembled without disconnecting the button cables.
- *Flexible:* The functions of the programmable buttons can be changed without hardware modifications. As the GPIO board supports the simultaneous toggling of multiple buttons (shift functionality) the number of functions may surpass the number of buttons. Due to the integration in the RT communication of the robotic system the buttons can both be used as RT-capable sensors and trigger besides actions of the robot itself also actions of 3rd party devices in the same RT network.

The main advantages for the *robot user* are:

- *Usability:* The buttons simplify the interaction with the robotic system. The user can switch the operation mode, select a workflow step or confirm an action directly at the robot.
- *Easy integration in existing workflow:* Less separate input devices are required and the interaction with the robotic system is no longer exclusively bound to separate input devices.

REFERENCES

[1] U. Hagn, et al.. "The DLR MIRO: a versatile lightweight robot for surgical applications." Industrial Robot; 2008; 35(4): 324 – 36.

[2] U. Hagn, et al.. "DLR MiroSurge - A Versatile System for Research in Endoscopic Telesurgery." International Journal of Computer Assisted Radiology and Surgery; 2010; 5 (2): 183-93.

[3] S. Haddadin, et al.. "Requirements for safe robots: Measurements, analysis and new insights." International Journal of Robotics Research; 2009; 28(11-12): 1507-27.

[4] T. Bahls, et al.. "Extending the Capability of Using a Waterjet in Surgical Interventions by the Use of Robotics." IEEE Trans Biomed Eng; 2016; 99.

[5] N. Padoy, et al.. "Statistical modeling and recognition of surgical workflow." Medical Image Analysis; 2012; 16(3): 632-41.

microCYCLOPS: A Robotic System for Microsurgical Applications

T.J.C. Oude Vrielink, A. Darzi, G.P. Mylonas
Department of Surgery and Cancer, Imperial College London
t.oude-vrielink15@imperial.ac.uk

INTRODUCTION

In previous work a prototype named *neuroCYCLOPS* was developed and tested [1]. The prototype is a manually controlled tendon-driven instrument based on the original *CYCLOPS* concept [2]. The *neuroCYCLOPS* is combined with the cylindrical tissue retraction device Neuroendoport[SM] (NEP) and allows for accurate dissection of deep-seated brain lesions [3]. Experimental validation on an FLS pick-and-place task demonstrated accurate and safe control, without significant increase in task execution time when compared to rigid instruments. Additionally, the device has a wider range of motion compared to standard rigid instruments (Fig. 1B). The current abstract focuses on the development of a robotic version of the *neuroCYCLOPS*. Although neurosurgery was initially targeted, tubular tissue retraction devices are used in many microsurgical applications, allowing the concept of the neuroCYCLOPS to be applied more broadly. Applications include *Transanal Endoscopic Microsurgery* (TEM) and *Laryngeal Microsurgery*. The ***micro**CYCLOPS* robotic system presented here is designed for these applications and to the authors' knowledge is the first of its kind.

PROTOTYPE DESIGN

Fig. 1 shows the prototype *microCYCLOPS* robot, which consists of a standard flexible endoscopic grasper (FB-19N-1, Olympus, Japan) that can be controlled in a master-slave configuration. The design is based on a cylindrical tissue retractor with 21mm inner diameter.

In this design, 8 tendons are used with the tendon-driven CYCLOPS configuration, independently actuated by servomotors (2232S024BX4 CCD-3830 + 22F 25:1 Brushless DC, Faulhaber, Germany). The tendons are guided through Bowden cables to the remote motor units, thereby reducing the weight and size of the robot inserted in the tissue retractor. The 8 tendons are used for the actuation of 4 degrees of freedom (DOF), *y* and *z* translations, and *yaw* and *pitch* as shown in Fig. 1C. For movement along the *X*-axis two motors (Dynamixel RX-24F, Robotis, Korea) are symmetrically actuated to operate a rack and pinion mechanism (indicated in Fig. 1D as D1 and D2). The rack is incorporated with the inner-tube/scaffold of the *microCYCLOPS*. By using two motors, asymmetrical forces are avoided and in further developments independent actuation of each motor can be used for the actuation of two instruments for bimanual control. A third Dynamixel motor (coupled at D3, Fig. 1C) is used for the rotational movement of the tool, which is achieved by using the torsional rigidity of the grasper. A servomotor (S3305, Futaba Corporation, Japan) is used to actuate the opening and closing of the grasper. The majority of the system is 3D printed using an Ultimaker 2+ Extended (Ultimaker BV, The Netherlands).

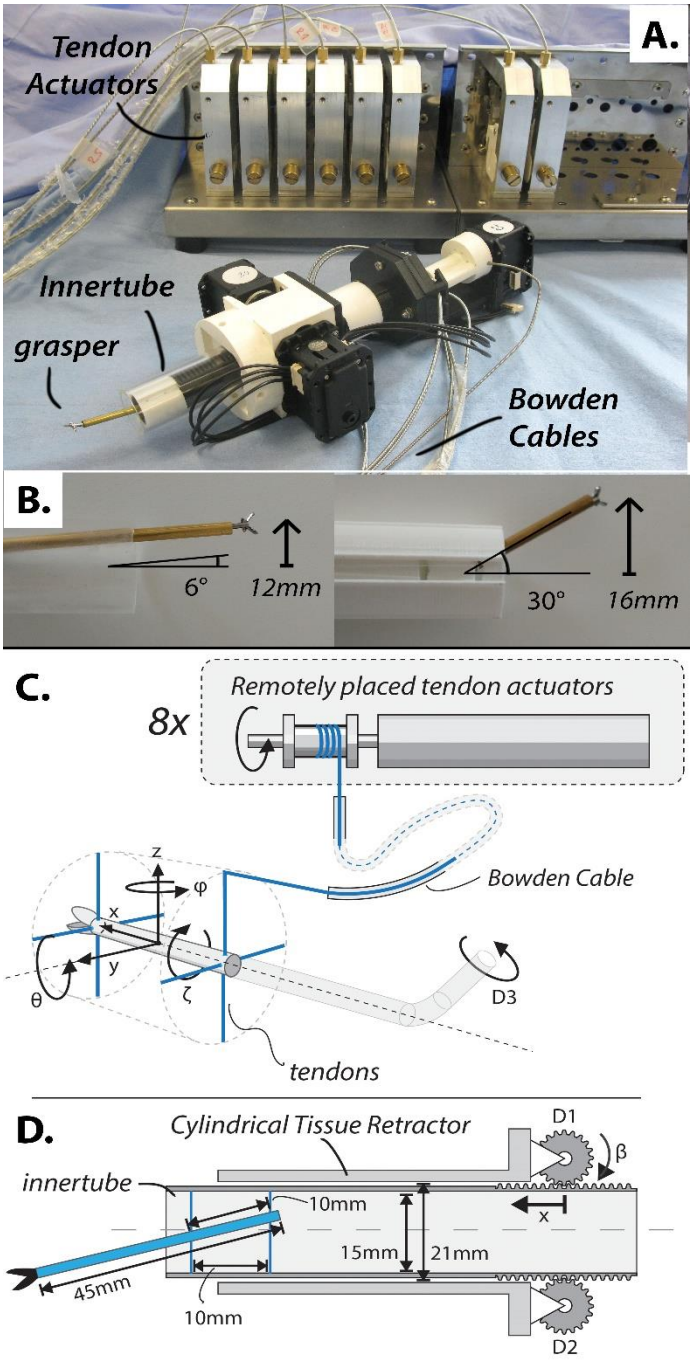

Fig. 1 – A) The *microCYCLOPS*, including the tendon motor actuators **B)** The increased range of motion of the neuroCYCLOPS (right) compared to rigid instruments (left), shown in earlier work [1] **C)** The CYCLOPS tendon configuration using 8 tendons to actuate *y*, *z*, θ and ϕ. The rolling motion of the instrument (ζ) is achieved by coupling the instrument to a motor at D3. **D)** The tubular scaffold placed into the cylindrical tissue retractor, actuated in *x* by two motors D1 and D2.

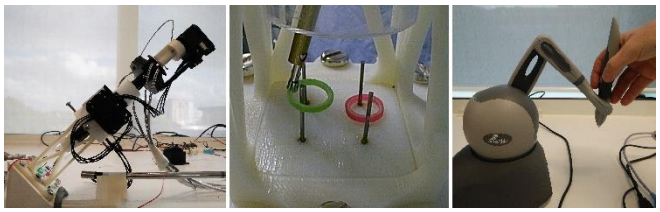

Fig. 2 – **Left:** The device placed into the setup for the pick-and-place task, and scope placement under an angle of 45 degree. **Middle:** View from the scope. **Right:** The orientation of the stylus master controller.

At the motor side, load cells (LCL-020, Omega Engineering Inc, USA) are included to measure the tension in the tendons, and acquired using a DAQ (i100, GW Instruments Inc, USA). A Phantom Omni (Geomagic, USA) haptic device was used for the master side of the system.

In particular for microsurgical applications, there are multiple reasons why it may be desirable to have 8 tendons driving 4 DOF, while 6 tendons would be sufficient [2]. Firstly, using 8 tendons allows for a larger reachable workspace. Secondly, by actuating the *X*-axis independently from the tendon-driven mechanism, an even larger reachable workspace is realized. The original CYCLOPS uses the tendons for actuation along the *X*-axis, achieved by increasing the distance between the entry points on the scaffold. However, this is at the expense of the dexterous workspace due to singularities and less control over the force exertion of the end-effector. By decoupling movement of the *X*-axis, the dexterity in the DOF denoted by *y*, *z*, θ and ϕ in Fig. 1C is not compromised, while also allowing for large movement along the *X*-axis. Lastly, the redundancy of the antagonistically placed tendons can be used for finer control of the stiffness in each of the available DOF, resulting in an extra tuneable parameter used for robotic control [4]. It should be emphasized that this includes control of stiffness in the x-direction, showing that the singularity in this direction can be used in our benefit. For surgical applications, a controllable stiffness can be useful to prevent damage to delicate tissues, while still offering higher rigidity when required.

EXPERIMENTAL SETUP

A pilot study has been conducted to compare the robotic prototype against conventional rigid instruments. During the pick-and-place task, completion time and amount of clashes of the instruments with peripheral structures were measured. The amount of clashes is considered a metric for stability and controllability of the instrument, and was recorded by making the instruments (anode) and task environment (cathode) conductive, and detecting contact with an Arduino Mega (Arduino, Italy). The workspace in which the task was performed was based on a previous study, indicating a 30x30x90mm opening for neurosurgical applications [5]. During the experiments, a 3D endoscope (Endoeye Flex 3D, Olympus, Japan) was used for visualisation, and placed in an orientation of 45 degrees. The stylus of the master device was oriented vertically to coincide with the end-effector orientation on the endoscope screen (Fig. 2). Haptic feedback of the master device was not used. After each task, the novice participants filled in a NASA-TLX questionnaire, a standardized method to assess subjective workload during tasks. The instrument first used by each participant was randomized to reduce bias towards a specific instrument.

RESULTS

The results for n = 11 participants are shown in Table 1. The initial study showed no significant difference in time (p=0.091), or reduction of amount of clashes when comparing the *microCYCLOPS* with rigid instruments (p=0.172, one-tailed paired t-test). Participants perceived a lower workload during the task when using the microCYCLOPS (p = 0.001).

Table 1 – Results of the pick and place task for n = 11. *$p < 0.05$

	microCYCLOPS	***Rigid Instruments***	***p-value***
Clashes [#]	16.6 ± 12.8	21.6 ± 11.48	0.174
Time [s]	47.0 ± 19.6	38.0 ± 12.2	0.091
NASA-TLX [-]	45.5 ± 18.6	67.1 ± 23.4	**0.001***

DISCUSSION

We have demonstrated a fully robotized extension of the *neuroCYCLOPS* system. The study has shown that the *microCYCLOPS* could achieve performance comparable to rigid instruments, with the novice participants perceiving the workload lower when compared to rigid instruments currently used in practice. It is important to take into account that this first prototype has not been optimized for intuitive control, haptic feedback or with additional human enhancing capabilities (e.g., motion scaling and guidance). Therefore it is likely that future developments will yield better results in terms of controllability and intuitive control of the *microCYCLOPS*. Current development focuses on the introduction of a second instrument for bimanual control and the evaluation of this concept for different microsurgical applications.

This work is supported by the ERANDA Rothschild Foundation.

REFERENCES

[1] T.J.C. Oude Vrielink et al., "NeuroCYCLOPS: A Novel System for Endoscopic Neurosurgery," in *Hamlyn Symp. for Medical Robotics*, London, 2016 *(in press)*

[2] G.P. Mylonas et al., "CYCLOPS: A versatile robotic tool for bimanual single-access and natural-orifice endoscopic surgery," in *IEEE Int. Conf. Robotics and Automation (ICRA)*, Hong Kong, 2014, pp. 2436-2442

[3] A.B. Kassam et al, "Completely endoscopic resection of intraparenchymal brain tumors: clinical article," in *J. neurosurgery*, vol.110, no. 1, pp. 116-123, 2009

[4] B.J. Yi et al, "Geometric characteristics of antagonistic stiffness in redundantly actuated mechanisms," in *IEEE Int. Conf. Robotics and Automation (ICRA)*, Atlanta, 1993, pp. 654-661

[5] H.J. Marcus et al., "Endoscopic and keyhole endoscope-assisted neurosurgical approaches: a qualitative survey on technical challenges and technological solutions," in *British journal of neurosurgery*, vol. 28, no. 5,pp. 606-610,2014

Making a clinical device from a laboratory prototype: from Prosper to Prosper^{OR}.

B.Veron[1], N.Hungr[1], J.Troccaz[1]

[1]*Univ. GrenobleAlpes, CNRS, TIMC-IMAG Laboratory, Grenoble, France*
firstname.name@imag.fr

INTRODUCTION

Prostate brachytherapy consists in inserting radioactive seeds in the prostate in case of localized cancer in order to kill cancerous cells whilst sparing healthy tissue or organ at risks (e.g. urethra, rectal wall). These seeds are inserted into the prostate using needles introduced through a guiding grid connected to a transrectal ultrasound probe. To handle limitations or difficulties of the conventional procedure, many systems have been designed worldwide (see [1] for a broad overview of systems existing in 2015). Developed systems provide different levels of assistance: from guiding the needle by positioning and orienting a guide out of the patient [2], to automatic insertion of the needle [3] or even injection of radioactive seeds through the needles into the patient [4]. Some of the systems also include ultrasound probe positioning and motion. Despite a very large number of prototypes, very few systems entered the operation room (OR). As far as we know, regarding brachytherapy applications, only the B-Rob system [2] developed by Johns Hopkins University and Queens University has been evaluated on patients. A feasibility study (NCT00381966 on ClinicalTrials.gov) was ended in 2012. The results of this study [5] confirm the interest of the robotic assistance in the needle placement. The EUCLIDEAN system [4], a fully automated device with needle insertion and seed injection, received FDA clearance for investigational studies. Reliability on phantoms was thoroughly studied [6] but, to the best of our knowledge, no clinical studies have been published. The reasons for such limited number of clinical evaluations and industrial developments come from the many issues to be solved such as safety, sterilizability, electromagnetic compatibility. The more invasive and autonomous is the robot, the most constraining and demanding are the regulations. In this paper, we will describe how the Prosper robot [3] has been modified based on our laboratory and cadaver experiments to be turned into a version usable in the OR for a clinical evaluation.

MATERIALS AND METHODS

PROSPER laboratory version: this system (shown in Figure. 1) was designed as a proof of concept for automatic brachytherapy. It allowed us to develop methods to calibrate the robot with the 3D transrectal ultrasound (TRUS) probe and to automatically correct positioning errors due to prostate motion and deformation using 3DUS to 3DUS registration. It consist of two modules: one 5 degrees of freedom (DoFs) module for positioning and orienting the needle close to the patient skin and a 2 DoFs module for needle insertion in the prostate. It was studied on both phantoms and cadavers [3]. These studies showed very promising results allowing to position a needle with an error lower than 2 mm considering prostate motion up to 7 mm.

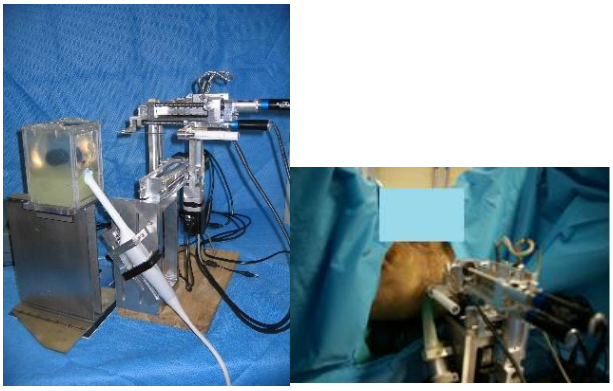

Figure. 1. Laboratory set-up of PROSPER (left: experiments on a deformable phantom; right: cadaver experiment).

Nevertheless, the system also showed some critical limitations. First, cadaver studies showed a lack of rigidity of the robot while inserting the needle. Moreover, from a clinical point of view, the system showed sterilization issues, and safety concerns because of the automatic needle insertion and the way the robot handled the needle (impossibility to quickly remove the needle).

PROSPER^{OR} version: this new system (shown in Figure. 2) was designed to deal with the limitations previously mentioned. Off-the-shelf components (Faullhaber brushless motors couple with THK linear carriage for instance) were re-designed. A global quality approach and risk analysis were undertaken leading to this new system with extra capabilities.

RESULTS

First, the robot workspace was increased to allow treatment of prostate with a larger volume and extra passive DoFs were added to ease the robot positioning with respect to the patient. Moreover, the structure of the system was reinforced and a fixation system to the OR table was added. This allows to make the system more rigid and ensure an accurate needle insertion.

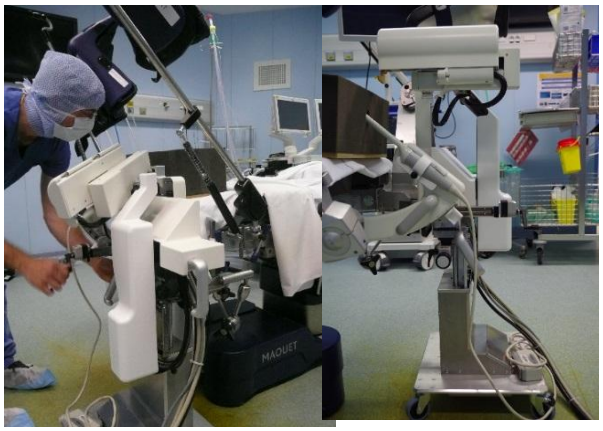

Figure. 2. Set-up of the PROSPER^{OR} systemin the OR.

To tackle with security and sterilization, protection hoods covering all the mechanical parts of the robot were designed. All hoods are made of sterilizable biocompatible plastic and the hoods being in the close environment of the needle and/or in contact with it are designed to be removable and autoclave compatible. Thus, the sterilization process is simple, fast and safe as it relies on the most standard sterilization procedure. Moreover, the needle holder was modified to enable a safe and fast removal of the needle at any time. The insertion procedure was reviewed to enable manual and/or automatic insertion. In both insertion modes, the robot acts as a needle guide positioning the needle in accordance with the trajectory chosen on the ultrasound images, and a programmable mechanical stop limits the insertion depth based on the target planned. If the manual insertion mode is selected, the needle insertion is let to the urologist.

Finally, for the system to adapt with a number of TRUS probes (brachytherapy side-fire or biopsy end-fire), a probe holder was designed. It allows to adjust the probe position and orientation in the sagittal plane. The system was delivered in 2015 and is currently under tests to validate its electromagnetic compatibility and its sterilization process.

CONCLUSION AND DISCUSSION

A very strict quality approach and risk analysis were led to bring the new PROSPER^{OR} system to the patients. Specific tests were designed to ensure the quality and safety of the system on both mechanical and software point of view. The system is currently under strong quality tests, including registration with the TRUS probe, accuracy measurement on synthetic phantoms, evaluation of the sterilization process and electromagnetic compatibility.

To ensure the proper use of the PROSPER^{OR} system, a new state-machine working with the CamiTK framework [7] has been designed. It allows, first to simply and rapidly implement complex medical protocols, second to ensure compliance with the established protocol in use.

Finally, a medical protocol is currently under discussion with urologists to bring the robot on patients and evaluate its accuracy and benefits to patients.

REFERENCES

[1] Podder, Tarun K., et al. "AAPM and GEC-ESTRO guidelines for image-guided robotic brachytherapy: Report of Task Group 192." *Medical physics* 41.10 (2014): 101501.

[2] Fichtinger, Gabor, et al. "Robotic assistance for ultrasound-guided prostate brachytherapy." *Medical image analysis* 12.5 (2008): 535-545.

[3] Hungr, Nikolai, et al. "A 3-d ultrasound robotic prostate brachytherapy system with prostate motion tracking." *Robotics, IEEE Transactions on* 28.6 (2012): 1382-1397.

[4] Yu, Y., et al. "Robotic system for prostate brachytherapy." *Computer Aided Surgery* 12.6 (2007): 366-370.

[5] Song, Danny Y., et al. "Robotic needle guide for prostate brachytherapy: clinical testing of feasibility and performance." *Brachytherapy* 10.1 (2011): 57-63.

[6] Podder, Tarun K., et al. "Reliability of EUCLIDIAN: An autonomous robotic system for image-guided prostate brachytherapy." *Medical physics* 38.1 (2011): 96-106.

[7] C. Fouard, A. Deram, Y. Keraval, E. Promayon. CamiTK: a Modular Framework Integrating Visualization, Image Processing and Biomechanical Modeling. In Soft Tissue Biomechanical Modeling for Computer Assisted Surgery, Y. Payan (ed.), pp. 323-354, 2012.

Teamwork Monitoring in Robotic Surgery: A Role for Computer Vision and Machine Learning?

Christopher L. Tarola[1], Pietro Perona[2], Yisong Yue[2], Stephen Yule[3], Jennifer Gabany[1], Ashwin Thangali[4] and Marco A. Zenati[1,3]

Medical Robotics & Computer Assisted Surgery Laboratory, Division of Cardiac Surgery, Veterans Affairs Boston Healthcare System, Boston, MA[1], Vision Laboratory, California Institute of Technology, Pasadena CA[2], Harvard Medical School, Boston MA[3], Vecna Inc., Cambridge, MA[4]
Christopher.Tarola@londonhospitals.ca

INTRODUCTION

The introduction of robotic surgery (RS) has modified the traditional placement of the surgical team in the operating room (OR): the surgeon, operating the master telemanipulation system at the console, no longer has physical proximity to the patient and the remaining surgical team. This unusual team placement, coupled with the complexity of remotely controlled surgery and the increased cognitive load, modifies teamwork in ways that are critically paving the way for new forms of error and ultimately negatively affecting patient safety and team performance.[1] Although human error is inevitable, anticipation and early management remain vital for optimal patient care. In a recent analysis of the United States' Food and Drug Administration Manufacturer and User Facility Device experience database over the last 14 years, the authors demonstrated an increasing number of adverse events related to RS being reported.[2]. The authors recommended introducing new safety engines for monitoring RS procedures.

Investigational efforts to enhance surgical quality and safety have shifted from strategies targeting individuals, i.e. surgeons, to the operating team. As such, a number of interventions including team training and surgical checklists have been implemented to improve teamwork and surgical safety, however, are limited by a lack of sensor-based (i.e. video recording) measurement approaches to observe team dynamics and performance.[3]

Sensor-based measurement allows for the real-time, automated collection of activity data, and offers an opportunity to investigate the efficiency of the surgical team during the intra-operative phase. In its current state, however, surgical safety research relies on human observers manually collecting potentially biased data for the duration of a surgical procedure.

Machine learning and machine vision, however, are yet to be applied to the robotic or non-robotic assisted cardiac surgery OR (COR), but represent additional tools to investigate human factors. Our objective is to leverage these disciplines to determine patterns of human behavior (e.g. surgical flow disruptions) in the COR that predispose to errors, error cycles and adverse events.

MATERIALS AND METHODS

This pilot investigation was initiated to design a prototype tool to identify risk factors for surgical flow disruptions (surrogates for errors) inherent between members of the COR team. The operating environment was captured utilizing two strategically placed, high-definition RGB cameras. After obtaining IRB approval and informed consents from all participants, we acquired audio/video sequences from non-emergency cardiac surgery procedures (N=14), and applied computer vision software solutions to identify and track healthcare professionals (HCP) in the COR. These software tools has been previously applied in two non-healthcare related fields: computational ethology (FlyTracker software in MathLab)[4] and human factors analysis in micro-gravity environments (AVIMA software, NASA International Space Station). For FlyTracker, two technologies (boosted classifiers and deep networks) are utilized in the tracking software. Tracking is performed via repeated detection and cross-time association, and identification using facial analysis is used to disambiguate individuals when they cross paths or bump into each other.

For detection of COR traffic (a major source of surgical flow disruptions) we propose dedicated software to process video streams to estimate the number of HCP and their trajectories. Algorithmic components of the traffic analysis system include color-based event detection and person detection and tracking. The tracking algorithm temporally filters the person detection bounding boxes to yield personnel trajectories. The temporal filtering step reduces false alarms and improves the accuracy of person counting integrate a mixture-of-Gaussians (MOG) background

modeling technique for representing background structures and for updating this representation when entities appear and disappear. Integration of a Multi-Target Tracking (MTT) algorithm is also applied to track HCP and compute their trajectories. The MTT algorithm integrates detections computed in each new video frame to update and extend the trajectories of tracked entities. Data association between tracked entities and detected entities is performed using the Hungarian algorithm. A new detection is associated with a tracked entity if there is a large overlap between the predicted and detected regions of interest.

RESULTS

We collected comprehensive video and audio recordings from 14 non-robotic assisted cardiac surgery cases. The tracker software was successfully applied and captured surgical team traffic movements throughout the COR. The tracking software was able to distinguish team member's faces from other operating room equipment (Figure 1). The tracking software determine the total number of ambulatory movements in each case, the distribution of the number of ambulatory movements between different team members, the primary ambulatory pathways utilized in the OR, the rate of procedural interruptions, and the primary purpose of ambulatory movements within each case (Figure 2).

CONCLUSION AND DISCUSSION

Sensor-based recording (e.g. video) has a number of potential significant applications for quality and safety improvement in the COR. As opposed to reliance on individuals to report safety issues intra-operatively, video recording has the ability to record how healthcare personnel interact during the intra-operative period, both with other members of the operative team and with surgical equipment. The utility of this data for research and, more importantly, clinical purposes is directly related to the speed at which this data can be collected, analyzed, and interpreted. In a recent report, analyzing 1 minute of communication events in the robotic OR took an average of 30 minutes and the authors recognized that it was very time-consuming.[5]

An automatic computer-vision based analysis of team activities would improve learning and accelerate implementation of patient safety strategies in the COR. We plan to apply these techniques to RS in the near future.

FIGURES

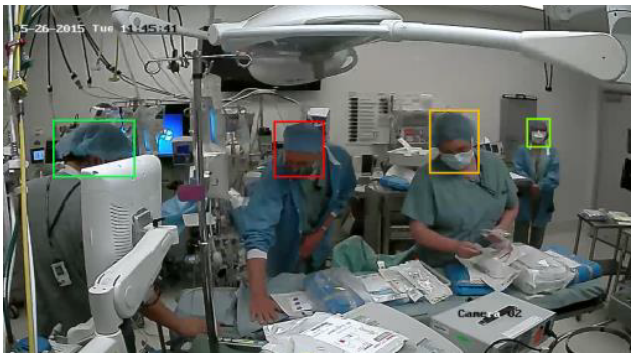

Figure 1: Still-frame of video annotation software capturing operating room preparation by the surgical team.

Figure 2: Applying AVIMA's filtering algorithms to the COR video.

REFERENCES

1. Zenati MA, Maron JK. "Communication and teamwork failure as a barrier to robotic surgical safety" in proceedings of the 3rd Joint Workshop on New Technologies for Computer Robot Assisted Surgery (CRAS) 2013;142-5.
2. Alemzadeh H, Raman J, Leveson N, Kalbarczyk Z, Iyer RK. "Adverse events in robotic surgery: A retrospective study of 14 years of FDA data." PLoS One;2016;11(4):e0151470.
3. Rosen MA, Dietz AS, Yang T, et al. "An integrative framework for sensor-based measurement of teamwork in healthcare." J Am Med Inform Assoc; 2015;22(1):11-8.
4. Anderson DJ, Perona P. "Toward a science of computational ethology." Neuron;2014;84:18-31.
5. Tiferes J, Hussein AA, Bisantz A, et al. "The loud surgeon behind the console: Understanding team activities during robot-assisted surgery. J Surg Educ;2016;73(3):504-12. [1]

Dr. Zenati was funded by NIH grants No. HL078839 and HL126896.

Safety enhancement in robotic neurosurgery through vessel tracking

S. Moccia[1,2], F. Prudente[2], E. De Momi[1] , C. Riviere[3], A. Perin[4], R. Sekula[5], L. S. Mattos[1]

[1]*Department of Advanced Robotics, Istituto Italiano di Tecnologia, Genoa, Italy*

[2]*Department of Electronics, Information and Bioengineering, Politecnico di Milano, Milan, Italy*

[3]*Robotics Institute, Carnegie Mellon University, Pittsburgh, USA*

[4]*Besta NeuroSim Center, IRCCS Istituto Neurologico C. Besta, Milan, Italy*

[5]*Department of Neurological Surgery, University of Pittsburgh, Pittsburgh, USA*

sara.moccia@iit.it

INTRODUCTION

Meningioma is a common type of primary intracranial neuroplasm that arises from the middle layer of meninges. Surgery is the gold standard treatment for meningiomas, since it lowers patient mortality or after-treatment morbidity. Large vessel preservation and bleeding avoidance are of primary importance during the surgery, since they strongly influence surgical outcomes. Bleeding requiring transfusion is recognized as one of the most common complications (10.2%) [1].

The final goal of this research is to provide a tool for safety enhancement in robotic neurosurgery through vessel tracking.

During surgery, the primary imaging source to obtain a magnified view of both brain and cerebral vessels is microscopy (Fig. 1). Main challenges in vessel segmentation and tracking arise from partial or total vessel occlusion (e.g. due to surgical tools, smoke and saline solution).

A large literature on vessel segmentation and tracking algorithms exists, and a recent review can be found in [2], where algorithms are divided into (i) pattern recognition techniques, (ii) matched filtering, (iii) vessel tracking/tracing, (iv) mathematical morphology, (v) multiscale approaches, (vii) model-based approaches and (viii) hardware-based approaches.

In this paper, a Geometrical Deformable Model-based approach (GDM) is used to perform vessel segmentation in the microscopy frames, and Kalman filtering is used to track the segmentation between consecutive microscopy frames. The GDM initialization here proposed requires minimum manual intervention, which consists in the selection of two seed points in the first microscopy frame that are then automatically connected employing a Minimum Cost Path (MCP) algorithm.

MATERIALS AND METHODS

The workflow of the proposed method is shown in Fig. 2. First, the user was required to initialize the segmentation algorithm by selecting two seed points, $\boldsymbol{p_1}$ and $\boldsymbol{p_2}$, in the first microscopy frame. The seeds were then connected using a MCP algorithm [3]. MCP finds the curve $C_{\boldsymbol{p_1 p_2}}$ that minimizes the cost path between $\boldsymbol{p_1}$ and $\boldsymbol{p_2}$, according to a tensor metric M.

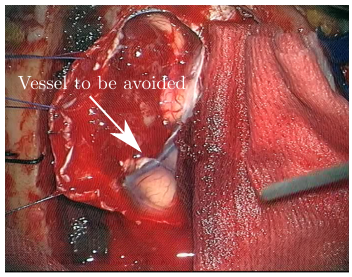

Figure 1. Microscopy frame recorded during meningioma surgery. The white arrow indicates the vessel to be avoided.

In order to drive the path evolution along the vessel main axis, an anisotropic M was built such that:

$$M = v * \Lambda * v^T$$

where $v = [v_1; v_2]$, with v_1 and v_2 image Hessian eigenvectors, and $\Lambda = [\lambda_1\ 0; 0\ \lambda_2]$, with $\lambda_1 \leq \lambda_2$ image Hessian eigenvalues. The cost path minimization problem was solved through the computation of the Minimal Action Map (MAM), whose values can be interpreted as the arrival time of a propagation front that starts from $\boldsymbol{p_1}$, which is the only MAM minimum, and moves with velocity dependent on M. The minimum path was retrieved with gradient descent (Runge-Kutta) from $\boldsymbol{p_2}$ on the MAM.

The $C_{\boldsymbol{p_1 p_2}}$ was used to initialize a GDM. GDMs are well known to successfully face complex vessel architectures, such as bifurcation and vessel kissing, as well as image intensity drops and non- uniform illumination [2]. GDMs consider curves ($\boldsymbol{S}$) that deform according to the curve-evolution theory described by:

$$\frac{\partial \boldsymbol{S}}{\partial t} = Z * \boldsymbol{n}$$

in which Z is called speed function and $\boldsymbol{n}$ is the unit normal to $\boldsymbol{S}$. In this research, distance regularized level set [4] was used to implement the $\boldsymbol{S}$ evolution since it guarantees the regularity of the level set ensuring stability during the evolution. The vesselness measure described in [5] was used to enhance vessels in each frame. The enhanced image was then used as speed function Z.

After having obtained the vessel segmentation in the first frame $I_{k=0}$, vessel tracking in the consecutive frames was performed exploiting Kalman filtering. For each frame $I_{k,k>0}$, the Kalman prediction of the vessel contour position provided the initialization for the $\boldsymbol{S}$ evolution in that frame. The $\boldsymbol{S}$ evolution was implemented using the GDM as in the first frame. The Kalman transition matrix was obtained by estimating the displacement between consecutive frames through Optical Flow (OF) [6].

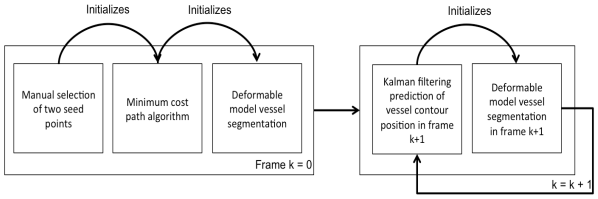

Figure 2. The workflow of the proposed algorithm for vessel segmentation and tracking.

Matlab® 2015b was used for the implementation of the described algorithms.

The proposed method was tested on a microscopy video recorded during a meningioma resection intervention at the Istituto Neurologico Carlo Besta, Milan, Italy. The patient gave informed consent.

RESULTS

Vessel segmentation was numerically evaluated with respect to manual segmentation performed by an expert, elected as gold standard. The evaluation was done in terms of Accuracy (Acc), Sensitivity (Se) and Specificity (Sp), where Acc is the proportion of true results, both True Positive (TP) and True Negative (TN), among the total number of pixels. Se measures the proportion of positives, both TP and False Negative (FN), correctly identified. Sp measures the proportion of negatives, both TN and False Positive (FP), correctly identified. Segmentation results are: Acc = 0.99, Sp = 0.99 and Se = 0.67.

Fig. 3 shows (a) the MAM and (b) the resulting minimum cost path computed in the first video frame. Fig. 4 depicts (a) the speed function Z computed for the first frame and (b) the resulting segmentation obtained with the GDM. Fig. 5 shows (a) the OF computed for two consecutive frames and (b) the segmentation obtained for the second frame.

CONCLUSION AND DISCUSSION

The proposed method showed to be able to face image noise, non-uniform illumination and intensity drops. The Kalman filtering successfully tracked the vessel contour, providing an automatic initialization for the segmentation in the consecutive frames. This way, the only user interaction required consisted in the selection of two seed points in the first frame.

This preliminary analysis on one video recorded during a real surgery showed the method to be effective.

Future work deals with real-time implementation. Moreover, the next step is the inclusion of OF-failure recognition strategy to ensure accurate tracking in case of sudden and prominent field of view changes.

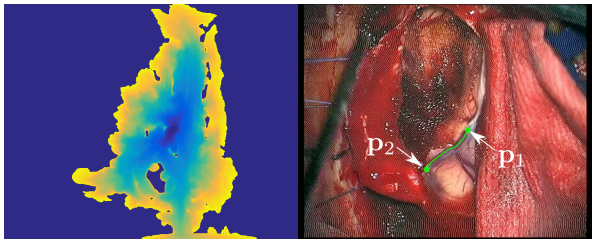

(a) (b)

Figure 3. (a) Minimal action map computed for the first frame and (b) resulting minimum cost path. The white arrows indicate the two manually selected seed points.

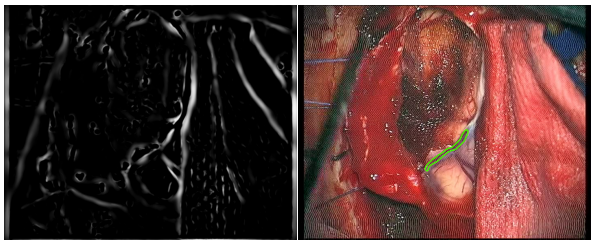

(a) (b)

Figure 4. (a) Speed function for the geometric deformable model evolution. (b) Segmentation obtained for the first microscopy frame.

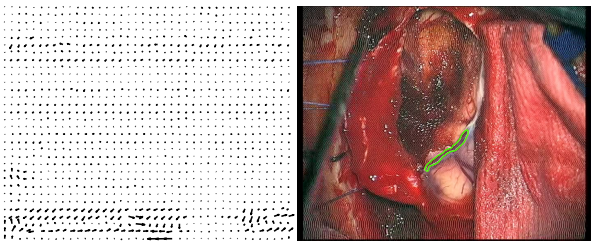

(a) (b)

Figure 5. (a) Optical flow describing the displacement between the first and second frame. (b) Kalman prediction (white) and obtained segmentation (green) for the second frame.

REFERENCES

[1] Michalak S, et al., "Predictors of complications and mortality in cerebrovascular surgery," *Neurosurgery*; 2016.

[2] Fraz MM, et al., "Blood vessel segmentation methodologies in retinal images–a survey," Computer methods and programs in biomedicine; 2015; 108(1): 407-433.

[2] Deschamps T, et al., "Fast extraction of minimal paths in 3D images and applications to virtual endoscopy," Medical image analysis; 2001; 5(4): 281-299.

[4] Chunming L, et al., "Distance regularized level set evolution and its application to image segmentation," Image Processing, IEEE Trans on, 2010; 19(12): 3243–3254.

[5] Frangi AF, et al., "Multiscale vessel enhancement filtering," Medical Image Computing and Computer-Assisted Interventation—MICCAI, 1998; 130-137.

[6] Sun D, et al., "Secrets of optical flow estimation and their principles," Computer Vision and Pattern Recognition (CVPR), IEEE Conference on, (2010), 2432-2439.

Hip Fracture Reduction Robot

Shekhar Gupta[1], Shwetha Macheri Ravishankar[1], Maarten Griffioen[1], Robert Babuška[1], and Taco Klem[2]

[1] *Delft Center for Systems and Control, Delft University of Technology, the Netherlands*
[2] *Sint Franciscus Gasthuis, Rotterdam, the Netherlands, e-mail: r.babuska@tudelft.nl*

1 INTRODUCTION

Currently, the treatment of choice for the multiple variety of intertrochanteric femur fracture is the standard technique of intramedullary nailing. Intramedullary nailing is a surgically optimized minimally invasive surgery which is carried out in two steps: fracture reduction and intramedullary fixation. We present a novel approach to automate the femur fracture reduction using a two degree of freedom (DOF) robot. The state-of-the-art manual fracture reduction has drawbacks like malalignment and radiation exposure to the patient and the operating team. By automating the reduction, we can overcome these disadvantages as there will be less radiation exposure and no scope for manual errors.

Warisawa et al. [1] developed a six-DOF robot for open femur fracture reduction; however our focus is on non-sterile closed reduction of intertrochanteric femur fracture, which does not involve adduction movement. During closed reduction, the patient's leg is attached to a traction table (Figure 1) and a shoe is put on the foot corresponding to the broken femur. The alignment of the broken femur is achieved by applying traction and endorotation or exorotation through the patient's leg. The surgeon first pulls and then rotates the patient's leg about the longitudinal axis until the fracture is aligned. The alignment is confirmed by fluoroscopic imaging in axial and anterior-posterior views. This type of reduction does not involve any lateral forces and therefore a two-DoF robot can perform the reduction by imitating the reduction procedure as done by the surgeon.

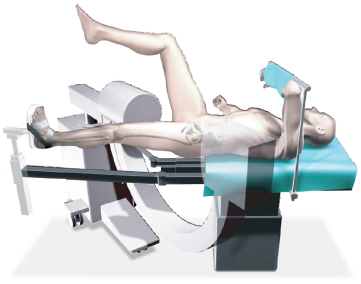

Figure 1: Patient on the traction table. Source: Stryker [7].

The robot can, in principle, perform this task much more accurately by using a geometric model of fractured bone and appropriate force control, thereby minimizing the soft tissue trauma to the patient. The robot can also speed up the procedure and therefore reduce the radiation exposure on the patient and medical staff.

In order to properly dimension the system and to select the actuators, we need to know the force, torque and the displacement during reduction. Maeda et al. [2] reported that the maximum force and torque during fracture reduction of proximal femoral fractures are 294.9 N and 4.4 Nm, respectively. However, an experienced surgeon estimates the maximum force to be 500 to 1000 N. Since the difference from the values reported in [2] is quite large, new measurements were performed. In addition to the force measurements reported in the previous work, we measured the displacement and the rotation angle during fracture reduction. The measurement data were used to obtain the relationship between the force and displacement and between the torque and rotation angle of the fractured leg. The measurement setup, procedure, data processing and the preliminary results are discussed below.

2 MEASUREMENT SETUP

During reduction, the surgeon uses the movable shaft of the traction table to pull the patient's leg and then uses the lead screw to fine tune the pull based on the fluoroscopic image data. We have equipped the traction table with a force-torque sensor (A), sonar sensor (B), laser sensor (C) and an inclinometer (D), see Figure 2.

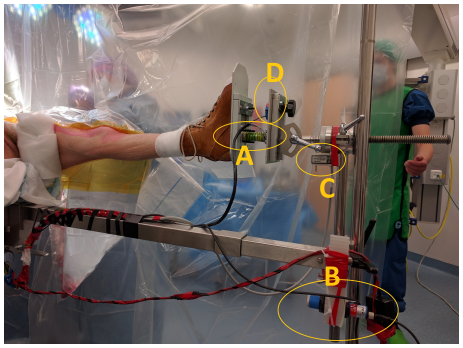

Figure 2: Measurement setup.

The force-torque sensor measures the amount of force and torque applied by the surgeon during reduction. The sonar sensor measures the distance moved by the shaft and the laser sensor is used to measure the distance moved by the leg during fine tuning. The inclinometer measures the angle of rotation of the patient's leg during reduction.

We have also recorded the patient parameters such as age, gender, weight, height, the length of the patient's leg, the thickness of the patient's thigh and the percentage of fat. This data will be later used to correlate the force and torque applied with the patient parameters.

3 MEASURED DATA AND MODEL

We have measured four reductions so far. During the reduction, the surgeon applied two to three consecutive pulls on the movable shaft of the fracture table and then fine-tuned the displacement using the lead screw. We used the recorded force and torque data to model the patient's leg as a double spring and a damper system as shown in Figure 3. Assuming that all the muscles can be lumped into one single equivalent muscle, the model is derived from Hill Muscle Model without any activation force.

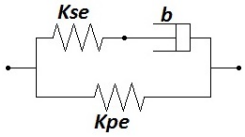

Figure 3: Double spring and a damper model.

Figure 4 shows force, torque, displacement and angle during reduction with respect to time. Surgeon applies two impulse forces to attain the required amount of pull, these can be seen as two peaks in the force graph followed by decline in muscle force to a steady state value due to muscle relaxation. Since the muscular forces are nonlinear, each of these peaks has been modelled as a double spring and a damper system giving us a finite dimensional piecewise spring-damper system. This allows us to do practical parametric identification of the model while preserving its spring-damper nature in its domain. Parametric identification was done using nonlinear least squares method. Figure 4 shows a comparison between the measured and modelled force and torque applied during reduction. This model will be used to control the robot by predicting the force and torque required for reduction.

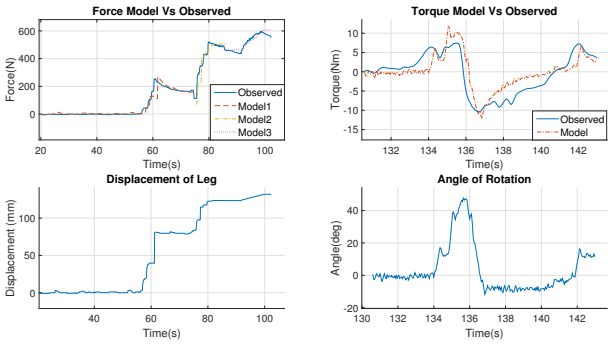

Figure 4: Model and Observed Data during Fracture Reduction

The force applied to the patient's leg during reduction depends on the patient's muscular strength, BMI, age and gender. The torque required for the rotation of the leg depends on the type of the fracture and also on the patient's parameters. The angle of rotation at the hip can be calculated from the Fluoroscopic C Arm images prior to operation. The maximum force applied during reduction was found to be 769 N and the maximum torque was 17.5 Nm.

4 ROBOT DESIGN

The robot will eventually autonomously carry out the reduction by applying the traction force and rotation torque in a way similar to the procedure currently executed by the surgeon. The design requirement for the two-DOF robot are obtained from the measurement data and are as follows: peak force 800 N, peak torque 20 Nm, linear range of motion 300 mm, rotational range of motion $\pm 60°$, maximum linear speed 5 mm/s, maximum rotational speed 1 rpm.

A graphical user interface will display in real time the traction and rotation data to the surgeon, so that the surgeon can closely supervise the fracture reduction. The interface will enable the switching between the manual and the robotic system at any point during the reduction.

References

[1] Warisawa S., Ishizuka T., Mitsuishi M., Yonenobu K., Sugano N. and Nakazawa T., "Development of a femur fracture reduction robot," *IEEE International Conference*, 2004.

[2] Maeda Y., Sugano N., Saito M., Yonenobu K., Sakuma I. and Ishizuka T., "Robot-assisted femoral fracture reduction: Preliminary study in patients and healthy volunteer,"

[3] Joung S., Kamon H., Liao H., Iwaki J ., Nakazawa T. and Mitsuishi M., "A robot assisted hip fracture reduction with a navigation system," 2008.

[4] Graham A E., Xie S Q., Aw K C., Xu W L. and Mukherjee S., "Design of a Parallel Long Bone Fracture Reduction Robot with Planning Treatment Tool," 2006.

[5] Graham A E., Xie S Q., Aw K C., Xu W L. and Mukherjee S., "Robotic Long Bone Fracture Reduction," 2008.

[6] Shadmehr R. and Wise S P., "Computational Neurobiology of Reaching and Pointing,"

[7] Stryker "Gamma3 Long Nail R1.5 and R2.0" https://www.strykermeded.com/media/1310/gamma3-long-nail-r15-and-r20-operative-technique.pdf

Towards an Objective Assessment of Comfort and Ergonomics during Surgery

A. Shafti[1], B. Urbistondo Lazpita[1], O. Elhage[2], H. A. Wurdemann[3] and K. Althoefer[4]

[1]*Dept. of Informatics, King's College London,*
[2]*Dept. of Urology, Guy's Hospital, King's College London,*
[3]*Dept. of Mechanical Engineering, University College London,*
[4]*School of Electrical Engineering & Computer Science, Queen Mary University of London.*
ali.shafti@kcl.ac.uk

INTRODUCTION

Work related musculoskeletal disorders (WMSDs) are the result of issues in comfort and ergonomics within the workplace left unnoticed and unattended, and this is particularly a big issue in clinical and surgical environments. It is therefore critical that an assessment scheme for comfort and ergonomics be in place for regular checks in the surgical environment. There are methods and techniques proposed and currently in use for this purpose. These range from subjective questionnaires to observation-based measurement and scoring of joint angles involved in a posture and task and are used regularly in clinical and industrial environments alike and are popular due to their ease of use and lack of a requirement for specific expertise. However, this simplicity has the downside of lack of objectivity and/or thoroughness. Questionnaires are based on the interviewee's subjective understanding of comfort whereas observational methods don't take into account specific muscle activation and load patterns or the potential effects of dynamic postures.

A more thorough and objective understanding of comfort and ergonomics can be achieved by relying on a person's biological signals rather than their subjective opinion. Biological signals can provide precious information about human behaviour and allow assessment of different activities in terms of health and comfort [1]. The acquisition of such data has traditionally been limited to laboratory environments due to the size and complexity of the equipment as well as the expertise required to conduct the tests and make sense of the data. That is why such signals are not typically a part of comfort and ergonomics assessments methods, as they are to be conducted regularly in workspaces at a low cost. The parameters of interest are effort, comfort and ergonomics. Such information can be applied when designing new tools in different fields to ensure comfort and ergonomics for the user. Furthermore, a real-time objective assessment of comfort will allow for better interaction between automated intelligent systems such as robots with humans.

This work was supported by the Horizon 2020 Research and Innovation Programme under grant agreement 287728 in the framework of EU project FourByThree.

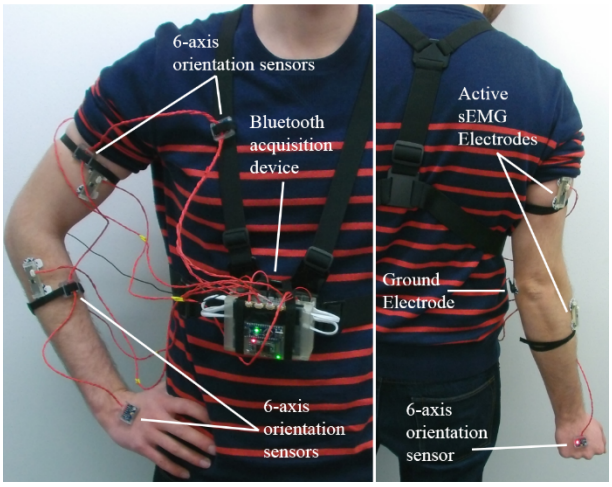

Figure. 1. The wearable muscle activity and joint angle estimation device used in this work to study correlation of different comfort and ergonomics assessment techniques.

This paper describes the use of low-cost, wearable sensors that bridge this gap, namely electromyography (EMG) and orientation sensors (accelerometer and gyroscope) to consider muscle activity and the kinematic behaviour of the body. Experiments are conducted to compare the results with those of already established subjective methods (Borg scale [2]) and observational tools (Rapid Upper Limb Assessment or RULA [3]).

MATERIALS AND METHODS

In order to compare the above mentioned methods, an experiment is designed to accommodate all techniques while subjecting the participants to tasks with different postures and varying levels of effort, comfort and ergonomics. The selected task is a buzz-wire test, i.e. a thick wire with random curves in different spatial planes that the participant needs to follow with a loop. The circuit connected to the buzz-wire will beep and record for every collision, called errors. Thus, performance can be rated as a mixture of time elapsed on each test and number of errors. The buzz-wire is set at three different height levels. The columns holding the buzz-wire are marked at 10cm intervals. The marking closest to the participant's shoulder height is selected as the mid-range level with the other two at ±20cm. The participant is seated at a desk, in front of the buzz-wire, and asked to only rely on movements in their dominant arm to conclude the test. The task is repeated 3 times at each height, with the order randomised. Participants are fitted

with a wearable sensing device consisting of orientation and EMG sensors that record the joint angles of the arm as well as muscle activity in the triceps brachii, biceps brachii, wrist extensor and wrist flexor muscles. The joint angles obtained through the orientation sensors are used to calculate an ergonomics score, using the RULA look-up table[1]. The Borg scale is applied by asking the participants to describe the level of discomfort they felt during the task with a number between 0 and 10, once the task is completed. The EMG sensors are custom built for this experiment, following recommendations of "Surface ElectroMyoGraphy for the Non-Invasive Assessment of Muscles" (SENIAM). The EMG signal was fed into a Bitalino® data acquisition device, which samples the data at 1 kHz, and transmits over Bluetooth. The orientation sensors are implemented with the InvenSense® MPU6050 breakout board and 'MotionApps' open source Arduino libraries developed by J. Rowberg. Ethical approval for these experiments was obtained, reference number: BDM/13/14-123.

RESULTS

Experiments are conducted on N=10 participants. A MATLAB script is created to analyse the EMG data. The signal for each muscle is normalised to the maximum voluntary contraction (MVC) of that muscle to allow for fair comparison. Each signal is then high-pass filtered with a 4th order Butterworth filter at 20 Hz, to remove motion artefacts before rectification. Once the signal is rectified, a sliding window (200ms) root mean square (rms) method is applied to acquire an envelope waveform. The average of this signal throughout the task is considered as the muscle effort score during that task. The RULA score obtained using the orientation sensors can vary in integer values between 1 and 9. The waveform resulting from the real-time variation in RULA score throughout the task is averaged to find a single measure of ergonomics for each task. The ANOVA statistical test is used to confirm or reject significant difference in mean values across the three different height levels of the buzz-wire test for the EMG, RULA and Borg scores. Performance score is obtained by using a time-penalty scheme where each error adds 10 seconds to the elapsed time. Therefore, a higher performance value means a longer time and more errors, i.e. worse performance. Table 1 summarises the results, averaged across all 10 participants. The values with significant mean difference within each column are highlighted. According to Table 1, a significant difference in EMG score is not witnessed across levels for the wrist extensor and flexor muscles. This makes sense as the force involved in holding the wrist steady does not change across different levels. There is however a significant difference across all levels when looking at the triceps and when changing between levels 2 and 3 for the biceps. This also follows expected behaviour, as when the arm is lifted to different heights, the effort is being applied mainly by the triceps and biceps muscles. The RULA score shows significant difference across all levels which confirms its usefulness in detecting different ergonomic levels however small they might be. This is not the case for the Borg scale which only detects large differences, i.e. from level 1 to level 3, based on Table 1.

[1] http://ergo-plus.com/wp-content/uploads/RULA.pdf

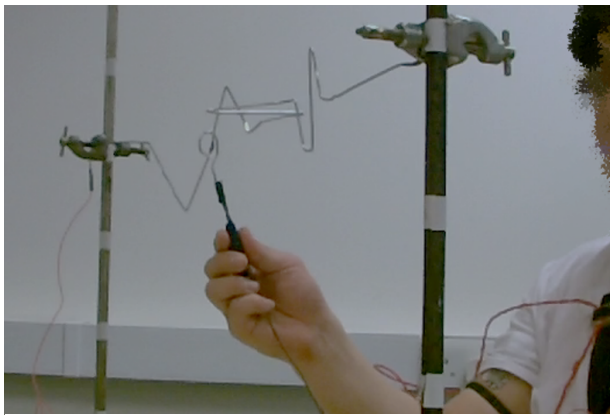

Figure. 2. the buzz-wire test used during the experiments.

CONCLUSION AND DISCUSSION

The above results show that the Borg scale cannot be relied on for minor changes in comfort and ergonomics. Furthermore, the subjectivity in the Borg scale was evident throughout the experiment, as participants answered the Borg scale question differently and some struggled to relate their discomfort to the given number scale. The result is a varying Borg score range across the participants which makes it difficult to compare the comfort of one participant with another and is the reason why Borg is mainly useful in large sample populations.

This is not the case with the RULA score or (normalised) EMG values however. These values can be compared across participants and are all within the same range and original bias. While the Borg scale is popular in clinical settings, the results of this preliminary study show that there is room for improvements. The RULA score presents a less subjective and more precise solution, but it does not take into account detailed muscle behaviour that can be obtained using low-cost, wearable EMG sensors. Thus, a combination of these two methods may be the best solution to move forward.

REFERENCES

[1] A. Shafti et. al., "Comfort and Learnability Assessment of a New Soft Robotic Manipulator for Minimally Invasive Surgery," in EMBC, 2015.

[2] G. Borg, "Psychophysical bases of perceived exertion," Med Sci Sport Exer, vol. 14, no. 5, pp. 377-381, 1982

[3] L. McAtamney and E. N. Corlett, "RULA: a survey method for the investigation of work-related upper limb disorders," Appl Ergon, vol. 24, no. 2, pp. 91-99, 1993.

Table 1. Average results for 10 participants.

	Ext.	*Flex.*	*Tri.*	*Bi.*	*Borg*	*RULA*	*Perf.*
1	0.08012	0.031	0.014	0.027	2.63	4.062	120.3
2	0.07610	0.033	0.017	0.028	2.90	4.176	129.7
3	0.07583	0.030	0.023	0.032	3.96	5.082	145.5

Spine surgery and biorobotics: clinical experience and research challenges

M. Tenucci[1], S. Mazzoleni[2], M. Galgani[1], G. Ciuti[2], G. Calvosa[1], P. Dario[2]

[1]*Orthopaedic and Traumatology Department, Ospedale S.Maria Maddalena, Volterra, Italy*

[2]*The BioRobotics Institute, Scuola Superiore Sant'Anna, Pisa, Italy*

mtenux@gmail.com

INTRODUCTION

Spine surgery has been always charged by high risk of iatrogenic lesions due to the complexity and fragility of structures surrounding vertebral column only partially visible to the surgeon during the procedure.

The phase of the surgical procedure associated with significant intraoperative and postoperative complications corresponds to the pedicle screw placement [1, 2].

During the last two decades the objective of the bioengineering research has been to reduce the risk of pedicle screws misalignment which can potentially cause severe vascular and nervous lesions.

Since mid-90's for the first time pedicle screws have been positioned with the support of computer-assisted stereotactic navigation [3].

Currently the highest level of safety in spine surgery is represented by the use of stereotactic navigation system working on 3D images acquired intraoperatively or the use of a robotic arm that leads the trajectory for placement of pedicle screws.

The use of this technology has significantly increased the safety and dependability of the surgical procedure and has led to better training of young surgeons [4, 5].

MATERIALS AND METHODS

The computer-assisted navigation system (StealthStation® S7®, Medtronic, MN, USA) equipped by an intraoperative TC scan (O-arm® Surgical Imaging System, Medtronic, MN, USA) is being used since 2013 at the Orthopedic and Traumatology Department, Ospedale S.Maria Maddalena, Volterra, Italy.

The O-arm® Surgical Imaging System can capture and subsequently is able to provide an auto-merging of the surgical anatomy using a CT scan and allows for an accurate navigation (Figure 1).

In a period of 30 months n=250 consecutive patients affected by lumbar deformity underwent spinal surgery with pedicle fixation using the O-arm® and the StealthStation® navigation system.

After surgery all patients underwent a CT scan in order to evaluate and rank the screw positions.

The position of the screw was classified into five grades according to the violation of the pedicle cortex: (0) no violation; (1) up to 2 mm; (2) from 2mm to 4 mm; (3) from 4mm to 6 mm; (4) more than 6 mm (Figure 2) [6].

Misplaced screws inside the pedicle was ranked as lateral, inferior, medial, or superior according to Laine's classification [7, 8].

All surgical procedures were performed by two experienced surgeons.

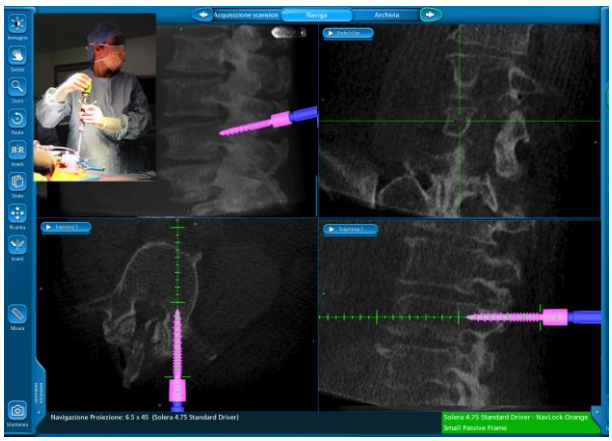

Figure 1. Computer-assisted navigation during a spine surgery procedure.

RESULTS

In two and a half years 1440 screws have been positioned using the surgical navigation system: among these 1423 screws were correctly (grade 0 and grade 1) positioned (98.8%).

No patient underwent revision surgery for misplaced screws.

The authors concluded the learning curve in six months: after this period a significant reduction in the total duration of the surgical time has been observed.

Moreover the correct use of image navigation for spinal surgery is able to decrease radiation exposure for the surgeons and nurses [9-12].

A recent review revealed that an average of 91.4 % (weighted average 89.3 %) of pedicle screws placed with free-hand or fluoroscopy technique was within the safe zone in comparison to an average of 97.3 % (weighted average 96.6 %) of pedicle screws placed with navigation or robot-assisted surgery (statistically significant difference, $p<0.001$) [13].

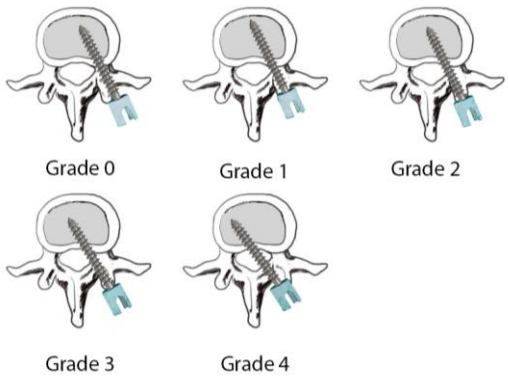

Figure 2. Laine's grading system.

CONCLUSION AND DISCUSSION

The computer-assisted navigation system is particularly useful in surgery of spinal deformities which increase the accuracy and safety in the placement of pedicle screws and in revision surgery where can makes visible anatomical and iatrogenic abnormalities under bone plans of arthrodesis or tissue scarring [14, 15].

Our results confirm the high pedicle screw placement accuracy using a computer-assisted navigation system if compared to traditional surgical procedures.

During the latest years different robotic arms guided by stereotactic systems and able to place pedicle screws or showing the path to the surgeon by tubes systems have been developed.

We strongly believe that robotic technology represents the future of spine surgery as it can make the surgical procedure safe, reliable and repeatable.

REFERENCES

[1] Castro WH, Halm H, Jerosch J, Malms J, Steinbeck J, Blasius S. "Accuracy of pedicle screw placement in lumbar vertebrae." Spine; 1996; 21(11):1320-4.

[2] Esses SI, Sachs BL, Dreyzin V, "Complications associated with the technique of pedicle screw fixation: a selected survey of abs members." Spine; 1993; 18(15): 2231–2239.

[3] Bourgeois AC, Faulkner AR, Pasciak AS, Bradley YC. "The evolution of image-guided lumbosacral spine surgery." Ann Transl Med; 2015; 3(5):69.

[4] Van de Kelft E, Costa F, Van der Planken D, Schils F. "A prospective multicenter registry on the accuracy of pedicle screw placement in the thoracic, lumbar, and sacral levels with the use of the O-arm imaging system and stealthstation navigation." Spine; 2012; 37(25): E1580–E1587.

[5] Laine T, Schlenzka D, Mäitalo K, Tallroth K, Nolte LP, Visarius H. "Improved accuracy of pedicle screw insertion with computer-assisted surgery." Spine; 1997; 22(11):1254–8.

[6] Laine T, Lund T, Ylikoski M, Lohikoski J, Schlenzka D. "Accuracy of pedicle screw insertion with and without computer assistance: a randomised controlled clinical study in 100 consecutive patients." Eur Spine J; 2000; 9(3):235-40.

[7] Gertzbein SD, Robbins SE. "Accuracy of pedicular screw placement in vivo." Spine 1990;15:11-4.

[8] Laine T, Mäitalo K, Schlenzka D, Tallroth K, Poussa M, Alho A. "Accuracy of pedicle screw insertion: a prospective CT study in 30 low back patients." Eur Spine J; 1997; 6(6):402–5.

[9] Smith HE, Welsch MD, Sasso RC, Vaccaro AR. "Comparison of radiation exposure in lumbar pedicle screw placement with fluoroscopy vs computer-assisted image guidance with intraoperative three dimensional imaging." Journal of Spinal Cord Medicine; 2008; 31(5):532–537.

[10] UI Haque M, H. L. Shufflebarger HL, O'Brien M, Macagno A. "Radiation exposure during pedicle screw placement in adolescent idiopathic scoliosis: is fluoroscopy safe?" Spine; 2006; 31(21):2516–2520.

[11] Sasso RC, Garrido BJ. "Computer-assisted spinal navigation versus serial radiography and operative time for posterior spinal fusion at L5-S1." Journal of Spinal Disorders and Techniques; 2007; 20(2):118–122.

[12] Perisinakis K, Theocharopoulos N, Damilakis J, Katonis P, Papadokostakis G, Hadjipavlou A, Gourtsoyiannis N. "Estimation of patient dose and associated radiogenic risks from fluoroscopically guided pedicle screw insertion." Spine; 2004; 29(14):1555–60.

[13] Aoude AA, Fortin M, Figueiredo R, Jarzem P, Ouellet J, Weber MH. " Methods to determine pedicle screw placement accuracy in spine surgery: a systematic review." Eur Spine J (2015) 24:990–1004.

[14] Davies B. "A review of robotics in surgery." Proc Inst Mech Eng H; 2000; 214(1):129-40.

[15] Park P, Foley KT, Cowan JA, La Marca F. "Minimally invasive pedicle screw fixation utilizing O-arm fluoroscopy with computer-assisted navigation: feasibility, technique, and preliminary results." Surgical Neurology International; 2010; 1:44.

Surgical Gripper with Embedded Soft Tactile Array for NOTES

Junghwan Back[1], Guokai Zhang[2], Shuxin Wang[2], Hongbin Liu[1]

[1]*Centre for Robotics Research, Department of Informatics, King's College London, UK*

[2] School of Mechanical Engineering, Tianjin University, China

INTRODUCTION

During an open surgery, a surgeon's ability to gently palpate an organ is a natural diagnostic method to identify an abnormality of tissue. The advance of surgical methodology to replace classical open surgery by minimally invasive surgery is leading to develop of millimeter-scale MIS tools. Resultingly, it causes a difficulty to adapt tactile sensors on MIS tools such as a gripper, and to provide a sense of touch. To this end, we propose a new type of natural orifice transluminal endoscopic surgery (NOTES) surgical instrument with the feedback of sense of touch. The graspers of this instrument are embedded with distributed tactile elements made of compliant material. The compliant material can both provide the tactile feedback to the surgery also in the meantime increase the stability of the grasping.

Compared to the existing graspers without tactile feedback, the added sense of touch will facilitate surgeon to identify calcified arteries or localise tumours within a solid organ. During the procedure for treating liver cirrhosis, this instrument can help to diagnose the abnormal tissue and carry out the dissection efficiently. In procedures such as vessel separation and revascularization and blood vessel anastomosis, the detailed tactile distribution on the vessels will help surgeon to avoid damage to healthy tissue and vessels, while increasing the accuracy of the operation.

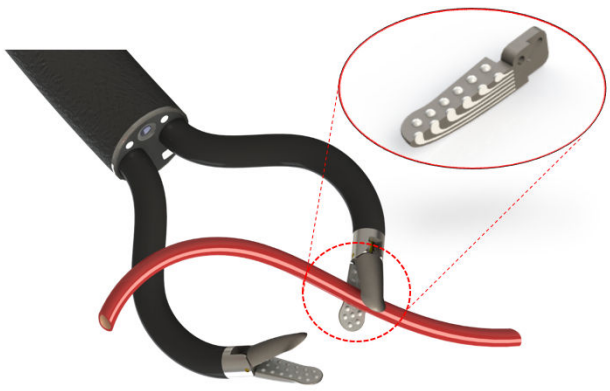

Figure 1 The proposed new type of NOTES surgical instrument and design of the soft tactile array sensor embed grasper.

Numerous tactile sensors for millimeter scale MIS tools had been reported such as PVDF, MEMS base method, Conductive liquid, and optical fiber [1-4]. However, these sensing mechanisms have the common difficulties including miniaturizing the size, increasing spatial resolution of tactile elements, adapting sensor to non-planar tool shape, simplifying fabrication complexity, and reducing the cost. To overcome challenges to create distributed tactile sensing capability on the millimeter scale grippers, we make use of the method proposed in [5] to 3D print the gripper with embedded multiple micro-channels. The sensor body is fabricated using 3D printing and silicone rubber casting. Each soft channel measures contract force by light intensity variation using optical fiber. Thus, the proposed sensor has the following advantages: 1) making use of 3D printing and soft material casting, it is suitable to design high density of tactile elements; 2) it easily applies to an arbitrary shape to fit various MIS applications; 3) compared to other light-intensity based tactile sensors, it is easy to fabricate and miniaturize by avoiding the complexity of attaching reflectors to individual sensing elements; 4) it is immune to electromagnetic interference.

INTERNAL STRUCTURE OF THE SOFT TACTILE ARRAY SENSOR

The soft array tactile sensor is consisted of the soft tactile array pad including multiple soft channels and light receiver as shown Fig. 3. The 3D printed sensor body has empty channels following the shape of soft channels. The empty channels are filled by silicone rubber casting to be compliant tactile elements. The casted soft channel is divided into three parts; the hemisphere to receive contact force, the soft channel in the sensor body to transmit contact force and the end of the soft channel to reflect emitted light.

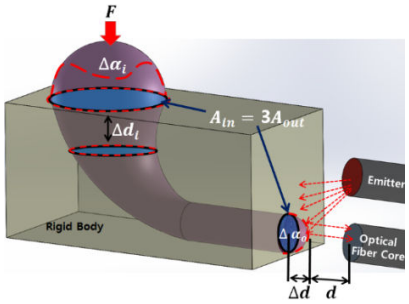

Figure 2 Diagram of soft material channel, and diagram of light reflection

When the hemisphere (the part of the channel that extends outwards) is compressed by applied pressure, the end of the channel is axially protruded as shown in Fig 2. The axial displacement of the protrusion changes reflected light intensity on the end of the channel. Thus,

a key assumption is the soft material has low compressibility to be protruded.

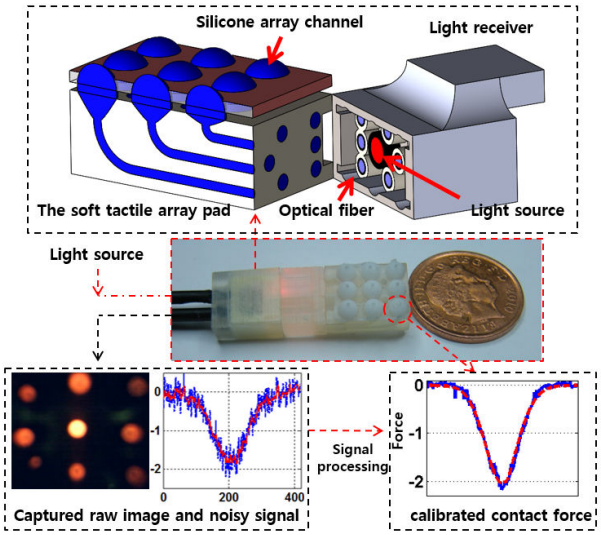

Figure 3 The first prototype soft tactile array sensor system [5]

The reflected light intensity I depending on the distance d between receiver and the end of the channel can be represented using the inverse-square law,

$$\mathrm{I} \propto \frac{r}{d^2} \qquad (1)$$

where r is a constant value denoting the radiation of light at initial distance. Thus, when d is reduced by the soft material's axial protrusion displacement (Δd), the light intensity is increased as shown in Fig 3. The channel shape designs base on the volume difference to magnify the displacement of the axial protrusion of the soft material. For example, when the diameter of protrusion area (A_o) is larger than contact area (A_i) as shown in Fig 2, the axial protrusion displacement is magnified to have equilibrium between the pressed volume of the hemisphere and the protruded volume. To observe variation of the reflected light intensity from the multiple soft channels, a multi-core fibre bundle is used to transmit the light patterns to a camera. The acquired light intensity patterns are then converted into images, the individual force values can be interpreted as indicated in Fig2.

PROTOTYPES OF SENSOR

The first prototype was developed to study the feasibility of the soft tactile array sensor as Fig. 3. The soft array tactile sensor mainly consists of the soft array pad and the light receiver. The array pad includes nine independent soft tactile channels, and the light receiver includes an optical bundle which has nine optical fibers and one light emitter. The nine soft material channels cover the first prototype sensor area of 9.5 × 11 mm^2. Each soft material channel was first fabricated using 3D printing and silicone rubber (Eco-Flex 50) casting. In the first prototype sensor, to amplify the displacement of silicone axial protrusion, the radius of protrusion area A_{out} and contact area A_{in} are designed as 1 mm and 3 mm respectively. An USB camera was utilized to capture the reflected light image. Each silicone channel was calibrated individually using 6-axes force sensor (ATI Nano-17). The validation tests showed that each of the sensing nodules has average measureable force range from 0 to 1.622 N, with an average accuracy of 97%, average crosstalk-to-signal ratio of 1.8%, and no signal drifting. Moreover, other prototypes such as the ellipse palpation head and the square head was successfully fabricated with 16 soft channels as shown Fig 4.

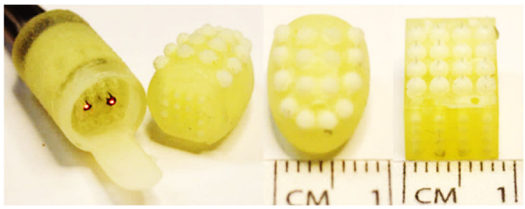

Figure 4 Miniturized soft tactile array sensors

FUTURE WORK

We are in a process to develop a NOTES surgical instrument with the feedback of sense. We believe that the proposed soft tactile array sensor is adaptable for NOTES surgical instrument. To enhance the sensor specifications, we will explore light intensity variation depending on the type of soft material and the area ratio. Therefore, the sensing mechanism will be further optimized.

ACKNOWLEDGEMENT

This research has received support from EPSRC ESSENCE project Grant ref: EP/N020421/1 and NSFC Major International (Regional) Joint Research Project "Flexible Tactile-Sensing Surgical Instrument Perception Mechanism and Design Methodology", Grant No: 51520105006

REFERENCE

[1] H Liu, J Li, X Song, LD Seneviratne, K Althoefer, "Rolling Indentation Probe for Tissue Abnormality Identification during Minimally Invasive Surgery", IEEE Transactions on Robotics, vol.27, issue.3, 450 – 460, 2011.

[2] S Russo, T Ranzani, H Liu, S Nefti-Meziani, K Althoefer, A Menciassi, Soft and Stretchable Sensor using Biocompatible Electrodes and Liquid for Medical Applications, Soft Robotics, 2(4) pp: 146-154, 2015.

[3] K. Kuwana, A. Nakai, K. Masamune, and T. Dohi, "A Grasping Forceps with a triaxial MEMS tactile sensor for quantification of stresses on organs", IEEE International Conference of IEEE Engineering in Medicine and Biology Society, pp. 4490-4493, 2013

[4] TC Searle, K Althoefer, L Seneviratne, H Liu, An optical curvature sensor for flexible manipulators, 2013 IEEE International Conference on Robotics and Automation (ICRA), 4415-4420.

[5] J. Back, P. Dasgupta, L. Seneviratne, K. Althoefer, and H. Liu, Feasibility Study – Novel Optical Soft Tactile Array Sensing for Minimally Invasive Surgery, IEEE International Conference on Intelligent Robots and Systems(IROS), pp. 1528-1533, 2015

A Robotic Hyperspectral Scanning Framework for Endoscopy

F.B. Avila-Rencoret[1,2], D.S. Elson[1,2], G. Mylonas[2]

[1]*The Hamlyn Centre for Robotic Surgery,* [2]*Department of Surgery and Cancer*

Imperial College London, UK.

fba13@ic.ac.uk

INTRODUCTION

Gastrointestinal (GI) endoscopy is the gold-standard procedure for detection and treatment of dysplastic lesions and early stage GI cancers [1]. In spite of its proven effectiveness, its sensitivity remains suboptimal due to the subjective nature of the examination, which is substantially reliant on human-operator skills. For bowel cancer, colonoscopy can miss up to 22% of dysplastic lesions, with even higher miss rates for small (<5 mm diameter) and flat lesions [2]. The proposed system seeks to improve the sensitivity of GI endoscopy by automated scanning and real-time classification of wide tissue areas based on their hyperspectral (HS) features. A "hot-spot" map is generated to highlight dysplastic or cancerous lesions for further scrutiny or concurrent resection [3]. The device works as an add-on accessory to any conventional endoscope and to our knowledge is the first of its kind.

ENGINEERING SPECIFICATIONS

The device comprises a radial array of optical sensors that can be partially rotated and translated along the GI tract while acquiring optical data (Fig. 1, A-C). The optical sensor array consists of eight single-point diffuse reflectance spectroscopy (DRS) fibre optic probes, introduced in a collapsed configuration as an over-tube add-on accessory to any conventional endoscope. Deployment of the collapsed sensors is achieved by externally actuated tendons and respective Bowden force transmission conduits. Each probe contains an illumination fibre that emits white light (Fig. 1, A). The light is diffusely scattered inside the tissue and a parallel fibre collects and transmits it to a spectrograph (V10, SPECIM) where is diffracted into its spectrum and finally captured by an sCMOS camera (optiMOS, QImaging). From each spectral image acquired, an image processing sub-routine converts it to 8 DRS spectra (Fig. 1, A-left). The device is simultaneous and continuously translated and rotated to scan and obtain a 2D map of the entire lumen under interrogation. Rotation is provided by an external hollow rotary actuator through which the endoscope is inserted (SMH88, Stogra). Translation along the lumen using the endoscope as a rail is achieved by a stepper motor (SM56, Stogra) actuating a linear stage (404XE, Parker). Actuation control, data

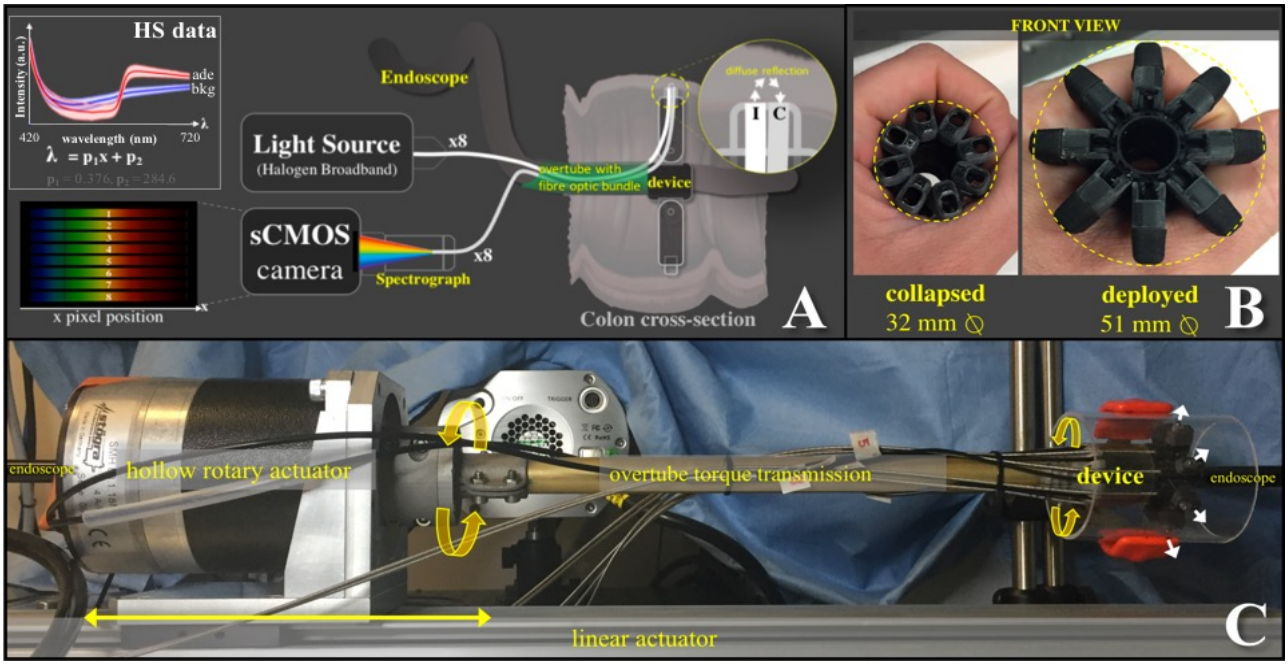

Fig. 1: (**A**) Optical design of an individual DRS sensor: the DRS signal is acquired in each probe by an illumination [I] and a collection [C] fibre (core:cladding=200:20 µm, N.A=0.22). All terminations of the collections fibres are arranged in a 1x8 array (not shown) in front of a spectrograph attached to an sCMOS camera that captures images containing the spectra of each probe. Pre-defined pixel-to-wavelength calibration factors p1 p2 and white standard references are used to convert spectral images to DRS spectra. Top-left plot: representative 781 DRS spectra (mean ±SD) of simulated adenomas (*ade*) *vs.* 3049 DRS spectra of simulated mucosa (*bkg*). (**B**) Front-view of the device in a collapsed and deployed configuration. (**C**) Current fixed scanning mechanism based on a hollow rotary actuator mounted on top of a linear actuator. The device is axially translated as an over-tube add-on to any conventional endoscope.

acquisition, HS data processing and visualisation, are fully integrated into a MATLAB framework. The position of all probes is derived from a single angular and linear position reported by the actuators. Each scanning position is co-registered with its corresponding DRS spectrum. Grayscale images are reconstructed by integrating total intensities from each DRS spectrum. A user interface allows real-time visualisation of acquired raw and processed data as 2D and 3D maps, where the 3D map corresponds to the 2D image texture-mapped to a cylinder, simulating a 3D representation of the colon (Fig. 2, d-e).

EXPERIMENTAL VALIDATION

This abstract focuses on characterising the optical resolution achievable with the current setup on rigid and deformable targets simulating the colon. For rigid targets, we scanned a plastic tube internally covered with a standard resolution target (1959 USAF). The scanning sequence comprised a 48º partial rotation (step size=1º) while axially advancing the device along the tubular target (step size=0.4 mm). Actuation errors were measured as $\sqrt{(pos_{ro} - pos_{re})^2}$, where pos_{ro} is the rounded pixel coordinate of the reconstructed image, and pos_{re} is the real position reported by the encoders. As deformable targets, silicone phantoms were manufactured (Ecoflex 00-30). The phantoms included simulated flat lesions (cylindrical features Ø = 0.5 to 6.0 mm, height = 0.7 mm) that were pigmented to provide a clear HS signal (*ade*, top-left Fig. 1A) over the simulated mucosa background colour (*bkg*).

RESULTS

The average angular rotation error of the current device is 0.02º (SD 0.06º). The linear stage positioning error is stated to be at ±0.02 mm. The optical resolution achievable is 0.5 line pairs per mm (Fig. 2a). This optical resolution is consistent with the smallest simulated flat pre-cancerous lesions resolved (0.75 mm), even while the scanning was performed inside deformable and stretchable phantoms (Fig. 2, b-e).

DISCUSSION

We report for the first time 2D and 3D reconstruction of endoscopic HS data acquired via robotic scanning of a simulated colon by a radial array of contact single-point DRS probes. Sub-millimetre optical resolution has been demonstrated, which could allow the identification of flat pre-cancerous lesions that are currently missed. The size of the device is compatible with the anatomical dimensions of the colon, but further miniaturisation is desirable. Our work towards the clinical applicability of the device currently concentrates on negotiating the variable diameter, folds, and flexures of the colon. Angular actuation along highly tortuous paths via a torque transmission cable is at the centre of our investigations, as well as the integration of safety features like pressure sensing on the probes. Ultimately, classified HS data could be spatially registered with the video stream of any conventional endoscope. This device will pave the way towards the next generation of augmented reality endoscopy while increasing its sensitivity and specificity.

This work is supported by the Institutional Strategic Support Fund: Networks of Excellence Scheme 2015 (GM), UK ERC award 242991 (DSE) and *Becas Chile* scholarship from the Chilean Government (FBA).

REFERENCES

[1] Pawa, N., T. Arulampalam, and J.D. Norton, Screening for colorectal cancer: established and emerging modalities. Nat Rev Gastroenterol Hepatol, 2011. 8(12): p. 711-22.

[2] van Rijn, J.C., et al., Polyp miss rate determined by tandem colonoscopy: a systematic review. Am J Gastroenterol, 2006. 101(2): p. 343-50.

[3] Avila-Rencoret, F., et al, Towards a robotic-assisted cartography of the colon: a proof of concept, in IEEE ICRA, Seattle, WA, 2015, pp. 1757-1763.

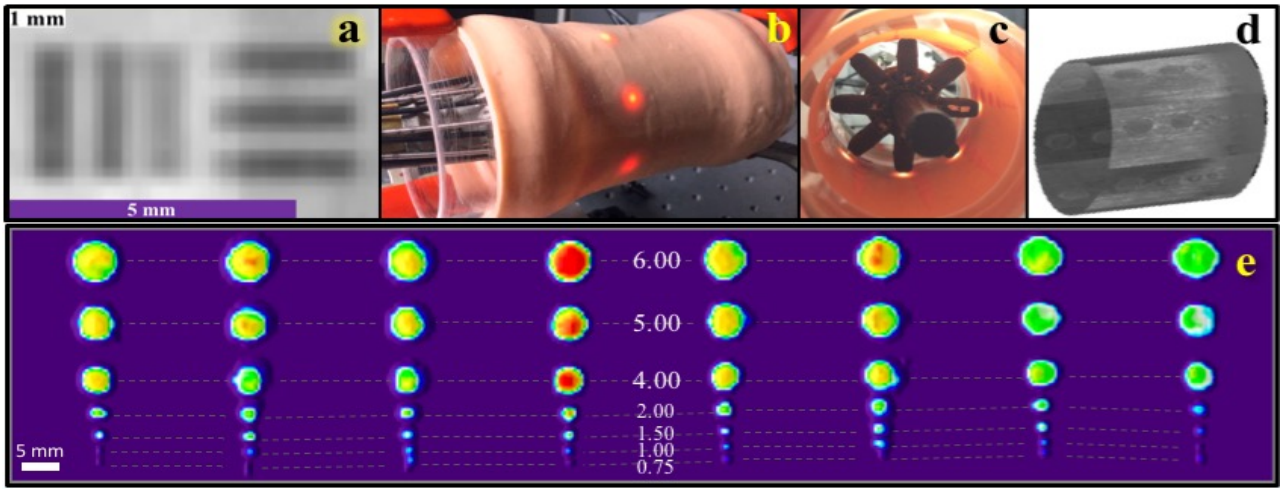

Fig. 2: *In vitro* optical resolution validation experiment. (**a**) cropped sub-section of a scanned paper 1951 USAF target showing a maximal optical resolution of 0.5 line pairs per mm. (**b**) External and (**c**) proximal view of a scanning inside a 5 cm diameter silicone phantom containing patterns of simulated flat pre-cancerous lesions of different diameters. (**d**) Resulting reconstructed 3D grayscale image (texture mapped from 2D), and (**e**) 2D image "hotspot" map based on grayscale pixel intensities. It can be seen that the smallest simulated flat pre-cancerous lesions resolved by the device are 0.75 mm in diameter

3D Reconstruction of the Retinal Surface for Robot-Assisted Eye Surgery

M. Havlena[1], K.K. Maninis[1], D. Bouget[2], E. Vander Poorten[2], L. Van Gool[1]

[1]*Computer Vision Laboratory, D-ITET, ETH Zürich, 8092 Zürich, Switzerland*

[2]*Department of Mechanical Engineering, University of Leuven, 3001 Heverlee, Belgium*
michal.havlena@vision.ee.ethz.ch

INTRODUCTION

Robot-assisted eye surgery is the central topic of the EU funded project EurEyeCase. Major objectives of the project comprise of the development of methodologies to perform two surgical procedures that cannot be easily carried out by sole human surgeons, namely retinal vein cannulation and retinal membrane peeling. In the proposed assistive system, the surface of the retina is modeled prior to the operation using image data from the available stereo microscope.

Pre-operative 3D reconstruction aims to provide the surgeons with a detailed 3D mesh model of the surface of the retina to facilitate their pre-operative planning. Namely, the visualization of the detected vessel structure and/or the optic disc in 3D gives the surgeons a unique opportunity to examine the structure of the eye from novel viewpoints and to plan the path of the tool with a higher confidence.

MATERIALS AND METHODS

The proposed method relies on the availability of stereo image data, which is in our case provided by a stereo microscope. A Haag-Streit ophthalmologic surgical microscope augmented by a stereo vertiscope with two C-mounted Allied Vision Prosilica GC 1290 cameras is able to acquire synchronized stereo videos having a 1280x960 resolution at 25 fps, see Fig. 1.

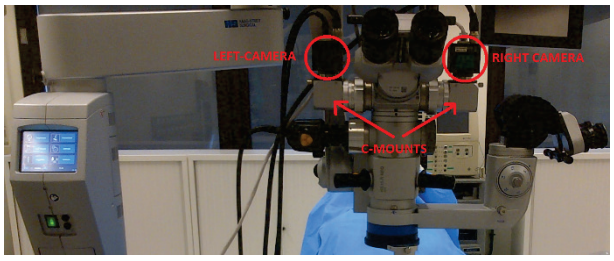

Figure 1. EurEyeCase data acquisition setup. A Haag-Streit ophthalmologic surgical microscope augmented by a stereo vertiscope (a 60° adapter to shorten the microscope body) with two C-mounted Allied Vision Prosilica GC 1290 cameras.

In the following, we describe in detail two practicable 3D visualizations of the retinal surface: (i) a fast depth-map generation from a single stereo-image pair and (ii) a complex textured 3D mesh modeling from multiple stereo pairs of images. We use a pre-calibrated stereo setup on a single zoom level with the focal length of both cameras fixed to 7680 pixels.

To generate a depth-map from a single stereo-image pair, we use the functionality of MATLAB Computer Vision System Toolbox to perform image rectification, disparity computation, and noise filtering of the resulting dense 3D pointcloud. The relative left↔right eye transformation in the form of a fundamental matrix [1] is known thanks to the stereo calibration.

Rectification is a commonly used technique which transforms the problem of depth-map estimation from a 2D to a 1D correspondence search, thus speeding up the computation significantly. Once the stereo-image pair is rectified, it is sufficient to search for correspondence only on the individual lines of the two images. To create the rectified pair, we employ two MATLAB functions `estimateUncalibratedRectification()` and `imwarp()`. Disparity, i.e., the reciprocal depth, is then computed by the semi-global matching algorithm (SGM) [2] using the function `disparity()`. Providing that the disparity map is quite complete, i.e., it does not contain many holes, it is possible to generate a visually pleasing dense 3D pointcloud by instantiating each of the pixels in 3D space at the depth inversely proportional to the estimated disparity. Function `pcdenoise()` is then employed to remove noise, i.e., inconsistent 3D points, from the resulting pointcloud using the method of [3].

In order to be able to fuse the information from multiple stereo-image pairs, the corresponding cameras have to be externally calibrated in the same coordinate system. To this end, we use a publicly available Structure-from-Motion (SfM) tool, VisualSFM [4]. The tool follows the standard SfM pipeline design where extracted natural image features, in this case SiftGPU [5], are matched between different image pairs and resulting multiview feature tracks are triangulated into 3D points. Multiple stereo-image pairs are then combined to estimate a consensual 3D surface mesh which matches well to the available observations. A state-of-the-art method is employed, based on Delaunay tetrahedralization of the 3D space and global surface estimation by a graph-cut [6] in the implementation of [7], available either as a binary or through a web service [8].

RESULTS

Due to the lack of human-eye targets, we limit ourselves to ex-vivo pig eyes for our experiments. Namely, we use the stereo video sequences of open-sky eyes, i.e., eyes of which the lenses have been removed. If a real in-vivo eye target were used, the optical effect of the actual eye lens would need to be accounted for [9].

The particular sequence we work with is a 110 seconds long stereo video viewing the eye at different zoom levels and slightly sliding to the sides. To reduce the number of processed data and remove the inherent redundancy, we restrict ourselves to a subsequence representing a single pre-calibrated zoom level and extract frames at 0.5 fps, leading to 10 stereo-image pairs.

First, we show how a depth-map and a 3D point-cloud can be generated for one of the stereo-image pairs. Note that one can easily visualize semantic information, e.g., the vessel segmentation results [10], in 3D. Instead of the original image, a "heatmap" is used to assign colors to the resulting 3D points, see Fig. 2.

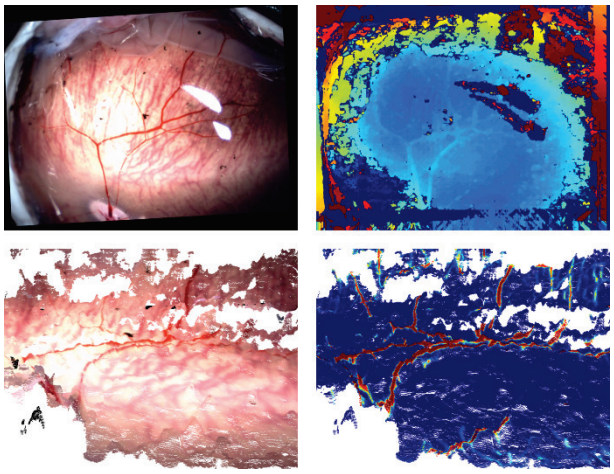

Figure 2. Rectification (top left), disparity computation (top right), and de-noised dense 3D pointcloud generation. The colors of the points correspond either to the pixel colors from the respective image (bottom left) or to the results of vessel segmentation [10] (bottom right). Blue denotes a very low while red a very high confidence of a certain area being a vein.

Second, we externally calibrate the 10 stereo-image pairs in few tens of seconds and submit a 3D surface reconstruction job to the web service [8]. Due to the specific acquisition conditions which do not bring a sufficient translation baseline for the frames in the sequence, we decreased the threshold for the minimum allowed triangulation angle `min_apical_angle` to 1 degree. The job exited in slightly over 10 minutes giving a textured 3D mesh consisting of more than 130 thousand triangles. Such a mesh gives the surgeons a nice overview of the relative configurations of different eye structures and helps them to plan the trajectories of the tools accordingly, see Fig. 3.

CONCLUSION AND DISCUSSION

We presented two techniques to construct the 3D retinal model from a stereo video sequence: (i) a fast depth-map generation from a single stereo-image pair and (ii) a complex textured 3D mesh modeling from multiple stereo pairs of images. Currently, no prior knowledge about the expected shape of the eye is input to the reconstruction, mainly due to the fact that open-sky eyes do not have the — close to perfect — spherical shape of the closed eyes. Incorporating such a shape prior, when relevant and satisfied, would make the reconstruction more robust and the 3D surfaces more accurate.

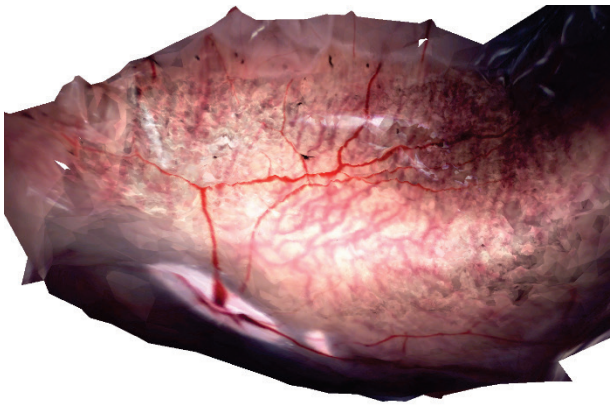

Figure 3. Reconstructed textured 3D surface mesh rendered from a novel viewpoint which cannot be attained by manipulating the microscope. Endowing the surgeons with the capability to generate such a view helps them to better understand the positions and relative configurations of the eye structures.

ACKNOWLEDGEMENT

Research funded by the EU's Horizon 2020 Programme under grant agreement No 645331 – EurEyeCase.

REFERENCES

[1] Hartley R., Zisserman A. "Multiple View Geometry in Computer Vision," 2nd edition, Cambridge University Press, 2003.

[2] Hirschmüller H. "Accurate and efficient stereo processing by semi-global matching and mutual information," in Proceedings of the 18th IEEE Conference on Computer Vision and Pattern Recognition (CVPR) 2005; 807-814 vol. 2.

[3] Rusu R.B. et al. "Towards 3D point cloud based object maps for household environments," RAS; 2008; 56(11): 927-941.

[4] Wu C. "VisualSFM: A visual structure from motion system – http://ccwu.me/vsfm," 2013.

[5] Wu C. "SiftGPU: A GPU implementation of scale invariant feature transform (SIFT) – http://cs.unc.edu/~ccwu/siftgpu," 2011.

[6] Labatut P., Pons J.-P., Keriven R. "Efficient multi-view reconstruction of large-scale scenes using interest points, Delaunay triangulation and graph cuts," in Proceedings of the 11th IEEE International Conference on Computer Vision (ICCV) 2007; 1-8.

[7] Jancosek M., Pajdla T. "Multi-view reconstruction preserving weakly supported surfaces," in Proceedings of the 24th IEEE Conference on Computer Vision and Pattern Recognition (CVPR) 2011; 3121-3128.

[8] Heller J. et al. "3D reconstruction from photographs by CMP SfM web service," in Proceedings of the 14th IAPR International Conference on Machine Vision Applications (MVA) 2015; 30-34.

[9] Bergeles C. et al. "Wide-Angle Intraocular Imaging and Localization," in Proceedings of the 12th International Conference on Medical Image and Computer-Assisted Intervention (MICCAI) 2009; 540-548.

[10] Maninis K.K., Pont-Tuset J., Arbeláez P., Van Gool L. "Deep Retinal Image Understanding," in Proceedings of the 19th International Conference on Medical Image and Computer-Assisted Intervention (MICCAI) 2016; 1-8.

Wearable augmented reality displays for image guided surgery

V. Ferrari[1,2], F.Cutolo[1], M. Ferrari[1]

[1]*EndoCAS Center, University of Pisa, Italy*

[2]*Department of Information Engineering, University of Pisa, Italy*

vincenzo.ferrari@unipi.it

INTRODUCTION

The idea of integrating the surgeon's view with Augmented Reality (AR) visualization modalities has become a dominant topic of academic and industrial research in the medical domain since the 90's. The interest for AR solutions in medicine is encreasing, and over the past 12 months alone, 153 publications with the terms "Augmented Reality" in the title or in the abstract were indexed in the PubMed database.

It is known that the capacity of an AR system to smoothly supplementing the user's perceptive efficiency is strongly related on how and where the augmented information is provided [1] and for medical and surgical applications other specifically application-related features have to be taken into account [2].

Since wearable AR systems are intrinsically the most ergonomic solution for those medical tasks manually performed under user's direct vision (introduction of biopsy needle, palpation, open surgery, etc.), the selection of the most appropriate AR Head Mounted Display (HMD) for each specific medical task plays a fundamental role. The different classes of AR-HMDs have been deeply analysed in the past from a technological and a human-factor standpoint [3] but no specific guidelines for the surgical domain are today available. In this paper we describe the two main classes of AR-HMDs and we briefly discuss their potentialities and their limits for surgery. We will also report some pioneering works in the field that could possibly be a breakthrough in the future.

OPTICAL SEE-THROUGH DISPLAYS

In Optical See-Through (OST) HMDs, the user's direct view of the real world is augmented with the projection of a virtual 2D image on a beam combiner and then into the user's line of sight [3]. Lenses can be placed between the beam combiner and the display to focus the virtual 2D image so that it appears at a comfortable viewing distance on a semi-transparent surface of projection (SSP) [4]. As an alternative, the use of high-precision light guide technologies allows the removal of the bulky optical engine [5]. The OST paradigm (Figure 1) is particularly suitable for augmenting the reality by means of simple computer-generated elements (as patient-related textual or graphical data) but shortcomings remain on their eventual use as accurate and reliable image-guided surgical systems.

In any image-guided surgical system, the geometrical consistency of the virtual 3D anatomies (reconstructed from medical images) with the real patient is the key point. In OST displays, to achieve an accurate fusion between real scene and virtual content the following conditions must be satisfied:

I. Accurate registration of the virtual 3D anatomies to the real patient, as in any surgical navigator;

II. Accurate tracking of the pose between HMD SSP and patient. Tracking is a common requirement in any surgical navigator;

III. Consistent estimation of the user's eye projection model and of its position respect to the SSP;

IV. Rendering of the virtual 2D image (consisting in a projection of the virtual 3D anatomies) on the SSP taking into account conditions I, II and III, so as to properly match the light rays coming from the real world with the virtual 2D image pixels.

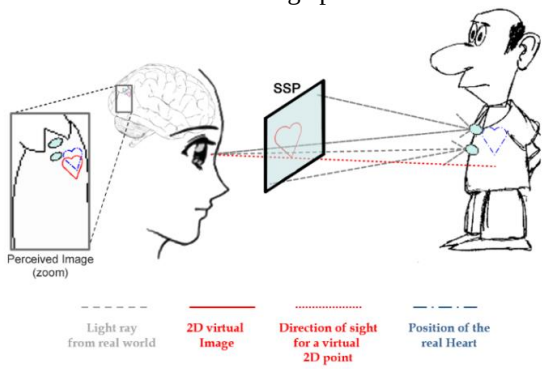

Figure 1. Optical see-through paradigm. A virtual 2D image (red heart) is rendered on the semi-transparent surface of projection (SSP). The user perceives the light rays coming from the real world merged with the virtual 2D image. The perceived image of the virtual 2D image can be not exactly registered to the real view of the world (see the heart apex) due to user-dependent calibrations issues.

The user-dependent calibration required at point III is an additional requirement in respect to traditional surgical navigators. This calibration step often entails a tedious and error prone methods [6, 7], and it should be repeated each time the HMD is moved on the head causing a change in the relative position between user's eye and SSP. Recent and more advanced calibration methods [8], albeit working in real-time, do not incorporate a user-dependent and real-time estimation of the eye projective model. The projective model of the user's eye may indeed change over time with the focus distance due to the accommodation process.

VIDEO SEE THROUGH DISPLAYS

With the Video See-Through (VST) paradigm, the view of the real world is mediated by a camera placed in front of the HMD. The 2D images acquired by the camera are

shown on the micro display close to the user's eye, and the real images can be accurately merged with virtual 2D images [9, 10] without the need to performing any user-dependent calibration, since the alignment between real and virtual information does not require the knowledge of the user's viewpoint.

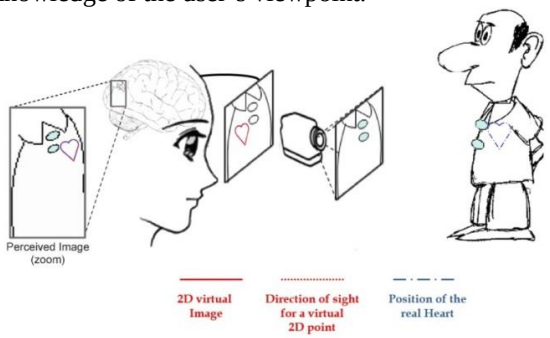

Figure 2. Video see-through paradigm. The external camera acquires 2D images of the real world that are merged with virtual 2D images. The mixed images are then showed on the display close to the user's eye. The alignment between real and virtual information does not involve the modelling of the user's viewpoint and can be really accurate.

In VST, the camera-mediated view can reduce the natural visual acuity, the viewpoint is often not exactly orthoscopic, there is a lag between the acquisition and the reproduction of the images, and, in case of stereoscopic implementations, the vergence of the stereo cameras can be an issue [11] [12].

OST LIGHT FIELD DISPLAYS

In traditional OST HMDs there is an intrinsic incompatibility between the nature of the 4D light field crossing the SSP [13], associated to the real world, and the nature of the virtual content rendered as a 2D image. Recent works [14] [15, 16] propose a radical rethinking of the OST displays paradigm by generating, through integral imaging technique [17], the virtual content as a light field. This solution seeks to overcome the typical limitations of the traditional OST approach based on 2D images projected over semitransparent surfaces.

CONCLUSION AND DISCUSSION

At the current technological level, the accurate registration of virtual 2D image to the real world view, fundamental prerequisite for the adoption of AR-based image-guided surgical systems, is ensured by adopting a standard VST solution. Nevertheless, VST displays introduce perceptual artifacts due to its bringing a non-natural view of the real world. OST light field displays could be the "Saint Grail" for AR-based image-guided surgery in the future. In any case, further research and complex technical developments are required to offer high resolution and real time rendering capabilities.

REFERENCES

[1] R. Azuma, Y. Baillot, R. Behringer, S. Feiner, S. Julier, and B. MacIntyre, "Recent advances in augmented reality," *Ieee Computer Graphics and Applications*, vol. 21, pp. 34-47, Nov-Dec 2001.

[2] M. Kersten-Oertel, P. Jannin, *et al.*"DVV: A Taxonomy for Mixed Reality Visualization in Image Guided Surgery," *IEEE TVCG*, vol. 18, 332-352, 2012.

[3] J. P. Rolland and H. Fuchs, "Optical Versus Video See-Through Head-Mounted Displays in Medical Visualization," *Presence: Teleoper. Virtual Environ.*, vol. 9, pp. 287-309, 2000.

[4] N. S. Holliman, N. A. Dodgson, G. E. Favalora, and L. Pockett, "Three-Dimensional Displays: A Review and Applications Analysis," *Ieee Transactions on Broadcasting*, vol. 57, pp. 362-371, Jun 2011.

[5] H. Mukawa, K. Akutsu, *et al.*, "Distinguished paper: A full color eyewear display using holographic planar waveguides," *2008 Sid International Symposium, Digest of Technical Papers*, 89-92, 2008.

[6] S. J. Gilson, A. W. Fitzgibbon, and A. Glennerster, "Spatial calibration of an optical see-through head-mounted display," *Journal of Neuroscience Methods*, vol. 173, 140-146, 2008.

[7] F. Kellner, B. Bolte, *et al.*, "Geometric Calibration of Head-Mounted Displays and its Effects on Distance Estimation," *Ieee Transactions on Visualization and Computer Graphics*, vol. 18, pp. 589-596, Apr 2012.

[8] A. Plopski, Y. Itoh, C. Nitschke, K. Kiyokawa, G. Klinker, and H. Takemura, "Corneal-Imaging Calibration for Optical See-Through Head-Mounted Displays," *Ieee Transactions on Visualization and Computer Graphics*, vol. 21, pp. 481-490, Apr 2015.

[9] G. Badiali, V. Ferrari, F. Cutolo, C. Freschi, D. Caramella, A. Bianchi, *et al.*, "Augmented reality as an aid in maxillofacial surgery: Validation of a wearable system allowing maxillary repositioning," *Journal of Cranio-Maxillofacial Surgery*, 2014.

[10] V. Ferrari, G. Megali, *et al.* "A 3-D mixed-reality system for stereoscopic visualization of medical dataset," *IEEE Trans Bio Eng*, pp. 2627-33, 2009.

[11] V. Ferrari, F. Cutolo, *et al.* "HMD Video See Through AR with Unfixed Cameras Vergence " in *IEEE ISMAR*, 2014.

[12] A. State, J. Ackerman, *et al.* "Dynamic virtual convergence for video see-through head-mounted displays: Maintaining maximum stereo overlap throughout a close-range work space," *ISMAR*, 2001.

[13] M. Levoy, "Light Fields and Computational Imaging," *Computer*, vol. 39, pp. 46-55, 2006.

[14] H. Liao, T. Inomata, I. Sakuma, and T. Dohi, "3-D augmented reality for MRI-guided surgery using integral videography autostereoscopic image overlay," *IEEE Trans Biomed Eng*, vol. 57, pp. 1476-86, 2010.

[15] H. Hua and B. Javidi, "A 3D integral imaging optical see-through head-mounted display," *Optics express*, vol. 22, pp. 13484-13491, 2014.

[16] V. Ferrari and E. M. Calabro, "Wearable augmented reality light field optical see-through display to avoid user dependent calibrations: a feasibility study," in *To be appear in SAI Conference* 2016.

[17] A. Stern and B. Javidi, "Three-dimensional image sensing, visualization, and processing using integral imaging," *Proceedings of the IEEE*, vol. 94, pp. 591-607, 2006.

Clip-on stiffness sensor for endoscopic cameras retrieving sense of touch in minimally invasive intervention

Angela Faragasso[1], Agostino Stilli[1], Joao Bimbo[2], Helge A. Wurdemann[3] and Kaspar Althoefer[4]

[1]*Centre for Robotics Research, Department of informatics, King's College, London,*

[2]*Department of advanced robotics, Istituto Italiano di Tecnologia Genova, Italy*

[3]*School of Electrical Engineering & Computer Science, Queen Mary University of London*

[4]*Dept. of Mechanical Engineering, University College London,*
angela.faragasso@kcl.ac.uk

INTRODUCTION

Minimally invasive procedures use state of the art technology to reduce damage to human tissues that can occur during medical interventions. In minimally invasive procedures clinicians make several small incisions on the patient's skin, one of which is usually reserved for the endoscopic camera. Images from the endoscopic camera are projected onto monitors in the operating room. Thus, the medical team can see a clear and magnified view of the analysed anatomical area. Other instruments are inserted in the other openings and used to explore, remove or repair internal body parts. Notwithstanding all the advantages that minimally invasive procedures brought into the clinical settings, there is still a lack of haptic feedback which can help to localise malignant tissues and identify abnormalities while preserving blood vessels and nerves.

Identification of abnormalities can be cumbersome for an inexperienced practitioner, while the lack of direct palpation during minimally invasive procedures may lead to insufficient feedback and errors.

In response to the current state of minimally invasive interventions, sensing technologies for minimally invasive procedures have been developed. However, problems in size, compatibility with the medical settings, sterilisability, accuracy and reliability, make these systems unsuitable for real applications. In minimally invasive procedures practitioners use endoscopic instruments to inspect a specific part of the body, to diagnose a disease or find the cause of a patient's symptoms. Endoscopes are not only used for diagnostic purposes, but also for treatment or as part of a procedure aiming to prevent future health problems. Computer vision techniques, which are directly implemented on the endoscopic camera images, have been largely investigated [1]. However, vision solutions for soft tissue characterization employ costly and complex image processing algorithms which are not fully reliable.

Researchers have been investigating the use of endoscopic cameras as palpation instruments for medical examination [2].

This paper presents a novel stiffness sensor which is fashioned for a surgical endoscopic camera.

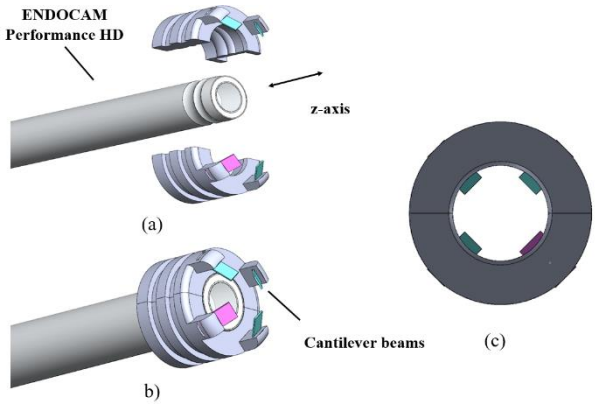

Figure. 1. Clip-on stiffness sensor CAD Drawings: (a) Exploded view of the sensor, (b) sensor assembled at the tip of an endoscopic camera, (c) camera field of view. The stiffer beam (in pink), has a lower elasticity than the others.

A clip-on sensing mechanism is attached to the camera tip and used to palpate soft tissue area. Hence, the integrated system can be used as a dual sensor: to visualise anatomical area and to evaluate its stiffness.

Multiple cantilever beams are indented into soft tissue. The movements of the cantilevers result in shape variations of the related visual features in the endoscopic camera images. The beams present different elasticity, thus they exhibit different displacements during indentation. The stiffness of the examined soft tissue is estimated by tracking the movements of the visual features in the camera images. The proposed sensor is light, cheap, disposable, passive and presents customisable range and resolution. The additional sensing mechanism slightly increase the diameter of the endoscopic camera allowing it to be inserted into the human body through a standard trocar port.

MATERIALS AND METHODS

The clip-on stiffness sensor has been fashioned for the medical rigid endoscope ENDOCAM Performance HD by Richard Wolf. The sensor is attached to the tip of the endoscopic camera by a clip so as to be easy to fasten or remove. The overall sensory system, composed by the endoscopic camera and the designed mechanism, can be inserted into the human body through a standard trocar.

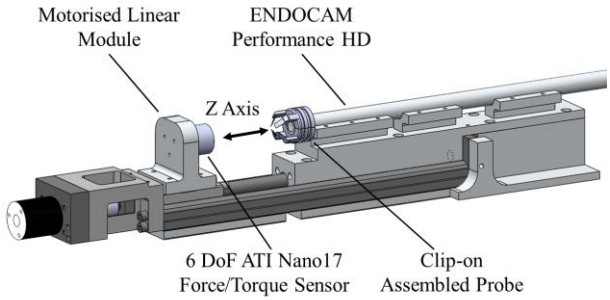

Figure. 1. Calibration device: the motorised linear module pushes the Force/Torque sensor against the stiffness sensor whist recording the interaction forces and the displacement.

The overall sensory system, composed by the endoscopic camera and the designed mechanism, can be inserted into the human body through a standard trocar port of 10-15mm diameter, thus it fits the size requirements of minimally invasive procedures. The exploded and assembled views of the sensor are shown in Figure. 1. The sensor consists of two semi-cylindrical symmetrical parts with a cylindrical cavity along the central axis which is used to mount the device onto the camera tip. Each part has two rectangular cantilever beams, made by nitinol, a metal alloy of nickel and titanium, tapered with an angle of 40˚, as shown in Figure. 1. Three beams have identical cross sections, hence, they have identical elasticity. The fourth beam has a bigger cross section; thus it has a lower elasticity than the others. When the beams palpate soft tissue they bent towards the camera changing their positions in the camera images. An image processing algorithm tracks the visual appearance of the beams in the images which are related to their bending in the 3D space. In previous work the authors proposed a multiaxial stiffness sensor probe for medical palpation which related the compression of linear springs to the movements of spherical visual features in the images to estimate the contact forces and the stiffness [3]. Therefore, due to the similarity between the beams and springs the sensing principle has been fashioned and adopted to model the cantilever sensor.

The image processing algorithm evaluates the relationship between the bending of the cantilevers and the visual appearance of their centroid in the images. The image has been subdivided into four Regions of Interest (ROIs). Each ROI is associate to one cantilever and capture its full range of motion. The simulation results of the finite element analysis (FEA), have been

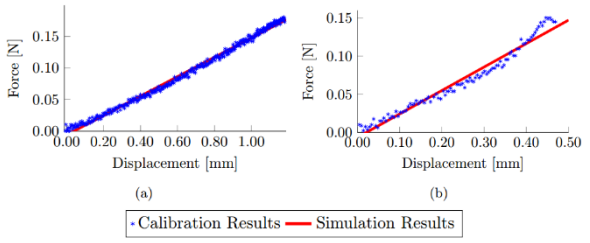

Figure. 2. Clip-on sensor for endoscopic camera: The displacements of the cantilevers along the z-axis in simulation and calibration of the soft (a) and the stiffer (b) beams.

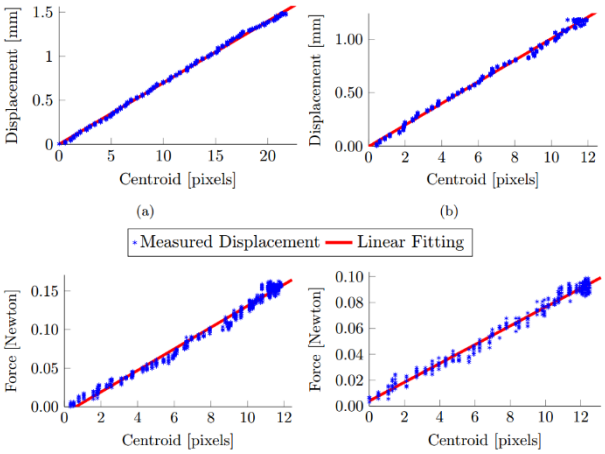

Figure. 3. Relation between feature centroid and displacement of the soft beam (a) and stiffer beam (b). The variation of feature centroids due to an external force for the soft beam (c) and stiffer beam (d).

compared with the results obtained using a calibration device which ensures that the endoscopic camera is at a steady state during contact, as shown in Figure. 2. The system employs a motorised linear module which embeds the ATI Nano17 Force/Torque sensor.By sliding the linear module against the sensor prototype, the displacements of the beams and the interaction forces generated by the contact are recorded in real-time.

RESULTS

The results of the calibration tests demonstrate that the relationship between the displacement of the nitinol beams and the applied normal force is linear (Figure. 3). The results of the image processing algorithm also show that there is a linear relationship between the position of the centroids in the image and the displacements of the beams, Figure. 4. (a) and (b). The relationship between the movements of the beams and the variation of the centroids in the images allows to directly compute the applied force as a function of the beams' centroids, Figure. 4 (c) and (d).

CONCLUSION AND DISCUSSION

In this paper a novel clip-on sensor for endoscopic cameras has been presented. The computation of soft tissue stiffness will help clinicians to diagnose abnormalities and recover the "sense of touch" in minimally invasive and remote applications. Future work will explore other fabrication materials and tests with soft tissue phantoms.

REFERENCE

[1] D. Stoyanov, " Surgical vision.," *Annals of biomedical engineering.*, pp. 40(2), 332-345, 2013.

[2] T. Iwai, "Three-axis force visualizing system for fiberscopes utilizing highly elastic fabric," in *Advanced Intelligent Mechatronics (AIM), 2014 IEEE/ASME International Conference on. IEEE*, 2014.

[3] A. Faragasso, A. Stilli, J. Bimbo, H. Wurdemann and & Althoefer, "Multi-axis stiffness sensing device for medical palpation," in *IEEE International Conference on Intelligent Robots and System (IROS)*, Hamburg, 2015.

In-eye Optical-Coherence-Tomography-based proximity control

Y.G.M. Douven, M.J.G. van de Molengraft, M. Steinbuch
Control Systems Technology Group, Eindhoven University of Technology
P.O. Box 513, 5600MB Eindhoven, the Netherlands. E-mail: y.g.m.douven@tue.nl

I. Introduction

Vitreoretinal surgery addresses sight-threatening conditions on the back of the eye. Since structures on the back of the eye are often only a few micrometers, the technical demands placed on the surgeon by these procedures are very high. Robotic systems can provide a distinct and positive alteration in patient outcome when they can show to really enhance the surgeon's capability by providing both physical and mental assistance. The back of the eye is viewed through a stereo-microscope, which provides a three dimensional image to the physician. Still, determining distance between instrument-tip and retina proves to be very hard.

II. Control scheme for robot-assisted safety

Until now, the focus of surgical robotic systems has been on precision. To further improve patient safety and surgical performance, new concepts for (semi-)automated robot-assisted surgeries are being developed. These concepts incorporate sensor guarded and sensor guided motions. From a control point of view, this leads to a cascaded control loop that exists of three layers (see Fig. 1). The innermost layer (denoted in blue) ensures closed-loop stability of a telemanipulator system. The complete loop is closed by the surgeon (denoted by the orange feedback line). The green loop is established by adding a local sensor to provide fast and reliable information about the distance between the instrument and the retina. This information is primarily used to prevent accidental penetration of the retinal surface. The third layer (denoted in red) combines all measurements of the environment into a world model of the inside of the eye.

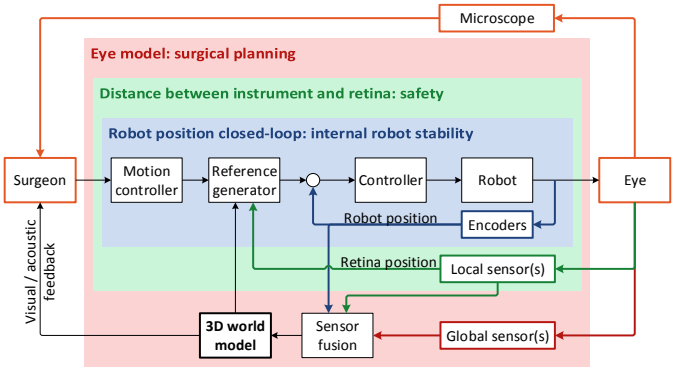

Fig. 1: Sensor integration in the surgical system.

For improving safety, the green loop is used. A proximity sensor can be placed in line with the surgical instrument, providing distance measurements exactly where the surgeon cannot provide them himself.

III. Optical Coherence Tomography probe

A local sensor providing distance information between the instrument tip and the retina should satisfy a couple of requirements:

1) it should be possible to integrate it in an instrument,
2) the measurement window should be large enough to be able to detect the retina early enough for application of a virtual bound.
3) since vitreoretinal surgery is very close the retina, the accuracy of the sensor should be in the micrometer range,
4) since it is mainly used for safety, the measurement frequency should be sufficiently high, i.e. an update rate of at least 100Hz with a delay smaller than 10ms.

Surgeon position commands are typically in the band of 0Hz to 5Hz, including instrument positioning motion and reaction to disturbances, e.g., eye movement. To achieve dynamics fast enough to respond to these commands whilst guaranteeing proper position tracking, the motion control bandwidth needs to be typically 10Hz. In order to close a safety loop with a local sensor, the sensor needs to have an update rate of at least 100Hz with a delay smaller than 10ms.

Optical Coherence Tomography (OCT) [1] is a sensor solution based on interference between two light paths, a reference path and a path that reflects on the to be measured sample. An interference spectrum is measured and processed to obtain a one-dimensional depth image (A-scan) of the sample. This technique is used in combination with a fiber probe with focusing optics. A small piece of glass and a gradient index (GRIN) lens are connected to a piece of fiber, to focus the optical beam approximately 3mm in front of the probe tip. To remove optical disturbances, the measured spectrum is apodized [2] using a custom apodization spectrum. Generally, a spectrum measurement of air would include all optical disturbances inside the probe and reference stage. But these disturbances can change over time. Since the sensor is used in a closed-loop implementation, it is not preferred to interrupt surgery for a new apodization measurement. Therefore a low-pass filter with a time constant of 120s is applied to the measured spectra. It is assumed that the probe will move sufficiently, so that the sample is filtered out. Hence the apodization will not remove the sample. During initialization, the time constant of the low-pass filter is increased over time, starting from 0 seconds, until the 120s are reached.

IV. Probe tip calibration

To accurately measure the distance between the instrument tip and the retina, the position of the OCT measurement window should be known. The OCT probe is rigidly connected to the instrument, and hence the distance between probe tip and instrument tip is known. By changing the reference stage length by a known value, the measurement window can be shifted to include the probe tip. The offset between probe tip and the position of the OCT measurement window can then be calculated. Temperature changes and movement of the probe might change the length of the fiber connected to the probe, and can hence influence the position of the measurement window. Therefore, this calibration step should be performed every few seconds. For the change of the reference stage length, an optic switch can be used. This switch then only takes a few milliseconds, and hence the closed-loop safety control is not undermined.

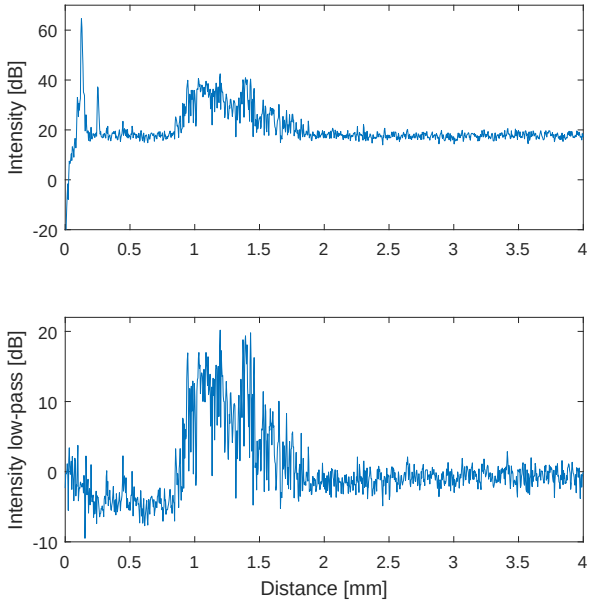

Fig. 2: A-scan of a porcine retina. In the top plot an average of 36 A-scans is shown. The retina is located at approximately 0.9 mm. The peaks near 0.13 and 0.25 mm are a result of a crack in the fiber. The bottom plot shows the same measurement, but with the offset removed and with a temporal high-pass filter applied.

V. Proximity sensing using OCT

The one-dimensional A-scan measured using the OCT probe provides information about the amount of change in reflective index or the amount of scattering of light. An average of 36 A-scans of a porcine retina is shown in Fig. 2. The OCT setup measures 36.000 A-scans per second, and hence the averaged A-scan covers 1 ms. The back of the eye scatters the light coming from the probe and is shown in the A-scan as a set of peaks between 0.9 mm and 1.9 mm. The top signal in Fig. 2 is subjected to a temporal high-pass filter, and the offset is removed to obtain the bottom signal. The bottom signal is then smoothed over distance to remove some of the noise. A hypothesis tree of Kalman filters keeps track of the local maxima detected in the latter signal. For safety reasons, the tracked peak closest to the surgical instrument tip is considered the proximity to the retina.

VI. Virtual bounds

As a first proof of concept, a virtual bound is implemented on a paper phantom eye. The distance to the paper is sent to the robot, which limits the tracking of the surgeon's movement to the position of the virtual bound. When the distance to the paper is closer than the bound, the reference to the slave robot is reset to the bound value, and the telemanipulation setup is essentially being decoupled in one direction.

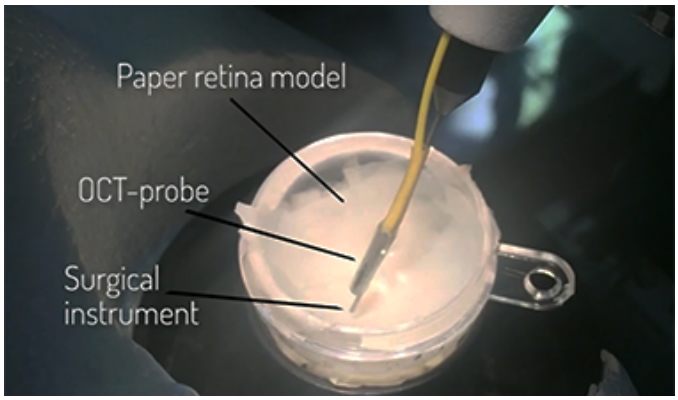

Fig. 3: The OCT-probe connected to a surgical instrument. The test setup is viewed by the surgeon through the microscope, similar to actual surgery.

To test the algorithm in a realistic environment, an ex-vivo porcine eye was used. The eye was prepared by removing the cornea and lens, without removing the vitreous. The virtual bounds were successfully applied and several surgeon tests showed that is was no longer possible to accidentally touch the retina.

VII. Conclusion & future work

This work showed a successful application of optical coherence tomography integrated in a probe to measure the distance from the tip of a surgical instrument to the retina. This distance was used to apply virtual bounds on the instruments' position with respect to the retina, making it impossible to accidentally touch the retina.

Future work involves improving the detection and tracking algorithm to be able to distinguish between retina and other tissue, dirt and blood floating inside the eye.

References

[1] Yaqoob, Z., Wu, J., & Yang, C. (2005). Spectral domain optical coherence tomography: a better OCT imaging strategy. BioTechniques, 39

[2] Marks, D., Carney, P. S., & Boppart, S. a. (2004). Adaptive spectral apodization for sidelobe reduction in optical coherence tomography images. Journal of Biomedical Optics, 9

Synthesis of a New Concentric Tube Robot for Olfactory Cells Exploration

C. Girerd[1], K. Rabenorosoa[2], P. Renaud[1]

[1]*AVR-ICube, CNRS, Université de Strasbourg, INSA Strasbourg, France*

[2]*FEMTO-ST, AS2M, Université de Bourgogne Franche-Comté, ENSMM, CNRS, Besançon, France*
cedric.girerd@insa-strasbourg.fr

1. INTRODUCTION

Recent findings show possible links between the development of neurodegenerative diseases such as Alzheimer's disease and olfactory deficiency. In the NEMRO project [1], we therefore intend to explore objectively the olfactory neuroepithelium in order to assess the occurrence of neuropathological changes for neurodegenerative diseases. This implies to develop a tool for *in vivo* exploration of olfactory cells to be used at a research level, on selected patients. OCT imaging appears as a very interesting modality for the inspection given its resolution, depth of inspection, and the possibility of using an optical fiber-based OCT probe. The challenge is to bring such a probe in the area of interest, the so-called olfactory cleft, a very narrow zone in the upper area of the nose. This cannot be performed today with existing manual instruments. We thus introduce the current developments in the design of a new robotic platform, with the synthesis of a dedicated concentric tube robot (CTR).

2. MATERIALS AND METHODS

Robot synthesis has been studied in three steps, with first the estimation of exact requirements, then the computation of patient-related data for a precise formulation of workspace requirements and third the determination of a robot geometry.

2.1. Initial Design Choices from Task Requirements

The OCT probe has to be guided from the nostril to the olfactory clefts. Each cleft is a very narrow space, with a width that does not exceed 1 to 2 mm. From the entrance point of the cleft, inspection consists in moving the probe in a plane parallel to the top of the olfactory clefts. Around the entrance point, the presence of olfactory cells makes the area very sensitive, which excludes any contact between the robot and the mucosa. On the contrary, contacts between the robot and the soft tissue of the nostril are admissible even if not desired.

Concentric tube robot (CTR) architectures seem adequate in such a context characterized by strong size constraints. We therefore propose to build the robotized OCT probe-holder as a CTR, decomposed in two subsystems. The navigation section aims at reaching the olfactory cleft entry from the nostril. The exploration section is inserted in the navigation section and it aims at conducting the olfactory cells inspection. This second section will be the association of the optical fiber and an electro-active polymer-actuated tube to perform the scan. Embedded actuation will be used to modify the tube curvature [1]. The main issue concerns the synthesis of the navigation section, given the constraints on the size and the exclusion of contacts with the mucosa in the upper part of the nasal cavity. The deployment of a CTR can be a complex issue in the general case, with a variable volume swept by the robot body. We here impose a follow-the-leader (FTL) [2] constraint to more easily solve the robot/mucosa contact issue: the robot body follows the path of its tip, which means that undesired contacts can be analyzed by focusing on the configuration after full deployment.

2.2. Determination of Anatomical Constraints

The robot synthesis requires precise information on the space inside the nasal cavity. Such information is not available to the knowledge of the authors, in particular with inter-patient variability. 3D reconstructions have therefore been performed. A set of 19 subjects was selected, for which CT scans are available. Left and right nasal cavities are considered. Image segmentation and 3D reconstruction are performed using Invesalius [2] software. The 3D geometry of each nasal cavity is finally reconstructed and the variations of the width of the olfactory clefts are determined as well.

2.3. Synthesis of the Navigation Section

2.3.1. Selection of a synthesis method

Different patient-based robot design methodologies for CTR such as [2] are proposed in the literature. These methods are iterative and make use of CTR kinematic models that are complex, in particular when the presence of tube torsion is included. Even though they constitute powerful frameworks, alternate methods can be considered for simple CTR geometries, which are favorable for design and manufacturing simplicity.

Since we consider a perfect FTL behavior, it is here sufficient to consider the final configuration of the robot. For this configuration, the analysis is decomposed in two steps. Admissible robot shapes are first identified by simulation using the 3D reconstructed data. Validation of the robot tube geometries is then performed by taking into account the impact of torsion and possible stability issues for the CTR.

2.3.2. Robot shape selection

Only limited solutions exist to obtain FTL behavior with a CTR. The easiest way to get this property is to build a planar robot made of tubes with constant curvatures.

[1] http://projects.femto-st.fr/projet-nemro/

[2] http://www.cti.gov.br/invesalius/

The number of tubes defines then the number of constant-curvature sections of the resulting robot.
Considering again the objective of simplifying the design and manufacturing of the system, solutions with a minimum number of constant-curvature sections have to be preferred. This also limits the number of tubes and therefore minimizes the outer diameter of the device. Given the cavity geometry, using only one section is obviously not admissible. On the contrary, the use of two sections can be of interest, in particular when combining a linear proximal section with a curved distal section, since the lower part of the nasal cavity is today accessed in conventional procedures with straight instruments. The CTR is then defined by the length of the two sections and the curvature of the distal section.

2.3.3. Assessment of robot geometries

First, candidate architectures are generated by discretization of values of length and curvatures. Variations of the robot position and orientation with respect to the nose are also considered. Then, the existence of contacts between the robot and the nasal cavity is assessed for all the obtained combinations. Collision detection between meshes representing the two entities is being used. Given the large number of evaluations to be performed, a computational-efficient implementation is needed. Parallelization is therefore adopted and about 80 solutions can be tested per second.

Once admissible sets of robot shapes are identified, it is needed to estimate the corresponding tube geometries using an inverse torsionally-rigid kinematic model. The stability of the robot during the deployment can then be evaluated following [3].

3. RESULTS

3D reconstructions are used to select the CTR outer diameter. The data for the 19 subjects show that a maximum diameter of 1.4 mm is acceptable. The internal diameter of the CTR is linked to the diameter of the exploration section of the robot. Given the expected size of the OCT probe, a diameter of 0.7 mm is chosen.
A single robot geometry is not sufficient to inspect a significant number of subjects. Our study shows however that 13 out of the 19 subjects could be included in a research protocol with the proposed CTR shape using only 3 different sets of tubes defined by curvatures of 0.03, 0.04 and 0.05 mm^{-1}. No contact then occurs between the robot and its environment, except along the soft tissue of the nostril for a few of them.
Nitinol is a great material for CTR given its superelasticity. It is therefore considered for the two tubes of the robots, with internal and external diameters respectively equal to (0.7, 1.0) and (1.0, 1.4) mm. Using an inverse kinematic model, the tube geometries are determined with curvatures equal to 0.03, 0.04, 0.05 mm^{-1} for the inner tubes, and 0.0080, 0.0107, 0.0134 mm^{-1} respectively for the outer tubes, inserted in opposition to the inner tubes. Using the analytical formulation of the robot stability introduced in [3], the robots are considered valid since maximum transmission lengths are equal to 232.4, 42.5 and 16.6 mm respectively for the inner tube. Such values ensure the possibility of integrating actuation solutions for the device. In other words, the identified robot geometries offer a proper access to the site of interest, unreachable today, with a simple geometry that is also safe without any phenomenon such as snapping.

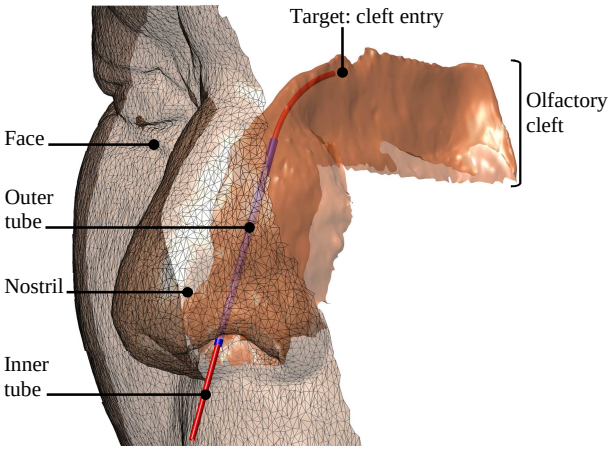

Figure. 1. Fully deployed CTR in one of the 3D reconstructed nasal cavities.

4. CONCLUSION AND DISCUSSION

In this paper, we have developed the synthesis of a new CTR for olfactory cells inspection. The design method takes into account inter-patient variability and it is simple in the fact that no complex kinematic model is required for the robot selection. We have shown that stable robots that respect our application requirements can be selected, therefore allowing an inspection of the olfactory cells for the first time at a research level. Further work will now be focused on the design of an actuation unit and early tests of the navigation capability.

REFERENCES

[1] M. T. Chikhaoui, K. Rabenorosoa and N. Andreff, “Kinematic Modeling of an EAP Actuated Robot for Active Micro-endoscopy” in Advances in Robot Kinematics 2014; 457-465

[2] C. Bergeles, A. H. Gosline, N. V. Vasilyev, P. J. Codd, P. J. del Nido and P. E. Dupont, “Concentric Tube Robot Design and Optimization Based on Task and Anatomical Constraints” in IEEE Transactions on Robotics 2015; pp. 67-84.

[3] H. B. Gilbert, R. J. Hendrick and R. J. Webster III, “Elastic Stability of Concentric Tube Robots: A Stability Measure and Design Test” in IEEE Transactions on Robotics 2016; pp. 20-35.

ACKNOWLEDGEMENT

This work is supported by the French National Agency for Research (NEMRO ANR-14-CE17-0013), and Investissements d'Avenir programs (Robotex ANR-10-EQPX-44, Labex CAMI ANR-11-LABX-0004 and Labex ACTION ANR-11-LABX-0001-01)

Light Intensity Based Optical Force/Torque Sensor for Robotic Manipulators

Y. Noh[1], A. Shiva[1], E. Hamid[1], H. Liu[1], K. Althoefer[2], Kawal Rhode[3]

[1]*Dept. of Informatics, Centre for Robotics Research, King's College London, UK*

[2]*Dept. of Informatics, Faculty of Science and Engineering, Queen Mary University of London, UK*

[3]*Dept. of Biomedical Engineering, Centre for Robotics Research, King's College London, UK*

(corresponding author): yohan.noh@kcl.ac.uk

INTRODUCTION

In minimally invasive surgical operations such as laparoscopy, or in robot assisted surgery, the surgeon is not in direct contact with the patient's body, hence loses the haptic sensation of the organs and tissues [1]. Usually in order to assist the surgeon, special cameras embedded in the surgical tools are employed to provide visual feedback, which on its own results in deploying more instruments during operations. Although visual information is highly desirable, however it does not completely replace the haptic perception attained by palpating the patient's organs, which typically provides valuable information to the surgeon [2-3]. Therefore, additional information retrieved from further sensor modalities may assist the surgeon when using robots for surgical procedures.

As part of The EU project STIFF FLOP (STIFFness controllable Flexible and Learnable Manipulator for Surgical Operations), which aimed at developing a novel soft continuum robot for MIS (minimally invasive surgery), we designed a novel force and torque sensor to provide sensory feedback on external forces and torques on the robot.

The based on light intensity sensing, we develop a three-axis force/torque sensor, using two approaches: 1) Optoelectronics, and 2) Fibre optic technology. The developed sensors are integrated within the soft continuum STIFF-FLOP robot arm to measure external forces and torques.

Though the sensor presented here is integrated within the STIFF-FLOP manipulator, but its geometry and structure allows it to also be integrated within any other flexible manipulator with similar structure as shown in Figure 1.

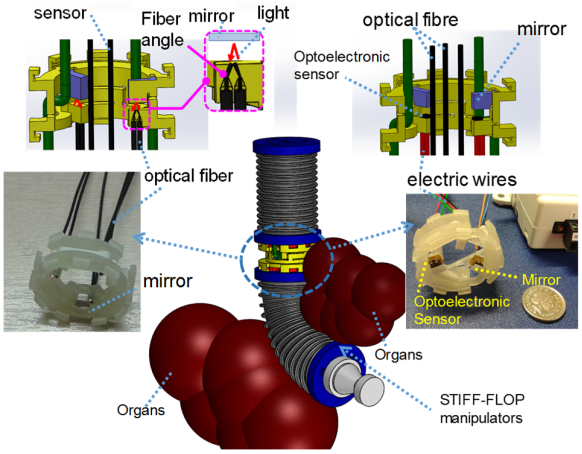

Figure. 1. Force/Torque sensors being integrated into Soft-manipulator (STIFF-FLOP): optoelectronic technology (right) and fibre optic technology (left)

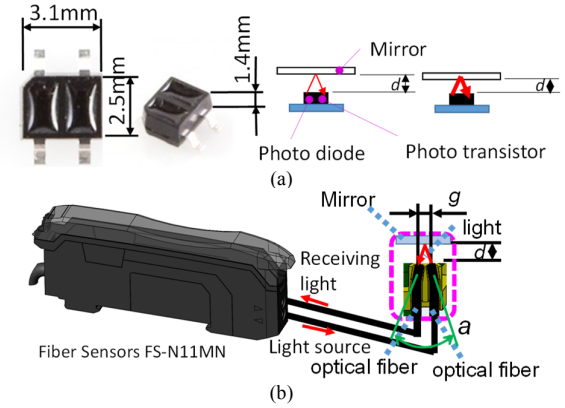

Figure. 2. Two sensing approaches: (a) Optoelectronic based sensing approach (b) Fibre optic based sensing approach: *d* distance between the mirror and the tips of the fibers; *a* angle between two optical fibers; *g* depth between the fibers

MATERIALS AND METHODS

A. Sensor design concept

The multi-axial force sensor should satisfy the following conditions:

1) Since the sensor structure is also serving as a connection between two mutually tangent segments of the STIFF-FLOP manipulator, it should have a hollow ring-like structure to allow actuation pipes for the subsequent segments of the manipulator to pass through proximal segments and reach distal ones.

2) The sensor should be capable of measuring at least three components of external forces and moments; namely the longitudinal force, F_z; and the two torques, M_x, and M_y (Figure 3). Note that the STIFF-FLOP manipulator has 3 degrees of freedom (DoF), including two omni-directional bending motions and one elongation motion.

B. Sensor configuration

The three-axis force sensor entails two types of light intensity based approaches: 1) optoelectronic sensors, and 2) optical fibres; as shown in Figure 2. In the first case, the three optoeletronic sensors (QRE1113, Fairchild Semiconductor Corp.) – or in the second case, the three pairs of optical fibre - are coupled with three mirrors (made of write-reflective plastic) and integrated in a flexible ring-like structure made of ABS plastic (a copolymer of Acrylonitrile, Butadiene, and Styrene)

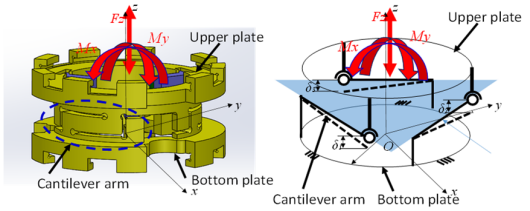

Figure. 3. Sensor operating principle based on 3 flexible cantilever beams [4-5]

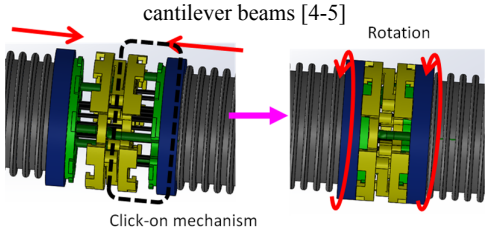

Figure. 4. The STIFF-FLOP manipulator and click-on mechanism

which is designed with a 3D rapid prototyping machine (Fig. 2) [4-5]. This structure accommodates three flexible cantilever beams on its periphery for measuring one force component F_z and two moment components, M_x and M_y.

The optoelectronic sensor consists of an LED and a phototransistor for emitting and receiving light, respectively. On the other hand, a pair of the two optical fibres are connected to KEYENCE™ Digital Fiber Sensors FS-N11MN which has an LED and a phototransistor inside. One fibre is connected to the LED, and another fibre is connected to the phototransisotor. The light emitted from the LED is reflected by the mirror and is received by the phototransistor. The closer the distance is between the mirror and the photo interrupter, the higher is the intensity of the reflected light received by the phototransistor [4-5].

When external force F_z and moments M_x and M_y are applied to the upper plate, the three associated cantilever beams are deflected. The three corresponding photo interrupters - or three pairs of the optical fibres - measure the resultant cantilever beam deflections (δ_1, δ_2, and δ_3) between the upper and bottom plates of the sensor (Fig. 3). From the three deflections, the external force F_z and moments M_x and M_y can be calculated by multiplying a calibration matrix.

In order to anchor the force sensor to the structure of the STIFF-FLOP manipulator, a clocking mechanism is also integrated in the sensor design (Fig. 4).

RESULTS AND DISCUSSION

For sensor performance test, the external force and moments are compared with the measured data from the two types of sensors. The two sensor errors are shown in Table I and II.

It should be noted that the difference in the error results for the two type of sensors are due to the different characteristic curves between the output voltage of the optoelectronic sensor and the fibre force sensor FS-N11MN. The optoelectronic sensor can be optimised by *d*, but the fibre optic sensor should be optimised by the three parameters *g*, *a*, and *d* to obtain an exactly linear curve of the output voltages with respect to the distance *d* as shown in Fig. 2. Both the optoelectronics and the fibre optics method have their advantages and disadvantages depending on the application.

The main advantage of the optoelectronic sensor is its simple integration into the manipulator. In case of the manipulator being damaged, the force/torque sensor can be removed and easily reinstalled again since its calibration matrix is always same, regardless of disconnecting or reconnecting the sensor's electrical wire to its circuit. The main advantage of the fibre optic approach is MR compatibility and the sensor being immune to magnetic or electrical fields. In contrast, once the optical fibre is removed and reattached from/to the fibre sensors FS-N11MN, the sensor's calibration matrix will change, hence requiring recalibration.

TABLE I. SENSOR ERROR PROPERTY (OPTOELETRONIC TECHNOLOGY)

Force / Moment	Range	Maximum error
Fz	+/- 5.0 N	0.65 N (6.5%)
Mx	+/- 3.5 Ncm	0.71 Ncm (10%)
My	+/- 3.5 Ncm	0.45 Ncm (6.4%)

TABLE II. SENSOR ERROR PROPERTY (FIBRE OPTIC TECHNOLOGY)

Force / Moment	Range	Maximum error
Fz	+/- 3.0 N	0.32 N (10.7%)
Mx	+/- 3.15 Ncm	0.38 Ncm (12.2%)
My	+/- 3.15 Ncm	0.59 Ncm (18.2%)

CONCLUSION

A novel metal free force/torque sensor based on optoelectronic and fibre optic technology for robotic and MIS has been presented. The sensor can be used for the STIFF-FLOP manipulator as well as other continuum or flexible manipulators which require pipes or tendons to be passed through proximal segments and reach distal ones, thanks to the hollow structure. The results of sensor performance test show an error of less than 18% of the sensor range, hence reliable enough to potentially contribute to haptic feedback in robot assisted surgeries. Due to the sensor manufacturing process, material, and optimizing parameters, a deeper analysis of its properties and, in particular, of the linearity and hysteresis of the response should be investigated to reduce the error.

REFERENCES

[1] N. Simaan, R. Taylor, et al. "A System for Minimally Invasive Surgery in the Throat and Upper Airways." Int. J. Rob. Res.; 2009 June; 28(9): 1134–1153.

[2] M. C. Yip, R. D. Howe, et al. "A Robust Uniaxial Force Sensor for Minimally Invasive Surgery" IEEE Trans. on Biomedical Eng.; 2010; 57(5): 1008-1011.

[3] N. Yu, R. Riener, et al. "Comparison of MRI-Compatible Mechatronic Systems with Hydrodynamic and Pneumatic Actuation." IEEE/ASME Trans. on Mechatronics; 2008; 13(3): 268-277.

[4] Y. Noh, K. Althoefer, et al. "A continuum body force sensor designed for flexible surgical robotics devices." 36th Annual Int. Conf. of Eng. in Medicine and Biology Society (EMBC), 2014; 3711-3714.

[5] Y. Noh, K. Althoefer, et al. "A three-axial body force sensor for flexible manipulators" 2014 IEEE International Conference on Robotics and Automation (ICRA), 2014; 6388-6393.

Development of a surgical stereo endoscopic image dataset for validating 3D stereo reconstruction algorithms

A.S. Ciullo*, V. Penza*†, L. Mattos†, E. De Momi*
*Department of Electronics, Information and Bioengineering, Politecnico di Milano, Milan, Italy
†Advanced Robotics Department, Istituto Italiano di Tecnologia, Genoa, Italy
E-mail: andrea.ciullo@mail.polimi.it

INTRODUCTION

In the last decades, endoscopic stereo images have been exploited to retrieve tissue surface information of the surgical site using 3D reconstruction algorithms [1], [2]. The application of such algorithms in Computer Assisted Surgery (CAS) tools for Minimally Invasive Surgery (MIS) requires a robust validation process in order to guarantee reliability and safety. 3D reconstruction algorithms are commonly evaluated comparing their result with respect to a reference Ground Truth (GT) [3]. However, few datasets providing endoscopic images and GT are openly available.
In [4], a stereo-image dataset of a moving heart phantom was generated using the *da Vinci*® surgical system, providing a CT scanner-based GT. In [1], a dataset of stereo-images of ex-vivo animal organs was developed providing a CT scanner-based GT, where different conditions were investigated, such as presence of blood and smoke, and different pose of the endoscope.
Considering the increasing necessity of surgical datasets, the aim of this work is the generation of an Endoscopic Abdominal Stereo (*EndoAbS*) dataset composed of stereo-images with associated GT for 3D stereo-reconstruction algorithm validation. To recreate the surgical scenario, a polyurethane surgical phantom abdomen was built. Images were captured with a stereo-endoscope, while for acquiring the GT a laser scanner (calibrated with respect to the stereo-endoscope) was used. This dataset is openly available on-line[1] for the benefit of the CAS community.

MATERIALS AND METHODS

The generation of the dataset consists in three main steps:
1) Surgical Scenario Development: An abdominal model made of kidneys, liver and spleen phantoms was developed through a molding process, using 3D organ models provided by 3DIRCADB[2]. The 3D negative molds were designed using the software Blender 2.7.4 and 3D printed using the Elite Dimension 3D printer (layer thickness: 0.25 mm). A bi-component polyurethane elastomer (F-105 A/B 5 shore, BJB Enterprise) was combined with a softening agent (SC-22, BJB Enterprise) in order to create the phantoms having approximately the real tissue characteristics.
The organs were also painted to simulate the tissue texture and small superficial vessels. Tubular structures were attached and painted on the surface of the liver and kidneys to represent main vessels, as it is shown in Fig. 1a. In addition, a ribcage-like support was 3D printed (Fig. 1b) to maintain the relative position between the organs.

(a) (b)

Figure 1: On the left liver, spleen and kidneys are shown; on the right the ribcage containing the organs is shown.

2) GT generation: The GT was generated using a laser scanner. A camera-laser calibration algorithm was designed to express the GT in the camera reference system, allowing the comparison with the point cloud obtained by a 3D reconstruction algorithm. The camera-laser calibration consisted in computing the rigid transformation $\mathbf{T}^{\mathbf{L}}_{\mathbf{C_l}}$ between the same set of points in the camera reference system $\{\mathbf{C_l}\}$ and in the laser reference system $\{\mathbf{L}\}$ (see Fig. 2); hence, a non-symmetric octagonal calibration plate was designed, which vertices $\mathbf{p}_{vert}$ were used for the calibration process. The 3D vertex coordinates were identified both in $\{\mathbf{C_l}\}$ and in $\{\mathbf{L}\}$ ($\mathbf{p}^{\mathbf{C_l}}_{vert}$ and $\mathbf{p}^{\mathbf{L}}_{vert}$ respectively), and $\mathbf{T}^{\mathbf{L}}_{\mathbf{C_l}}$ was computed solving the equation (1) with the Singular Value Decomposition (SVD) method:

$$\mathbf{p}^{\mathbf{C_l}}_{vert} = \mathbf{T}^{\mathbf{L}}_{\mathbf{C_l}} * \mathbf{p}^{\mathbf{L}}_{vert} \quad (1)$$

For facilitating the comparison between the GT transformed in $\{\mathbf{C_l}\}$ and the 3D reconstructed point cloud, the GT was stored into a 2D map so that, the (u, v) cell of the map contains the 3D coordinates of the point represented in the (u, v) pixel of the left image. In

[1] http://nearlab.polimi.it/medical/dataset/, Apr 2016
[2] http://www.ircad.fr/research/3dircadb/, Apr 2016

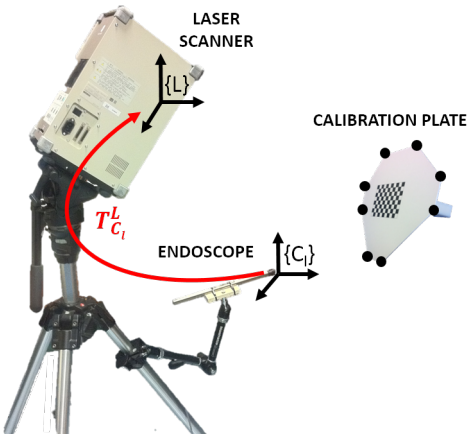

Figure 2: Setup for camera-laser calibration.

order to discard the GT 3D points having the same (u, v) coordinates, but different depth values, the GT point cloud was oversampled and, in each cell, only the point with minimum z was kept.

3) Dataset generation: The laser scanner and the stereo endoscope were positioned in order to have approximately the same point of view, looking towards the surgical scenario. Since a real stereo laparoscope was not available, two Ultra Mini CMOS Color Cameras (MISUMI) with 640×480 pixel resolution were assembled to create a custom-made endoscope with a baseline of $6\ mm$. In order to simulate laparoscopic lighting conditions, two white LEDs were integrated in the endoscope and the images were captured in a dark room. The GT was measured with the laser scanner VIVID 910, which has a sub-millimeter accuracy (x = $\pm 0.22\ mm$, y = $\pm 0.16\ mm$, z = $\pm 0.07\ mm$).

Thus, the obtained dataset was made of:

- 120 stereo-images of the surgical scenario (PNG format);
- GT point cloud (TXT format);
- Camera calibration parameters (TXT format);

The camera calibration was performed using the Stereo Camera Calibrator Toolbox of Matlab 2015b. In order to allow the validation of a 3D stereo-reconstruction algorithms under different conditions, the images were reproduced introducing: (i) presence of smoke, created immersing dry-ice in hot water; (ii) 3 different light levels, varying the led intensity; (iii) two phantom-endoscope distances ($\approx$ 5 cm and $\approx$ 10 cm).

EVALUATION AND RESULTS

A compressive mechanical test was done on polyurethane samples and a sample of porcine liver to identify the best percentage of the softening agent used to replicate real tissue mechanical properties. Results showed that using 50% in volume of the softening agent a Young's Modulus of 0.97 kPa was reached, similar to the Young's Modulus of the porcine liver (0.95 kPa).

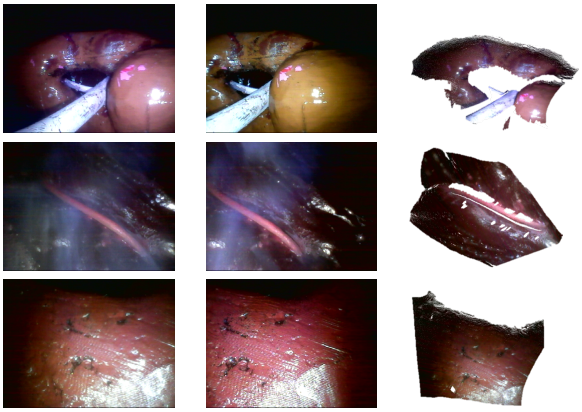

Figure 3: Samples of stereo-images and GT from EndoAbS dataset: left (top-down): kidney at $\approx$ 10 cm distance and 3rd light level, liver at $\approx$ 5 cm with smoke and spleen at $\approx$ 5 cm at 3rd light level; right: the relative GT of each image.

The abdominal phantom organs were qualitatively evaluated comparing the obtained images with respect to real surgical images. Realistic features, such as light specularity, homogeneous texture, vessels and smoke presence were reached as shown in Fig. 3.

Regarding the camera-laser calibration, the calibration error was 0.43 mm (25-75 $perc$: 0.41 mm - 0.43 mm), computed as the median Euclidean distance between a set of points in $\{\mathbf{C_l}\}$ and the same set of points in $\{\mathbf{L}\}$, transformed in $\{\mathbf{C_l}\}$ using the computed $\mathbf{T^L_{C_l}}$.

CONCLUSION AND DISCUSSION

This work presents a stereo endoscopic surgical dataset for the validation of 3D reconstruction algorithms, providing stereo-images of a phantom abdomen with an associated GT and camera calibration parameters. Future work aims at improving the dataset generating video sequences representing tissue motions and deformations due to the contact with surgical instruments. Since the images generated are noisy due to the intrinsic characteristic of the image sensor, it could be interesting to generate the same dataset with an high quality HD stereo endoscope.

REFERENCES

[1] L. Maier-Hein, A. Groch, A. Bartoli, S. Bodenstedt, B. Guillaume, P.-L. Chang, N. Clancy, D. Elson, S. Haase, and D. Stoyanov, "Comparative Validation of Single-Shot Optical Techniques for Laparoscopic 3D Surface Reconstruction." *IEEE transactions on medical imaging*, 2014.

[2] V. Penza, J. Ortiz, L. S. Mattos, A. Forgione, and E. De Momi, "Dense soft tissue 3d reconstruction refined with super-pixel segmentation for robotic abdominal surgery," *International journal of computer assisted radiology and surgery*, 2015.

[3] P. Jannin and C. Grova, "Model for defining and reporting reference-based validation protocols inmedical image processing," *International Journal of Computer Assisted Radiology and Surgery*, vol. 1, no. SUPPL. 7, pp. 63–65, 2006.

[4] D. Stoyanov, M. V. Scarzanella, P. Pratt, and G.-Z. Yang, "Real-time stereo reconstruction in robotically assisted minimally invasive surgery." *International Conference on Medical Image Computing and Computer-Assisted Intervention*, 2010.

Implementation of a Soft-Rigid Collision Algorithm in an Open-Source Engine for Surgery Realistic Simulation

F. Fazioli[1], F. Ficuciello[1], G. A. Fontanelli[1], B. Siciliano[1], L. Villani[1]

[1] *University of Naples Federico II, DIETI*

INTRODUCTION

The aim of this work is to integrate a soft-rigid collision algorithm proposed by Fukuhara [1] in an open source physics engine, Bullet Physics [2]. In surgical applications this can be the case of a clamp grabbing deformable organic materials or of a spatula opening a brain fissure. The default soft-rigid collision algorithm proposed in Bullet is not very effective in the case of thin tools interacting with deformable objects. In particular, if the rigid body (surgical tool) moves slowly, i.e. its displacement covers a small distance compared to the simulation step size, the collision is detected regularly, otherwise the default algorithm does not recognize the collision. As a consequence, the object penetrates into the soft body. Besides the implementation in [2] of the soft-rigid collision algorithm in [1], the new contribution consists on generalizing the algorithm to different shaped rigid object such as convex rigid bodies with thin thickness along one of the three main directions. Moreover, the haptic rendering has been realized by controlling the spatula in the 3D virtual space with the Novint Falcon 3D Haptic Controller. The default linear elastic model of the interaction force has been replaced with a more realistic and physical consistent non-linear viscoelastic model [3]. As a second step, the algorithm has been further extended to a clamp constituted by two rigid colliding objects grabbing deformable materials.

MATERIALS AND METHODS

The Scene

In the first step, a single rigid object (like a spatula) interacting with a deformable sphere has been considered. The sphere is composed by a 128 triangular meshes, and is placed on a ground plane. The position of the spatula in the 3D space is given by the Novint Falcon 3D Haptic Controller. The visual rendering has been realized using OpenGL. In the second step, the scene is constituted of a clamp realized with two collidable rigid objects and a handle not collidable but with solely aesthetic functions. The haptic interface allows three degrees of freedom (DoFs) for the controlled object motion. However, the clamp requires one DoF for closing and opening. Therfore for simulation purpose, the motion of the clamp has been limited to a plane and the extra DoF has been used to control the closing/opening on different object shapes, such as a sphere and an elongated object shape, that simulate more realistically vessel and in general organic tissues.

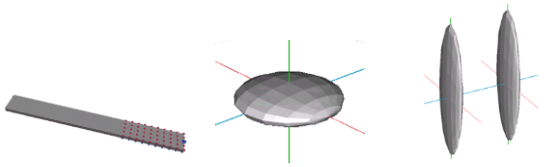

Figure. 1. Example of a spatula and nodes displacement in [1] (left image). 3D Model of the convex rigid body (middle image). The two collidable bodies of the clam (right image).

Extension of the algorithm to convex thin bodies

The rigid body used in [1] is a parallelepiped and the nodes used for collision detection are placed only on the two larger surfaces. The symmetrical shape of the body allows an easy placement of the nodes by defining the resolution along the planar directions of the two surfaces, see Fig. 1 (left image). In this work, the proposed algorithm has been extended from rigid boxes to generic convex objects modelled with triangular meshes. The algorithm in [1] requires that nodes on parallel surfaces are associated in pairs that belongs to the same surface normal. For convex objects, as in Fig. 1 (middle image), the nodes association is realized by placing a node in the centroid of each triangle mesh and by associating it to a node that belongs to the triangle intersected by the ray casting. The ray source is the node itself and the direction is the opposite of the normal to the triangle to which the nodes belongs. In this way each triangle finds its opposite pair. With respect to [1] where if a node x is associated to a node y also the vice-versa holds, in this case the nodes are not always mutual associated. This is not intrinsically critical for the algorithm application, nevertheless some problems arise. The rigid object represented in Fig. 1 (left image) presents triangular faces in close proximity to the side edge, thus, very close to one another. Indeed, the distance between two triangles on the side edge may be of two orders of magnitude smaller than the thickness of the object, as in Fig. 2 (left side). Moreover, as an effect of triangle orientation, if a node on the top left, that belongs to a triangle in proximity to the edge side, casts a ray in the opposite direction of its normal, a node on the bottom right can be associated, as represented in Fig. 2 (right side). This can be critical for the proper application of the algorithm. Indeed, when the symmetrical arrangement of the associated nodes is lost, the wrong triangle associations can cause unfeasible deformations. To solve the problems arising for these critical nodes,

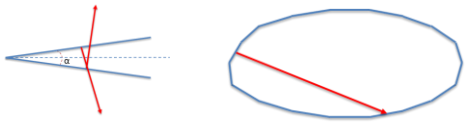

Figure. 2. Triangular faces in close proximity to the side edge.

the ray casted has no more infinite extension but limited according to the dimensions of the scene and especially of the colliding soft bodies. In this way infeasible collisions are highly reduced. Moreover, since there is no mutual association between the nodes, it is no possible to study the state of a node by verifying only the state of the opposite one. When a node belongs to an infeasible pair, the associated index is stored in a vector collecting all the indices of the nodes that cannot collide in the current simulation step. Thus, a cross-check is necessary at each step.

The interaction force model

In order to improve the sense of realism during the simulation, the contact force has been modeled using the Hunt Crossley model [3]. The model incorporates a non linear spring in parallel with a non-linear damper to model the viscoelastic dynamics:

$$F(t) = \begin{cases} kx^n(t) + \lambda x^n(t)\dot{x}(t) & x(t) \geq 0 \\ 0 & x(t) < 0 \end{cases}$$

where x is the deformation, k and λ are the elastic and viscous parameters of the model, and n is a real number (usually close to one), that takes into account the geometry of contact surfaces. At each time step, the deformation x is the distance between the current centroid of a triangle and the centroid of the same triangle at time zero. For this purpose, during the object initialization, the original position of each triangle vertices is stored. Obviously, the calculation of x is executed if and only if at least one of the nodes belonging to the triangle is in a colliding state. The total force is computed by adding the components related to each deformed triangle involved in the collision.

RESULTS AND FUTURE WORKS

By applying the default collision detection method proposed by Bullet Physics, it follows that the spatula collides with the soft body in a consistent way only for small displacements and slow motion. Fast displacement of the spatula can cause a complete penetration into the soft body surface without further collision, see Fig. 3 (left image).

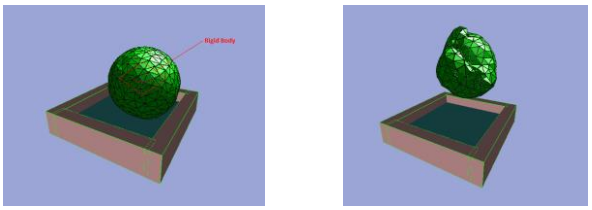

Figure. 3. Soft-rigid collision Bullet default algorithm.

Moreover, the application of only the ray casting method without node association (second step of the algorithm) causes drawbacks if the dimension of the rigid body along the collision direction is not large enough. The collision appears unstable, as in Fig. 3 (right image), when both the nodes belonging to opposite surfaces apply collision forces to the soft body even if they are unfeasible. This drawback is overcome by applying also the second step of the algorithm, that detects the unfeasible collisions and excludes them from the study at the current simulation step. The algorithm has been extended to convex rigid objects and to a clamp grabbing deformable objects, see Fig.4. The results are realistic both in terms of visual rendering and in terms of force feedback, Fig. 5.

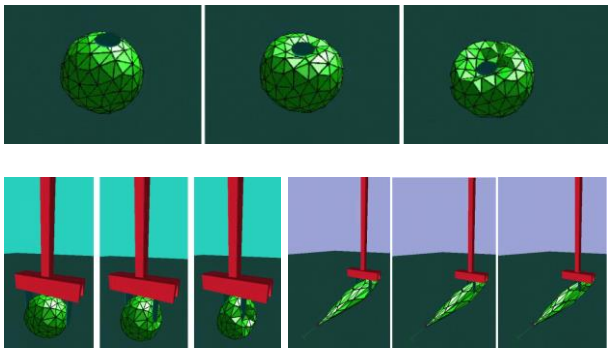

Figure. 4. Simulation results of the collision algorithm extended to different object shapes and to a clamp.

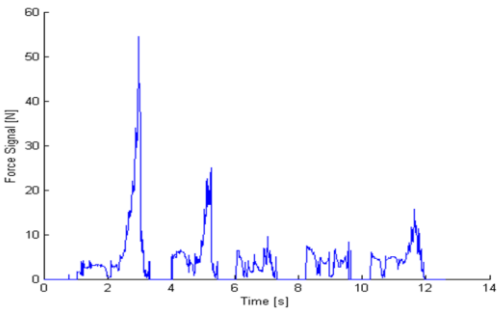

Figure. 5. Resultant force on the sphere grabbed by the clamp.

Since the promising results w.r.t the Bullet default collision algorithm, for future works is worth continuing to investigate toward improved solutions, such as for concave objects, friction models for the interaction force and future integration within different engines such as SOFA [4].

REFERENCES

[1] A. Fukuhara et al., ROBOMECH Journal, 2014.
[2] http://bulletphysics.org/wordpress/.
[3] F. Ficuciello et al., IROS, 2010.
[4] https://www.sofa-framework.org/.

Residual-based interaction force estimation for haptic feedback in teleoperated needle insertion

D. Evangelista[1], F. Iodice[1], A. Perica[1], M. Cefalo[1], E. Magrini[1],
M. Anzidei[2], M. Vendittelli[1]

[1]*Dipartimento di Informatica, automatica e gestionale, Sapienza Università di Roma*

[2]*Dipartimento di Scienze radiologiche, oncologiche e anatomo-patologiche,*

Sapienza Università di Roma
vendittelli@diag.uniroma1.it

INTRODUCTION

Needle insertion is performed in a variety of medical procedures, including relevant oncological indications such as biopsies and tumor ablation. The conventional approach to these procedures is based on free-hand percutaneous placement of needles and probes under image guidance, either with ultrasound (US), computed tomography (CT), fluoroscopy (XA) or magnetic resonance (MR). While US and XA offer real-time guidance but are somewhat limited in the visualization of deep organs and soft tissues, CT and MR are more effective in the visualization of normal anatomy and pathologies of visceral organs but don't support real-time image acquisition. This adds significant complexity to interventional procedures performed under CT and MR guidance, in particular in terms of accuracy of needle placement, and exposure to ionizing radiation. Developed assisting devices include robotic platforms such as the RobioEX and iSYS. However, systems available on the market are limited in terms of real-time image guidance and scope of clinical applications. Ideally, a robotic platform for interventional procedures should feature real-time or near real-time guidance, force feedback, inter-modality compatibility and indication to various types of procedures in several anatomical regions.

Teleoperated needle insertion complies with the above cited requirements as it allows to operate under real-time image guidance (e.g., XA), while protecting the medical staff from radioations. In addition, an appropriate kineamtic design and control of the slave robot can fit the very constrained environment of an MR gantry without constraining the operator mobility. Beside the surgeon's comfort, this is expected to improve task manipulability. Finally, procedure performance can be considerably improved by combining imaging and needle-tissue interaction force information [1]. The introduction of force sensors would however increase cost and size of the robotic system.

We propose the use of a model-based approach to interaction force estimation that eliminates the need of force sensors, providing the benefits of force feedback at no additional cost or complexity of the system. In particular, we analyze here the dynamic accuracy of the residual-based interaction force estimation method [2] by performing insertion experiments in the line of [3] and comparing the estimates with force measures.

Methods and systems for teleoperated needle insertion with force feedback proposed in the litearture, including [4, 5] and the references therein, either use measures from force sensors or are based on interaction models to generate the feedback. While the approach proposed here requires an initial effort in developing a reliable robot dynamic model, it does not depend on a specific needle-tissue interaction model, and thus in principle should perform well in penetration of any tissue.

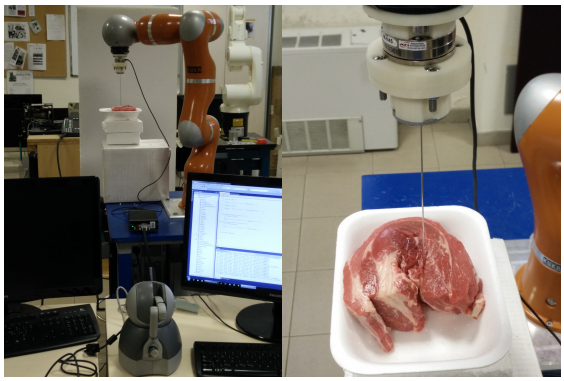

Figure. 1. Experimental setup for remote needle insertion.

MATERIALS AND METHODS

The dynamic model of a rigid manipulator interacting with the environment at a robot point $\boldsymbol{x}_c$ is given by

$$\boldsymbol{M}(\boldsymbol{q})\ddot{\boldsymbol{q}} + \boldsymbol{C}(\boldsymbol{q},\dot{\boldsymbol{q}}) + \boldsymbol{g}(\boldsymbol{q}) = \boldsymbol{\tau} + \boldsymbol{J}_c^T(\boldsymbol{q})\boldsymbol{F}_c$$

with $\boldsymbol{M}$ the inertia matrix, $\boldsymbol{C}$ the Coriolis and centrifugal terms, $\boldsymbol{g}$ the gravitational terms, τ the control torque. Denoted by $\boldsymbol{J}_c$ the jacobian at the contact point, the last term represents the joint torque due to the interaction force $\boldsymbol{F}_c \in R^3$. The residual-based method [2] allows to estimate the unknown contact force $\boldsymbol{F}_c$ knowing the robot model and the joint torques.

In the considered application, the interaction point is the tip of a rigid needle.

The analyzed interaction force estimation method is integrated in the master-slave experimental system

shown in Fig. 1 where a 17-G, 13 cm, stylet of a co-axial needle (SURECUT, TSK Laboratory) has been fixed to the KUKA LWR end-effector through a 3D printed flange. During teleoperation, the needle is remotely controlled through a Geomagic Touch haptic interface. In the implementation of the residual method we use the LWR model identified in [6] and measures from the torque sensors at joints. An ATI Mini 45 6D force sensor, mounted on the robot wrist, provides the ground truth measurements (at 62.5Hz with 1/16N resolution) that are used here to evaluate the accuracy of the residual-based force estimation method.
The needle can be considered as rigid if it is not reoriented after insertion, as confirmed by the experimental data.

RESULTS

In assessing the method accuracy the robot is not teleoperated with the aim of obtaining a robot motion clean from noise introduced by the operator and, thus, an increased legibility of results. The sinusoidal motion $z(t) = a\ sin(\omega t)$, with a=0.065, ω=0.3, along the vertical direction is therefore commanded to the needle tip. At starting, the needle is not in contact with the phantom made of fat, muscle and fibrous tissue.

Figure 2 reports the estimated and measured force relative to one insetion-extraction cycle in tissues characterized by different stiffness: muscle in the upper plot and fibrous tissue in the lower one. Interaction includes the loading deformation, rupture, cutting and unloading deformation events taking place during needle insertion [3] and corresponding to negative values of the force (the needle is pushed upward). Positive forces, pulling the needle downward, are associated to the extraction phase and are mainly due to friction. The delay introduced by the residual method is of the order of milliseconds, the medium error is less than 0.1N, while the maximum error is smaller than 1.5N following a rupture event (after the negative peaks in force measurements).

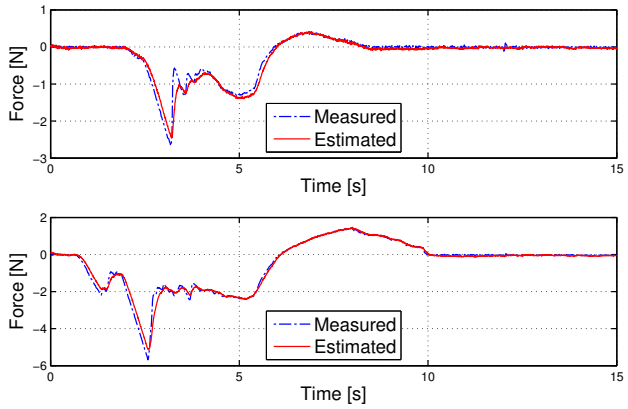

Figure. 2. Comparison of estimated and measured force.

Figure 3 reports the estimated force vs needle displacement relative to the same experiments confirming that the maximum error occurs at tissue rupture (steepest part of the measured force curve). This is due to the filtering effect of the residual method.

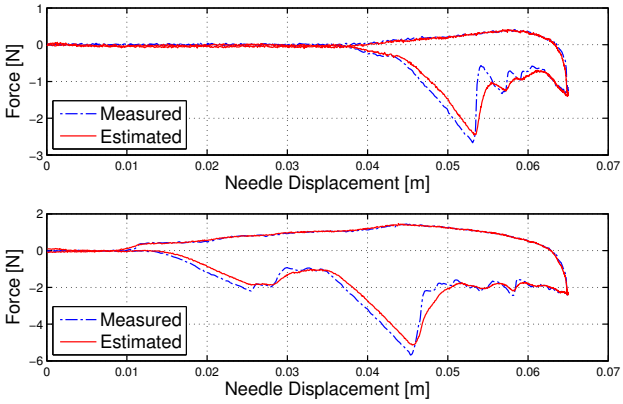

Figure. 3. Force vs needle displacement.

CONCLUSION AND DISCUSSION

We have proposed the use of a needle-tissue interaction force estimation method that does not require the use of force sensors. The estimate is used to generate the force feedback in a teleoperated system for needle insertion in interventional radiology procedures.
Needle deformation is not considered, to allow accuracy assessment based on the ground truth provided by a force sensor mounted on the robot wrist. Future work include the combined use of a deflection model and imaging information to correct the estimate provided by the proposed method. Estimation of the interaction moments, here assumed to be null, in combination with a deflection model of the needle should allow to determine the actual needle tip position. The proposed approach allows force feedback integration with visual information, as in the manual procedures, and eliminates the need to interrupt the insertion to avoid surgeon exposure to radiations.

REFERENCES

[1] O. Gerovich, P. Marayong, A. M. Okamura, "The effect of visual and haptic feedback on computer-assisted needle insertion," CAS, 2004.

[2] A. De Luca and R. Mattone, "Sensorless robot collision detection and hybrid force/motion control," ICRA 2005.

[3] M. Mahvash and P. E. Dupont, "Mechanics of Dynamic Needle Insertion into a Biological Material," IEEE Trans. on Biomedical Engineering, vol. 57, no. 4, 2010.

[4] E. Dorileo, N. Hungr, N. Zemiti, C. Fouard and P. Poignet, "A modular CT/MRI-guided teleoperation platform for robot assisted punctures planning," 28th CARS, 2014.

[5] C. Pacchierotti, M. Abayazid, S. Misra and D. Prattichizzo, "Teleoperation of steerable flexible needles by combining kinesthesic and vibratory feedback," IEEE Trans. Haptics, pp. 1-1, 2014.

[6] C. Gaz, F. Flacco, A. De Luca, "Identifying the dynamic model used by the KUKA LWR: A reverse engineering approach," ICRA 2014.

High-fidelity simulation in newborns therapy through an active soft pulmonary simulator

Margherita Brancadoro*, Selene Tognarelli, Irene Scarcella and Arianna Menciassi

The BioRobotics Institute, Scuola Superiore Sant'Anna, Pisa, Italy

m.brancadoro@sssup.it

INTRODUCTION

Respiratory function is mandatory for extrauterine life, but it is sometimes impaired in newborns due to prematurity, congenital malformations, or acquired pathologies. Mechanical ventilation provides standard care [1], but long-term complications are still largely reported [2]. Furthermore, there is a disparity between the rapidly increasing ventilator options (e.g. different ventilation modalities) and the clinical knowledge of how to optimally ventilate the patients [3].

In this context, continuous training of health staff is mandatory for education purposes and for upgrading comprehensive knowledge and skills, while guaranteeing newborn patients' safety. High-fidelity simulation is the best methodology for this purpose because it is a completely interactive educational method in a realistic clinical scenario [4]: a neonatal respiratory simulator represents the main tool to provide education while keeping patients safe. However, commercially available breathing function simulators (e.g. SimNewB (*Laerdal Medical)*, Premi HALS3009 and Newborn Hall S3010 (*Gaumard Scientific)*, ASL 5000 Breathing Simulator (*IngMar Medical)*) are rarely suitable for the lack of anatomical and physiological complexity typical of the neonatal respiratory apparatus. In order to overcome these imitations, innovative research simulators [5] have been recently developed; because of their potential accuracy, they represent a step forward with respect to commercial simulators. Anyhow, problems of extreme bulkiness and device complexity are still evident, thus restricting their practical use.

These are the reasons why the interest of the research community is continuously growing both for updating the current commercial systems and for developing innovative devices able to simulate with high accuracy, stability and repeatability the physiological/pathological respiratory patterns of the newborn, yet maintaining an intuitive and simple design for facilitating their integration into training and educational courses.

The purpose of this study is the design, implementation and assessment of an innovative soft neonatal respiratory simulator with variable compliance able to reproduce the anatomy and the proper functionalities of the neonatal respiratory system.

MATERIALS AND METHODS

For obtaining a high-fidelity representation of the physiological pulmonary features, the neonatal active respiratory simulator was designed as a multi-compartmental model having five cameras with variable volumes, one for each of the lobes as in normal human lungs (i.e. two lobes in the left lung and three lobes in the right lung) linked to each other by a dedicated circuit of plastic tubes that accurately reproduce the neonatal airway system. A pressure sensor is fixed on the lobes to detect measurement profiles during the respiratory cycle (Figure 1).

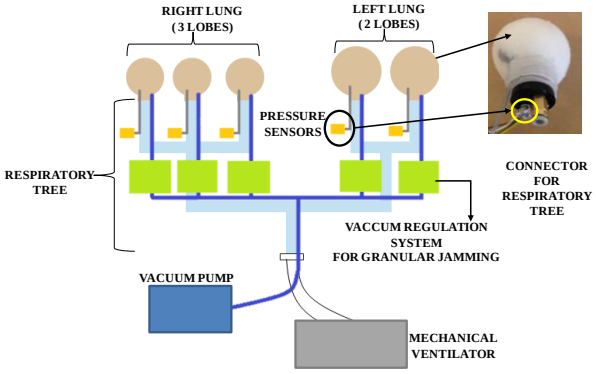

Figure. 1. General scheme of the simulator system

Pulmonary compliance, i.e. index of the lung's ability to stretch and expand (Compliance C = $\Delta V/\Delta P$ with V=lobe volume and P=lobe pressure), is one of the most critical feature of the newborn lung that has to be correctly reproduced in the simulator. In the proposed model, each compartment is characterized by its own adjustable compliance by exploiting the jamming process, and right and left respiratory branches are subjected to an independent and adjustable resistance level (Figure 2). This novel design allows the device to simulate the lack of uniformity with regard to pulmonary features, as well as to outline conditions of localized barotraumas or airway obstructions. Finally, the simulator is designed to be compatible with mechanical ventilators commonly used in Neonatal Intensive Care Units (NICUs).

Jamming is the physical process by which some materials, such as granular materials, glasses, foams, and other complex fluids, become rigid by increasing density [6]. In this system, five lobes have been realized by using two concentric elastic (e.g. silicon and latex) spheres (i.e. chambers) coupled by means of specific granular material (e.g. sugar particles, coffee or sand) as reported in Figure 2. By varying the vacuum level in the intra-chambers space (i.e. by means of the vacuum regulation system properly controlled with a voltage

signal), a stiffness change in the whole structure is induced, that entails a different internal compliance.
Being C the ratio between ΔV and ΔP, we can assess the C variation by applying a defined ΔP (i.e. 20 cmH_2O which is the commonly imposed pressure value in NICUs) to the system by using a traditional infant mechanical ventilator (BEAR CUBr750 PSV Infant Ventilator) and evaluating the ΔV. Pressure sensors (MS1451-005-GT, Measurement Specialties), properly integrated into the system as in Figure 1, have been used for having a double control on the Peak Inspiratory Pressure (PIP) induced in each chamber and for guaranteeing a proper mechanical ventilation. High stiffness simulates a low compliance neonatal lung.

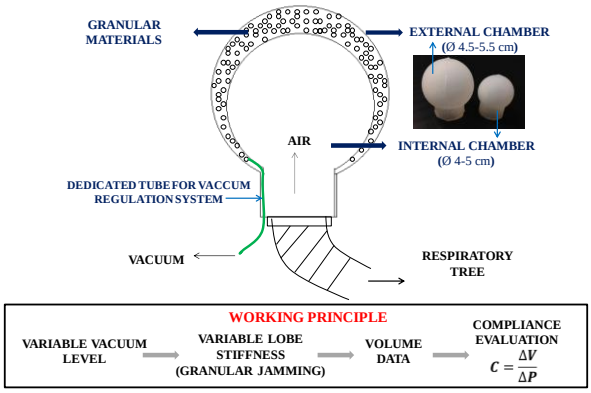

Figure. 2. Single lobe structure with details about the implemented working principle. The internal chamber of each lobe was designed by using respiratory parameters of a term-infant of 3 kg weight (i.e. 47.25 ml volume for the two lobes of the left lung and 31.5 ml volume for the three lobes of the right lung)

By means of a simple LabView (LabVIEW System Design Software, National Instruments) human machine interface (HMI), the clinicians are able to independently change on-fly the C of each lobe by setting different vacuum levels.

RESULTS

In order to properly design the mechatronic system, a deep analysis of the jamming process has been carried out evaluating both the most promising granular material and elastic membrane. Several test sessions (e.g. bending test, compression test) and materials characterizations have been performed for identifying the most appropriate elements used for simulating the lung lobes (i.e. sugar particles and silicone membrane - Ecoflex-0030).

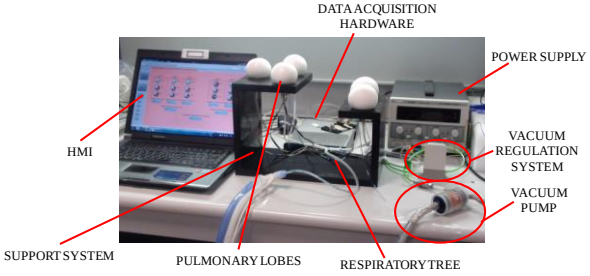

Figure. 3. Final prototype of the whole simulator system

The whole system has been realized by integrating each different element and properly validated. The final system prototype is reported in Figure 3.
In order to assess the functional principle used for implementing the pulmonary simulator, the final prototype was intensively tested with a clinical ventilator and different compliance values were simulated (i.e. partial/total/no malfunctioning of the respiratory system). First of all, each lobe was correctly ventilated and the internal pressures measured by the sensors resulted comparable with the PIP. The rigidity of each lobe was then changed on-fly by using the implemented interface and the final volume was evaluated as in Figure 4.

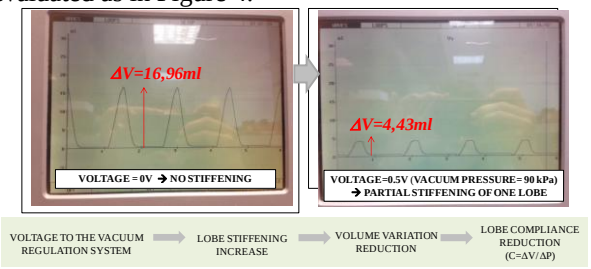

Figure. 4. Final assessment of the system performances. The mechanical ventilator automatically adapts the volumetric gradient as a direct consequence of the compliance variation (i.e. high rigidity) of a single lobe induced by the jamming effect. Higher rigidity --> lower volume--> lower C

CONCLUSION AND DISCUSSION

The soft pulmonary simulator for newborns is able to simulate both the physiological respiratory pattern and pathological conditions, by exploiting the granular jamming physical process.
It represents a useful simulator system for medical training, especially for a deeply investigation of the complex interaction between the baby and the mechanical ventilator.

REFERENCES

[1] Ramanathan R. "Optimal ventilatory strategies and surfactant to protect the preterm lungs." Neonatology; 2008; 93(4):302–308.
[2] Mosca F, Colnaghi M, Fumagalli M. "BPD: old and new problems." J Matern Fetal Neonatal Med.; 2011; 24 Suppl 1:80–82.
[3] Claure N and Bancalari E. "New modes of mechanical ventilation in the preterm newborn: evidence of benefit." Arch Dis Child Fetal Neonatal; 2007; 92(6): F508–F512.
[4] Gaba DM. "The future vision of simulation in health care." Qual Saf Health Care; 2004; 13(1): i2–i10.
[5] Baldoli I, Tognarelli S, Cecchi F, Scaramuzzo R et al., "An active one-lobe pulmonary simulator with compliance control for medical training in neonatal mechanical ventilation." Journal of clinical monitoring and computing; 2014; 28(3):251-260.
[6] Liu AJ, and Nagel SR. "Nonlinear dynamics: Jamming is not just cool any more." Nature; 1998; 396(6706):21-22.

Requirement and design of safe medical device software architecture

Miklos Kozlovszky[1], Khulan Batbayar[2], Gernot Kronreif[3], Eszter Jósvai[4]

[1,2]*BioTech Knowledge center, Obuda University, Budapest, Hungary*

[3,4]*Austrian Center for Medical Innovation and Technology,Wiener Neustadt,Austria*

kozlovszky.miklos@nik.uni-obuda.hu[1], batbayar.khulan@phd.uni-obuda.hu[2], gernot.kronreif@acmit.at[3], eszter.josvai@acmit.at[4]

Abstract – Medical surgery robots must operate in contact with people. In an ideal world 100% safety can be achieved, the world is not ideal and errors in software and failures of hardware do occur. We have designed and build up a prototype safety framework for surgery robots and trying to implement in an eye surgery robot software. In this paper we provide description of its monitoring and inbuilt safety mechanisms.

INTRODUCTION

In a real world errors in software and failures of hardware do occur, despite duplication of systems and extensive testing. Every effort should be taken to ensure that the system is as safe as possible. The medical robot is designed to fail in a safe manner and come to a controlled halt so that it can be removed and the surgical procedure can be completed manually. Such systems are keen on controlled stop in the event of a failure and manual (mechanically assisted) tool retraction can be a solution in most of the cases. We are focusing on retinal vein occlusion and membrane peeling robot-assisted surgery robot. Our software system is developed in component based fashion, therefore, we are implementing component-based safety framework which checks continuously the availability of the components, collects error messages and reacts to errors in a pre-configured way. We have identified generic and component specific error groups. The source of errors in the system are categorized, and each error type has a severity level. One important component in the error handling is the HealthMonitor component, which monitors the action of all other components. Our error handling is built up from multiple levels; at the lowest level the errors captured by the component and the component is handling the occurred errors with its inbuilt functionalities, the highest error handling level is the system level. When an error occurs, the component tries to fix the problem. The error handling based on the type and severity level of the error. When the error handling at component level is not possible, the error is handled over to the HealthMonitor, which analyses the problem and initiate system level error handling. has to ensure that the control can be fully taken over by the surgeon. Another feature of the HealthMonitor component is detecting the error based on the incorrect or erroneous operation which will trigger automatic messaging to the HealthMonitor component and the HealthMonitor will take action according to the error.

MATERIALS AND METHODS

In component-based software system, one of the popular trend is to integrate traditional safety analysis techniques with a component model. Kaser et al proposed an idea to convert traditional fault tree analysis into components which allows partitioning fault tree into multiple components. Our safety framework follows Component Fault Tree Analysis to classify potential errors and estimate severity of the errors.

We are reusing ideas also from Jung et al's Safety Framework (SF) which provides runtime software safety platform for component-based medical and surgical robot systems. Thus their main idea is to decompose safety features or implementation into reusable safety mechanisms and safety specifications. Our error handling solution adapts, reusable and modular and extensively reuse features such as ease of development, error identification and error handling.

RESULTS

Main design requirements

Requirement 1. Robustness

The error handling should be available and able to serve during the whole system. It should support error identification, error handling and safe working environment of all the other components.

Requirement 2. Ease of development

The error handling solution should be easily configured and used for all system components. The lowest level of the multi-level error handling should be implemented at component level.

Requirement 3. Human factor

Since robot-assisted surgery robot software system is dealing with the sensitive information and patient safety, human-in-the-loop should be involved in order to comply with the safe working environment. Surgeon should be informed during the decision making process of the safety framework. System should allow full participation of the surgeon in order to handle critical condition of the system.

Requirement 4. Monitoring and event handling

The safety framework should be able to monitor each components failure information as well as its own failure information. Every failure in the software system

has to be notified to the Health Monitor and in parallel also logged.

Requirement 5. Early identification of possible failures

Based on the log data, if there is a suspicious event occurs, HealthMonitor should be able to catch the error and find the possible solution. For each failure, there should be a set of appropriate solutions and each solution should be ranked in order to give priority of execution.

Design of the safe medical device component based software architecture

System architecture consists of three main mechanisms which are shown in Figure 1. During the active running of the system, every action of the system will be monitored and logged. If there is an unusual pattern or erroneous action happens, then framework will detect the error and based on the error intensity, impact and the state of the error.

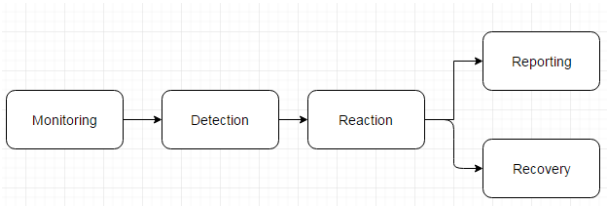

Figure. 1. Mechanism view of the safe component architecture

Safe medical software architecture shown in Figure 2 is a layered architecture, therefore, error handling is built in layered fashion. Each component has an error handling feature built inside and try to solve the problem inside using exception handling and report it to the HealthMonitor component. If the error handling in the component level is not possible, then component will report to the HealthMonitor to take an action. In this case, the HealthMonitor will search for the error information and take a reaction.

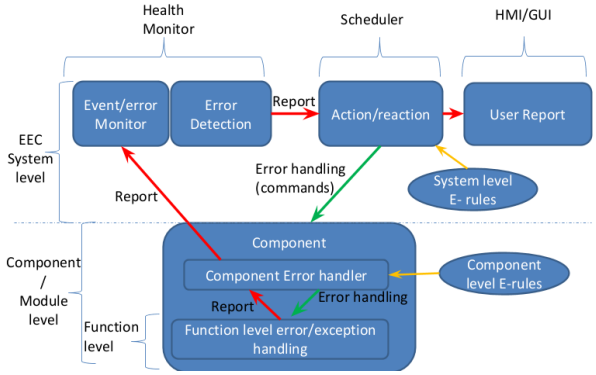

Figure. 2. Basic structure of safety framework

Compatibility with safety standards and regulation body

One of the major part of the medical robot system is that it has to be approved by regulatory authorities such as Food and Drug Administration (FDA) depend on the market of the medical device. Since the main goal of these standards are to ensure correct, precise working of the robot and avoid any harm for the patient as well as the surgeon. We are designing the software architecture in a safe manner, therefore we are trying to develop software as safe as possible. Further compatibility will be studied thoroughly.

CONCLUSION

Medical robot systems are safety critical system which are specially designed according to the environment, functionality and regulation requirement. The design of the requirement is based on the component-based software systems and safety engineering of the medical robot software. The fault analysis of the HealthMonitor component will use Component Fault Tree Analysis to estimate the failure and possible reaction of the system. The HealthMonitor component is responsible to fault detection, fault removal and ability to sustain safe running environment of the entire software system. The HealthMonitor component can be applicable to the other domain of the medical robot system which are built using component-based architecture.

REFERENCES

[1] B. Kaiser, P. Liggesmeyer, and O. Maeckel. A new component concept for fault trees. In Proc. of the 8th Australian workshop on Safety critical systems and software, volume 33 of SCS ’03, pages 37–46. Australian Computer Society, Inc., 2003.

[2] Min Yang Jung, Peter Kazanzides; Runtime safety framework for component-based medical robots; Medical Cyber Physical Systems Workshop (formerly known as HCMDSS (High Confidence Medical De- vices, Software, and Systems)), CPSWeek 2013, Philadelphia, PA, USA, 2013.

[3] A. Kapoor, A. Deguet, and Peter Kazanzides, Software components and frameworks for medical robot control, in IEEE Intl. Conf. on Robotics and Automation (ICRA), May 2006, pp. 3813–3818.

[4] Min Yang JUNG, Marcin BALICKI, Anton DEGUET, Russell H. TAYLOR, Peter KAZANZIDES; Lessons learned from the development of component-based medical robot systems; Journal of Software Engineering for Robotics 5(2), September 2014, 25-41 ISSN: 2035-3928.

Indipendent control of magnetic millirobots for targeted drug delivery: simulation-based feasibility study

G. Lucarini, V. Iacovacci, L. Ricotti, A. Menciassi

The BioRobotics Institute, Scuola Superiore Sant'Anna, Italy.

INTRODUCTION

The goal of targeted delivery of therapeutic agents, *e.g.* drugs, nucleic acids and cells, is to overcome the limitations and side effects of conventional therapeutic strategies. Most delivery systems under investigation at present, such as nanoparticles and colloidal systems, smart triggerable materials, etc. are affected by low controllability and the impossibility of retrieving the delivery system once the therapy has been completed, thus raising toxicity-associated risks [1]. Medical robotics and microsystem technologies can greatly contribute to the development of devices able to navigate in a wide network of small-diameter canals and to controllably get in the hard-to-reach areas of the human body [2]. Several strategies have been proposed for milli and microrobot locomotion and magnetic propulsion has emerged as one of the most promising approaches in this context, so far [3].

The authors have recently proposed a magnetically controllable targeted delivery system able to navigate through body canals featured by relatively small diameters (spine subarachnoid space, ureters, ovaries, pancreatic duct, etc.), and to release therapeutic agents *in situ*, in areas not reachable by catheters [4]. The platform consisted of a pair of millimeter-size robots, namely a carrier, in which the therapeutic agent was embedded, and a squeezing element able to trigger drug release, when desired. In this system, external magnetic fields can be used to propel and independently bring the robots to the neighborhood of the target site, whereas intermagnetic attraction forces generated by on-board permanent magnets, acting when the carrier and the squeezer are in close proximity, are responsible for docking the two parts. The docking event implies a compression of a drug-loaded hydrogel, thus activating drug release.

The design, fabrication and *in vitro* testing of the drug release mechanism have been already reported by the authors in [4]. However, to enable future clinical translation of this therapeutic procedure, accurate and independent magnetic locomotion of the two robots must be guaranteed. The independent control of two or more magnetic robots is difficult whenever the same magnetic field is applied to all robots. For such underactuated systems, independent control can be achieved by exploiting nonlinearities in the system dynamics. By designing the robots to maximize the difference in their nonlinearities (*i.e.* by changing mass, shape and magnetic content) it is possible to design a motion planner to achieve independent control of their position on the plane [5, 6].

The objective of this paper is to demonstrate the feasibility of an independent control strategy for the two proposed millirobots. Robots locomotion can be achieved by using, for example, a magnetic resonance image (MRI) scanner, able to generate a strong magnetic field along a single axis and magnetic gradients along three axes.

MATERIALS AND METHODS

The platform consists of two millimeter-sized near-neutrally buoyant magnetic robots (*i.e.* carrier and squeezing element) (Figure 1).

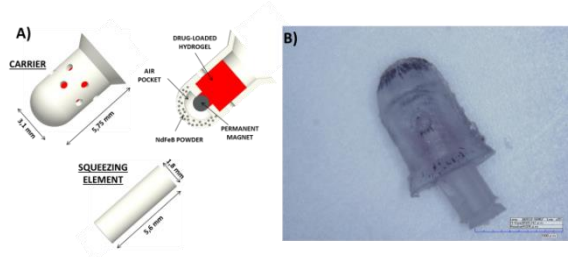

Figure 1 (A) Representation of the magnetic millirobots for targeted drug delivery, proposed in [4] (B) Image of carrier and squeezing element after docking.

The motion equations for the two robots are given by:

$$m_1\ddot{x_1} = F_{d1} + F_{m1}$$
$$m_2\ddot{x_2} = F_{d2} + F_{m2} \quad (1)$$

where m_i., $F_{di,}$ F_{mi} i={1,2} are the mass, the drag force and the magnetic force of the two mentioned robots [5]. In this case, a single axis of motion is considered but the analysis can be easily extended to 3 axes. The robots are aligned thanks to the strong MRI magnetic field (z axis, as a convention) and propelled by means of magnetic field gradients. Considering the expressions for drag and magnetic forces (i.e. cylindrical shape and dipole-dipole interactions) eq.(1) can be written as [5]:

$$\ddot{x_1} = -\frac{\pi\rho C_1 A_1}{2m_1}x_1^2 sign(\dot{x_1}) + \frac{\dot{V_1}M_1}{m_1}\frac{\partial B_z}{\partial x}$$
$$\ddot{x_2} = -\frac{\pi\rho C_2 A_2}{2m_2}x_2^2 sign(\dot{x_2}) + \frac{\dot{V_2}M_2}{m_2}\frac{\partial B_z}{\partial x} \quad (2)$$

Where ρ_i, C_i, A_i, V_i are the density, drag coefficient, frontal area and magnetic volume of the robots, respectively, whereas $\delta B_z/\delta x$ is the magnetic gradient that represents the control input. Eq. (2) is a second order nonlinear system with drift, resulting in an under-actuated system when two or more robots are considered. However, as already demonstrated in [5], the exploitation of nonlinear damping in combination with inertial transients, may enable motion differentiation for carrier and squeezing element, if such robots are featured by sufficiently different parameters (*i.e.* shape and magnetic context). By using sequences of control input pulses with different width (Δt_1 and

Δt_2), the robots can reach terminal speed or stay in the transient phase depending on robot parameters. If sufficiently short pulses are used, transient phase and variations in robots relative displacement occur, thus favouring their independent control. The individual displacements, written as $x_{1,2}(\Delta t_{1,2})$ can be expressed by means of a control matrix, to provide a linear equation which relates the desired final displacements, $x_{1,2}^{f}$, to the numbers $n_{1,2}$ of pulses of duration Δt, as follows:

$$\begin{bmatrix} x_1^f \\ x_2^f \end{bmatrix} = \begin{bmatrix} x_1(\Delta t_1) & x_1(\Delta t_2) \\ x_2(\Delta t_1) & x_2(\Delta t_2) \end{bmatrix} \begin{bmatrix} n_1 \\ n_2 \end{bmatrix} \quad (3)$$

As long as the pulse widths correspond to different displacement ratios, the control matrix has full rank and unique solutions for n_1 and n_2 exist.

A preliminary feasibility study was carried out, by implementing and validating this model by means of a Simulink routine (Matlab, MathWorks Inc) which considers the robot features reported in [4] in order to predict if the effective independent control of the two designed robots is feasible.

Both robots embed a spherical permanent magnet (NdFeB N45, 1 mm in diameter). The carrier consists of a polydimethylsiloxane shell (PDMS, SYLGARD® 184, Dow Corning) provided with holes to allow drug exit and with NdFeB powder (Magnequench MQA-37-11, MolyCorp) included in its tip to increase magnetic heterogeneity of the two robots, thus enhancing independent control of the components (Figure 1A). The carrier includes a drug-loaded agar-gelatin hydrogel, properly customized in order to deliver an effective quantity of drug (few ng) during the squeezing procedure as demonstrated in [4].

RESULTS

Simulations were performed in Simulink environment to demonstrate the efficacy of the motion planner. The parameters used in all simulations are reported in [4]. Figure 2 illustrates the implemented Simulink routine.

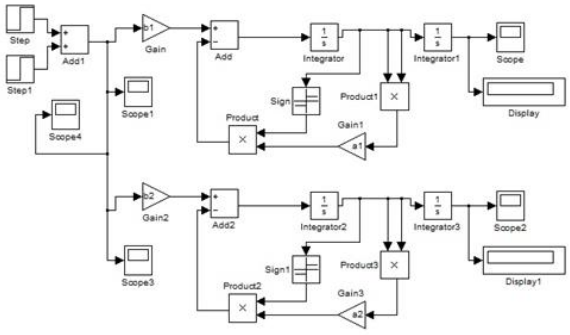

Figure 2 The Simulink routine used for demonstrating the feasibility of an independent control of the magnetic robots. The Simulink routine implemented the model expressed in (2).

The simulation demonstrated that the algorithm is able to generate motion plans that independently drive the robots to their target positions. In particular, an example is reported in Figure 3: by considering the robots in the same initial position, it is possible to drive only one of them to a target position even if they are subjected to the same stimulus. A 10 mm final displacement was imposed to the carrier, whereas the squeezing element was supposed to remain in its initial position. To obtain that, the selected pulse widths were Δt_1=0.05s and Δt_2=1s. Such widths were selected because the two points are sufficiently apart and their ratio n_2/n_1 is approximately an integer value (~ 5). The errors between the desired displacement and the simulated one are 1,425 mm and 0.96 mm, for the carrier and the squeezing element, respectively.

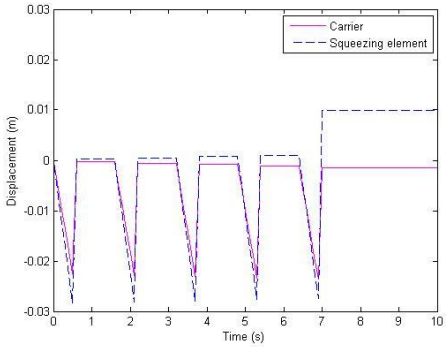

Figure 3 Simulation results, showing the initial and final positions for carrier and squeezing element.

CONCLUSION AND DISCUSSION

This paper proposes a preliminary feasibility study in order to demonstrate the independent control of two robots for targeted drug delivery. In this paper, simulations are used in order to demonstrate that an independent control of two millirobots, already proposed in [4], is actually possible. This can be achieved by using a single control input (*i.e.* magnetic gradient), generated, *e.g.*, by an MRI scanner. The proposed control algorithm exploits inertial transients together with the nonlinear damping to produce differentiated motions. Simulation results are promising and confirm the theoretical predictions. However, some errors are still present because arbitrary desired displacements do not correspond to integer numbers of pulses, thus resulting in errors in the actual displacement. Finally, it is important to note that the pulse sequence affects the path, but it does not affect the final robot positions. Future work will focus on further strategies to reduce the mentioned errors, also based on a partial robot re-design, and to experimentally demonstrate the locomotion results, thus validating the proposed models and simulations.

REFERENCES

[1] B.P. Timko et al.. Remotely triggerable drug delivery systems. Adv. Mater. 22(44): 4925-4943, 2010.

[2] J. Abbott et al., Z. Robotics in the small. IEEE Rob. Autom. Mag. 14: 92-103, 2007.

[3] B.J. Nelson, et al. Microrobots for minimally invasive medicine. Annu. Rev. Biomed. Eng. 12: 55-85, 2010.

[4] V. Iacovacci et al. Untethered magnetic millirobot for targeted drug delivery. Biomedical microdevices, 17(3), 1-12,2015.

[5] P. Vartholomeos et al. Motion planning for multiple millimeter-scale magnetic capsules in a fluid environment. Proc. IEEE Int. Conf. Robot. Autom. 2012; 1927–1932.

[6] E. Diller et al. Control of multiple heterogeneous magnetic micro-robots in non specialized surfaces. IEEE International Conference on Robotics and Automation (ICRA), 2011.

A novel venipuncture detection system based on electrical impedance measurement

Zhuoqi Cheng[1], Brian L. Davies[1,2], Darwin G. Caldwell[1], Leonardo S. Mattos[1]

[1]*Istituto Italiano di Tecnologia, Genova, Italy*

[2]*Imperial College London, London, U.K.*

zhuoqi.cheng@iit.it

INTRODUCTION

Nearly 1 billion IV insertions take place in the United States annually, and 28% of those insertions fail on the first attempt [1]. For some specific patients such as infant and patients with low blood pressure, the situation may be even worse. The traditional method of percutaneous intravenous access is done freehand, and the likelihood of success depends heavily on the patient's physiology and the practitioner's experience. In recent years, the problems associated with difficult intravenous catheterization have driven the development of technologies to improve the accuracy of catheter placement. Most of these devices are designed to enhance the visualization of the vein's location. However, these devices leave the ultimate determinant of catheter insertion to the human practitioner, who normally uses a combination of visual and tactile perception to achieve high demands of first stick accuracy. This accuracy, restricted to the penetration of the first wall of the vein and to stop the catheter inside the vein, is difficult to achieve. If the distal wall of the vein is punctured, the injecting fluid could flow into the tissues surrounding the vein, potentially causing cellular toxicity. In addition, blood may leak into the soft tissue after the injection and cause an edema.

Ultrasound technology can be applied to guide the catheter insertion thanks to its capability of showing the venous structure. However, ultrasound imaging requires specific training and increases the treatment cost. Another possible solution is to use infrared 3D imaging to generate a 3D view of the vein. But the accuracy of reconstruction could be affected by skin conditions such as color, scars and blotchy skin. Force sensing is another common method used for detecting venipuncture in robot-assisted intravenous insertion. But its accuracy suffers from noise due to patient motions and tremors, and sideways motions of the vein.

An alternative approach investigated in this research consists in exploiting the electrical impedance of tissues to detect venous access, since different types of tissues present different electrical impedances. This concept has been demonstrated by [2], in which a closed loop circuit was designed for controlling the needle insertion through measuring the electrical conductivity between the needle and an electrode attached to the skin.

In this study we propose a robotic system that uses local electrical impedance detection to supervise a servo motion stage for the needle insertion. A series of experiments were conducted to assess this robotic system. The obtained results demonstrated excellent capability of venipuncture detection.

SYSTEM CONFIGURATION

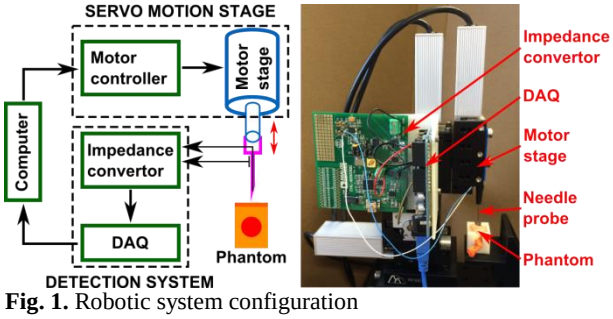

Fig. 1. Robotic system configuration

An overview of the proposed robotic system is shown in Fig. 1. A servo motor stage (MX7600R, Siskiyou Corp.) is used to drive the needle insertion into the phantom. During the insertion, the detection system continuously measures the electrical impedance of the needle's reached tissue layer using an impedance converter AD5933 (Analog Devices Inc.) in 200Hz sampling rate. A standard hypodermis needle is modified with a polyurethane-coated copper wire placed inside the needle tube so as to enable the electrical impedance sensing between the wire's exposed end and the needle tube. The sensing impedance is transferred to the control computer for processing and display. Once the impedance value is found within the range of blood, a command is sent from the computer to the motor stage for stopping the insertion. The robotic system is initially calibrated and tested to guarantee that it was appropriate for the application with high accuracy of impedance measurement and fast system response (mean detection time of 21ms).

Fig. 2. Phantom for system evaluations, made by inserting a balloon (filled with saline solution) inside a pig belly slab.

A realistic phantom is used to simulate the environment of intravenous catheterization, in terms of both anatomy and bio-impedance properties. As shown in Fig. 2, the phantoms are produced using slabs of pig belly tissue with epidermis, dermis and fat layers, and in each slab a

tubular rubber balloon (Ø = 6mm) filled with saline solution is embedded to simulate vein and blood.

EXPERIMENTS DESIGN

Three experiments were designed for a comprehensive evaluation of the robotic system in venipuncture detection. **Experiment 1** is designed to characterize the electrical impedance of 4 tissue types related to intravenous catheterization, namely, blood, dermis, fat and muscle. Furthermore, the needle probe was inserted through all layers of the realistic phantom, aiming to evaluate the system's capability of distinguishing blood from the other 3 bio-materials. In **Experiment 2,** the system's detection distance based on real time impedance measurement is evaluated. The robotic system drove the needle probe perpendicularly towards a saline solution container and stopped the insertion once the needle probe detects the saline solution. The detection distance, representing the final position of the needle tip to the liquid surface, was measured by the motor stage's built-in encoder. **Experiment 3** assesses the effectiveness of the robotic system through phantom trials. The motor stage was required to insert the needle starting from the epidermis layer with a constant insertion speed of 1 mm/s. Once the electrical impedance sensed at the needle tip was found falling within the range of the blood's, the needle insertion motion stopped. After that, the balloon of the phantom is removed from the phantom to check if the venipuncture detection was successful.

RESULTS AND DISCUSSION

Experiment 1: Fig. 3 shows the experimental results (median values and standard deviation) of 4 different tissue types, namely, dermis, fat, blood and muscle. It can be noted that the impedance range of blood has an obvious difference compared to the other tissue types, which offers an initial indication that the impedance detection system can perform robust venipuncture detection. In addition, the continuous measurements of electrical impedance from the needle insertion through all tissue layers of the phantom is shown in Fig. 4. The results match the values measured for each tissue type separately, and demonstrate the system is capable of identifying blood from the other tissues.

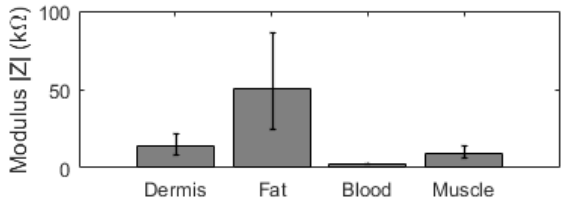

Fig. 3. Measured electric impedance of 4 tissue types related to intravenous catheterization.

Experiment 2: This experiment was repeated 20 times and the results reveal a mean detection distance of 817μm. This fast detection is potentially enough for the venipuncture detection, since vessel size for catheterization is normally bigger than that.

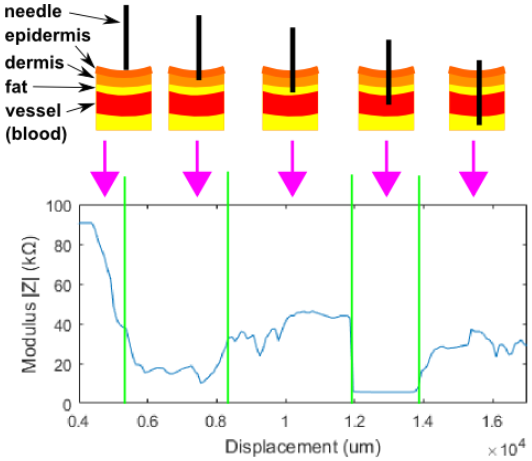

Fig. 4. Typical experimental result of the impedance change during the needle inserting into the designed phantom.

Experiment 3: The experiments demonstrated that the needle could successfully penetrate through the dermis and fat layer, and then stopped when the balloon wall was punctured. In this experiment, 10 phantom insertion tests were performed. Visual inspection of the balloons after each trial confirmed the presence of only one hole, demonstrating successful insertions for all 10 trials. These results prove the feasibility and effectiveness of the venipuncture detection system proposed for robot-assisted intravenous catheterization.

CONCLUSION

In this study, a novel venipuncture detection system for robot-assisted intravenous catheterization is introduced. The system is able to discriminate vascular entry during the needle insertion by measuring the electrical impedance of tissues at the needle tip. This sensing method was demonstrated robust and highly promising given the fact that the impedance value of blood is significantly different from that of surrounding tissues. It was then used to determine when the needle tip penetrates the vein wall and contacts the blood. Experiments were performed on a realistic phantom, and demonstrated the system was successfully able to detect the impedance change and stop the needle insertion as soon as venipuncture occurred, guaranteeing successful insertions.

REFERENCES

[1] Jacobson, Ann F., Elizabeth H. Winslow. "Variables influencing intravenous catheter insertion difficulty and failure: an analysis of 339 intravenous catheter insertions." Heart & Lung: The Journal of Acute and Critical Care; 2005; 34(5): 345-359.

[2] Saito, H., Mitsubayashi, K., & Togawa, T. "Detection of needle puncture to blood vessel by using electric conductivity of blood for automatic blood sampling." Sensors and Actuators A: Physical, 125(2), 446-450.

Design of robot assisted microsurgical forceps for Transoral Laser Microsurgery

Manish Chauhan, Nikhil Deshpande, Darwin G. Caldwell, and Leonardo S. Mattos
Department of Advanced Robotics, Istituto Italiano di Tecnologia (IIT), Via Morego 30, Genova, 16163, Italy
Email: {manish.chauhan, nikhil.deshpande, darwin.caldwell, leonardo.mattos}@iit.it

I. Introduction

The human oropharynx can be considered anatomically an irregularly shaped cylinder. It is this cylinder which has to be accessed and resected for a certain subset of tumors [1]. One way to treat these malignancies without any incision is called Trans-oral Laser Microsurgery (TLM). In TLM, state-of-the-art pre-curved single purpose, one degree-of-freedom (DOF) long and rigid microsurgical tools are used for intra-operative tissue manipulation. Simultaneously, a laser beam is used for aiming at the malignant tissue for performing an incision while the microsurgical tool is orienting and stretching the tissue perpendicular to its path. In recent years, great interest has developed for increasing the reachability of these tools. Thus, the focus of this research is to introduce a modular architecture in the design of microsurgical forceps which would allow changing the interface of the traditional hand operated tools while complying with surgical setup constraints. A serial six degree of freedom robot allows for easy tool movement between the vocal folds. A force sensor provided with the tool actuation mechanism measures force during tissue manipulation. This opens the possibility of teleoperation along with haptic force feedback (7-DoF Force Dimension Omega.7) for accurate and efficient pathology removal.

II. Traditional Constraints in TLM

TLM surgical setup presents various challenges to the surgeons which can be broadly categorized into three types, namely due to dimensional constraints of the surgical site, surgical tools and TLM user interface. These constraints can quantitatively listed as shown in Table I. Due to reasons of clear view and focus, the approximate distance between the surgical microscope and the surgical site is $400mm$ (Refer fig.1a). The surgical site is seen through a laryngoscope which is inserted through the mouth until the endotracheal tube. The approximate length of the laryngoscope is $180mm$ and has an oval cross-section ($16 \times 21mm^2$). The long (length $200 - 240mm$, exclusive of tool handle) rigid microsurgical tool shaft are used for tissue micro manipulation through the laryngoscope. Simultaneously, a laser beam is targetted through the manually controlled laser manipulator. This laser manipulator setup consumes an approximated depth of $110mm$. Hence, the surgeons are left with a narrow range of $50 - 90mm$ range for microsurgical tool movement and tissue manipulation. In addition, when viewed through the microscope the laryngoscope view is occluded due to microsurgical tool (Refer fig. 1b). In order to effectively perform TLM procedure, it is imperative to improve functionality and reach of these tools by adding automated robotic control at the surgeons end.

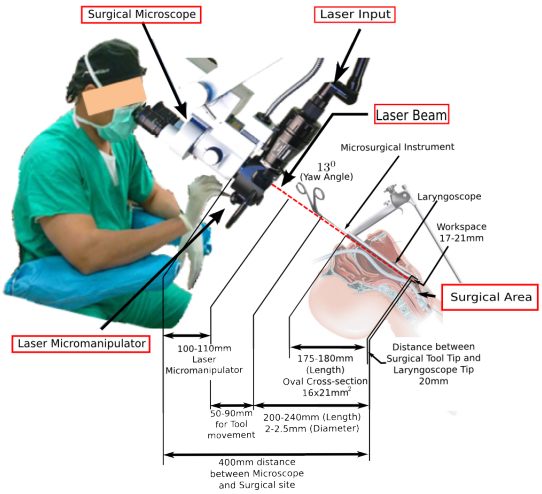

(a) Dimensional cross-section of TLM surgical site

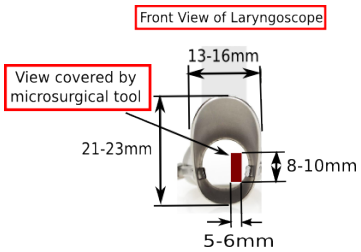

(b) General view of laryngoscope via Microscope

Fig. 1. Traditional constraints in TLM operating room

III. Microsurgical forceps design

Considering the constraints offered by TLM surgical setup, the novel design is based on a modular architecture consisting of three components: (i) the modular tool shaft; (ii) the tool actuation mechanism; and (iii) the microsurgical tool-shaft holder.

A. Modular tool shaft

The tool shaft is a modified version (maintaining the same length of 200∼220 mm) of traditional microsurgical tools used

TABLE I
CONSTRAINTS EXPERIENCED IN TLM

Surgical Site	Surgical Tool	TLM user interface
Vocal Cord limited size and closed cylindrical structure: 17–21 mm (males) 11–15 mm (females) [2]	Access to all areas of vocal cord not possible with single tool due to: • 13 degreeYaw angle • Long, rigid, one DOF, Pre-curved tip. • 40-50mm operating range. • 60-100mm displacement from microscope line of sight.	Coordinated control of instruments and laser demand considerable skill. • High psycho motor skills with hand-eye-foot coordination. • Activate laser from distance. • Fatigue, Hand-tremor, Inaccurate cuts. • Excessive carbonization • Peripheral tissue damage.

in TLM. The traditional forceps are made up of an outer shaft (ϕ 2.5 mm) which holds an inner translating rod (ϕ 1 mm). The translation of this rod (motion of about 3 mm) provides the open-close DOF, where the jaws move from completely open to closed configuration. A short hollow tube with M3 threading is provided at the proximal end of tool shaft which allows modular attachment into tool-shaft holder (Refer Fig. 2(a)).

B. Tool actuation mechanism

The tool actuation mechanism consists of a set of linkages ("L1" and "L2"), which provide linear translation of the inner translating rod through simple kinematic inversion. As discussed, a displacement of 3mm of inner translating rod provides open/close DOF of tool jaw. Here, link "L2" actuates the inner translating rod which is connected to the wire pusher (Refer Fig. 2(b)). Additionally, a force sensor (Futek LSB200) is attached in line with the axis of the linear actuator and link "L1". This is done to allow measurement of force on performing tissue manipulation during TLM.

C. Microsurgical tool-shaft holder

This component forms the backbone of the design which connects the mechanisms for the open/close of tool jaw with surgical tool shaft. (Refer Fig. 2(c)). The tool shaft holder is comprised of three sub frame components called 'F1', 'F2' and 'F3'. The tool shaft is attached to sub frame 'F1' rigidly at point 'P1' such that it's axis is at an offset of 200mm from the axis of linear actuator. This is done to maintain distance between the tool base (attached to robot's end effector) and patient's face. The cross-sectional thickness of frame 'F1' is designed to be 5mm, which is equal to the thickness of the traditional tools. This design decision ensures limited occlusion through microscopic view. Further, the sub frames 'F1' and 'F2' rigidly connected at 'P2'. The sub frame 'F3' is designed to be fixed at the face of end effector, which is 6 degree's of freedom (DOF) serial manipulator robotic arm at point 'P3'. A linear actuator (Nanotec L2018-QV20041) along with linear slide is rigidly fixed at the top face of sub frame 'F3'.

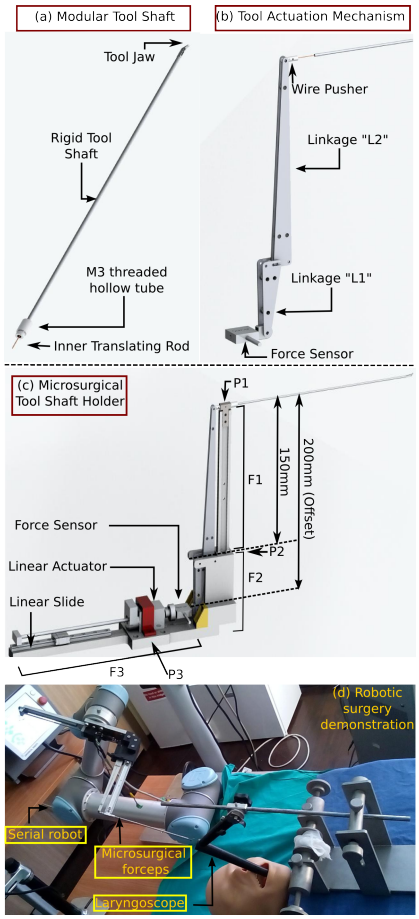

Fig. 2. Robot assisted Microsurgical forceps design

IV. DISCUSSION

Figure 2 shows the design of motorized microsurgical forceps along with demonstration of its use. The tool design incorporates open/close DOF of the tool jaw. The design of the tool relies on the serial manipulator kinematics for rotational DOF which improves the reachability of the tool. This rotational DOF allows the surgeon to reach all sections of the vocal cords with the same tool while simultaneously improving surgical interface, opening possibility of teleoperation by haptic device. The proposed tool length is $200 - 280mm$ (for different tool shaft length) inclusive of tool actuation mechanism which easily complies with TLM constraints. One of the extension of this work is to add another DOF within the same tool design such that the tool shaft could be controlled independently for flexibility.

REFERENCES

[1] P. A. Liverneaux, S. H. Berner, M. S. Bednar, S. J. Parekattil, G. M. Ruggiero, and J. C. Selber, *Telemicrosurgery: robot assisted microsurgery*. Springer Science & Business Media, 2012.

[2] M. Hirano, "Morphological structure of the vocal cord as a vibrator and its variations," *Folia Phoniatrica et Logopaedica*, vol. 26, no. 2, pp. 89–94, 1974.

Preliminary design of hybrid soft rigid actuators for MIS

L. Paternò, G. Tortora, A. Menciassi

The BioRobotics Institute, Scuola Superiore Sant'Anna. Pisa, Italy

INTRODUCTION

In recent years scientific research in the field of MIS (Minimally Invasive Surgery) revealed a growing interest in implementing fluidic solutions which can provide better performance in terms of generated stroke and force in microscale. They offer several advantages with respect to other types of actuation. Unlike electrostatic actuators, piezoelectric, electromagnetic motors or electroactive polymers, they do not need electrical connections, and operate at low temperature, differently e.g. from SMA and thermal actuators [1]. Fluidic actuators are divided into two major types of devices: elastic fluidic and piston-cylinder actuators. Fluidic elastic actuators have the main drawback of generating low forces with small displacements compared to the piston-cylinder one. In such actuators, high output forces require high pressures, and consequently more robust and rigid body walls, which in turns limit deformation and system efficiency. On the other hand, piston-cylinder actuators need low friction seal, which are challenging to fabricate [2]. The concept we propose in this paper is based on a hybrid soft-rigid fluidic actuation system, which aims to overcome the limitations of traditional elastic soft actuators by integrating them in rigid yet simple mechanical structures which appropriately shape the elastic system during actuation. Furthermore, compared to traditional piston-cylinder, the proposed solution allows to overcome the problem of the seals, being the elastic actuator hermetic thus not requiring stringent tolerances of the manufactured mechanical parts. This approach results in very compact, powerful and low cost actuators which are highly customizable and adaptable to determined sizes. The choice of fluid depends on the desired characteristics. Hybrid soft-rigid actuators support both a hydraulic and a pneumatic implementation, but the choice of the final fluid will be done after the testing phase. The goal of this paper is to present the design and the validation of a new concept of actuator, with the final objective of integration into a multi-DOFs robotic arm for MIS. In particular, basic joints (pitch and roll) are presented, providing higher dexterity and flexibility to MIS procedures. The mechanical properties of silicone have been also investigated by means of stress-strain tests in order to build a model of the soft actuator for future design and validation, as described in the following sections.

MATERIALS AND METHODS

In order to be applied a broad number of MIS scenarios, the proposed actuators should have a diameter ranging from 12 mm (as for MIS or for Natural Orifices Transluminal Endoscopic Surgery-NOTES applications [3]) to 30 mm (as for Single Port Laparoscopy-SPL [4]). The required forces depend on the specific surgical procedure. I.e. in TEM (Transanal Endoscopic Microsurgery) less than 1.5 N forces are necessary for the tissue manipulation [5]. For the preliminary design of the hybrid soft rigid actuator, a diameter of 14.5 mm was considered, in order to facilitate the prototyping phase and the proof of feasibility. Anyway the actuator design is scalable down to 10 mm, since there are no limitations due to the presence of traditional motors, cable-mechanisms or seals. The main concept of these actuators is to exploit the deformation of the soft material, due to air pressure inlet, to produce a mechanical effect on a rigid structure in which the soft actuator is embedded. The movement results in basic rotational DOFs for implementing the mechanical kinematics of surgical robots. The designed pitch actuator has a ± 90° range of motion, and roll actuator has a span of ± 180°.

A design of pitch and roll actuators is shown in Figure 1 and Figure 2 respectively, with a simple scheme of the actuation concept. Preliminary prototypes of pitch and roll basic joints have been manufactured with rapid prototyping 3D printing (Figure 1, right, and Figure 2, right) for qualitative tests that confirmed the proposed working principle. Thanks to the presence of two identical soft actuators actuating pressure of both sides can be regulated, finally determining the joint position. After the design phase, it was necessary understanding if the mechanical behaviour of the silicone in the rigid structure really responds to the concept. So we have been investigated the mechanical properties of silicone, non-linear hyper elastic material, with a computational/experimental approach [6] [7].

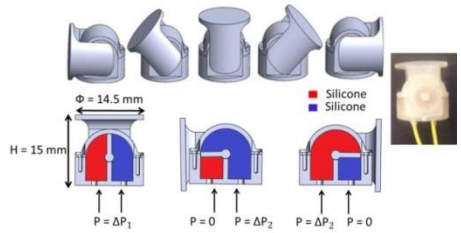

Figure 1. Soft hybrid actuator for pitch motion. Schematic of actuation (Left); manufactured prototype (Right)

The silicone (Ecoflex 00-30 Shore A, Smooth-On, Inc., Macungie USA) was chosen as material for manufacturing the soft actuator since it is high deformable, biocompatible, low-cost and resistant to high temperature during possible sterilization. The soft actuators deformations are constrained by the rigid structure. In future internal silicone design will optimized in order to improve actuators performance. The proposed actuators can generate high output forces,

since the external rigid structure keeps the silicone deformations limited for preventing bursts. During preliminary tests we obtain forces from 1.4 N of the pitch to 2.64 N of the roll. Force values have been measured only for assessing the proposed working principle, for non-optimized soft actuators and using rapid prototyping materials for the mechanical structure. The presence of silicone guarantees air-tightness without needs of hermetic seals. In this way, contacts between the piston and cylinder can be eliminated, as they cause large friction forces in traditional piston-like actuators. Indeed, precise manufacturing and stringent tolerances are not required anymore, thus easing manufacturing and reducing the production costs.

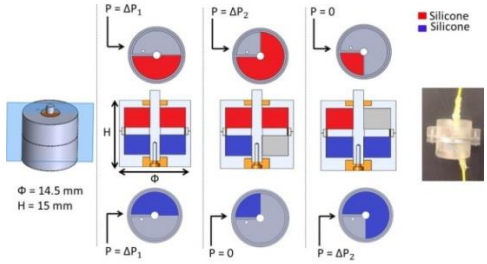

Figure 2. Soft Hybrid actuator for roll motion. Schematic of actuation (Left); manufactured prototype (Right)

EXPERIMENTAL RESULTS

In order to build a model of the soft actuator for future design and validation, experiments on the silicone have been performed. The stress-strain data of the silicone were obtained by uniaxial tension tests at Instron Materials Testing Machine (Figure 3, Left), to assess the behaviour of the material during deformation. The sample geometry was a standardized 2 mm thick dumb-bell test piece ASTM D412 Type C (Figure 3, Right). Tests were carried out with five samples subjected to five loading cycles at 400% strain level and 10 mm/min speed deformation. Four theoretical models (Neo-Hookean, Mooney-Rivlin, Yeoh and Ogden Model), based on a non-linear theory of the elasticity, were analysed in order to individuate the model that best replicated the trend of the experimental curve. In this way it is possible to obtain a formulation of the silicone stress, utilizable in a future modelling of the actuators.

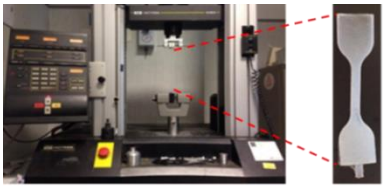

Figure 3. Instron Materials Testing Machine (Left) and uniaxial tension dumb-bell test pieces (Right)

The Ogden Model, based on the the principal Cauchy stress equation (Eq. 1), was finally chosen:

$$\sigma = \sum_{p=1}^{N} \mu_p \left(\lambda^{\alpha_p} - \lambda^{\frac{\alpha_p}{2}}\right) \qquad (1)$$

We used N = 4 and a Matlab script to identify the material constants in the models [7]. The comparison between the experimental data and the theoretical data, and the relative percentage error are shown in Figure 4. The values of stretch closed to 1 have been discarded in order to avoid large errors due to zero stress.

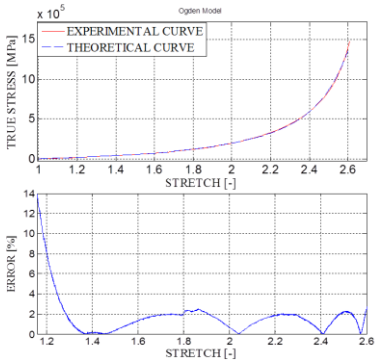

Figure 4. Stress vs stretch test data and relative error

CONCLUSION AND DISCUSSION

The main objective of this paper is to present a new concept of actuator for robotic surgery based on a hybrid soft-rigid fluidic actuation system. This approach results in very compact hybrid soft-rigid actuators that are highly customizable, powerful and low cost. The design of two actuators (pitch and roll) was proposed with the final aim of integration in an articulated manipulator characterized by high dexterity and flexibility. Tests to characterize the silicone mechanical behaviour were performed and a theoretical model was chosen for replicating experimental results. This will be used in future to improve the actuators design. Prototypes of pitch and roll basic joints have been manufactured to confirm the feasibility of the approach. The relation between pressure and position will be investigated on future prototypes with optimized actuators.

REFERENCES

[1] De Greef A, Lambert P, Delchambre A. “Towards flexible medical instruments: Review of flexible fluidic actuators.” Precis Eng; 2009; 33(4): 311–321.

[2] De Volder M, Reynaerts D. “Pneumatic and hydraulic microactuators: a review.” J Micromec Microeng; 2010; 20(4): 043001.

[3] Tortora G, Dario P, Menciassi A. “Array of robots augmenting the kinematics of endocavitary surgery.” IEEE/ASME Trans Mech; 2014; 19(6): 1821–1829.

[4] Sekiguchi Y, et al. “In vivo experiments of a surgical robot with vision field control for Single Port Endoscopic Surgery.” Conf Proc IEEE Eng Med Biol Soc; 2011; 2011: 7045–8.

[5] Ranzani T, et al. “A Novel Device for Measuring Forces in Endoluminal Procedures.” Int J Adv Robot Syst; 2015;12.

[6] Martins PALS, et al. “A Comparative Study of Several Material Models for Prediction of Hyperelastic Properties: Application to Silicone-Rubber and Soft Tissues.” Strain; 2006; 42(3): 135–147.

[7] Berselli G, et al. “Hyperelastic Modeling of Rubber-Like Photopolymers for Additive Manufacturing Processes.” Rap Prot Tec-Prin Fun Req; 2011; 135–152.

Failure of surgical insertion of tungsten needles into *in vivo* suine peripheral nerves: a hybrid procedure to assess the influence of biotic factors

Ken Yoshida[1], Winnie Jensen[2], Silvestro Micera [3,4,5], Pier Nicola Sergi[5*]

[1]Department of Biomedical Engineering Indiana University - Purdue University, Indianapolis USA,[2]Department of Health Science and Technology, Aalborg University Denmark, [3]Bertarelli Foundation Chair in Translational NeuroEngineering, Institute of Bioengineering, School of Engineering, Ecole Polytechnique Federale, Lausanne, Switzerland, [4]Center for Neuroprosthetics, Ecole Polytechnique Federale de Lausanne, Switzerland, [5]The Biorobotics Institute, Scuola Superiore Sant'Anna, Italy

**p.sergi@sssup.it*

INTRODUCTION

Needle-based therapeutic interventions are widespread in modern medicine. Indeed, needles were used to perform brachytherapy [1], to extract tissue specimens from less accessible biological sites (biopsy) [2, 3], to inoculate drugs inside the body (several types of injections) [4], as well as to perform microneurography [5,6]. In addition, needle-based interventions are performed in neuroprosthetics, where needles are the key factor to insert intraneural electrodes within peripheral nerves [7]. In this case, although stiff self-penetrating electrodes could be suitable for puncturing nerves, they may damage internal substructures, since they are much more stiff than the surrounding tissue. As a consequence, the use of needle-based procedures to insert compliant intraneural electrodes is an effective way to couple the intimate contact between axons and active sites with the use of bio-inspired structures closely matching the characteristics of biological tissues [8]. Nevertheless, the effectiveness of the insertion procedure is strictly related to the ability of the needles to withstand force/pressure interactions with peripheral nerves. Therefore, the needle design, which is the crucial factor for the success of the whole manual or robotic procedure, requires not only a strong knowledge of structural details, but also a clear vision of the influence of biotic factors on the needle reliability. To this aim, this work describes how to integrate biotic factors for optimizing the probability of success of surgical insertion of tungsten microneedles into *in vivo* suine peripheral nerves.

MATERIALS AND METHODS

A. Surgical insertion of tungsten needles

As previously reported [9], acute experiments were performed on a big animal model. More specifically, three Danish Landrace pigs were used (all experimental procedures were approved by the Animal Experiments Inspectorate under the Danish Ministry of Justice). The pigs were anaesthetized, intubated and placed on a veterinary anaesthesia ventilator. Anaesthesia was maintained while animals were prevented by dehydration though a saline solution. Analgesia was also provided. A surgical access was, then, created in the upper forelimb to the ulnar nerves and precise insertions of tungsten needles were performed at a constant velocity [10] of 2 mm/s. The compressive force was measured using a load cell (Sensotec model 31, Sensotec Inc.).

B. Estimation of interactions

Reciprocal interactions between peripheral nerves and tungsten needles were expressed though closed formulas accounting for the main geometrical features of the needle structure. More specifically, the interaction force was expressed as:

(1) $F = \xi(\theta, \psi, E, \nu, z)$

where θ was the half opening angle of the needle tip, ψ was a term accounting for the finite radii of curvature of the tip, E and ν were the apparent stiffness and the Poisson ratio of the peripheral nerve, z was the needle tip displacement, while $\xi : \Re 5 \rightarrow \Re$ was a rational function (see [11] for details).

C. In silico models of peripheral nerves

In silico models of peripheral nerves were built using the Finite Element (FE) methods. More specifically, the global equilibrium equation was achieved by minimizing the total potential energy of the structure, and the global vector of the nodal loads was built to account for the presence of the narrowed surface force which derived from the interaction with the needle tip. The real geometry of specimens was approximated through four node tetrahedral elements, deriving from a tassellation procedure performed in Ansys (Ansys Academic, Ansys Inc. USA). The in silico models were trained to closely reproduce experiments and used to account for the difference of apparent stiffness between *in vivo* [9] and *in vitro* [12] nervous specimens. Finally, the percentages of success of surgical insertion were related to the diameter of the tungsten needles, showing the existence of a relationship between experimental outcomes for both *in vivo* and *in vitro* conditions and allowing the influence of biotic factors to be accounted for.

RESULTS

In Fig. 1A, the surgical environment for the insertion of tungsten microneedles into peripheral nerves is shown. The needle-tissue force interactions were modelled through closed form equations (i.e. Eq.(1)), which were used to train in silico models to closely reproduce the

needle displacement before the puncture point. In Fig. 1B, the stress field is shown for an in silico nervous specimen undergoing interactions with a local force due to the presence of the tungsten needle (projection in the y direction along the interaction trajectory). These computational models were able to keep the main features of the real needle-nerve interaction, thus they allowed similar *in vivo* and *in vitro* experiments to be compared and the influence of biotic factors on the nerve response to be assessed. Finally, thanks to this crucial information, the safety factor for *in vivo* needle-based insertions was assessed starting from *in vitro* data and mechanical differences in the nerve response between the two conditions, as shown in Figs. 1C,D. In particular, the percentage of successes for *in vivo* insertions of a tungsten needle with ∅ 75 µm was predicted by using a variant of the procedure in [11].

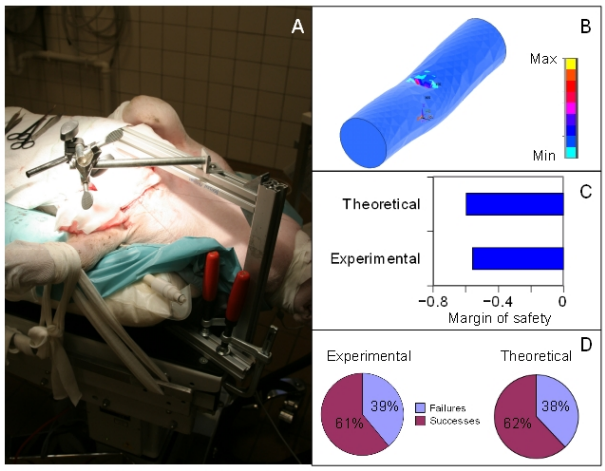

Figure. 1. A) Surgical environment for needle insertion. **B)** In silico model of a nervous specimen before the puncture: stress field distribution. **C)** Assessment of the margin of safety for *in vivo* experiments. **D)** Prediction of the success percentage for *in vivo* insertions of a ∅ 75 µm tungsten needle compared to experimental outcomes.

DISCUSSION AND CONCLUSION

In this work, the outcomes of a hybrid procedure (variant of [11]) were described. This synergistic procedure involved *in vivo* and *in vitro* experiments, theoretical models of needle-nerve interactions, in silico models of nervous specimens and computational relationships between needle dimensions and their reliability. This computational framework, (together with its ongoing refinements), is suitable to become part of a synergistic strategy to enhance the quality of clinical needle-based insertions, which are still critical just at the needle level. Indeed, although other ways are currently explored to improve the physical connection between peripheral nerves and neural interfaces, the effective clinical insertion of minimally invasive intrafascicular interfaces through tungsten needles still remains a challenge.

ACKNOWLEDGEMENTS

This work was partly funded by the project ENABLE - Effortless Natural Bidirectional Prosthesis for Complete Functional Restoration for Amputees. The EU project FP7-611687 NEBIAS ("NEurocontrolled BIdirectional Artificial upper limb and hand prosthesis") is also thanked.

REFERENCES

[1] Nath S., Chen Z., Yue N., Trumpore S., Peschel R.," Dosimetric effects of needle divergence in prostate seed implant using 125I and 103Pd radioactive seeds", Med Phys; 2000; 27(5): 1058-66.

[2] Gupta S., Madoff D.C.," Image-guided percutaneous needle biopsy in cancer diagnosis and staging", Tech Vasc Interv Radiol.; 2007; 10(2): 88-101.

[3] Youk J.H., Kim E.K., Kim M.J., Lee J.Y., Oh K.K.," Missed breast cancers at US-guided core needle biopsy: how to reduce them", Radiographics; 2007; 27(1): 79-94.

[4] Abolhassani N., Patel R., Moallem M.,"Needle insertion into soft tissue: a survey", Med Eng Phys.; 2007; 29(4): 413-31.

[5] Gandevia S.C., Hales J.P.,"The methodology and scope of human microneurography", J Neurosci Methods.; 1997; 74(2): 123-36.

[6] Vallbo A.B., Hagbarth K.E., Wallin B.G.," Microneurography: how the technique developed and its role in the investigation of the sympathetic nervous system", J Appl Physiol.; 2004; 96(4): 1262-9.

[7] Normann, R.A., "Technology Insight: future neuroprosthetic therapies for disorders of the nervous system", Nat Clin Pract Neuro, Nature Publishing Group; 2007**;** 3: 444-452.

[8] Minev, I. R., Musienko, P., Hirsch, A., Barraud, Q., Wenger, N., Moraud, E. M., Gandar, J., Capogrosso, M., Milekovic, T., Asboth, L., Torres, R. F., Vachicouras, N., Liu, Q., Pavlova, N., Duis, S., Larmagnac, A., Vörös, J., Micera, S., Suo, Z., Courtine, G. & Lacour, S.P.,"Electronic dura mater for long-term multimodal neural interfaces", Science, American Association for the Advancement of Science; 2015**;** 347: 159-163.

[9] Sergi P.N., Jensen W., Micera S., Yoshida S., In vivo interactions between tungsten microneedles and peripheral nerves, Med. Eng. Phys.; 2012; 34: 747–755.

[10] Okamura A.M., Simone C., O'Leary M.D..,"Force modeling for needle insertion into soft tissue", IEEE Trans Biomed Eng.; 2004; 51(10): 1707-16.

[11] Sergi, P.N., Jensen, W. & Yoshida, K., "Interactions among biotic and abiotic factors affect the reliability of tungsten microneedles puncturing *in vitro* and *in vivo* peripheral nerves: A hybrid computational approach", Mater Sci Eng C Mater Biol Appl.; 2016; 59: 1089-99.

[12] Yoshida K., Lewinsky I., Nielsen M., Hylleberg M.,"Implantation mechanics of tungsten microneedles into peripheral nerve trunks", Med Biol Eng Comput; 2007; 45(4): 413-20.

Single Fiber OCT-based Retina Detection for Robot-assisted Retinal Vein Cannulation

G. Borghesan*, D. Bouget*, E. Lankenau†, R. Neffin†, P. Koch‡,
K. Willekens§, P. Stalmans§, D. Reynaerts*, E. Vander Poorten*
*Dept. of Mechanical Engineering, KU Leuven, †OptoMedical Technologies GmbH, Lübeck, Germany
‡Medical Laser Center Lübeck, Lübeck, Germany, §Dept. of Ophthalmology, University of Leuven
gianni.borghesan@kuleuven.be

***Abstract*—Vitreo-retinal surgery concerns a set of particularly demanding micro-surgical interventions that take place at the back of the eye. Expert micro-surgeons are to manipulate fragile membranes or vessels while taking great care not to damage the underlying retina. Despite using high quality stereo microscopes, depth perception remains limited. Efforts have been conducted to enhance depth awareness through adding OCT or even force sensing. Whereas OCT has been predominantly used to assist in retinal membrane peeling procedures, so far little work has been conducted to use it for offering assistance during retinal vein cannulation. This abstract describes some first results of a novel algorithm that has been designed to reliably estimate the distance to the retina from an instrument with integrated OCT-fiber. However, it is anticipated that the algorithm can be further expanded to estimate other useful characteristics as well. It could for example help to automatically detect vessels on the retina, or to estimate the diameter or center of a targeted vessel. Equipped with this knowledge more sophisticated assistive control schemes could be designed to further increase cannulation reliability.**

I. Introduction

Vitreo-retinal (VR) surgery is currently performed in a fully manual manner. Upon start of the procedure the surgeon carefully puts up to four trocars into place at 3 to 4 mm from the corneal limbus, the border between the cornea and the sclera (Fig.1). Through these trocars thin instruments are inserted to operate on the interior part of the eye. The micro-surgeon observes the retina and relative instrument motion via a stereo-microscope positioned above the patient's eye. From the binoculars the optical path goes through the different lenses of the stereo-microscope, additional wide-angle lenses such as the EIBOS (Haag-Streit Surgical GmbH, Rosengarten, Germany), the BIOM®(Oculus Surgical, Florida, US) or contact lenses, the natural lens of the patient and finally through the vitreous humour a gel-like substance that occupies the interior volume of the eye-ball[1]. The complex optical path and the difficulty of getting sufficient light through small incisions at the target site, severely limit the surgeon's depth perception. Given the small size of the structures the micro-surgeon is to deal with - for *epiretinal membrane peeling* (ERM-peeling) a membrane up to about 60μm is to be peeled off; for ILM peeling the *internal limiting membrane* is only about 4μm thick; veins that are to be cannulated to treat *retinal vein occlusion* typically have diameters in the order of 100μm - it is clear that inaccurate depth perception and depth control can cause serious complications [1], [2]. Accordingly significant research has been conducted to improve depth perception through adoption of alternative sensing techniques. OCT and force sensing are some of the more mature techniques that have been investigated.

[1]If that was not replaced by mineral oil.

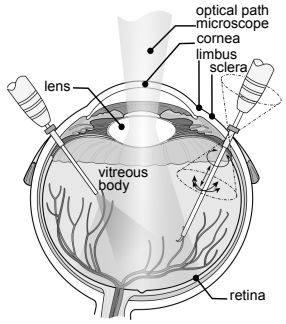

Fig. 1. Anatomy of the eye, focus on structures relevant for VR surgery.

II. Goals and Related work

OCT images have been previously employed in a number of algorithms targeting, for example, automatic segmentation of retinal layers [3]; detection of vessels [4] or to identify markers that predict certain diseases [5]. Most of these results rely on 2D or 3D OCT images, referred to as B- and C-scans respectively. This data is obtained from a scanner that is mounted at the far end of the complex optical path. Similar to [7] we aim to employ OCT data that is acquired via an optical fibre incorporated directly inside the surgical instrument. By doing so the complex optical path can be by-passed and direct i.e. more accurate measurements of the retina can be obtained. Only a single ray of laser light can be passed at a time through the laser fiber offering a one-dimensional depth aka A-scan. In order to reconstruct a larger surface the instrument could be controlled to make a scanning pattern. Despite the improved accuracy, the obtained signal remains quite noisy and the limited field of view, i.e. absence of a broader context, necessitates adequate filtering to use this kind of data in critical applications such as robotic control loops.

Balicki *et al.* implemented such approach when mounting an OCT probe on an micro-surgical pick [7]. The experiments reported by Balicki *et al.* however are conducted on synthetic phantoms and therefore the signals that are employed are much less noisy than the signals one typically gets. The objective of this work consists in evaluating the feasibility of using A-scans for robustly identifying the upper layer of the retina in a more realistic setting. Here, noisy OCT data from ex-vivo pig

eyes is employed and a novel algorithm to deal with this data is proposed. Note, although the proposed approach is used to detect membrane layers, the proposed approach is more general and is believed to be also helpful in discriminating the location of vessels on top of or even below the retinal surface. With only very limited loss of generality B-scans (fig. 2) are employed to test the concept. Each time only a single line of these B-scans is used, simulating a corresponding A-scan. By removing the vitreous humour and the lenses from an ex-vivo pig eye and EIBOS, the obtained lines from these B-scans approximate A-scans closely. To filter out the noisy artefacts a methodology similar to the one employed in [8] is adopted. The method employs *probabilistic principal component analysis* (ppca, [9]) to characterize a number of *latent* variables. In the following sections the algorithm and some experimental results are introduced.

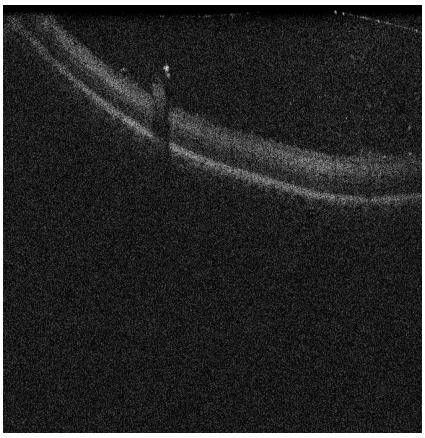

Fig. 2. Example of B-scan; as A-scan, a single vertical line of the image is considered. Each image has 1000 lines, each composed of 1024 depth pixels.

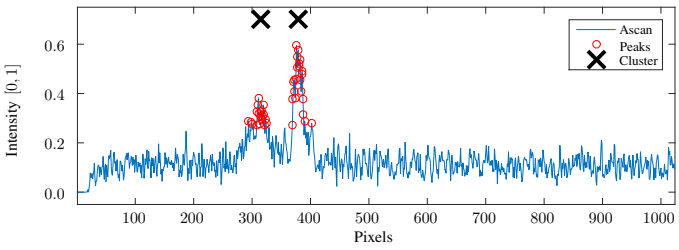

Fig. 3. Peak detection and clustering are the initial step for normalising the data. The data is averaged on 8 images taken consecutively to reduce noise.

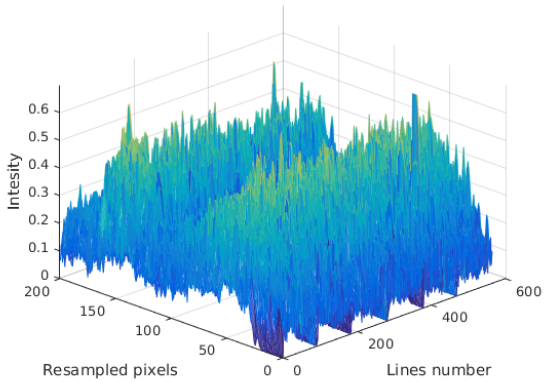

Fig. 4. Data set used in ppca.

III. Proposed Algorithm

The proposed procedure consists of a learning phase (off-line, that makes use of more than one line at a time) and a run-time identification phase (using a single line, as produced by an OCT fiber probe). Both phases are described next.

A. Learning phase

Ppca needs a normalised training set (i.e. each pixel must represent the same information). To achieve this, we extract in a semi-automatic way some landmarks around important features. The data set is then re-sampled in such a way that these landmarks appear in the same area.

In the first phase 6 sets of B-scans (from ex-vivo porcine eyes, each set taken on a given position) are averaged to reduce noise. Then peaks (brightest pixels) are used to identify the center of a membrane layer. In the current image (fig. 2) two layers are visible. k-means is used to cluster these pixels into 2 clusters. The results of these operations are shown in fig. 3. The procedure is run on a whole image. Then we consider the distance between the 2 clusters as a representative measure and discard outliers. From the selected line samples, the region around the average distance, with a span equal to twice the distance between the clusters is selected, and re-sampled on a fixed span of 200 pixels. The resulting data set is represented in fig. 4. From the ppca only two latent variables are kept.

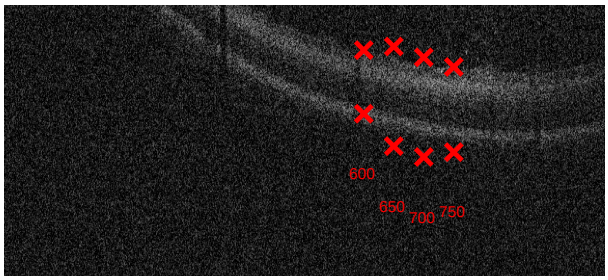

(a) Representation of P_0 and $P_0 + \Delta P$ computed after initialization.

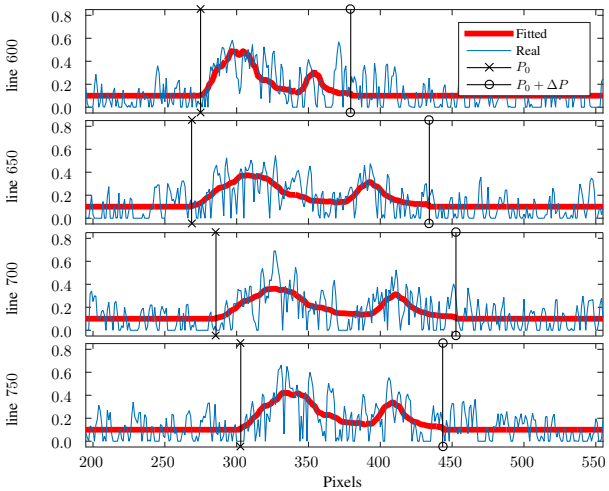

(b) Fitting of the profile

Fig. 5. Results of iterating the UKF on the same input data in the initialization phase. The red fat line represents the expected output.

B. Filter initialization and run-time execution

In order to track the position of the retinal layers in the image an unscented Kalman filter is used. The filter states are the initial pixel that maps in pixel 1 of the dataset (P_0), the number of pixels that maps in the whole data set (ΔP), and the two latent variables (x_l). The expected measurements are computed as follows: first, the modes are multiplied by x_l, then, the points are stretched and translated as dictated by P_0 and ΔP, lastly, the output is re-sampled between 1 and 1024 (the size of the sensor measurement), using a default value for the part of the image that is outside the $[P_0, P_0 + \Delta P]$ interval.

One of the most critical parts is to determine which parameters to use to initialise the filter. In this regard, we employ the same rationale used in the data set segmentation, *e.g.* peak detection and clustering. In order to allow the filter to converge, several update iterations (30–60) are executed with the same measurement. Four examples of initialised filters are depicted in fig. 5.

C. Filter execution on varying measurements

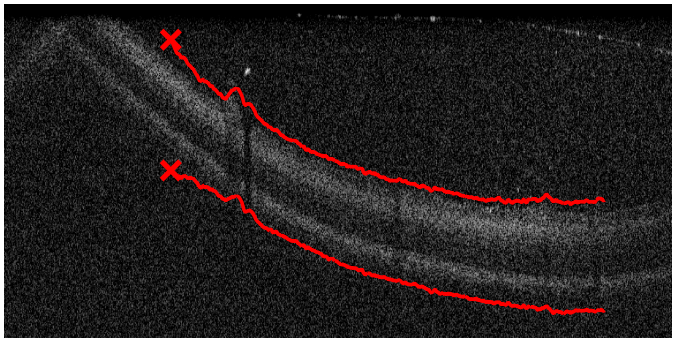

(a) Overlay of P_0 and $P_0 + \Delta P$ on OCT B-scan.

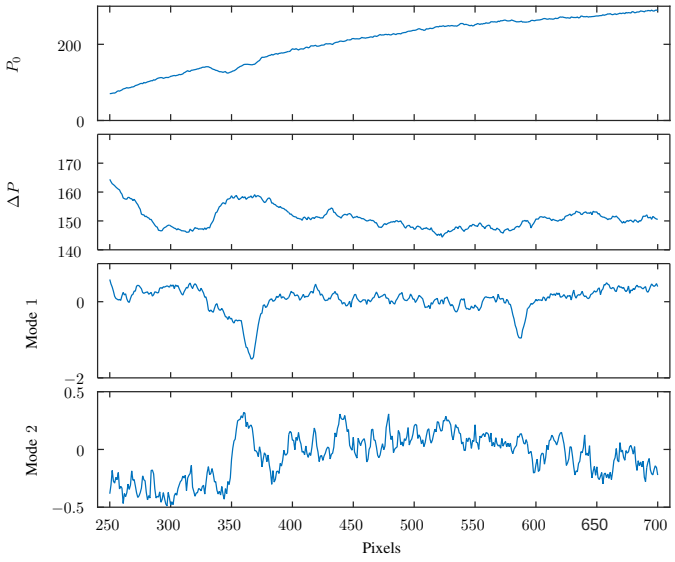

(b) Values of the UKF variables.

Fig. 6. Example of a filter executed with a time varying input. After initialization (results in red crosses), at each time step the filter is moved one pixel to the right. The data reported in red are $[P_0, P_0 + \Delta P]$

In order to test the proposed filter in a situation more similar to reality, but yet enough controlled to be able to evaluate the results, a B-scan was employed, and an single input line was used for each iteration, shifting one pixel each time, simulating a horizontal movement of the OCT fiber probe. For small travel this motion is fairly representative. The overall results for this scan are reported in fig. 6. It can be observed qualitatively that at locations artefacts are present, the values of Mode 1 changes drastically. This suggests that analysis of the state can be used to classify tissue and e.g. detect the presence of vessels or other features.

IV. Conclusion

This abstract presented a way to formalise an UKF to track the position of the retina. The approach takes advantage of the structure present in retinal layers, in contrast to [7], to get a robust estimate of the distance to the surface. While the presented results are still preliminary, the filter showed good robustness to artefacts and noise. Two main drawbacks should be pointed out: first of all, the filter is strongly influenced by the numerous local minima; for this reason, wrong initialization can cause the filter to converge to a wrong state. At this end, at least the initialization could be delegated to a global search method, such as a particle filter. Secondly, the filter was not trained on vessels. In fact a number of filters could be operated in parallel each trained with specific data-sets e.g. one that focuses on vessels, to discriminate those from retinal layers.

Acknowledgment

Research funded by The EU Framework Programme for Research and Innovation - Horizon 2020 - Grant Agreement No 645331.

References

[1] R. Sjaarda, B. Glaser, J. Thompson, R. Murphy, and A. Hanham, "Distribution of iatrogenic retinal breaks in macular hole surgery," *Ophthalmology*, vol. 102, no. 9, pp. 1387–1392, 1995.

[2] K. Nakata, M. Ohji, Y. Ikuno, S. Kusaka, F. Gomi, and Y. Tano, "Sub-retinal hemorrhage during internal limiting membrane peeling for a macular hole," *Graefe's Archive for Clinical and Experimental Ophthalmology*, vol. 241, no. 7, pp. 582–584, 2003. [Online]. Available: http://dx.doi.org/10.1007/s00417-003-0676-y

[3] A. Yazdanpanah, G. Hamarneh, B. R. Smith, and M. V. Sarunic, "Segmentation of intra-retinal layers from optical coherence tomography images using an active contour approach," *IEEE Transactions on Medical Imaging*, vol. 30, no. 2, pp. 484–496, Feb 2011.

[4] S. Lu, C. Y. l. Cheung, J. Liu, J. H. Lim, C. K. s. Leung, and T. Y. Wong, "Automated layer segmentation of optical coherence tomography images," *IEEE Transactions on Biomedical Engineering*, vol. 57, no. 10, pp. 2605–2608, Oct 2010.

[5] R. Kafieh, H. Rabbani, and S. Kermani, "A review of algorithms for segmentation of optical coherence tomography from retina," *J Med Signals Sens*, vol. 3, no. 1, pp. 45–60, 2013.

[6] A. Gijbels, N. Wouters, P. Stalmans, H. Van Brussel, D. Reynaerts, and E. V. Poorten, "Design and realisation of a novel robotic manipulator for retinal surgery," in *Intelligent Robots and Systems (IROS), 2013 IEEE/RSJ International Conference on*. IEEE, 2013, pp. 3598–3603.

[7] M. Balicki, J.-H. Han, I. Iordachita, P. Gehlbach, J. Handa, R. Taylor, and J. Kang, "Single fiber optical coherence tomography microsurgical instruments for computer and robot-assisted retinal surgery," in *Medical Image Computing and Computer-Assisted Intervention–MICCAI 2009*. Springer, 2009, pp. 108–115.

[8] E. Aertbeliën and J. de Schutter, "Learning a predictive model of human gait for the control of a lower-limb exoskeleton," in *5th IEEE RAS/EMBS International Conference on Biomedical Robotics and Biomechatronics*, Aug 2014, pp. 520–525.

[9] M. E. Tipping and C. M. Bishop, "Probabilistic principal component analysis," *Journal of the Royal Statistical Society, Series B*, vol. 61, pp. 611–622, 1999.

Computer-assisted robotic platform for USgFUS treatment

A. Diodato[1], A. Cafarelli[1], A. Schiappacasse[2], L. Chanel[1], S. Tognarelli[1], G. Ciuti[1], A. Menciassi[1]

[1]*The BioRobotics Institute, Scuola Superiore Sant'Anna, Pisa, Italy,*

[2] *Camelot Biomedical Systems S.r.l.*

a.diodato@sssup.it

INTRODUCTION

Focused Ultrasound Surgery (FUS) is a non-invasive therapeutic technology that enables the treatment of several pathologies [1]. FUS delivers ultrasound energy onto the human tissue for treating tumours by causing hyperthermia and necrosis into the target area without harming adjacent tissues. Although Ultrasound guided FUS (USgFUS) does not guarantee high quality images and quantitative temperature maps if compared with Magnetic Resonance guided FUS (MRgFUS), it offers advantages such as lower cost and system size, the possibility to verify the treatment with an intrinsic higher frame rate (up to 1000 images per second) that allows real-time therapy monitoring and compensation of physiological movements. The use of a robotic-assisted approach for USgFUS may relieve the problems related to the predictability and repeatability of the current procedures by enhancing accuracy, safety and flexibility of the treatment, and thus enabling a larger use of FUS. The most widespread commercial USgFUS robotic platform is the HAIFU JC (Chongqingd Haifu Medical Technology Co. Ltd, Chongqingd, China), which mainly performs treatment of uterine fibroids, breast and liver tumours. Nevertheless, HAIFU JC is not able to monitor and track moving organs during the sonication, because the US images are completely distorted by the noise generated by the HIFU (high intensity focused ultrasound) transducer normally operating in continuous mode. These limitations are partially overcome in some research platforms [2] by exploiting a Pulse With Modulation (PWM) signal for the HIFU transducer. An all-in-one robotized FUS system was developed for real-time intra-abdominal organ motion compensation by exploiting a US visual servoing scheme [3]. This platform is equipped with a 2D US confocal probe; anyway, for a dynamic 3D targeting, it is necessary to use a further US probe in a different plane with respect to the US 2D confocal probe. In this framework, the FUTURA (Focused Ultrasound Therapy Using Robotic Approaches) project (*www.futura-project.eu*) proposes a robotic-assisted platform for flexible non-invasive HIFU therapy. The possibility to manage two dedicated anthropomorphic manipulators (one manipulator equipped with HIFU transducer and US confocal imaging probe and the other one with 3D US imaging probe) provides the FUTURA platform with a high flexibility in terms of workspace, thus overcoming the limitations of the aforementioned FUS platforms. The aim of this work is to demonstrate the workflow of the FUTURA procedure (*i.e.* target identification, sonication and lesion assessment phases), the effective use of two US imaging probes during different phases of the lesion treatment, and the possibility to monitor the lesion progress during the sonication phase.

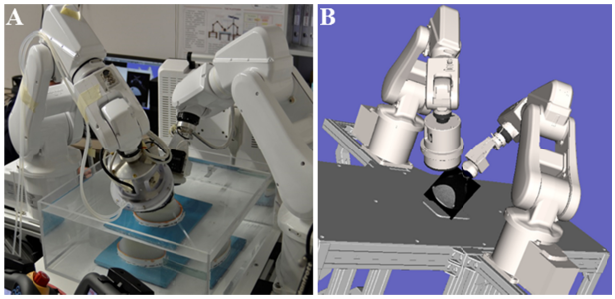

Fig. 1 – A. FUTURA platform with the robotic, monitoring and therapeutic modules. **B.** Real-time visualization of the simulated FUTURA working environment.

MATERIALS AND METHODS

In order to assess the possibility to use both the US imaging probes during the different phases of the FUS procedure, a simulation of the overall procedure is performed in *in-vitro* conditions. The FUTURA platform is composed by different modules (Fig. 1. A): *i)* a robotic module including two six degrees of freedom anthropomorphic manipulators (*i.e.*, monitoring and therapeutic manipulators - ABB IRB 120); *ii)* a therapeutic module with a dedicated broadband 16 channels wave generator with power output capability of 20W/channel and a 16 channels annular array HIFU transducer; *iii)* a monitoring module composed of two different US probes (a 2D imaging US probe - Analogic Ultrasound PA7-4/12 - confocal to the HIFU transducer mounted on the therapeutic manipulator; and a motorized 3D imaging US probe - Analogic Ultrasound 4DC7-3/40 - mounted on the monitoring manipulator), both connected to the Analogic Ultrasound SonixTablet machine. The platform control architecture (based on Robot Operating System software) allows controlling all components (*i.e.*, robotic, monitoring and therapeutic modules) involved in FUS treatments through a dedicated Human Machine Interface (HMI) with an accurate real-time visualization of the working environment (Fig. 1.B). The FUTURA platform implements a hybrid force/position control strategy, allowing: *i)* hand-guidance control of both the robotic end-effectors, and *ii)* force-based adaptive potision control of the ultrasound probes in contact with the patient's skin. The *in-vitro* simulation of the FUS procedure was accomplished by using a home-made agar

Research funded by the European Community (FP7/2007-2013) under grant agreement 611963 (FUTURA Project).

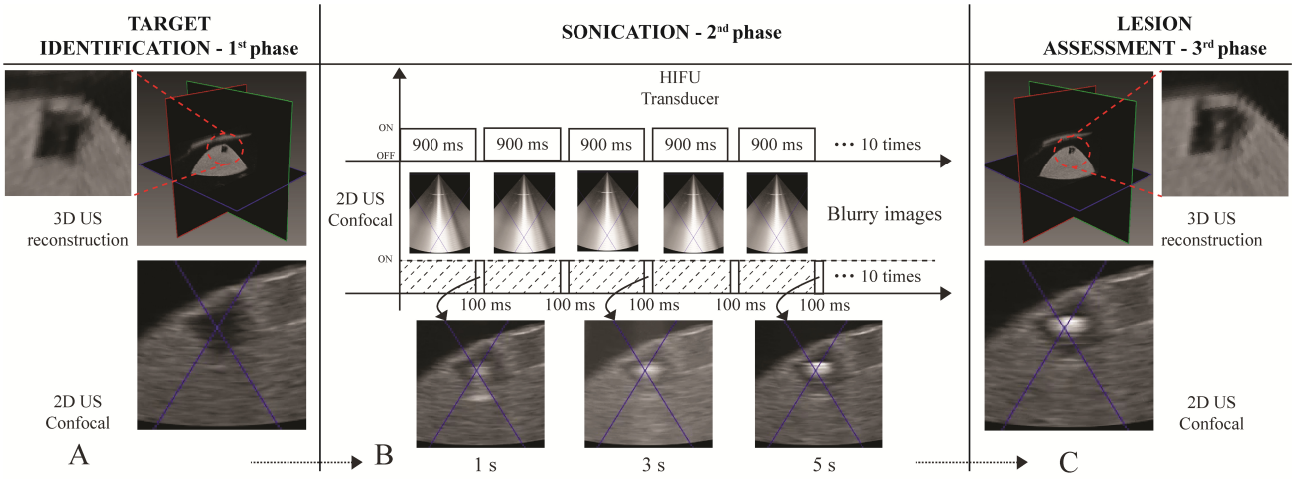

Fig. 2. - A. 3D US phantom reconstruction and 2D US confocal image after the therapeutic manipulator positioning before the sonication phase; **B.** Workflow of the sonication with the related 2D US confocal images acquired during the procedure at 1,3 and 5 second; and **C.** 3D US phantom reconstruction and 2D US confocal image after the sonication for lesion assessment.

phantom provided with cylinder targets of polyacrylamide and egg white, as presented in [4]. The phantom was immersed in a tank with degassed water ensuring a correct acoustic coupling between the two US imaging probes and HIFU transducer with respect to the agar phantom. The first phase of the FUS procedure consists of the identification of the target through the US probes. A 3D US phantom reconstruction was performed (Fig. 2.A top left); thus, by selecting the centre of the target to be sonicated (using the HMI), the therapeutic manipulator adjusts its position for performing the desired spot sonication. The images provided by the confocal 2D US probe (Fig. 2.A bottom left) verify the correctness in manipulator positioning. Indeed, the visualized blue cone in all the 2D US images of Fig. 2 indicates the HIFU focus position. After checking the therapeutic manipulator positioning, a sonication composed by 10 repetitions of 1 second with 90% duty cycle was set, as the second phase of the FUS process. The value of frequency and acoustic power of the sonication are 1200 kHz and 120 Watts, respectively (able to perform a target lesion visible by US, as defined through a pilot study). During the sonication procedure, the confocal 2D US probe was active for monitoring the lesion progress when the HIFU is switched off (10% of the time). Then, the final phase of the FUS procedure is the lesion assessment performed through both the US imaging probes.

RESULTS

Fig. 2 describes the different phases of the FUS procedure. During target identification, both the US imaging probes are used. The manipulator positions at the end of target identification are depicted in Fig.1.B. Although the US confocal probe is rigidly attached to the HIFU transducer, the FUTURA platform maintains US imaging flexibility thanks to the 3D US probe mounted on the second manipulator. Indeed, the 3D US probe can be positioned according to the requirements of the FUS procedure. The 3D US phantom reconstruction and the related 2D US confocal images (Fig. 2.A left) acquired before sonication show the target without any lesion. In addition, the estimated HIFU transducer focus, located in the center of the target, assesses the correctness in positioning the therapeutic manipulator. During the sonication process an on-line monitoring of the lesion is performed by exploiting a PWM signal for the HIFU transducer generator. Fig. 2.B shows the 2D US confocal images acquired during the target sonication. As expected, when the HIFU transducer is on, only blurry images were acquired. Instead, useful US images for monitoring the lesion progress were acquired when the HIFU transducer is off. Finally, the lesion assessment phase (Fig. 2.C) shows the 3D US phantom reconstruction and the related 2D US confocal images acquired after sonication with the lesion performed on the center of the target (*i.e.,* accuracy better than 1 mm [4]).

DISCUSSION

This work assesses the possibility to use a robotic platform for USgFUS treatment, using two US imaging probes for the different phases of the procedure. By synchronizing the HIFU transducer shot with the US imaging acquisition enables to monitor the lesion progress during the sonication phase, which is very important for patient safety. In addition, the use of both US probes during the sonication phase enables the tracking of moving 3D organs. Further tests will be performed in order to assess the accuracy of USgFUS treatment in ex-vivo and dynamic conditions.

REFERENCES

[1] J. L. Foley et al., "Image-guided focused ultrasound: state of the technology and the challenges that lie ahead," Imaging in Medicine, vol. 5, pp. 357-370, 2013.

[2] L.-A. Chanel et al., "Robotized High Intensity Focused Ultrasound (HIFU) system for treatment of mobile organs using motion tracking by ultrasound imaging: An in vitro study," EMBC 2015, pp. 2571-2575.

[3] N. Koizumi et al., "An extremely robust US based focal lesion servo system incorporating a servo recovery algorithm for a NIUTS," IROS 2015, pp. 2625-2632.

[4] A. Cafarelli et al., "A computer-assisted robotic platform for Focused Ultrasound Surgery: Assessment of high intensity focused ultrasound delivery," EMBC 2015, pp. 1311-1314.

A novel magnetic platform for active endoscopic investigations

G. Lucarini, G. Tortora, C. Quaglia, G. Ciuti, A. Menciassi

The BioRobotics Institute, Scuola Superiore Sant'Anna, Italy.

INTRODUCTION

Gastrointestinal (GI) cancer ranks third in terms of incidence rate among all cancers in high-income countries, but survival rate can reach 90% in cases of early diagnosis [1]. Flexible endoscopy has established itself as the standard method due to its diagnostic accuracy and reliability, but several limitations still remain. The physician needs a lot of practice to acquire the necessary skills to manipulate the endoscopic tool; the movements performed by the endoscope inside the body produce pain and trauma frequently, and are poorly tolerated by patients. In the recent past, wireless capsule endoscopy (WCE), which entails the ingestion of a miniaturized camera that navigates passively along the GI tract by means of peristalsis, enabled inspection of the digestive system without discomfort or need for sedation [2]. Several companies produce "smart pills", but there are limitations, mainly related to the unpredictable and uncontrollable locomotion of the capsule [4]. As an intrinsic limitation, WCE does not allow the operator to control navigation: the movement of the capsule is passive and the capsule proceeds by means of visceral peristalsis and gravity, so that some portions of the GI internal wall are unlikely to be visualized. Another drawback of WCE is the fact that, in case of areas of clinical interest are identified, the endoscopist cannot manoeuvre the capsule more precisely for detailed inspection. All these factors contribute to dramatically limit the diagnostic outcome. Therefore, solving the manoeuvring problems would significantly enhance the accuracy and reliability of endoscopic investigation with an expected improvement of diagnostic efficacy. Using magnetism for the actuation and localization of endoscopic capsules in the GI tract has become an active topic of research and it is a promising approach to solve the problem of control by avoiding integration of internal actuation [3-6].

Olympus Endoscopy (Tokyo, Japan) and Siemens Healthcare (Erlangen, Germany) joined their effort to produce a modified endoscopic capsule endoscope controlled by magnetic guidance, for the upper GI [7]. Nevertheless, despite the growing scientific interest in magnetically controllable WCE, no effective system with straightforward clinical applicability has yet been demonstrated.

In this framework, the authors present a feasibility study and assessment for the design of a novel electromagnetic system for capsule endoscopes. Although a preliminary approach has previously been presented [8], here the authors propose the complete platform together with an experimental evaluation. The primary difference between the proposed platform and existing magnetic control platforms is the combination of the advantages of electromagnets with the flexibility of robotic manipulation in order to reduce the number of electromagnetic modules and thus the size of the related hardware, while maintaining a tuneable and reliable control of the magnetic force in the operating workspace.

MATERIALS AND METHODS

The proposed WCE platform is composed of two primary modules (Figure 1): *i)* a magnetic capsule with dimensions and specifications *ad hoc* for navigation and diagnosis throughout the colon; *ii)* an external driving system including an electromagnetic source, based on a single electromagnet, a cooling system needed for overheat issues and a manipulator that supports the system. The physician, as the first action, introduces the endoscopic capsule through the rectum of the patient and he/she insufflates the colon with air. After this, the medical doctor performs a complete exploration by navigating the endoscopic capsule along the colon, assisted by an external electromagnetic manipulator. The steering and locomotion of the capsule is made possible by creating a magnetic link between the capsule and the external electromagnet.

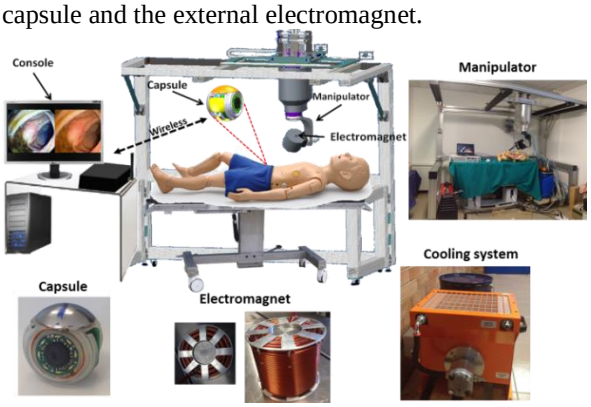

Figure 1 The proposed magnetic platform for endoscopic capsule (shown at the bottom left) and system modules (i.e. console, manipulator, electromagnet and cooling system).

The endoscopic device is a small spherical capsule with a diameter of 26 mm.

The inner and outer parts of the capsule are mutually movable and can freely orient at 360° via a system of friction bearings. This double concentric sphere structure allows the capsule to proceed along the colon with reduced friction, while the camera maintains stable position thanks to an appropriate combination of weight and magnetic forces.

The capsule is equipped with a commercial image sensor with small dimensions (NanoEye_GS, Awaiba, Portugal) with custom optics and illumination. A small

battery (CP1254, Varta, Germany), an RFID tag (TRPGR30TGC LF 1, Texas Instrument) for localization, a custom electronics (i.e. illumination, control and telemetry boards) and a custom N52 NdFeB spherical cap magnet (400 mm^3 volume for navigation) are integrated into the endoscopic device.

The external electromagnetic manipulator consists of a custom electromagnet with an integrated cooling system and a manipulator. The electromagnet was designed considering that it has to be able to generate suitable forces and torques for 3D navigation against a high friction and deformable environment, in a range of distances between the external magnetic source and the endoscopic device which is at least equal to the abdominal thickness (i.e. about 30 to 100 mm). Moreover, the fine control of pitch (visualization of upper and lower wall of the lumen) and yaw (visualization of right and left wall of the lumen) through specific magnetic torques has to be properly exerted on the capsule. A theoretical model of force equilibrium was supposed and confirmed by FEM (COMSOL Multiphysics, Comsol inc., USA) simulations and preliminary experimental tests. The designed electromagnet has an internal iron core of 70 mm in diameter, an external diameter of 167 mm and 370 winding (i.e. 10 layers per 37 turns). The 10 layers are separated by holes of 5 mm in diameter where the oil of cooling system flows. A current density of 6 A/mm^2 is used for powering. The electromagnet generates at a distance of 100 mm a maximum magnetic field and gradient of 0.4 T and 0.2 T/m, respectively. The electromagnet is inserted in an oil jacket that is connected to a commercial cooling system (13 l/min, 0.5 kW, RAS 3000, Sesino) . Moreover, due to the large weight and encumbrance of the electromagnetic system (around 13 kg), a 5 DoFs robotic manipulator has been designed for holding and accurately moving the electromagnetic source by the physician. The manipulator was designed in no ferromagnetic materials (mainly aluminium and stainless steel) considering that 5 DOF are needed. The weight of the electromagnet was compensated by means of four springs that eliminate the medical doctor's fatigue; the electromagnet can be moved in a workspace of 650 mm x 500 mm x 500 mm. Translational movements are performed using ball bearing rail guide, while the pitch and yaw are guaranteed by double ball bearings. Ball bearings make possible to build low friction mechanisms that help physician in performing accurate movements with low fatigue. Finally an antenna for RFID tag (Texas Instruments MRD2EVM Microreader Evaluation Kit - 134.6 KHz) was integrated to localize the capsule when the electromagnet is switched off.

RESULTS

A preliminary experimental test session was performed in-vitro in order to validate the design of the platform and to preliminary evaluate the navigation of a magnetic capsule. The task consisted of exploring a colon-like plastic phantom arranged to mimic the anatomical shape of the human colon, from the rectum to the cecum (about 900 mm in total length). The endoscopic capsule was controlled by moving the external electromagnet and by controlling the current through a foot pedal. A total number of five users (one endoscopist and four technical users) participated in the study. The results demonstrated that all users were able to perform the task and the mean ± standard deviation, minimum and maximum times were 78 ± 42 s, 40 s and 199 s respectively.

CONCLUSION AND DISCUSSION

The objective of this paper was to design and develop an active magnetic platform based on a single electromagnet for performing diagnostic procedures in the colon. The proposed idea is to design a platform that combines the tunability typical of electromagnet-based systems with the feasibility and intuitiveness of controls featuring external permanent magnets. Preliminary tests demonstrated the feasibility of the platform for locomotion and future use in clinical setting.

REFERENCES

[1] Siegel, Rebecca L., et al. "Cancer statistics, 2015." CA: a cancer journal for clinicians 65.1 (2015): 5-29.

[2] Iddan, Gavriel, et al. "Wireless capsule endoscopy." Nature 405 (2000): 417.

[3] Singeap, Ana-Maria, et al. "Capsule endoscopy: the road ahead." World journal of gastroenterology 22.1 (2016): 369.

[4] Mahoney, Arthur W., and Jake J. Abbott. "Five-degree-of-freedom manipulation of an untethered magnetic device in fluid using a single permanent magnet with application in stomach capsule endoscopy." The International Journal of Robotics Research (2015): 0278364914558006.

[5] Lucarini, Gioia, et al. "Electromagnetic Control System for Capsule Navigation: Novel Concept for Magnetic Capsule Maneuvering and Preliminary Study." Journal of medical and biological engineering 35.4 (2015): 428-436.

[6] Ciuti, Gastone, et al. "A comparative evaluation of control interfaces for a robotic-aided endoscopic capsule platform." Robotics, IEEE Transactions on 28.2 (2012): 534-538.

[7] Keller, H., et al. (2012). Method for navigation and control of a magnetically guided capsule endoscope in the human stomach, IEEE RAS and EMBS Int conf. on biom. robotics and biomech, pp. 859–865.

[8] Lucarini, Gioia, et al. "A new concept for magnetic capsule colonoscopy based on an electromagnetic system." International Journal of Advanced Robotic Systems 12 (2015).

Estimating the interaction forces on the body wall during minimal invasive fetal surgery

A. Javaux[1], M. Denhaen[1], Y. Hagenimana[1], A. Devreker[1], C. Gruijthuijsen[1], T. Vercauteren[2], S. Ourselin[2], D. Stoyanov [3], J. Deprest[2,4], K. Denis[5], D. Reynaerts[1], E. Vander Poorten[1]

***Abstract*— Little is known about the interaction forces and torques that are taking place at the level of the body wall during minimal invasive surgical procedures. This abstract reports on the interaction forces and torques that were measured during simulated fetal surgical procedures. It was confirmed experimentally that a proper alignment of the pivot point with the incision point into the patient has a large effect upon the lateral forces that are developing. The thickness and stiffness of the body wall obviously have a strong effect on the amplitude of the generated forces. Interestingly, while large differences in interaction forces were measured during experiments on a synthetic body wall versus experiments on a pig abdominal wall, participants did indicate that both interfaces felt quite realistically and were very much similar. This apparent contradiction calls for further validation of the different models as well as for the necessity to conduct similar experiments in an *in-vivo* setting.**

I. Introduction

Minimally Invasive Surgery (MIS) is steadily gaining importance in modern surgery. With smaller scars, shorter hospital stay and faster recovery there is an obvious patient benefit. Assistive technology is being developed to overcome some of the hurdles that surgeons are facing when conducting MIS. Robotic technology can be seen taking in a prominent role at one end of the spectrum. Most MIS robots foresee a method to establish a remote centre of motion (RCM)[1], [2]. This feature ensures that the instruments carried by the robot will pivot around a fixed point in space. By properly aligning the RCM with the incision point into the patient's body wall the stresses applied upon the tissue can be reduced. An increased prevalence of hernia after robotic surgery suggests that proper alignment is not as easy as it sounds [3], [4]. However, even for manual surgery little is known on how experts are manipulating their instruments and what kind of forces or torques they apply upon the body wall. This abstract presents force and torque measurements that were conducted during simulated fetal surgical interventions. The measurements were possible through a dedicated virtual reality simulation of the surgical procedure. While executing the virtual reality task, the motions and interaction with

Research funded by Wellcome Trust and EPSRC, project GIFT-Surg

[1]KU Leuven, Department of Mechanical Engineering, Leuven, Belgium allan.javaux@kuleuven.be

[2]Department of Medical Physics & Biomedical Engineering, University College London, United Kingdom

[3]Department of Computer Science, University of College London, United Kingdom

[4]University Hospital Leuven, Leuven, Belgium

[5]KU Leuven, Department of Mechanical Engineering Technology, Leuven, Belgium

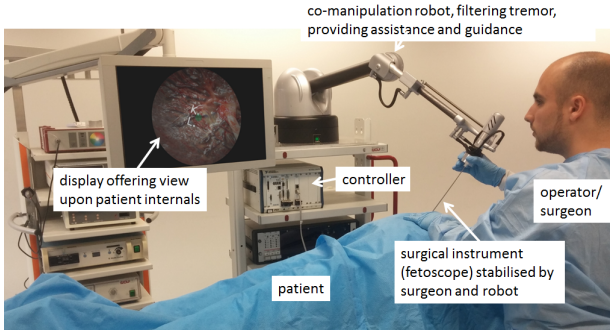

Fig. 1. View upon experimental setup. The operator co-manipulates the instrument with the Virtuose 6D ®(Haption SA, La-Valle, France), a haptic device that tracks here the pose of the instrument. Based upon the measured motion the view upon the placenta is updated in the VR.

respectively a synthetic replica and a pig body wall were recorded. Knowledge of the interaction forces is extremely valuable for fetal surgery in particular as iatrogenic Preterm Prelabor Rupture of Membranes (iPPRoM)[5] could possibly be caused by excessive stresses on the amniotic membranes. A parallel interest consists in investigating whether applied interaction forces/torques can serve as a metric for surgical skill. The latter is however out of the scope of this abstract.

II. Materials and Methods

Fig. 1 gives an overview of the experimental setup that was used. The operator is asked to execute a number of virtual fetal surgical lasering tasks. The instrument motion is tracked by a haptic device that is used in a co-manipulation manner. In the current configuration the robotic device is simply used as an instrument tracker, but in further work it can be used to experiment with various assistive control schemes. A foot pedal is placed below the operating bed to command the laser ablation. Aside from ablation commands also the interaction forces/torques that are exerted on the body wall are recorded. The body wall, consisting of skin, fat, muscle and the amniotic membrane, is replicated by a synthetic set of layers (EcoFlex $00-50$) with a total width of 40mm. They are clamped onto a force-torque sensitive plate. All motion and force/torque data is recorded at framerates of respectively 1kHz and 50Hz. To investigate the realism of the synthetic wall, an excised part of a pig abdominal wall has been prepared replacing the synthetic version of the body wall. Also here an incision was made to position a cannula. Forces and torques exerted on the pig tissue are measured in exactly the same fashion as in the former case.

Two sets of experiments were conducted. A first set

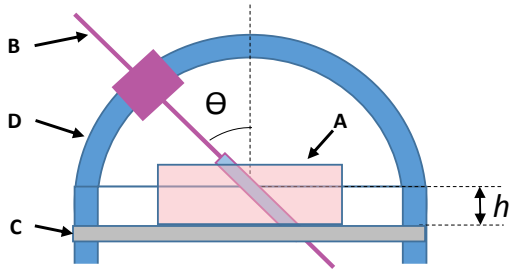

Fig. 2. Below the blue drape of Fig.1 the patient's abdominal wall is replicated by a 40mm thick set of Ecoflex layers (A). The surgical instrument (B) is passed through a cannula that is inserted in a central incision of the synthetic tissue. The model is mounted on a dedicated 6 DoF (Degree-of-Freedom) force-torque sensing plate (C). A mechanical frame (D) ensures a pure rotational motion θ of the instrument around a fixed point whose height h can be chosen.

of experiments is aimed at investigating the effect of the location of the pivot point on forces that develop within the tissue. A mechanical frame consisting of two circular guides (Fig.2) was constructed and rigidly fixed onto the ground. A carriage, in which a surgical instrument is clamped, is slid along the circular guides, that ensure a pure rotational motion of the instrument about the center of the circle. The pair of guides can be adjusted up or down to adjust the height of the pivot point and this relative to the thickness of the artificial body wall. In a second set of experiments the surgeon is asked to conduct a laser task in the virtual reality simulator. The task consists in identifying a number of laser targets and lasering these in a certain order. While manipulating a real scope and manoeuvring it through the cannula of the artificial or pig wall, the instrument pose is tracked and mapped to the motion of a corresponding scope that moves throughout the virtual reality environment. The time, trajectory and forces applied on the force sensitive plate are recorded for analysis.

III. Experiments

Fig.3 summarizes the forces and torques that were measured during 5 sets of experiments moving the instrument over an angle from 90° (corresponding to vertical position of the scope) to 45° along the circular guides. In each experiment the location of the pivot point was adjusted 10mm upwards, starting from 0mm (where the pivot point coincides with the lower surface of the pig wall) up to a height of 40mm (the pivot point lies at the upper surface of the pig wall). The plots show that lateral forces F_y (forces in the plane of the circular guides and parallel to the pig wall) rises as the instrument angulation drops to 45°. Only if the pivot point is vertically centred along the body wall, there is no resulting lateral force. This is expected as contributions from tissue deformations of the upper layers cancel out the contributions from deformations of the lower layers. The corresponding moment M_x about the axis of the circular guides (right-hand side of the figure) is seen to steadily rise as function of the instrument angulation. Here it is found that the height of the pivot point hardly has any influence on the amplitude of the interaction torques.

Interestingly, when repeating the above experiments with the synthetic Ecoflex interface, the above trend could not be

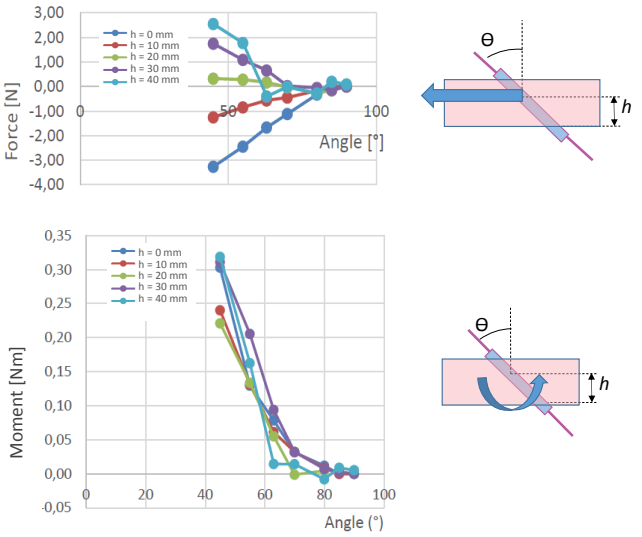

Fig. 3. Interaction forces and torques measured during experiments with adjustment of the pivot point location, w.r.t. the bottom (at height H=10mm) of a 40mm thick pig abdominal wall. For height H=20mm the pivot point is located approximately in the center of the pig abdomen.

reproduced. While no noticeable differences were perceived, the Ecoflex interface was measured to be substantially more stiff than the abdominal pig wall. The difference was so large that the instrument itself underwent significant amounts of bending while being angulated, explaining the differences in force and torque distributions.

In a second set of experiments participants were asked to conduct a number of lasertasks programmed in virtual reality (VR). Instrument motion and interaction forces were measured during these procedures. Table I summarizes the maximum forces and torques in the plane of the tissue F_{XY}, M_{XY} and perpendicular to the tissue plane F_Z, M_Z that were exerted during VR laser surgical interventions on respectively synthetic (test 1, test 2) and pig abdominal tissue (test 3, test 4). From the data it can be seen that especially in the plane sufficiently higher interaction forces are exerted when the synthetic model is used. The forces in the Z-axis are negative. This is mainly caused by the large friction between the instrument and the cannula. Indeed surgeons reported that especially when retracting the instrument and due to this friction it happens that the cannula is involuntary extracted from the patient. To avoid this problem from occuring surgeons typically grasp the cannula by their non-dominant hand while retracting the instrument.

TABLE I
Maximal forces and torques during VR experiments

Force component	test 1	test 2	test 3	test 4
F_{XY}	9N	11N	5N	5N
F_Z	−11N	−13N	−11N	−12N
M_{XY}	0.8Nm	1.1Nm	1.1Nm	1.2Nm
M_z	0.13Nm	0.15Nm	0.22Nm	0.18Nm

IV. Conclusion

At present little is known about the interaction forces that take place at the level of the abdominal wall (and/or uterine wall in case of fetal surgery) during MIS procedures. This abstract reports on experiments that were conducted on synthetic and pig abdominal tissue. Whereas significant differences in forces/torques were measured, participating surgeons indicated both models were quite similar and representative for the human body wall. To avoid drawing wrong conclusions by possibly inadequate models it is found important and necessary to conduct similar experiments during *in-vivo* conditions with other means of force sensing. This will form a topic of further investigations.

References

[1] R. H. Taylor, J. Funda, B. Eldridge, S. Gomory, K. Gruben, D. LaRose, M. Talamini, L. Kavoussi, and J. Anderson, "A telerobotic assistant for laparoscopic surgery," *Engineering in Medicine and Biology Magazine, IEEE*, vol. 14, no. 3, pp. 279–288, 1995.

[2] G. Zong, X. Pei, J. Yu, and S. Bi, "Classification and type synthesis of 1-dof remote center of motion mechanisms," *Mechanism and Machine Theory*, vol. 43, no. 12, pp. 1585–1595, December 2008.

[3] G. S. Kilic, T. B. Bildaci, O. L. Tapisiz, I. Alanbay, T. Walsh, and O. Swanson, "Trocar site hernia on an 8-mm port following robotic-assisted hysterectomy," *Journal of the Chinese Medical Association*, vol. 77, no. 2, pp. 112 – 114, 2014.

[4] G. Scozzari, M. Zanini, F. Cravero, R. Passera, F. Rebecchi, and M. Morino, "High incidence of trocar site hernia after laparoscopic or robotic roux-en-y gastric bypass," *Surgical Endoscopy*, vol. 28, no. 10, pp. 2890–2898, 2014.

[5] V. Beck, P. Lewi, L. Gucciardo, and R. Devlieger, "Preterm prelabor rupture of membranes and fetal survival after minimally invasive fetal surgery: a systematic review of the literature," *Fetal diagnosis and therapy*, vol. 31, no. 1, pp. 1–9, 2012.

A Monolithic Underactuated and Compliant Endoscopic Tool Design

K. Meiswinkel[1], T. Horn[1], E. Klang[1], S. Zani[2], T. Pappas[2], E. Grant[1]

[1]*College of Engineering, North Carolina State University, USA,*

[2]*School of Medicine, Duke University, USA*

egrant@ncsu.edu

INTRODUCTION

This paper is focused on the design and fabrication of a new class of monolithic endoscopic tools for robotic surgery. This novel endoscopic tool is underactuated, compliant, and fabricated using 3D printing. The endoscopic tool has been designed to be a combined trocar/endoscopic tool. The design allows for this endoscopic tool to be taken from its current scale, i.e., in the upper regime of the meso-scale, to the miniature scale. By incorporating proximal and distal flexibility into the endoscopic tool design makes grasping action mimic human grasping, i.e., it can grasp tissue conformally when fully extended, or pinch tissue if partially extended. By 3D printing monolithic endoscopic tools there are reductions in: cost; assembled components; machining; assembly time; and calibration and testing time; over the current generation of surgical endoscopic tools.

MATERIALS AND METHODS

Meiswinkel [1] designed an armature that exceeded the minimum load specification of the iRobot DARPA ARM-H project. That iRobot gripper achieved excellent anthropomorphic grasping based on a proximal and distal joint system only. In [1, 2] it was reasoned, after three design iterations and flexure fractures, that the number of finger segments could be reduced to two. This design resembles the iRobot DARPA ARM-H finger design, see Fig. 1. With two finger segments the moment initially applied to the proximal flexure joint is less severe than that experienced by a three segment finger. A design was created to monolithically fabricate a scaled two segment per digit finger.

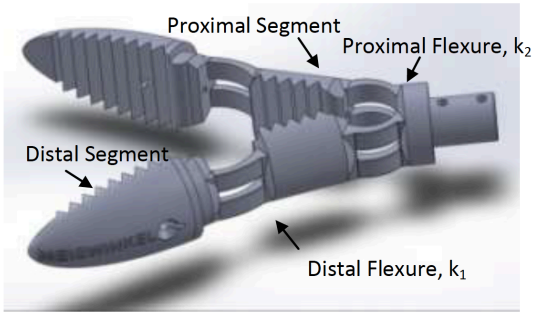

Fig. 1. Solidworks design of a two-fingered monolithic finger.

Prior to fabricating the monolithic endoscopic tool a review was made of three suitable materials for 3D printing the endoscopic tool. Finite element analysis (FEA) was also carried out on these three materials under two load conditions. In the end Vero White resin manufactured by Stratasys was chosen for fabricating the two fingered monalithic endoscopoic tool, see Figs . 2 and 3.

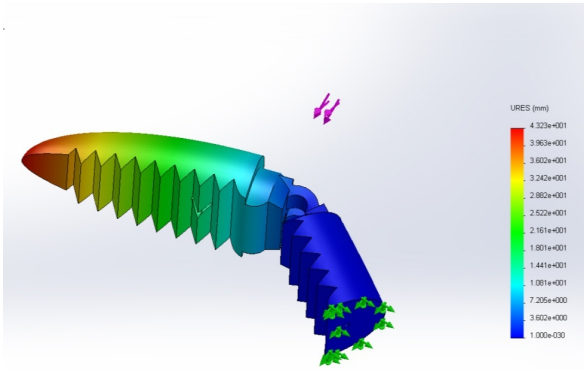

Fig. 2. FEA Analysis of a two fingered flexural and rigid geometries.

These two fingered flexural joints emulate three springs per digit in series, and these approximate to two springs in parallel, see Equ. 1. Here, proximal flexure joints were designed to have a larger spring modulus than the distal flexure joints. It was noted in [2] that finger compliance is maximized if the distal flexure has a lower spring constant than the proximal flexures. Grasping force is bounded, on the upper limit, not by cable tension but by the restitution of the elastomeric deflections of the flexure joints. Note, the maximum grasping force is not from adding the two sides of the monolithic flexures in parallel, but from a single side's elastomeric reactions. If the flexures were assumed symmetric, this analysis will hold [3-5].

$$\frac{1}{\left[\left(\frac{1}{k_1}\right)+\left(\frac{1}{k_2}\right)\right]} = k_{equivalent}, where\ k_1 < k_2$$

Equ. 1: Equivalent proximal and distal spring stiffness.

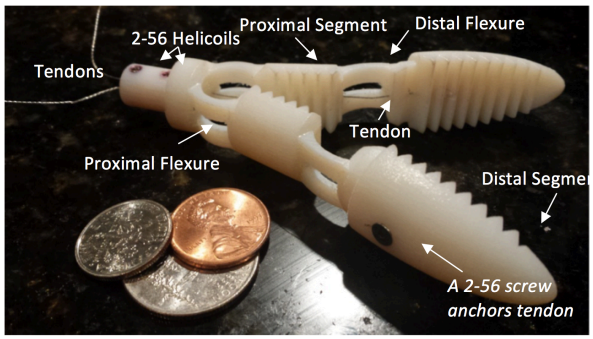

Fig. 3. The monolithic, underactuated, compliant, endoscopic tool fabricated in Vero White resin.

RESULTS

The flexure acheived by the first two fingered monolithic assembly was considerably better than in all previous versions. However, it too succumbed to failure in the proximal flexure joint. The problem appeared to lie in the properties of the Vero White resin. Design adjustment was required to: (1) decrease the initial applied moment, and (2) adjust the geometry. The geometry was adjusted to improve the flexural characteristics oft he endoscopic tool. A second prototype was then assembled for experimentation. Precision fasteners (helicoils) were firmly anchored in the Vero White. The tendons cables were attached to the helicoil fasteners so addressing problematic characteristics found in the Vero White resin flexure properties. Prior to conducting grasp experiments the endoscopic tool flexure properties were relaxed by immersing the tool in heated water.

Fig. 4. Two fingered monolithic and compliant endoscope demonstrating irregular shape grasp.

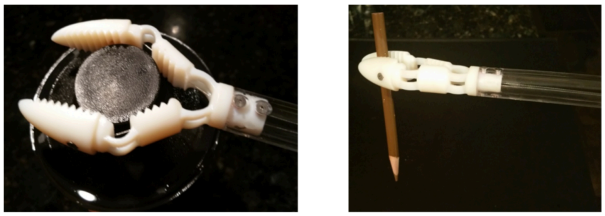

Fig. 5. Two fingered monolithic and compliant endoscope demonstrating geometric shape grasp..

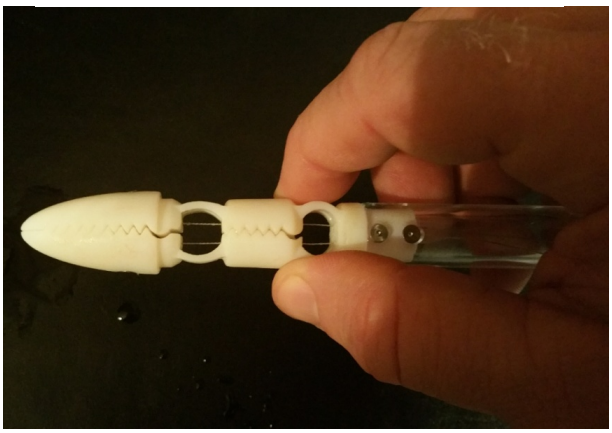

Fig. 6. Two fingered monolithic and compliant endoscope demonstrating precise closure.

CONCLUSION AND DISCUSSION

This investigation into designing monolithic, underactuated, and compliant endoscopic tools for robotic surgery using 3D additive manufacturing methods gave mixed results. First, the material characteristics of Vero White resin did provide accurate geometric reproductions from Solidworks designs. Second, Vero White resin has the potential to provide scalable monolithic endoscopic tools. Third, the elastomeric property of Vero White resin could only produce good proximal and distal flexure after heating an endoscopic tool prior to conducting grasp experiments. When relaxed, through heating, the monolithic endoscopic tool could grasp both irregular and geometric shapes, see Fig. 4 (irregular shape), Fig. 5. (geometric shape), and close precisely, see Fig. 6. Tendons were used to grasping and releasing objects. Because of the material properties certain aspects of underactuation in a monolithic design could not be validated. However, once the tool was queued into position, wider and thinner objects were grasped with the same confidence that was demonstrated by [2]. It is concluded that endoscopic tools that are, monolithic, underactuated, and compliant, will allow grasping and manipulation a variety of shapes and materials, in a manner that mimics human grasp. 3D printing allows fine-detailed endoscopic tools to be fabricated at scales representative of reproducing the hands of the surgeon in miniature. Novel designs of monolithic, scaleable, underactuated, compliant, endoscopic tools can be achieved by 3D additive manufacturing. However, resin material properties need further examination. Lastly, monolithic edoscopic tool designs reduce components, precise machining and assembly, and calibration and test. And, the monolithic endoscopic tool design here retracts into its own insert tube when not in use, Fig. 6.

REFERENCES

[1] Meiswinkel, K. “Novel Designs of Robotic Manipulators and Compliant Underactuated Grasping Mechanisms for Endoscopy,” Ph.D., North Carolina State University, November 2015. http://www.lib.ncsu.edu/resolver/1840.16/11156

[2] Odhner LU and Dollar AM (2011) Dexterous manipulation with underactuated elastic hands. In: 2011 IEEE international conference on robotics and automation (ICRA), May, IEEE, pp. 5254-5260.

[3] Rosen, J., et al. (1999). "Force controlled and teleoperated endoscopic grasper for minimally invasive surgery-experimental performance evaluation." Biomedical Engineering, IEEE Transactions on **46**(10): 1212-1221.

[4] van der Smagt, P., et al. (2009). "Robotics of human movements." Journal of Physiology-Paris **103**(3–5): 119-132.

[5] Won-Ho, S. and K. Dong-Soo (2013). "Surgical Robot System for Single-Port Surgery With Novel Joint Mechanism." Biomedical Engineering, IEEE Transactions on **60**(4): 937-944.

A Tele-manipulator Robotic Assistant for Endoscopic Surgery

A. Kracht[1], F. Livingston[1], S. Zani[2], T. Pappas[2], E. Grant[1]

[1]*College of Engineering, North Carolina State University, USA,*

[2]*School of Medicine, Duke University, USA*

egrant@ncsu.edu

INTRODUCTION

This research deals with the development of a surgical robot assistant to control the localization of an endoscopic tool. The kinematic analysis required that a constant point in space, termed the trocar point (TL) be maintained along a rigid tool while the manipulator was repositioned. Results show that the localization algorithm, along with two force feedback joysticks and a custom interactive user interface, successfully accomplishes this unique robot localization task. For this system, positioning error was the performance metric. Results show that this surgical assistant positioned the endoscopic tool, relative to the world coordinate frame, to within 0.05 inches. Localization error in maintaining a constant point in space during endoscopic tool repositioning was caused by limitations inherent in the robot arm.

MATERIALS AND METHODS

The main goal of this research is designing simpler surgical robotic assistants and interactive user interfaces. Here, an industrial linear based articulated arm was used for positioning an endoscopic tool. So, can full endoscopic tool localization control and accuracy be provided to a surgical system by a 5-axis A250 CRS Plus robot, 2-Saitek evo force feedback joysticks, an Intuitive Surgical EndoWrist, and an interactive user interface? Robotic arms with similar configurations have been used as surgical robots [1, 2] but not in the configuration presented here. This surgical assistant assists endoscopic procedures by holding and physically manipulating an endoscopic tool under the direct control of the surgeon. The surgeon (Master) controls the robotic system (Slave: robotic arm and endoscopic tool) via a Tele-manipulator, see Fig. 1.

Robot Arm Joystick Control	**A250 CRS Robot Response**
X-axis	X-displacement
Y-axis	Y-displacement
Rotation	Z-displacement
EndoWrist Joystick Control	**Endoscopic Tool Response**
X-axis	Pitch
Y-axis	Yaw
Rotation	Roll
Button 1	Close fingers
Button 2	Open fingers

Fig.1. Telemanipulator system joysticks control.

Here, the tele-manipulator took the form of an interactive user interface, i.e., a GUI. The GUI design was based on the control requirements in Fig. 1, and provides the user with the ability to communicate with and control the complete robotic system. The GUI has four states: (1) Initialization: establishes and verifies communication with the robotic arm; endoscopic tool; joysticks; informs the user; fails to safe; aligning physical robot arm with its mathematical model; and positions the robot arm relative to the world frame. (2) Trocar Placement: positions the robot arm using the robot teach pendant, (3) Insertion/Retraction: locks the robot arm position; allows the user to safely insert or remove the endoscopic tool; perform operations but only after the endoscopic tool length is entered manually, (4) Operation: polls the two joysticks for motion commands; recognizes joystick movement; decodes values and communicates motion commands to the robotic system. Pressing the "Shut Down" button on the GUI makes the robot arm perform a docking procedure.

The surgical robotic assistant is the slave of the master/slave tele-manipulator system. The robotic system provides all the physical motions that a surgeon requires in performing an endoscopic procedure. This system is divided into two subsystems: (1) the robotic arm; and (2) the surgical endoscopic tool manipulator.

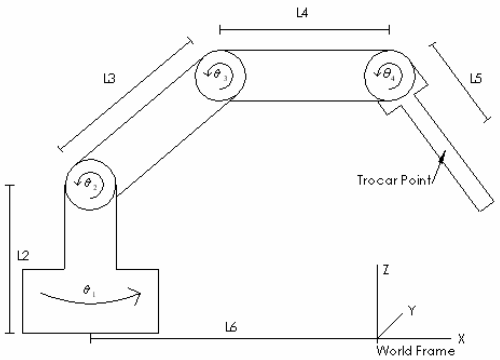

Fig.2. Robot system configuration.

The overall transformation matrix relating the robot base to the frame at the trocar point in Fig. 2., was found by assigning Denavit-Hartenberg parameters and computing individual transformation matrices. Then by incorporating the kinematics of the endoscopic tool, see Fig. 3. (a) and (b), the overall transformation matrix was computed, Equ. 1. In knowing the kinematic constants

of the robotic arm, e.g., lengths etc., the inverse kinematics were computed to control the system about the Trocar Point, see Fig. 2.

$$T_{10}^{0} = \begin{bmatrix} c1c234 & -s1 & -c1s234 & L5c1c234+10c1c23+10c1c2-2c1s234-L6 \\ s1c234 & c1 & -s1s234 & L5s1c234+10s1c23+10s1c2-2s1s234 \\ s234 & 0 & c234 & L5s234+10s23+10s2+10+2c234 \\ 0 & 0 & 0 & 1 \end{bmatrix}$$

Equ. 1. The overall kinematic equation of the robotic arm/endoscopic tool system.

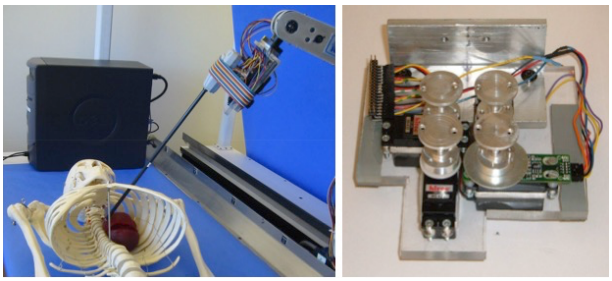

Fig. 3. (a) Endoscopic tool attached to CRS robot, (b) Endoscopic tool attachment drive system.

RESULTS

Prior to any physical system control being performed, the kinematic equations and the control algorithm were simulated using Matlab. The simulation calculates all the joint values, and the linear axis position relative to the world coordinate frame. These values were used in the individual link transforms of Equ.1. to produce a visual graphic of the robot and endoscopic tool's position and orientation, Fig. 4. This simple graphic verified that the overall system was capable of performing the desired motions.

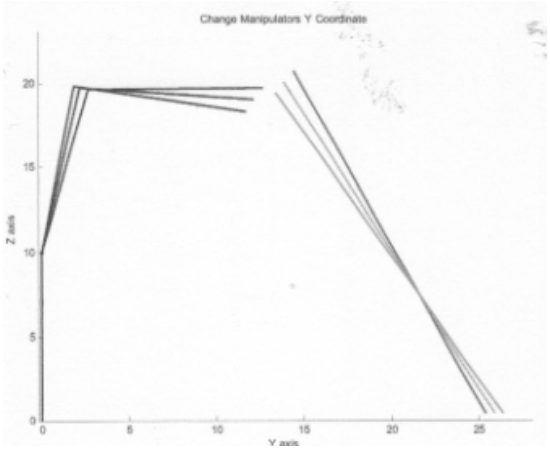

Fig. 4. MATLAB simulation output.

Now that the analysis of the kinematics of the robot arm and the endoscopic tool was completed and verified a program to control the robotic system was implemented. In simulation 40 different motion commands were sent to the robot controller and the average error and maximum error in each joint angle was recorded. Results showed that the maximum error in each joint led to an endoscopic tool error in the X, Y, and Z axis of approximately 0.0055 inch, 0,0035 inch, and 0.0032 inch respectively. The first physical experiment conducted determined precise robots motion, in the XY and YZ planes. In the experiments the endoscopic tool was placed close to one of these planes and commanded to move 1 inch. This distance was chosen because it was decided that any error associated with a movement would become more observable as the distance increased. Experiments were conducted on smaller motions (approximately 0.1 inch) but there was no observable error. A second set of experiments into motion control experiments used three different trocar lengths: 9, 11.5, and 14 inches, because endoscopic tool localization depends on this length. Three lengths were chosen because of the fulcrum effect, i.e., with a fulcrum closer to the robot arm small robot motions produce large endoscopic tool motions, and vice versa. The results in Fig. 5, show that the surgical robot assistant localization was controlled with reasonable accuracy and that there is no direct correlation between the manipulator error and trocar length.

Trocar Point (inch)	Av.Abs.Error X inch	Av.Abs.Error Y inch	Av.Abs.Error Z inch
9	(0.004,0.023,0)	(0.026, 0.027,0)	(0, 0.006, 0.013)
11.5	(0.013, 0.023,0)	(0.029, 0.027,0)	(0, 0.006, 0.014)
14	(0.012, 0.033,0)	(0.037, 0.027,0)	(0, 0.014, 0.008)

Fig. 5. Average absolute error (inches).

CONCLUSION AND DISCUSSION

In this research a surgical robotic assistant, using a linear base articulated arm for localizing an endoscopic tool provided: functionality to an Intuitive Surgical EndoWrist; and used tele-manipulation, to perform surgical motions. There is no similar configuration to the surgical robot assistant created here. Analysis and experiments showed that repositioning the endoscopic tool is possible to within 0.05 inches and that the control algorithm maintained the trocar point; even when the length of that point varied. The major error observed was due to repositioning the surgical robot assistant, but the CRS robotic arm was not designed for tele-manipulation. Nevertheless, this research produced a unique surgical robot assistant configuration for endoscopic surgery, one that did provide precise localization. The research conducted is a first step in understanding the limitations of simplifying and miniaturizing surgical robotic assistants.

REFERENCES

[1] Mayer, Hermann, et al. "An Experimental System for Robotic Heart Surgery." In Proceedings: 18th IEEE Symposium on Computer-Based Medical Systems (2005), pp 55-60.

[2] Venere, Emil. "Lower cost, portable surgical robots could be smooth operators." In Purdue News: 2 March 2006. http://www.purdue.edu/UNS/html4ever/2006/060302.Peine.robots.html.

Augmented Reality in surgical training

Rosanna Maria Viglialoro[1], Sara Condino[1], Simone Fani[2], Matteo Bianchi[2,3], Mauro Ferrari[1,5], Antonio Bicchi[2,3], Vincenzo Ferrari[1,4, 5]

[1]*EndoCAS Center, Department of Translational Research and New Technologies in Medicine and Surgery, University of Pisa, Italy*

[2]*Research Center "E.Piaggio" Faculty of Engineering", University of Pisa, Italy*

[3]*Department of Advanced Robotics, Istituto Italiano di Tecnologia, Genova, Italy*

[4]*Department of Engineering Information, University of Pisa, Italy*

[5]*Vascular Surgery Unit, Cisanello University Hospital AOUP, Pisa, Italy*

rosanna.viglialoro@endocas.org

INTRODUCTION

The surgical training in a real-life setting is not always possible for economic, safety, organizational and ethical issues. The medical simulation represents an alternative way to achieve clinical excellence, because allows the skills practice in a safe and controlled environment. However, to improve the skills transfer, a realistic visual/haptic feedback should be integrated in a training simulator [1].

The Augmented Reality (AR) technology, thanks to the insertion of virtual information (real time and spatially coherent data) in the real world, is able to enhance the user's sensory perception of reality. The virtual information can appeal to all senses, not just sight [2]. In this paper, we present two examples of AR applications dedicated, respectively, to the visual and the tactile augmentation for surgical training. In both applications, AR is used an aid for the recognition of anatomical tubular structures during training sessions.

KEYWORDS: surgical training, augmented reality visualization, augmented reality tactile.

MATERIALS AND METHODS

The following paragraph describes two examples of AR applications for training simulation systems.

1) AR *visualization of hidden deformable tubular structures for surgical training*

Many surgical procedures involve the task of identification and isolation of not always visible tubular structures, such as blood vessels, biliary tree and nerves. For example, the most crucial step of cholecystectomy is the identification and isolation of the cystic duct (part of the biliary tree) and artery (part of the arterial tree) [3].

In our previous studies, we have provided examples of dedicated AR visualization for surgical training. More in particular, we have demonstrated the feasibility of a novel AR method providing the real time visualization of deformable tubular structure (such as arterial and biliary tree) by means of electromagnetic (EM) localization technology [4]. The simulation system includes: realistic physical replicas of the biliary and arterial tree, gallbladder and connective tissue (described in detail in [5, 6]) (Figure 1a); an EM tracking system; an optical calibration-acquisition system; and a laptop. The biliary and arterial tree are sensorized with 5 DOF EM sensors and tracked in real time for the implementation of AR functionalities. The anatomical replicas do not comprise ferromagnetic materials to reduce possible electromagnetic interferences (for an exhaustive dissertation of source of errors refer to [4, 6]). The optical calibration-acquisition system allows the user to perform a calibration routine, it acquires the real scene, and displays the augmented real scene on the laptop screen. The AR scene (Figure 1b) consists of red and green virtual structures showing the position of the arterial and biliary tree (AT and BT) on the grabbed image (described in detail in [6]).

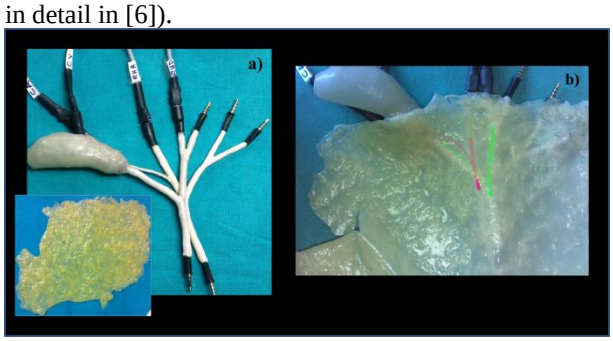

Figure.1. The AR as an aid for identification of cystic duct and artery in cholecystectomy: a) Realistic physical replicas; b) The corresponding AR view which overlays the red and green pathways on arterial and biliary tree.

This AR application assists the trainee in the identification of the cystic duct and artery, covered by connective tissue, during cholecystectomy simulation.

2) *AR tactile for arteries palpation in open surgery training*

The touch sense plays a large role in a wide variety of surgical procedures providing information about: the localization of hidden anatomical structures and anatomical landmarks (such as muscle, bones and blood vessels); the health state of tissues and organs. In particular, arterial pulse palpation is an essential step for the recognition of blood vessels avoiding their perforations/ruptures in open surgery [7, 8]. In a previous work, we have proposed a method, based on the EM tracking of the arterial replicas and the user finger, which provides a pulse feedback during palpation through a tactile display W-FYD (Wearable Fabric Yielding Device, described in [9]) (Figure 2). This AR tactile system comprises: a sensorized arterial tree covered by synthetic connective tissue, a sensorized prototype of W-FYD which can be worn on user's finger (described in details in [10]), an EM tracking system, an optical calibration-acquisition system, and a laptop [10]. More in particular, the W-FYD is equipped with: a 6DOF EM sensor and a load cell (FSR model 400 round, thickness 0.1-0.3 mm) to detect the pressing force exerted by the user.

A calibration procedure is required to derive the position of the user finger pad from the EM sensor data so that to activate the pulse simulation when the user touches the sensorized arterial tree. More in particular, before every simulation trial, a digitizer is used to calculate the relative position (constant over the time) of the finger pad with respect to the EM sensor.

A pulsating force feedback is rendered when two criteria are contemporaneously satisfied: the user fingertip is sufficiently close to the artery (positions derived from EM data); the pressure exerted by the user on the artery is comprised between the standard systolic and diastolic pressure.

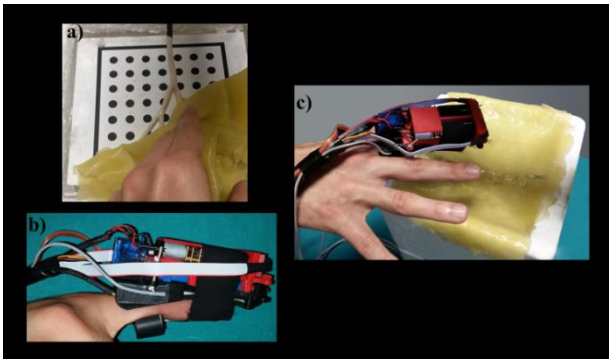

Figure.2: The AR tactile as an aid for arterial pulse detection: a) Sensorized arterial tree covered with synthetic connective tissue; b) W-FYD sensorized with a 6DOF EM Aurora Sensor and a load cell (FSR model); c) The AR tactile system in use.

RESULTS

Preliminary tests were performed to evaluate the proposed visual and tactile augmented reality applications.

In particular, qualitative and quantitative tests were performed to evaluate the accuracy and usefulness of the obtained AR visualization. The AR accuracy was quantitatively estimated using the strategy proposed in (4), by calculating the Target 2D Visualization Error (TVE2D, expressed in pixel) which provides a measure of the offset among virtual and real objects (among the barycenter of each EM sensor virtual representation and the barycenter of the corresponding real portion as showed in Figure 3).

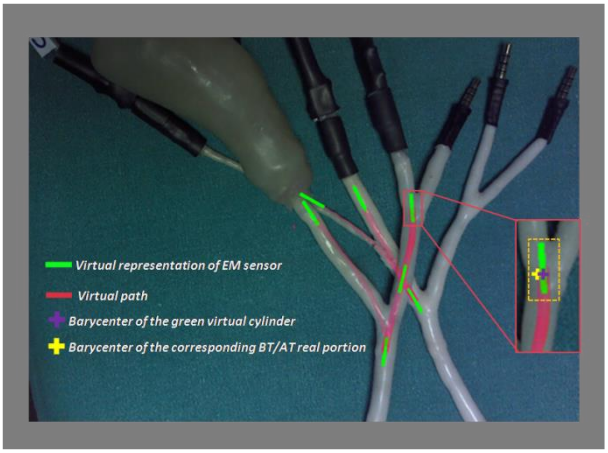

Figure.3: AR view with virtual green cylinders representing sensors inside the tubular structures and red splines that mimic the paths between the sensors. The zoomed detail shows the barycenter of a virtual cylinder (violet cross) and the barycenter of the corresponding real portion (yellow cross)

Starting from the TVE2D and knowing the intrinsic camera parameters and the distance between the camera optic center and target, the 3D target visualization error (TVE3D, expressed in mm) was estimated. Obtained results are promising since the TVE3D does not exceed 1 mm. This error is lower than the anatomical structures radius. A positive qualitative feedback was received by a group of expert surgeons about the accuracy and the usefulness of AR visualization [4, 6]. As for the evaluation of the developed tactile AR application, a preliminary qualitative feedback was obtained from a total of ten surgeons (eight general surgeons and two vascular surgeons from the Cisanello University Hospital in Pisa). All participants were asked to wear the tactile display and palpate the mockup for the recognition of the cystic or right hepatic artery. After the trial, they were asked to complete a questionnaire about the realism of the arterial pulse feedback and the usefulness of integrating this kind of haptic interface in open-surgery simulators [10]. Obtained results show a general consensus among surgeons concerning both the realism of the feedback (also in term of location of the arterial pulse which was considered sufficiently accurate for the proposed application [10]) and the usefulness of the simulator.

CONCLUSION AND DISCUSSION

In this paper we present two examples of AR applications dedicated, respectively, to the visual and the tactile augmentation for surgical training. Both the applications aid the trainee in the recognition of anatomical tubular structures during simulation sessions.

The obtained results preliminary demonstrate the usefulness and the potentialities of AR augmentation to improve the effectiveness of surgical simulation.

REFERENCE

[1] Fisher, J.B., Porter, S.M.: Using mixed reality, force feedback and tactile augmentation to improve the realism of medical simulation. Studies in health technology and informatics 85,144-149 (2002)

[2] Kamphuis, C., Barsom, E., Schijven, M., Christoph, N.: Augmented reality in medical education? Perspectives on medical education 3,300-311 (2014)

[3] Abdalla, S., Pierre, S., Ellis, H.: Calot's triangle. Clinical anatomy 26,493-501 (2013)

[4] Ferrari, V., Viglialoro, R.M., Nicoli, P., Cutolo, F., Condino, S., Carbone, M., Siesto, M., Ferrari, M.: Augmented reality visualization of deformable tubular structures for surgical simulation. The international journal of medical robotics + computer assisted surgery : MRCAS (2015)

[5] Viglialoro, R., Ferrari, V., Carbone, M., Condino, S., Di Puccio, F., Ferrari, M., Mosca, F.: A physical patient specific simulator for cholecystectomy training.in Proceedings of Computer Assisted Radiology and Surgery (CARS) (2012).

[6] Viglialoro, R., Condino, S., Gesi, M., Ferrari, M., Ferrari, V., Freschi, C., Cutolo, F.: AR Visualization of "Synthetic Calot's Triangle" for Training in Cholecystectomy. 12th IASTED International Conference on Biomedical Engineering, BioMed 2016 (2016)

[7] Poorten, V.E., Demeester, E., Lammertse, P.: Haptic feedback for medical applications, a survey. Proc. Actuator 18–20 (2012)

[8] Hu, J., Chang, C.Y., Tardella, N., Pratt, J., English, J.: Effectiveness of haptic feedback in open surgery simulation and training systems. Studies in health technology and informatics 119,213-218 (2006)

[9] Bianchi, M., Battaglia, E., Poggiani, M., Ciotti, S., Bicchi, A.: A Wearable Fabric-based display for haptic multi-cue delivery. In: 2016 IEEE Haptics Symposium (HAPTICS), pp. 277-283. (Year)

[10] Condino, S., Viglialoro, R., Fani, S., Bianchi, M., Bicchi, A., Morelli, L., Ferrari, M., Ferrari, V.: Tactile augmented reality for arteries palpation in open surgery training. Submitted to: MIAR 2016.

Segmentation of pancreatic solid tumors and texture analysis to discriminate pancreatic ductal adenocarcinomas from neuroendocrine neoplasms

B.M. Maris[1], P. Fiorini[1], R. De Robertis Lombardi[2]

[1]*Department of Computer Science, University of Verona, Italy*

[2]*Department of Medicine, University of Verona, Italy*
bogdan.maris@univr.it

INTRODUCTION

A limitation that applies to all imaging modalities is that image interpretation in radiology is based on a visual process [1]. Yet, there are features within each image that may not be appreciated readily by the naked eye. Furthermore, when images are analyzed in a more quantitative manner, standard regions of interest analysis may provide a mean parameter value, but does not typically describe the underlying spatial distribution. Thus, a non-invasive method of assessing inner pathological features within a tumor might be of clinical benefit, to provide a more precise characterization and to assess tumor heterogeneity, a parameter that have been shown to be correlated with poorer prognosis.

Texture analysis refers to a variety of mathematical methods that can be used to evaluated the gray-level intensity and position of the pixels within an image to derive so-called "texture features" that provide a detailed description of tumor components and a measure of intralesional heterogeneity.

Magnetic resonance (MR) imaging is one of the recommended imaging modalities for the evaluation of pancreatic tumors. Diffusion-weighted MR imaging (DW-MRI) allows non-invasive assessment of biological tissues based on the molecular motion of water molecules in the extracellular, intracellular, and the intravascular spaces. In tissues, such as tumors characterized by high cellular density, increased tortuosity of the extracellular space and high density of hydrophobic cellular membranes, restricted diffusion is seen. Apparent diffusion coefficient (ADC) maps have been used to characterize tumoral tissues. These maps provide a quantitative index of water diffusivity for each voxel, allowing visualization of molecular diffusion in the different tissue compartments and providing indirect information on its microstructure. Recently, there has been growing interest in the histogram analysis of the entire tumor volume, as this approach provides quantitative information on the distribution and frequency of ADCs and consequently on the heterogeneity of water molecules diffusivity within the whole tumors.

The purpose of this work is to explore the role of histogram analysis of apparent diffusion coefficient (ADC) MRI maps based on the semiautomatic segmentation of the entire tumor volume data in distinguishing pancreatic ductal adenocarcinomas (PDACs) from neuroendocrine neoplasms (PanNENs).

MATERIALS AND METHODS

Pre-operative MR examinations of 50 patients with PDAC (26) or PanNEN (24) were retrospectively evaluated. Regions of interest containing the lesion were semi-automatically drawn on the slice where tumor showed its larger size and histograms were automatically obtained for entire tumor volume.

The tumors were segmented using the Fraunhofer's Mevislab platform [2]. In order to precisely extract the volumes, it was built a network script that allows the user to draw contours on some slices and then automatically interpolate by computing a three-dimensional implicit function that describes a surface, and this surface is scanned using a recursive marching-cubes algorithm. The surface represents the border of the tumor and may be visually inspected and improved by selecting more contours. Once the result is satisfactory and validated by the radiologists, a dataset of images containing only the segmented area is save for the statistical analysis (Figure 1).

The statistical analysis was implemented in Matlab and, aside the standard functions, we have customized the implementation of the entropy and of the histogram of the three-dimensional images. The customization was required in order to normalize the values extracted in the segmentation process, since they do not cover the entire range of image values.

Calculated parameters included mean ADC (mADC), median ADC, standard deviation (SD), minimum and maximum ADC, 25th percentile ADC (ADC25), 75th percentile ADC (ADC75), 95th percentile ADC (95ADC), interquartile range, variance, entropy, uniformity, skewness and kurtosis. Histogram parameters were compared between histotypes by repeated Student's T tests. P values below 0.05 were considered statistically significant.

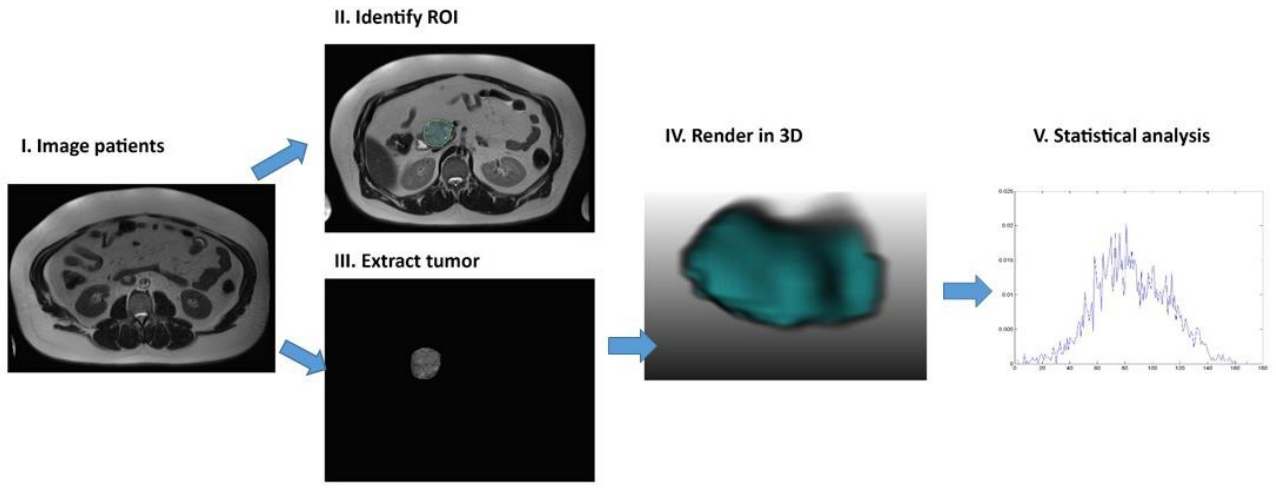

Figure. 1. Flowchart shows the segmentation and statistical analysis process. The analysis begins with acquisition of high-quality images. From these images, a region of interest (ROI) that contains the whole tumor can be identified. This is segmented with operator edits and eventually rendered in three dimensions (3D). Quantitative features are extracted from this volume to generate a report, which is placed in a database along with other data, such as clinical data.

RESULTS

Some of the statistical results derived from the ADC images such as mean, minimum, median, and the first quartile were significantly higher in PDACS (1465.1 ± 230.4; 705.8 ± 373.7; 1435.3 ± 228.7; 1262.4 ± 228.5 $x10^{-6}$ mm^2/s) compared to PanNENs (1268.3 ± 330.7; 485.2 ± 302.1; 1246.9 ± 354.5; 1012 ± 283.4 $x10^{-6}$ mm^2/s). Uniformity was significantly lower in PDACS compared to PanNENs (0.005 ± 0.004 vs 0.15 ± 0.23).

CONCLUSIONS AND DISCUSSION

Histogram analysis of ADC maps on the basis of the entire tumor volume can be useful in differentiating PDACs from PanNENs. The preliminary analysis we have performed in this work shows that with only some of the statistical results one can derive a discrimination between PDACS and PanNEN.

As far as we know, there are still no analysis of data that arrive to 50 patients. The workflow we have implemented, aside the partially automatic segmentation, requires little or no interaction and generates large database of results that may be integrated with clinical data.

Aside ADC we are analyzing other types of MRI data such as: T1-weighted, T2-weighted, diffusion weighted MRI and so on.

The Hospital of Verona is one of the largest center for pancreatic surgery and treatment, and we can have more than 100 patients, therefore we envision to obtain representative results.

REFERENCES

[1] R. J. Gillies, P. E. Kinahan, and H. Hricak, "Radiomics: Images Are More than Pictures, They Are Data.," *Radiology*, vol. 278, no. 2, p. 151169, 2015.

[2] F. Heckel, M. Schwier, and H. Peitgen, "Object-oriented application development with MeVisLab and Python," *Lect. Notes Informatics*, vol. 154, pp. 1338–1351, 2009.

Gaze-Driven Human-Robot Interaction in the Operating Theatre

A.A. Kogkas, A. Darzi, G.P. Mylonas

Department of Surgery and Cancer, Imperial College London, UK
a.kogkas15@imperial.ac.uk

INTRODUCTION

A safe operating room has to constantly adapt to the increasing complexity of introduced new technologies and surgical procedures. Although new technologies may add complexity to the surgical workflow, at the same time they offer unique opportunities to improve patient safety, operational workflow and clinical outcome. The operating theatre is an environment where unintentional patient harm is most likely to happen, with most influential factors relating *to suboptimal communication* among the staff, *poor flow of information, staff workload and fatigue* and environment *sterility* [1].

For communication in particular, 30.6% of all team exchanges in the operating room are classified as failures, with one third resulting to immediate effects that can imperil patients [2]. Main cause for such failures is the lack of familiarity between the surgeon and the nurses, causing team instability and incoordination [3].

Therefore, keeping the surgeon in the loop of the decision making and task execution process is likely to reduce communication errors. Moreover, it is expected to improve the performance and efficiency of the surgeon. For example, a hand-gestures and voice-driven robotic nurse introduced by Jacob et al. has been shown to reduce the number of movements without significantly affecting task execution time compared to collaboration with human nurses [4]. Hands-free interactions could prove more beneficial.

Eye-tracking methodology has the potential to provide a "third hand" and a seamless way to allow "perceptually enabled" interactions with the surgical environment. Previous work demonstrated screen-based gaze control of surgical instruments [5] and improved collaboration among staff during surgery [6].

More recently, we have introduced a novel framework for theatre-wide and patient-wise 3D gaze localisation in a simultaneous and unrestricted/mobile fashion [7]. An extension of this framework is presented here, that allows hands-free gaze-driven interactions with the environment and a robotic manipulator. The framework is expected to facilitate seamless and meaningful integration of human and technology in the theatre for improved safety, collaboration and clinical outcome.

MATERIALS AND METHODS

The original framework presented in [7] uses wearable eye-trackers and their integrated scene cameras to provide 2D gaze information from one or more users. Concurrently, RGB-D cameras are used for real-time 3D reconstruction of the theatre environment. The Parallel Tracking and Mapping (PTAM) methodology [8] is employed to estimate the user's head pose within the reconstructed theatre. The pose is then used to map the 2D gaze information reported by the eye-tracker to a unique 3D fixation in the world frame-of-reference. For the work presented here, the framework is complemented by an articulated collaborative robotic arm, which is also co-registered with the reconstructed theatre environment. In a nutshell, depending on the required behaviour and a decision making procedure, the robot can perform tasks modulated by one or more users' 3D fixations and gaze behaviour (Figure 1).

Based on the eye-tracker's monocular scene camera, PTAM first generates a 3D keyframe and scaled map of the unknown environment. Then it updates the keyframe map and tracks the relative camera pose in parallel.

For eye-tracking, the SMI (SensoMotoric Instruments GmbH) glasses are used, with a stated accuracy of 0.5° of visual angle and a scene camera with a resolution of

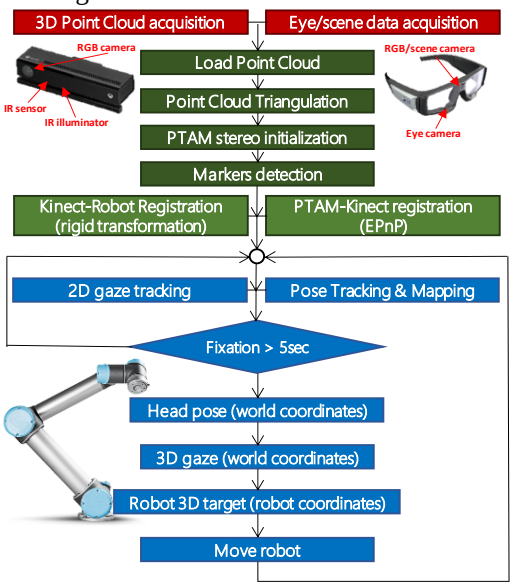

Figure. 1. The implementation consists of three main phases: data acquisition (in red), initialization (green), run-time (blue). PTAM is initialized by two keyframes. The first camera pose in PTAM coordinate system is estimated on the second keyframe, where we use 4 fiducial markers and EPnP [9] to estimate the real head pose (world coordinates) and then the transformation matrix between the two coordinate systems. Similar transformation matrix is estimated by the rigid transformation of the fiducial markers coordinates to register the RGB-D camera to the robot coordinate system. When the subject fixates for more than 5 sec, the head pose is transformed to world coordinates, the intersection of the 2D gaze vector with the triangulated point cloud provides the 3D fixation and the robot moves to these coordinates.

1280x960 pixels. For RGB-D sensing, the Microsoft Kinect 2 is used, with an RGB resolution of 1920x1080 pixels at 30Hz, 512x424 depth resolution with 70° (horizontal) and 60° (vertical) field of view, infrared sensor, time-of-flight technology and 30ms latency. The robot is a UR5 by Universal Robots, with 6 DOF, ±360° joint ranges, a reach radius of up to 850mm and payload of up to 5 kg.

EXPERIMENTAL SETUP

For the evaluation of our framework an experimental setup is used, including four fiducial markers (for the initialization phase) and three objects of different sizes (Figure 2). The task involves gazing in a random order at marked points on the objects. Four subjects, 2 males and 2 females, 25-60 years old, normal uncorrected vision, took part in the study. Off-line processing is performed and recorded 2D fixations are mapped to 3D. Fixations are transmitted to the robot if the dwell time is over 5sec. The robot then approaches the resolved 3D coordinates from above and according to the order of fixation, in a simulated gaze-guided manipulation task.

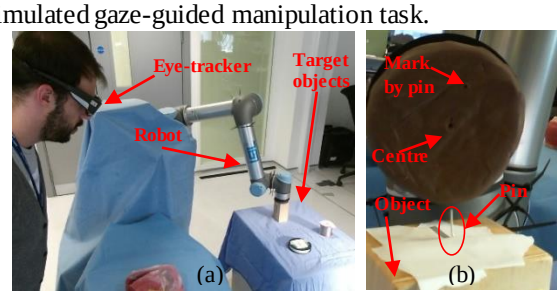

Figure. 2. (a) The experimental setup as seen from Kinect camera. (b) Plasticine used on the robotic tool for validation.

RESULTS

The accuracy of 3D fixation and gaze-guided manipulation task is evaluated. The error is calculated as the Euclidean distance between an object marker's actual coordinates and the respective recovered fixation coordinates. For task related error evaluation, a thick layer of plasticine is pasted on the robot end-effector. A thin pin is positioned on each of the three target objects. The distance from the centre and the depth of the pin imprint on the plasticine provides a measure of task accuracy.

The results summarized in Table 1 show the error averaged over all subjects. The 3D gaze error is 4.22cm and the gaze-guided task error is 4.20cm. While these values are expected identical and refer to theoretical and actual results respectively, a slight difference is caused by inaccurate robot to world registration.

Table 1: Mean error, std deviation and max. error for all subjects.

	Mean	SD	Upper
3D Gaze error (cm) (compounded by eye-tracking error)	4.22	0.37	4.56
Gaze-guided task error (cm)	4.20	0.39	4.51

DISCUSSION

A novel framework has been presented that allows gaze-driven interaction with an operating theatre environment and a collocated robotic manipulator. This is achieved by the combination of unrestricted wearable gaze-tracking, theatre 3D reconstruction and advanced computer vision concepts. The investigation supports our hypothesis that human vision can be used to achieve seamless and accurate collaboration between a surgeon and a table-side robot, but further studies are required for practical evaluation. The 3D gaze error is not uniformly distributed over the entire theatre as it depends on many parameters. Application specific considerations can be used for error minimisation. For instance, task accuracy is expected to improve with the integration of a robot force/torque sensor. Immediate work will focus on *safety, ergonomics, object and body recognition*, as well as *real-time* aspects. Further plans involve the implementation of *workflow segmentation* and *task-phase recognition* functionalities, based on the plurality of real-time data provided by the framework. *Context-awareness* will reveal a vast array of perceptual information and unlock new applications.

This work is supported by NIHR Imperial Biomedical Research Centre (BRC) award P61946. We would like to thank Mikael Sodergren for providing the eye-tracking hardware.

REFERENCES

[1] C. K. Christian, M. L. Gustafson, E. M. Roth, T. B. Sheridan, T. K. Gandhi, K. Dwyer, M. J. Zinner, and M. M. Dierks, "A prospective study of patient safety in the operating room," *Surgery*, vol. 139, no. 2, pp. 159–173, 2006.

[2] L. Lingard, S. Espin, S. Whyte, G. Regehr, G. R. Baker, R. Reznick, J. Bohnen, B. Orser, D. Doran, and E. Grober, "Communication failures in the operating room: an observational classification of recurrent types and effects.," *Qual. Saf. Health Care*, vol. 13, no. 5, pp. 330–4, 2004.

[3] J. Carthey, M. R. De Leval, D. J. Wright, V. T. Farewell, and J. T. Reason, "Behavioural markers of surgical excellence," *Saf. Sci.*, vol. 41, no. 5, pp. 409–425, 2003.

[4] J. P. Wachs, M. Jacob, Y.-T. Li, and G. Akingba, "Does a robotic scrub nurse improve economy of movements?," *Proc. SPIE - Int. Soc. Opt. Eng.*, vol. v 8316, p. 83160E, 2012.

[5] D. P. Noonan, G. P. Mylonas, A. Darzi, and G.-Z. Yang, "Gaze contingent articulated robot control for robot assisted minimally invasive surgery," *2008 IEEE/RSJ Int. Conf. Intell. Robot. Syst.*, pp. 1186–1191, 2008.

[6] A. S. A. Chetwood, K.-W. Kwok, L.-W. Sun, G. P. Mylonas, J. Clark, A. Darzi, and G.-Z. Yang, "Collaborative eye tracking - a potential training tool in laparoscopic surgery," *Surg. Endosc.*, vol. 26, no. 7, pp. 2003–2009, 2012.

[7] A. A. Kogkas, M. H. Sodergren, A. Darzi, and G. P. Mylonas, "Macro- and Micro-Scale 3D Gaze Tracking in the Operating Theatre," in *The Hamlyn Symposium on Medical Robotics 2016 (accepted for publication)*.

[8] G. Klein and D. Murray, "Parallel tracking and mapping for small AR workspaces," *2007 6th IEEE ACM Int. Symp. Mix. Augment. Reality, ISMAR*, 2007.

[9] V. Lepetit, F. Moreno-Noguer, and P. Fua, "EPnP: An Accurate O(n) Solution to the PnP Problem" *Int. J. Comput. Vis.*, vol. 81, no. 2, pp. 155–166, 2009.

Magnetically Actuated Surgical Laser Scanner for Endoscopic Applications

Alperen Acemoglu, Leonardo S. Mattos,

Department of Advanced Robotics, Istituto Italiano di Tecnologia, Genoa, Italy

(alperen.acemoglu, leonardo.mattos)@iit.it

INTRODUCTION

In today's practice, surgeons use free-beam laser systems for transoral resection of malignant tissue in the larynx. Free-beam lasers started to be used in laryngology in 1970's, when the CO_2 laser was first coupled to a microscope [1]. In these systems, the typical operating distance is 400 mm, which means the microscope and the laser control device are located that far from the surgical site. The surgical setup also includes a laryngoscope, a device that establishes and maintains a direct line of the sight to the larynx from the outside of the patient. The surgical laser is controlled by a micromanipulator attached to the microscope. This surgical setup is effective but suffers from significant limitations and controllability issues. In addition to the direct line of sight requirement, proper usage of the micromanipulator is highly dependent the dexterity and experience of the surgeon [2]. Given these limitations, the European project µRALP has recently focused on developing an endoscopic laser scanning system for robot-assisted surgeries, enabling the replacement of the micromanipulator with a laser control interface based on a graphics tablet [3].

Scanning lasers offer advantages such as high incision quality with minimum carbonization and thermal damage during soft tissue ablations. In free-beam systems, the scanning of the laser is performed with fast steering mirrors. However, the size of such mirrors and their actuators make the system large, restricting their application in endoscopic systems. On the other hand, micro-electro-mechanical-systems (MEMS) can actuate micro-mirrors to perform high speed scan. Different actuation mechanisms are used with MEMS, including electro-thermal [4], electro-static [5] and electro-magnetic [6]. Even though these systems can have diminutive mirror dimensions (around a few millimeters) and reach scanning angles up to 30°, they are typically too fragile for endoscopic surgical applications. As an alternative to steering mirrors, optical fibers can be used for direct laser manipulation. Researchers have shown that an optical fiber coated with magnetic material can be remotely controlled using electromagnetic fields for scanning applications [7].

Here, we continue our efforts to find alternative ways for fast and continuous scanning of the laser spot with reduced system dimensions. To this this end, we propose electromagnetic actuation to deflect an optical fiber carrying a permanent magnet. Two plano-convex lenses are used to collimate and focus the laser spot. An experimental setup is developed to manipulate the optical fiber and perform ablations with a 1940 nm diode laser. Ablations are performed on plaster blocks and apple samples. Results show that different ablations shapes could be executed and up to 1.5 mm deep incisions could be produced on apple samples using the new electromagnetic scanning tool.

MATERIALS AND METHODS

In Fig. 1, the experimental setup is depicted. It includes an optical fiber, electromagnetic coils, a permanent magnet, collimating and focusing lenses. The system's working principle is based on the interaction between electromagnetic fields created by the coils and the permanent magnet. As current is fed through two orthogonal coil pairs placed around the tool, a magnetic field is produced in the workspace. This generates a magnetic force on the permanent magnet, which deflects the tip of the optical fiber causing the displacement of the laser spot on the target. Altering the coil currents, any desired scan trajectory can be executed.

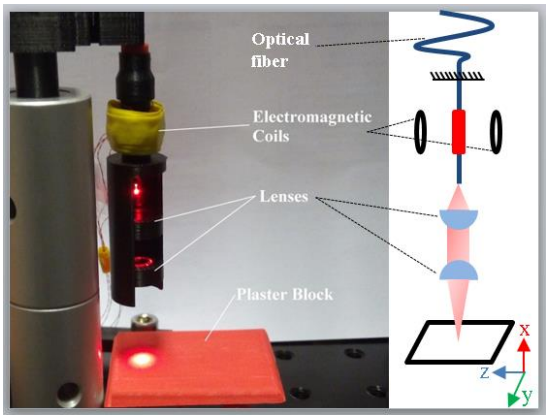

Fig. 1. Experimental setup with the electromagnetic scanning tool and plaster block as a target.

The magnetic scanning tool is coupled with a 1940 nm diode laser (Lumics, LuOcean P2) to demonstrate the ablation of different structures. The laser is connected to magnetic scanning tool using a 300 µm core multimode optical fiber (ThorLabs, FT300EMT).

Ablations were performed on the plaster blocks and apple samples for the preliminary evaluation of the system. Apple sample is chosen due to the high water content which makes it suitable target for diode lasers. In order to measure the ablation parameters, confocal images collected with a Leica SP5 microscope were processed with an extended depth of field algorithm [8]. These provide accurate depth maps of the ablation craters. Ablation depths were calculated by measuring and averaging the depth of 20 different cross sections in

the central region of the ablations. Cross sections were selected with 20 µm intervals.

The same current values are applied to the coils in the same axis. This enables maximum fiber optic bending along that axis. The current values can be presented as I_y and I_z for the coil pairs in **y**- and **z**- axis, respectively.

$$I_y = I_{\max} \sin(2\pi f t_1)$$

$$I_z = I_{\max} \sin(2\pi f t_2 + \varphi)$$

where I_{max} is the maximum current, f is the frequency and φ is phase angle. Changing the time scale (t_1/t_2) and phase angle, different trajectories can be executed.

RESULTS

The maximum scanning range of the new scanning tool was 2 mm x 2 mm at 30 mm distance from the target. In Fig. 2, the results of plaster block ablations are presented. Scan trajectories, in the shapes of 'W', 'Z', '8' and 'I', were executed on the plaster block. Ablations were performed with different laser scanning frequencies and similar results were observed.

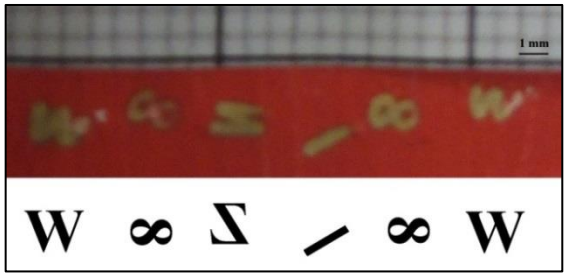

Fig. 2. Controlled ablations performed on plaster with 1940 nm diode laser. The different shapes show the magnetic scanning tool is create repeatable and precise scan trajectories.

Figure 3 shows the depth map of an ablation executed on the apple sample. For these samples, trials were performed using straight trajectories, laser power set to 2W, and 5 passes (repetitions). Average ablation depth for the sample presented in Fig. 3 was 1130 µm.

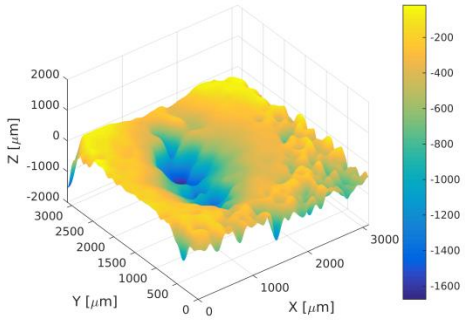

Fig. 3. Depth map of the ablation performed on apple sample.

CONCLUSION AND DISCUSSION

In this paper, we presented the first results of ablations performed on plaster and apple samples with 1940 nm diode laser and a new electromagnetic laser scanning tool. Ablations up to 1.5 mm deep could be executed on the apple sample, showing the system can successfully scan and focus the laser beam at a distant target.

The magnetic actuation provides stable and fast response. In scanning application for soft tissue surgeries, providing repetitions on the same path is crucial for the precision and usability of the tool. The electromagnetic laser scanning tool system is able to generate repeatable and precise scan trajectories, enabling scans with any required number of passes without diverging from the defined geometry.

As future work, the effects of the 1940 nm diode laser on different biological samples must be studied. In the literature, diode lasers with different wavelengths have become the focus of interest due to their advantages over free-beam lasers, which are now the standard for surgical applications in the head and neck regions. For example, researchers reported that the 980 nm diode laser is advantageous for healing wounds in oral surgery [9]. Additionally, they mention other intra and post-operative advantages, such as good coagulation properties for excision of the vascular tissues, bloodless operation, less or no pain [9].

This study creates an alternative approach for endoscopic scanning laser microsurgery, introducing an electromagnetically actuated scanning tool usable with any fiber-coupled surgical laser.

REFERENCES

[1] Strong, M. Stuart. "Laser excision of carcinoma of the larynx.", The Laryngoscope, 85.8 (1975): 1286-1289.

[2] L. S. Mattos, N. Deshpande, G. Barresi, L. Guastini and G. Peretti, A novel computerized surgeon machine interface for robot-assisted laser phonomicrosurgery, The Laryngoscope 124(8) (2014) 1887–1894.

[3] Mattos, L., Andreff, N., "The µRALP Project: New Technologies and Systems for Robot-Assisted Laser Phonomicrosurgery," 3rd Joint Workshop on New Technologies for Computer/Robot Assisted Surgery, DOI: 10.13140/RG.2.1.1346.9284, Verona, Italy, September, 2013

[4] Sun, Jingjing, et al. "3D in vivo optical coherence tomography based on a low-voltage, large-scan-range 2D MEMS mirror." Optics express 18.12 (2010): 12065-12075.

[5] Jung, Woonggyu, et al. "Three-dimensional endoscopic optical coherence tomography by use of a two-axis microelectromechanical scanning mirror." Applied physics letters 88.16 (2006): 163901.

[6] Yalcinkaya, Arda D., et al. "Two-axis electromagnetic microscanner for high resolution displays." Microelectromechanical Systems, Journal of 15.4 (2006): 786-794.

[7] Pandojirao-Sunkojirao, Praveen, et al. "A Magnetic Actuator for FiberOptic Applications." International Journal of Optomechatronics 3.3 (2009): 215-232.

[8] F. Aguet, D. Van De Ville and M. Unser, Modelbased 2.5-D deconvolution for extended depth of field in bright field microscopy, IEEE Transactions on Image Processing 17 (July 2008) 1144–1153.

[9] Romanos, George, and Georg-Hubertus Nentwig. "Diode laser (980 nm) in oral and maxillofacial surgical procedures: clinical observations based on clinical applications." Journal of clinical laser medicine & surgery 17.5 (1999): 193-197.

A Shape similarity framework for brain fibers classification based on Frénet Frame

M. De Piccoli, M. Capiluppi, P. Fiorini

Altair Robotics Lab, Department of Computer Science, University of Verona,

michela.depiccoli@univr.it

INTRODUCTION

Diffusion Tensor Imaging (DTI) is a structural magnetic resonance imaging (MRI) which provides a non-invasive way to explore organization and integrity of the white matter structures in the human brain. DTI information can be used in surgical planning and in the study of anatomical connectivity, brain changes and mental disorders. From DTI data, the white matter fiber tract can be reconstructed using a class of technique called tractography. The dataset derived by tractography is composed of a large number of streamlines, which are sequences of points in 3D space. To simplify the visualization and analysis of white matter fiber tracts obtained from DTI data, it is often necessary to group them into larger clusters or bundles [1]. In order to perform clustering, first a mathematical definition of fiber similarity (or more commonly a fiber distance) must be specified. Then, pairwise fiber distance may be calculated and used as input for a clustering algorithm [2]. The most common metrics used for distance measure only capture the local relationship between streamlines but not the global structure of the fiber. The global structure refers to the variability of the shape. Together, local and global information, define a good metric of similarity [3]. In order to provide such information, we are in the process of developing, summarized in Fig. 1, where both the local and the shape information are considered during the clustering.

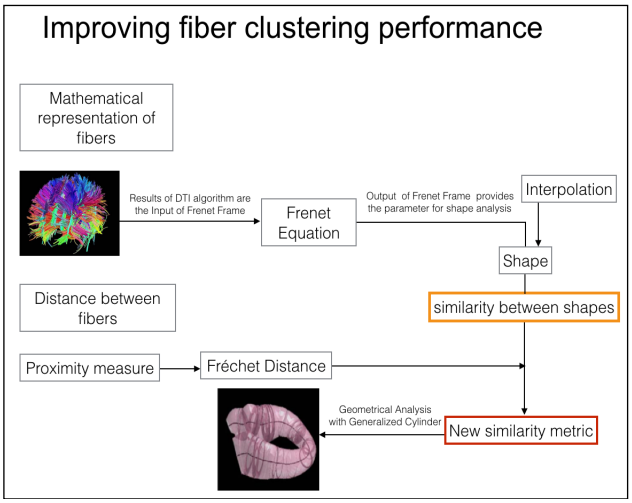

Fig. 1 Workflow.

Such workflow is based on the *mathematical representation* of the fiber obtained as a result of the *DTI algorithms*.

This mathematical representation is based on the study of the tract with the *Frénet equations*. The output of such study provides the parameters for the shape analysis, which, *interpolated*, gives a representation of the *shape* of the beam. This mathematical information is used for a first classification of the fibers based on the **similarity of the shape**. It is then applied to the study of the *measures of proximity* of the fibers through the *Fréchet distance*. This distance, together with the previous mathematical results, provides a new metric of similarity for the clustering, which is evaluated by analysing the geometric beam obtained.

In this paper we only focus on improving fiber-clustering performance for the *Mathematical representation.*

MATERIALS AND METHODS

Here we show the steps for: Fiber extraction and evaluation, Fiber study and Fiber classification.

1. Extraction of the fibers from DTI algorithms. The fibers refer to the arcuate fascicle in the clinical dataset of Fig. 2.

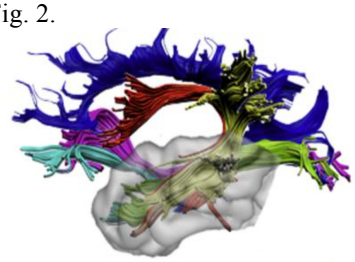

Fig. 2 Anatomical representation of the arcuate fascicle.

2. Interpolation and parameterization of the streamline. We identify the points candidates for the following two-step analysis:
   - correct matching between points on each streamline (with/without Distance Time Wrapping)
   - computation of the Frénet Frame for each point on the streamline and analysis of the parameters in Fig. 3.
3. Comparison of coefficients of the Frénet Frame
4. Finding a threshold index.

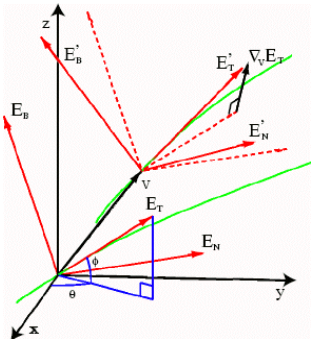

Fig. 3 A 3D streamline flow is represented as a frame field, locally tangent to the flow of the streamlines (green). The tangential component E_T of the frame is defined by orientation functions θ and ϕ with respect to a global coordinate system. A small translation of frame (E_T, E_N, E_B) along vector V results in a new frame (E'_T, E'_N, E'_B), rotated with respect to the original frame by angles θ and ϕ.

RESULTS

The results obtained in this study are summarized in the following figures.

To make the results more understandable, we extract few fibers. Some of them are spatially close to each other, while others are spatially distant from the group (Fig. 4).

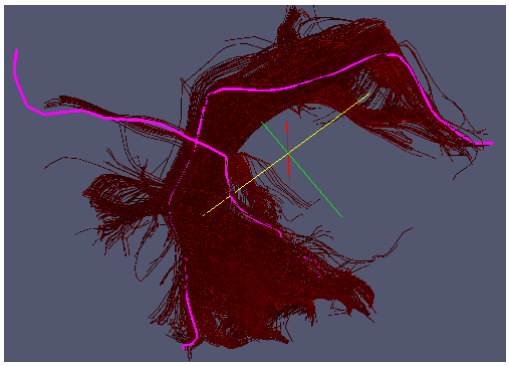

Fig. 4 The extraction of the fibers with ParaView software. The streamlines coloured in pink are the **eight** fibers (not distinguishable because spatially near) used for the analysis.

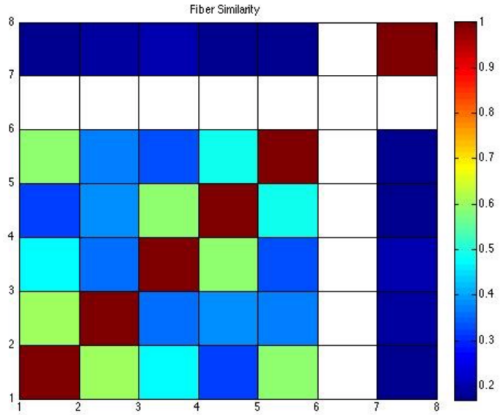

Fig. 5 Scheme that represents the similarity, based on the shape between each fiber. Red colour indicates the maximum match between fibers whereas blu colour indicates the minimum match between fibers. White colour represents the fiber that has a small length respect to the other fibers. This fiber is not considered.

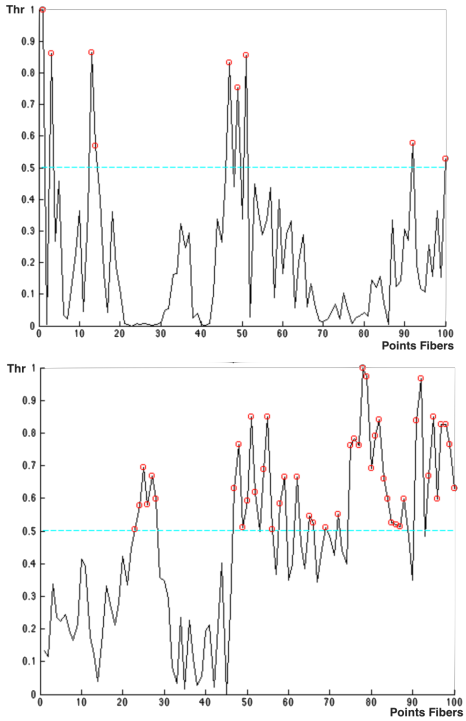

Fig. 6 In the top graph correspondence between two similar fibers, in the bottom one the correspondence between two fibers with different shape. In blue we represent the threshold and with red circles the selection points.

After this first analysis, we identify the fibers with similar shape. In Fig. 5 we can see the matrix of similarity between fibers and in Fig. 6 the analysis of two pairs of fibers. If two fibers are similar we have little points over the threshold line (Fig. 6 top), if two fibers are different we have many points over the threshold line (Fig. 6 bottom).

DISCUSSION

Enhance visualization of results of tractography is a challenging task in neuroimaging. The clustering algorithms can be helpful in this task. The performance of these algorithms depends on the similarity metrics between fibers. Future works include testing new distances to better understand the relationship between metrics and fiber clustering. We will exploit a free and open source software project for the analysis of data from diffusion magnetic resonance imaging experiments called Diffusion Imaging in Python (Dipy).

REFERENCES

[1] I. Corouge, G. Gerig, and S. Gouttard, “Towards a shape model of white matter fiber bundles using diffusion tensor mri”, in ISBI, 2004.

[2] S. T. Mai, S. Goebl, and C. Plant, “A Similarity Model and Segmentation Algorithm for White Matter Fiber Tracts”, in ICDM, 2012.

[3] Z. Ding, J. C. Gore, and A. W. Anderson, “Classification and quantification of neuronal fiber pathways using diffusion tensor MRI”, Magnetic Resonance in Medicine. 2003.

EndoVESPA: a computer-integrated robotic platform for magnetically-driven soft-tethered colonoscopy

G. Ciuti[1], D. Stoyanov[2], A. Arezzo[3], A. Koulaouzidis[4], S. Schostek[5], M. O. Schurr[5], B. Magnani[6], C. M. Oddo[1], A. Menciassi[1], and P. Dario[1]

[1]*The BioRobotics Institute, Scuola Superiore Sant'Anna, Pisa, Italy*

[2] *Department of Computer Science, University College London, UK*

[3]*Department of Surgical Disciplines, University of Torino, 10126 ITALY*

[4]*Endoscopy Unit, The Royal Infirmary of Edinburgh, Scotland, UK*

[5]*Ovesco Endoscopy AG, Tübingen, GERMANY*

[6]*Ekymed S.r.l., Livorno, 57014 ITALY*
g.ciuti@sssup.it

INTRODUCTION

Cancer is the leading cause of death worldwide (around 13% of all deaths), accounting for 7.6 million deaths in 2008. Moreover, death from cancer is projected to rise to over 13 million in 2030. Colorectal diseases and in particular colorectal cancer (CRC) represents the most significant pathology within the gastrointestinal (GI) tract affecting a large- number of people worldwide with a dramatic impact on healthcare systems. CRC is fourth in terms of incidence rate among all cancers in high income countries, accounting for 700.000 deaths worldwide in 2012. Nevertheless, the survival rate of CRC patients can reach 90% when diagnosis is made at an early stage falling to less than 7% for patients with advanced disease. For this reason, regular screening is highly recommended for patients older than 50 years or for those with a family history of CRC [1].

In 1868, Wolf and Schindler pioneered methodologies for inspecting the mucosa of the gastrointestinal (GI) tract with semi-flexible endoscopes, thus paving the way for the advent of current endoscopic procedures. To date, conventional colonoscopy is considered to be the most effective method for CRC diagnosis; it represents the gold standard for the evaluation of colonic disease due to its ability to visualize the inner surface of the colon, acquire biopsies, and treat the vast majority of polypoid lesions. However, take–up of screening colonoscopy is limited due to a variety of factors including invasiveness, patient discomfort, fear of pain, and the need for sedation. The technology behind standard optical colonoscopy basically consists of a long semi rigid tube with a steerable head, which is relatively stiff compared with the compliant nature of the colon; as a result of this "back-wheel drive" approach, looping occurs during insertion leading to pain and potential tissue damage or even perforation (0.1-0.3% for diagnostic procedures in colonic tissue) [2].

Capsule endoscopy (CE), established in the last decade, is considered an example of disruptive technology since it represents an appealing alternative to traditional diagnostic techniques. This technology, in its current clinical application, enables inspection of the digestive system (from the oesophagus to colon with different versions of capsules) without discomfort or need for sedation, thus preventing the risks of conventional endoscopy. Hence, it has the potential of encouraging patients to undergo GI tract examinations. However, currently available products are passive devices whose locomotion is driven by natural peristalsis, with potential drawback of failing to capture the images of important GI tract regions (mainly in the colonic tract where the lumen is largely collapsed on the camera capsule), since the doctor is unable to control the capsule's motion and orientation [3].

Robotics and computer-integrated technologies, in this application, holds the power to be the key solution for overcoming such drawbacks (*i.e.*, active and controlled locomotion), thus fulfilling the expectations of physicians for a new generation of active robotic systems for painless colonoscopy. Active wireless capsule devices and smart flexible robotic colonoscopes have been developed and are under investigation by several companies and research groups [4]. However, the lack of both diagnostic and therapeutic functionalities (mainly in wireless active capsule endoscopes) and, in some cases, the significant dimension of the system (mainly for the smart flexible endoscopes), lead to a low effectiveness and acceptability in the clinical practice. On the other hand, having a "front-wheel" magnetic-based steering and propulsion method, combined with a flexible thin tether (limited to the operating and washing channels and electric connectivity), would enable a drastic reduction of the dimension of the endoscopic system, still maintaining both diagnostic and therapeutic functionalities.

ENDOVESPA PROJECT OVERVIEW

In this framework, the EndoVESPA (Endoscopic Versatile robotic guidancE, diagnoSis and theraPy of magnetic-driven soft-tethered endoluminAl robots) Horizon2020 European project (www.endovespa.eu) aims to develop an active colonoscopic platform for robotic guidance of a painless, innovative, smart, and

soft–tethered device, in order to achieve accurate and reliable diagnosis and therapy of premalignant polyps and / or colonic pathologies.

The EndoVESPA system is featured as a novel and high impact colonoscopy platform: closed-loop magnetic navigation, enhanced diagnosis and therapy will be embedded into the EndoVESPA system to eradicate most of the limitations and drawbacks of current colonoscopy in terms of: *i)* discomfort for the patient, *ii)* dependence on medical doctor advanced skills, and *iii)* cost for the healthcare system. Navigation, diagnosis, therapy modules and safety strategies for interaction / cooperation will represent the main components of the colonoscopic platform, which will allow for a magnetic actuated and painless colonoscopic medical procedure. With regards to navigation, an on–line magnetic–based locomotion and localization control of the device would represent the approach for guaranteeing intraoperative navigation of the soft-tethered colonoscope with the aim of implementing a painless robotic colonoscopic platform. A magnetic-based localization method will be implemented and embedded in the platform for localizing the soft–tethered colonoscope and maintaining a closed–loop control of the optimal magnetic link with the external magnetic sources (driven by a master robotic manipulator). An image-based stereoscopic high-definition system will be integrated and exploited for reconstructing and mapping deformable surrounding environment and for supporting accurate closed-loop guidance, while a robust and reliable magnetic link between the external master robot and the internal slave colonoscope is maintained. Moreover, optical image enhancement technologies will be integrated onto the device for the purpose of a reliable and accurate diagnosis; in a one–shot procedure the EndoVESPA system will be able to achieve effective diagnosis and perform a focused and painless intervention.

A CAD representation of the advanced device, proposed with the EndoVESPA project, compared to the current development [5], is represented in Fig. 1. As indicated in Fig. 1 on the left, the EndoVESPA platform will be composed of a robotic manipulator (holding the external magnet for closed-loop control of the device) controlled through a human-machine interface by the operator.

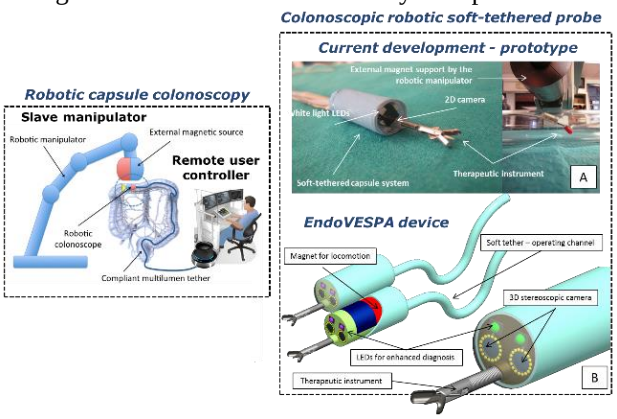

Figure. 1. (Left): general representation of the robotic platform. (Right) (A) Current and (B) innovative colonoscopic system (*i.e.*, EndoVESPA device).

CONCLUSION AND DISCUSSION

The ascertained acceptance of robotics in the medical theatre, as well as the mature implementation of computer–integrated technologies, represent the natural ingredients for the industrial–oriented development of the EndoVESPA platform. In this framework, robotics and computer science methodologies can provide dramatic benefits to the colonoscopy medical scenario, making EndoVESPA a mainstream solution for current needs in colonoscopy. EndoVESPA will allow a truly life-saving procedure for all, with the advantages of: *i)* a painless procedure and a high acceptance by patients for preventive mass screening; *ii)* ease of performing (due to robotic teleoperated guidance, diagnosis and therapy and embedded control capabilities); *iii)* reduction of required skills and thus standardization of procedure; and *iv)* a tremendous social benefit and reduced costs for the public healthcare systems.

The merging of navigation, high-effective diagnosis and targeted therapeutic strategies, enhanced emergence algorithms and human machine interface will lead to the development of a disruptive system for painless robotic colonoscopy. The EndoVESPA colonoscopic methodology arises as almost a natural progression of current colonoscopy platforms, towards clinical improvements. Thanks to the presence in the EndoVESPA Consortium of top–level academic, industrial and clinical partners in the field of robotics and computer science systems, and thanks to the expertise and background in robotic endoscopy of the coordinator and partners, the project objectives (*i.e.*, development of a reliable medical device for widely accepted, painless colonoscopy) will be fully achievable within the project lifetime with a real focus on developing an industrial medical product.

ACKNOWLEDGEMENTS

The research leading to these results has received funding from the European Community's Horizon 2020 Programme (H2020/2014-2020) under Grant Agreement num. 688592 (EndoVESPA Project). The authors wish to thank all the EndoVESPA members.

REFERENCES

[1] Cancer Research UK: www.cancerresearchuk.org

[2] Koulaouzidis A, Iakovidis DK, Karargyris A, Rondonotti E. “Wireless endoscopy in 2020: Will it still be a capsule?”, World Journal of Gastroenterology, 2015 21(17):5119–5130.

[3] Iddan G, Meron G, Glukhovsky A, Swain P. “Wireless capsule endoscopy”, Nature 405:417

[4] Sliker L, Ciuti G. “Flexible and capsule endoscopy for screening, diagnosis and treatment”, Expert review of medical devices, 2014 11(6):649-666.

[5] Valdastri P, Ciuti G, Verbeni A, Menciassi A, Dario P, Arezzo A, and Morino M. “Magnetic air capsule robotic system: proof of concept of a novel approach for painless colonoscopy”, Surgical endoscopy, 2’12 26(5):1238-1246.

Validating convolution neural networks for automatic polyp detection in robotic colonoscopy

P. Brandao[1], E. Mazomenos[1], G. Ciuti[2], F. Bianchi[2], Menciassi[2], P. Dario[2], A. Koulaouzidis[3], D. Stoyanov[1]

[1]*Centre for Medical Image Computing, University College London*
[2] *The BioRobotics Institute, Scuola Superiore Sant'Anna*
[3] *Endoscopy Unit, The Royal Infirmary of Edinburgh*

INTRODUCTION

Colorectal cancer (CRC) is the most frequent malignancy of the gastrointestinal tract and accounts for nearly 10% of all forms of cancer [1]. The survival rate of CRC patients is lower than 7% when the disease reaches an advanced stage, however, in cases of early diagnosis, with successful treatment, it increases to almost 90% [1]. Even though conventional colonoscopy is considered the most effective method for CRC screening and diagnosis, invasiveness, patient discomfort and fear of pain can lead to patient reluctance towards the examination [1,2]. Robotic endoscopic capsules and endoscopes can potentially overcome the drawbacks of pain and discomfort while still facilitating full movement control to the clinician on order to observe the entire endoluminal colonic wall [1].

In any kind of colonoscopy, the success of the exam highly depends on the operator's skills, as a high level of hand-eye coordination is required to examine the majority of the colon wall [1]. In 2012, Leufkens *et al.* reported that missed polyp detection rates in colonoscopy screenings could reach values as high as 25% [3]. One effective way to increase this detection rate is the incorporation of computer-aided diagnostic systems [1].

In this study, we propose an automatic polyp detection system using a deep learning framework that can aid clinicians to detect polyps more accurately in colorectal exams. This approach can be effective in helping endoscopists to detect high risk regions and can additionally be used to reduce observation times for capsule endoscopy (CE) procedures. To our knowledge, this is the first work to apply convolution neural networks (CNNs) for polyp detection in CE images.

MATERIALS AND METHODS

As a preliminary study, we evaluated the ability of the method to detect polyp-like structures in images of a colon phantom obtained from a robotically controlled endoscopic capsule. In this section we describe the experimental setup, the data used and the learning strategies adopted.

Experimental Setup

Our experimental setup comprised a PillCam™ SB3 capsule (Given Imaging, Yokneam, IL), shown in Figure. 1 a), attached to a plastic rigid rod that was controlled by an industrial anthropomorphic robotic arm (Mitsubishi RV-3SB robot, Tokyo, JP - Figure. 1 b)).

**The research leading to these results has received funding from the European Community's Horizon 2020 Programme (H2020/2014-2020) under Grant Agreement num. 688592 (EndoVESPA Project).*

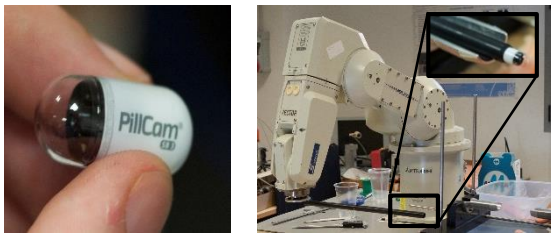

(a) **(b)**

Figure. 1. (a) PillCam™ SB 3 model; (b) Endoscopic capsule and plastic rigid rod attached to an industrial anthropomorphic robotic arm.

Figure. 2 a) shows the deformable and impermeable colon phantom used in this study (Lifelike Biotissue Inc, Ontario, CAN). During tests small coloured pins were inserted along the phantom track to emulate polyps, as shown in Figure. 2 b).

(a) **(b)**

Figure. 2. a) External view of the colon phantom; b) View of the opened phantom with the circular pins attached.

The study was conducted by inserting the capsule, with its camera end facing forward, into the phantom. To emulate a real colon exam, the robotic arm moved the camera horizontally throughout the track of the phantom and back. This procedure was repeated multiple times and all data was wirelessly recorded using Given Imaging software.

Dataset

From the video, containing several forward and backward sweeps of the phantom, 100 frames were randomly selected and extracted. Every visible pin was manually segmented and the data was randomly divided into same size training and testing datasets.

Fully Convolution Neural Network

Motivated by the success reported in general recognition tasks [4,5], we decided to apply CNNs for polyp detection. Even though CNNs are usually formulated to solve classification problems, some approaches were able to use CNNs for dense prediction by labelling each

pixel with the class of its enclosing object. This is usually achieved by post-processing super-pixel projection, multi-scale approaches or patch-wise training. In this study, we use the 8-strided variant of the VGG net proposed by Long *et al.*, where dense prediction is obtained by in-network deconvolution layers that are also learned during training [6][6]. This results in a very fast and effective upsampling that achieved state-of-the-art in semantic segmentation of the PASCAL VOC dataset [5]. Training a deep network from raw data is not practical considering the time and computational power required. In addition, it may not capture the full image complexity of the scene. Because of this, we fine-tune pre-trained layers on the ImageNet dataset [4] by backpropagation using our training data. The last fully connected layer of the CNN was replaced with a binary classification layer. Training was done iteratively by SGD with momentum using a batch size of 50 images and fixed learning rates of 10^{-11}. Due to memory constrains, all images were resized to 180×180 pixels. All processing was done using Caffe [7] in a NVIDIA Quadro K4000 GPU.

RESULTS

We evaluate the prediction results in three separate points during training. The resultant binary segmentations of each network were used to calculate the performance metrics on the testing dataset. Precision and recall results are presented in Table 1.

Table 1. Average pixel-wise precision and recall of the networks in the testing dataset during different training stages. fCNN-800, fCNN-900 and fCNN-1000 represents the network after 800, 900 and 1000 training iterations, respectively

Network	Precision	Recall
fCNN-800	0.55	0.95
fCNN-900	0.77	0.84
fCNN-1000	0.59	0.95

Figure. 3, illustrates the segmentation output of the networks for the same image.

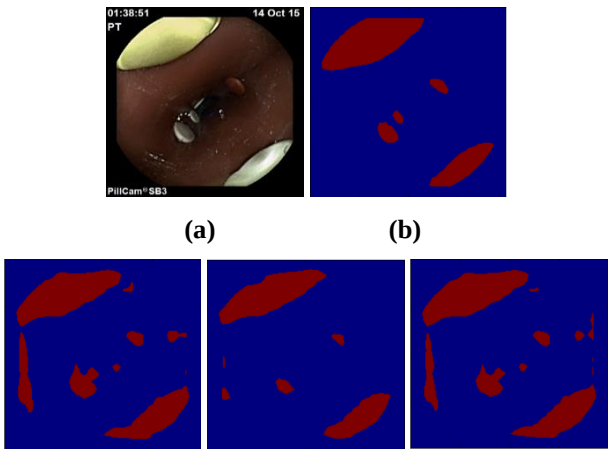

Figure. 3. (a) Example of a testing image; (b) Manual segmentation of the pins; (c), (d) and (e) binary segmentations produce by fCNN-800, fCNN-900 and fCNN-1000, respectively.

CONCLUSION AND DISCUSSION

The best polyp segmentation results were obtained by fCNN-900, with a precision and recall of 0.77 and 0.84, respectively. In the earlier training iteration, fCNN-800 has not converged to the best possible solution yet and the prediction results are less accurate. As we continue training, the fCNN-1000 starts to overfit to the training data, and inference ability is lost. The same principle is supported by Figure. 3, where the segmentation of fCNN-900 outperforms the others.

Figure. 3 d) shows that the method slightly underperforms in segmenting smaller pins compared to larger ones. This is expected, as the dense prediction is obtained from the deconvolution upsampling layer, where the minimum resolution is limited by the adopted stride. This effect could be minimized by using a GPU with more memory, which would not impose downscaling of the input images. Furthermore, the considerable amount of false positives suggests that the model struggles to classify small variations in the background. These can easily be corrected with the use of more training data.

In conclusion, we were able to successfully employ CNNs to automatically segment polyp-like structures in images from a robotically controlled endoscopic capsule. Even with a limited amount of training data and GPU memory, the method performs well, which is promising for translation into the clinical setting. Future work involves verifying our results to colonoscopy data using the large datasets available from the 2015 MICCAI sub-challenge on automatic polyp detection [8] and to data from real CE examinations.

REFERENCES

[1] G. Ciuti, R. Caliò, D. Camboni, et al., "Frontiers of robotic endoscopic capsules: a review," *J. Micro-Bio Robot.*, pp. 1–18, May 2016.

[2] W. C. Leung, D. C. Foo, T. Chan, et al., "Alternatives to colonoscopy for population-wide colorectal cancer screening," *Hong Kong Med. J.*, Jan. 2016.

[3] A. M. Leufkens, M. G. H. Van Oijen, F. P. Vleggaar, and P. D. Siersema, "Factors influencing the miss rate of polyps in a back-to-back colonoscopy study," *Endoscopy*, vol. 44, no. 5, pp. 470–475, 2012.

[4] O. Russakovsky, J. Deng, H. Su, , et al., "ImageNet Large Scale Visual Recognition Challenge," *Int. J. Comput. Vis.*, vol. 115, no. 3, pp. 211–252, 2015.

[5] M. Everingham, S. M. A. Eslami, L. Van Gool, C. K. I. Williams, J. Winn, and A. Zisserman, "The Pascal Visual Object Classes Challenge: A Retrospective," *Int. J. Comput. Vis.*, vol. 111, no. 1, pp. 98–136, 2014.

[6] J. Long, E. Shelhamer, and T. Darrell, "Fully convolutional networks for semantic segmentation," in *CVPR*, 2015, vol. 07–12-June, pp. 3431–3440.

[7] Y. Jia, E. Shelhamer, J. Donahue, , et al. "Caffe: Convolutional Architecture for Fast Feature Embedding," *Proc. ACM Int. Conf. Multimed.*, 2014.

[8] A. Bernal, J., Tajkbaksh, N., Sánchez, F.J., Liang, J., Chen H., Yu, L., Angermann, Q., Romain, et al., "Comparative Validation of Polyp Detection Methods in Video Colonoscopy: Results from the MICCAI 2015 Endoscopic Vision Challenge," *IEEE Trans. Med. Imaging*, 2016.

Soft endoscopic camera system for robotic surgery: a dVRK implementation

Haider Abidi[1], Matteo Cianchetti[1], Margherita Brancadoro[1], Alessandro Diodato[1], Giacomo De Rossi[2], Diego Dall'Alba[2], Riccardo Muradore[2], Gastone Ciuti[1], Paolo Fiorini[2], Arianna Menciassi[1]

[1]*The BioRobotics Institute – Scuola Superiore Sant'Anna, Pisa, Italy*

[2]*Altair Robotics Lab. – Department of Computer Science, University of Verona, Verona, Italy*
s.abidi@sssup.it

INTRODUCTION

Surgical robotics systems are trending towards combining the advantages of Minimally Invasive Surgery (MIS) with the precision and dexterity provided by robotic systems. The goal of the development of robotic tools for surgery is to reduce trauma and improve recovery times for the patients. This however should not compromise surgeon's ability to work. The daVinci Surgical System is one of the most known surgical robots used. With its articulated arms and end effectors, it provides improved dexterity compared to standard MIS surgical tools. However even with this superior dexterity, safe navigation and maneuverability in the confined spaces typical to MIS remains an open question. Such questions can be tackled with the use of soft robotics technology [1]. Not only do soft robots provide improved maneuverability and thus have a larger work space, but they are also safe due to their inherent softness and compliance. The use of rigid and soft instruments side by side could complement each other and create a synergy where one overcomes the limitations of the other. With this synergy in mind, this paper demonstrates the integration of a soft robotic arm with the standard daVinci rigid arms. Potential advantages of such a merger are also demonstrated.

A three arms daVinci Research Kit (dVRK) was used for the integration. The endoscopic camera manipulator (ECM) arm, which normally carries the rigid daVinci Endoscope Camera, is replaced by a soft manipulator.

The soft manipulator is a bioinspired surgical device composed of two silicone modules, each consisting of three equally spaced longitudinal fluidic chambers. This arrangement of chambers spaced at 120° allows elongation and omnidirectional bending [2]. Actuation is realised through pneumatic pressures, supplied by a circuit of valves which manages the pressure supplied to the chambers of each module. By controlling the supplied pressures, the arms may be manoeuvered according to the user requirements. The modules have a free lumen to allow the insertion of a miniaturized camera at the end-effector.

Since the soft robotic arm is actuated by pneumatic pressure, an interface between the dVRK and the soft robotic arm was also developed. The integration thus made it possible to control the soft arm using the dVRK Master Arms. Figure 1 shows the integration scheme.

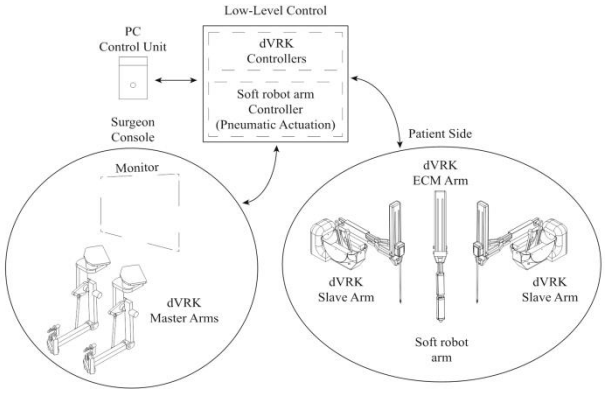

Figure. 1. Scheme of the integrated hardware system with dVRK and soft manipulator

MATERIALS AND METHODS

The integration consisted of two segments. One part was the mechanical interface the soft robotic arm with the dVRK, and the second was the integration on the software level. The aim was to develop an easy interface that does not alter the normal functions of the dVRK system.

Hardware integration.

The design of the soft robotic arm facilitated the hardware integration. The soft arm is mounted on a cylindrical rigid link that is used to position the soft robot to a desired position. An additional 3D printed adaptor was used to attach this rigid link to the daVinci ECM arm.

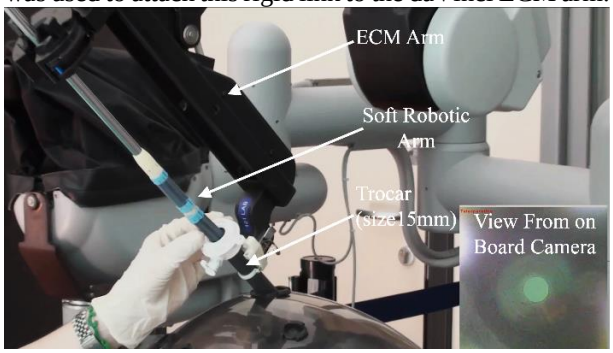

Figure. 2. Setup of the dVRK and Soft Arm. Inset picture shows the view from the on board camera

The manipulator diameter is small enough to allow insertion through a traditional 15 mm trocar port, hence

once the soft arm was mounted, no further alterations were necessary. The setup is shown in Figure 2.

Software integration. The different control phases of the complete system were modelled with a hybrid finite state machine shown in Figure 3a. Transitions between states are triggered by the user through foot pedals and by the control architecture through asynchronous events. Thus the user may switch between controlling the dVRK slave arms or the Soft Robotic arm mounted on the ECM. The ECM arm of the dVRK and the Soft Robotic Arm can be simultaneously controlled thanks to the software integration. The current state of the system is also shown to the user through the endoscope video stream, similar to Figure 3.

Teleoperation of the soft robot arm is achieved by mapping the Cartesian position of the right master manipulator into the first three ECM joints. The fourth joint of the ECM arm is controlled based on the master wrist roll. As this mapping is established, the soft modules are actuated by generating a map of chamber pressurizations from the orientation of the daVinci master arms. The generation of this mapping may be understood by considering the Z_b-axis of the Master Arms as a joy stick (Figure 3b). The magnitude of its motion, represented by the angle subtended between the base frame Z_b-axis and the displaced Z_g-axis, is mapped as the pressure level. The direction in which this motion was made, represented by the projection of the Z_g-axis on the base frame X-Y plane, dictates which chambers are to be pressurized.

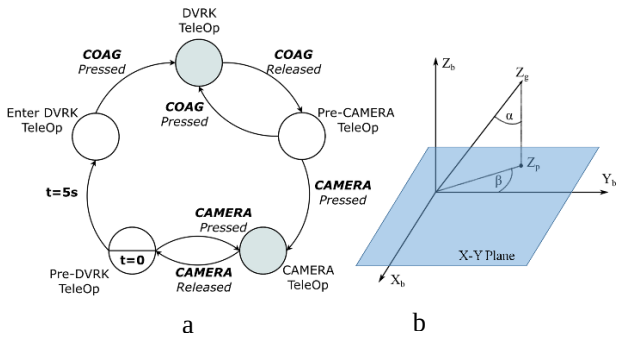

a b

Figure. 3. a) Hybrid state machine controlling the interaction process of the integrated system **b)** Pressure map generation scheme

RESULTS

A soft robotic arm was successfully incorporated with the dVRK platform. The integration which was on a hardware and software level was able to increase the workspace of the dVRK arms. A preliminary qualitative assessment was also carried out highlighting the infinite degrees of freedom of the soft arms compared to the rigid dVRK slave arms. The merger of the technology makes it possible to access difficult to reach areas, and is shown to improve the viewpoint available to the operator in a user friendly manner. The combination of this flexible camera system with the standard daVinci endo-wrist surgical tools can be useful in complex surgical procedures, and will not carry additional safety risks for the patient. It is envisioned that the integration would also help reduce stress for the surgeon [3] since anatomical areas with limited accessibility can be negotiated without fear of damage to the sensitive environment.

CONCLUSION AND DISCUSSION

To the best of the authors' knowledge this is the first time a soft surgical robot has successfully been integrated with the dVRK. An addition of a multi role soft robotic arm could increase the capabilities of the daVinci Surgical System. The soft arm, which houses a camera module in its lumen, can carry any other tool (*e.g.* gripper and cautery dissector) or be used as a channel. The integration results in a very intuitive control of the soft robotic arm, with the motions of the dVRK master arms mimicked by the soft arm. The mapping of the master console movements is similar to the mapping used for the standard daVinci endoscopic camera. It is thus expected to have minimal effect on training time and effort. The soft endoscopic arm not only improves the viewing angles, but also enables multiple viewpoints of the surgical target (Figure 4). Future work will focus on the evaluation of the proposed system in more realistic conditions and to integrate a stereo camera system to improve the image quality.

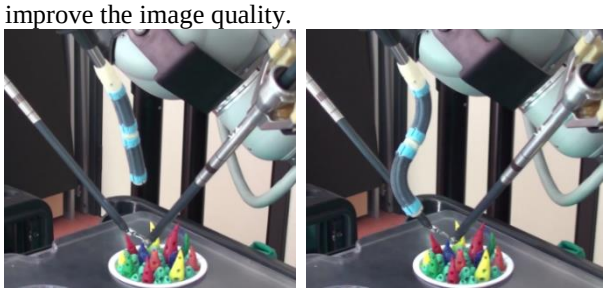

Figure. 4. Two different configurations of the soft manipulator providing a different view angle of the same scene

REFERENCES

[1] M Cianchetti, T Ranzani, G Gerboni, T Nanayakkara, K Althoefer, P Dasgupta, A Menciassi. "Soft robotics technologies to address shortcomings in today's minimally invasive surgery: the STIFF-FLOP approach." Soft Robotics; 2014; 1(2) 122-131.

[2] T Ranzani, M Cianchetti, G Gerboni, I De Falco, A Menciassi. "A Soft Modular Manipulator for Minimally Invasive Surgery: Design and Characterization of a Single Module." IEEE Transactions on Robotics; 2016; 32(1), 187-200.

[3] A Shafti, F Andorno, N Marchese, S Arolfo, A Aydin, O Elhage, Y Noh, H A Wurdemann, A Arezzo, P Dasgupta, KAlthoefer. "Benchmarking of Comfort and Learnability of a New Soft Robotic Tool for Key-hole Surgery". Joint Workshop on New Technologies for Computer/Robot Assisted Surgery (CRAS); 2015

Design and Prototyping of a Robotic Assistant For Microsurgery

L. Vanthournhout[1], B. Herman[1], J. Szewczyk[2], B. Lengelé[3], and B. Raucent[1]

[1]*Institute of Mechanics, Materials, and Civil Engineering and the Louvain Bionics, Université catholique de Louvain, lena.vanthournhout@uclouvain.be.*

[2]*Institute for Intelligent Systems and Robotics, Université Pierre et Marie Curie Paris 06 – CNRS.*

[3]*Morphology Research Group, Institute of Experimental and Clinical Research, Université catholique de Louvain, and the Department of Plastic and Reconstructive Surgery, Cliniques universitaires Saint-Luc.*

INTRODUCTION

Microanastomosis is a surgical gesture that consists in connecting two tiny blood vessels together with a series of stitches (see Figure 1). This gesture is used in many operations such as face allograft, torn member saving or breast reconstruction by DIEP (Deep Inferior Epigastric Perforator). It requires high dexterity and accuracy, and only few microsurgeons are able to perform such challenging gestures on vessels with sub-millimetric diameter. This is due to the tremor magnitude that, even for a skilled microsurgeon, rarely decreases below 100 µm with a frequency ranging from 6 to 15 Hz [1].

Figure. 1. Microanastomosis – Operating field during microsurgery.

In order to increase microsurgeon's accuracy, it is quite obvious to think of robotics. Several solutions use teleoperation for reducing the tremor magnitude, by filtering and scaling motions of the master interface while offering similar dexterity as the human hand, required for complex movements. Examples of telesurgery systems used in microsurgery include the Da Vinci, RAMS, MSR or a neurosurgery robotic platform from Tokyo University (references can be found in [2]). However, if these systems increase the surgeon's precision, they also induce a longer operation duration by slowing down the movements. But time is an important factor to reduce ischemia time of the tissue and prevent necrosis. The aforementioned systems only offer a fixed or a manually adjustable scaling ratio that is usually set as a compromise between speed (low ratio) and accuracy (high ratio).

This paper introduces the design of a first prototype of a teleloperated robot devoted to microsurgical gestures. Firstly, the needs analysis is summarized and the robot topology selection is explained. Optimization of the robot geometric parameters is then presented, so that it matches the specifications under several important constraints. Finally, the first prototype is described. Our final goal is to use this prototype in the near future to implement and compare several control schemes capable of (semi-) autonomously adjusting the motion reduction factor during gestures.

ROBOT SPECIFICATIONS AND TOPOLOGY

In order to quantify the required workspace, velocity, and acceleration of the slave robot, surgeons' movements study were recorded while performing dissection and microanastomosis on a rat. The procedure and the results are reported in minute details in [3] and [2]. The specifications are summarized in Table I.

	Workspace	Velocity	Acceleration
Translation	40x50x40 mm	100 mm/s	1000 mm/s²
Own rotation	> 360 °	74 °/s	520 °/s²
Transversal rotation		28 °/s	240 °/s²

Table. I. Robot Specification.

The robot topology was chosen subsequently to decouple translations from rotations. Indeed, if the positioning accuracy must be high (~10 µm) to achieve good quality anastomoses, the orientation accuracy does not need to be better than with a human hand. The robot is therefore made of 3 orthogonal linear axes followed by a spherical wrist allowing the tool orientation (see Figure 2).

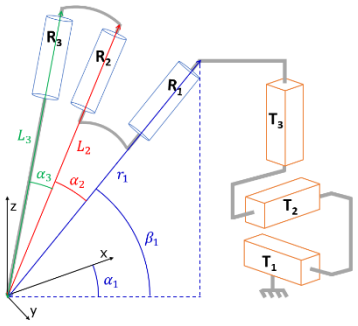

Figure. 2. Robot topology and geometric parameters of the spherical wrist to be optimized.

GEOMETRIC PARAMETERS OPTIMISATION

In order to make the robot fit at best the requirements and also the surgical context, an optimization procedure was performed to compute the best values for the 7 parameters of the spherical wrist (see Figure 2). The optimization algorithm systematically explores all the feasible geometric solutions by varying each parameter (see Figure 3B). Each solution is then evaluated with respect to three constraints and two objectives described in Figure 3A. Pareto front of the best solutions is depicted in Figure 3C. The chosen solution corresponds to good balance between a dexterity of 0.14 and a minimal distance to environment of 28.7 mm. Indeed, it is important that the robot remains far from microscope and patient to avoid any collision if the expected environment is slightly modified, and also to take into account the volume of motors and mechanical structure. A good dexterity is also required to reach all directions with the specified instrument velocity and acceleration without too high jumps in velocity and acceleration at motors.

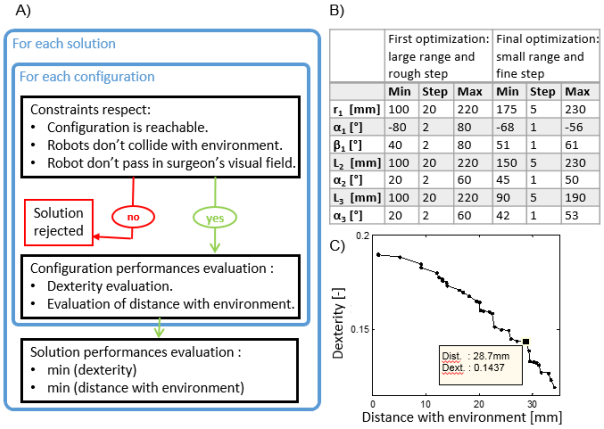

	First optimization: large range and rough step			Final optimization: small range and fine step		
	Min	Step	Max	Min	Step	Max
r_1 [mm]	100	20	220	175	5	230
α_1 [°]	-80	2	80	-68	1	-56
β_1 [°]	40	2	80	51	1	61
L_2 [mm]	100	20	220	150	5	230
α_2 [°]	20	2	60	45	1	50
L_3 [mm]	100	20	220	90	5	190
α_3 [°]	20	2	60	42	1	53

Figure. 3. Optimization scheme and results.

PROTOTYPE DESIGN

Based on these optimization results, a prototype was designed and built. The Cartesian table consists of 3 linear axes (Newport M-ILS100CC) with a stroke of 100 mm and a resolution of 1 µm. The first spherical wrist axis actuated by a DC-motor (Faulhaber 2657 W012 CR) with a planetary gearbox (26/1 S, 23:1), mounted perpendicularly to the R1 axis by means of a helical gear. On the main R1 shaft is mounted a high resolution encoder (7500 pulses/rev.). Axes R2 and R3 are made of DC motors (Faulhaber 2232 U012 SR and 1224 E 012 SR) with backlash-free planetary gearbox (22/5 69.2:1 and 12/5 69:2). Both motors are equipped with encoders (1024 and 100 pulses/rev.) and aligned with the R2 and R3 axes respectively, allowing to know the wrist orientation with the required precision. Indeed, this precision is needed to counterbalance by software the possible fabrication inaccuracies and play in the spherical wrist that could induce an unwanted linear movement. Finally the robot is controlled with a 6 DOF joystick (Phantom Omni) through a computer running on Linux and interfaced with a Technosoft control board. A picture of the current system robot is shown in Figure 4.

Figure. 4. Prototype.

FUTURE WORK

The mechanical performances of the prototype are currently being assessed. The geometric model of the robot will then be calibrated to take into account mechanical inaccuracies. A symmetrical prototype will then be built for bimanual telemanipulation. Finally, future work will be devoted to the implementation and comparison of specific teleoperation schemes, aiming at overcoming the traditional opposition between gesture accuracy and speed of motion thanks to adaptive strategies for adjusting the scaling factor in real time.

ACKNOWLEDGEMENT

This work was supported by own funds from UCL and ISIR, and by the F.R.S.-FNRS. Authors are grateful to Jérôme Dusit, François Château, and all members of microsurgery teams of Cliniques universitaires Saint-Luc who took part in discussions and experiments. Authors would like to thank all colleagues from the CEREM and ISIR for their help and support in this project.

REFERENCES

[1] K. Veluvolu and W. Ang, "Estimation and filtering of physiological tremor for real-time compensation in surgical robotics applications," The International Journal of Medical Robotics and Computer Assisted Surgery, 2010; 6(3):334–342.

[2] L. Vanthournhout, B. Herman, J. Duisit, F. Chateau, J. Szewczyk, B. Lengele, and B. Raucent, "Requirements analysis and preliminary design of a robotic assistant for reconstructive microsurgery," in Proceedings of the 37th Annual International Conference of the IEEE Engineering in Medicine and Biology Society (EMBC), 2015:4926–4930.

[3] L. Vanthournhout, B. Herman, J. Duisit, F. Chateau, J. Szewczyk, B. Lengele, and B. Raucent, "Toward user-friendly robotic assistance for enhancing accuracy and safety of reconstructive microsurgery," in Proceedings of the 4th Joint Workshop on New Technologies for Computer/Robot Assisted Surgery (CRAS), 2014:104–107.

Situation Detection for an Interactive Assistance in Surgical Interventions Based on Dynamic Bayesian Networks

P. Philipp[1], L. Schreiter[1], J. Giehl[2], Y. Fischer[3], J. Raczkowsky[1], M. Schwarz[2], H. Wörn[1], J. Beyerer[3,1]

[1] *Institute for Anthropomatics and Robotics (IAR), Karlsruhe Institute of Technology (KIT)*

[2] *Orthopaedic and Trauma Surgery Centre, University Medical Centre, Medical Faculty Mannheim, Heidelberg University*

[3] *Fraunhofer Institute of Optronics, System Technologies and Image Exploitation (IOSB)*

p.philipp@kit.edu

INTRODUCTION

For mastering challenges of contemporary medicine, the use of assistance functions for diagnosis and surgical interventions has become an evolving area [1], [2]. Assistance functions can help to prevent treatment errors, enhance the patients' outcome and preserve a high level of satisfaction for both, patients as well as employees [3]. In [3] we studied Random Forests to enable such functions in context of a computer assisted surgery (CAS). In this work, we elaborate the use of the interventions' underlying workflow, to further improve the prediction of a surgical step. I.e. we incorporate the knowledge that only specific sequences of actions are reasonable - e.g. cutting before sewing. The situation detection we propose is based on Dynamic Bayesian Networks (DBN). By using the DBN filter mechanism, the progress of an on-going surgery can be facilitated to provide tailored (i.e., context sensitive) information on the fly. Examples range from patient specific imaging to medical records or general emergency procedures. This can be seen as an important aspect to carry out more advanced assistance functions not only focusing on the progress of the surgery.

MATERIALS AND METHODS

Fig. 1 depicts a sketch of a re-enacted and simplified hip replacement surgery. Simplifications are made in terms of the number of acting persons and the level of detail of the performed actions. Consequently, the reenactment focuses on characteristic aspects of a real surgery, e.g. the change of positioning.

The deployed perception system comprises four Kinect V2. The used algorithms which are based on skeleton tracking [4] deliver the current positions of each person in the operating team (cf. P_1 and P_2 in Fig. 1). Furthermore, the number of persons and the number of used instruments in the operation theatre is captured. For the latter, the ARTTrack2 system [5] was used. To utilize all data for exploration and the subsequent on-line classification, the ROS-based OP:Sense environment is employed [6]. The setup delivered 12 datasets $D_{1...12}$ of the 7 step workflow (cf. surgical steps a-g in Tab. 1). Each data set D consists of a set of feature vectors. A feature vector $\mathbf{x} := (x_1, x_2, x_3)^T$ is given by three values of the features "Positioning", "Number of Persons" and "Number of Instruments Used". The expected value of each feature is given by the matrix in Tab. 1. Evidently, the actual values in a data set D deviate from this perfect characteristics, inter alia, because of sensor accuracy or occlusions during the re-enactment.

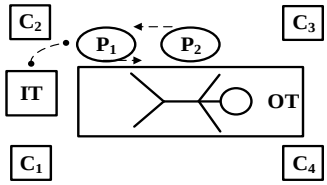

Figure. 1. The figure shows a top view of the surgery of interest. C_1 to C_4 represent the four cameras which are mounted on the ceiling. The instrument table (IT) is used to store currently unused instruments – which is indicated by the dashed handle. The operating team (represented by person P_1 and P_2) is depicted in the so-called "normal positioning" in relation to the operating table (OT). During the procedure. P1 and P2 change their positions two times (cf. dashed arrows).

To enable supervised learning, all feature vectors used for training are associated with a specific surgical step as they are captured – i.e. the class $\omega(\mathbf{x}) \in \{a, \dots, g\}$ is known for all elements of $D_{1...12}$. For the prediction of a surgical step, a Naïve DBN is used [7]. The root of the DBN's tree topology contains the probabilities for the presence of a surgical step. Using the Closed World

		Surgical Steps						
Feature	**Value**	**a**	**b**	**c**	**d**	**e**	**f**	**g**
x_1: Positioning of the Operation Team	Normal	x	x	x			x	x
	Switched				x	x		
x_2: No. of Persons at Operating Table	1	x						x
	2		x	x	x	x	x	
x_3: No. of Instruments Used	0	x	x		x		x	x
	1			x				
	2					x		

Table. 1. In the first column, the three features used for the classification are shown. Column 2 contains the corresponding values. Columns are marked by an "x" iff a feature value is typically present in the indicated surgical step (a-g) above.

Assumption, the probabilities sum up to 1, since one of the 7 steps has to be present. The leaves of the Naïve DBN contain the estimated conditional probabilities of observing a certain feature value, given the probability of a step - i.e. $\hat{P}(\text{value}|\text{step})$. The temporal aspect is represented by relating two consecutive, adjacent time steps. Transition probabilities specify the probability of switching from one surgical step to another.

RESULTS

Cross-validation with a leave-one-out iterator was used on the datasets $D_{1...12}$ to assess the performance of the proposed method. The averaged results are shown as normalized confusion matrix (Fig. 2).

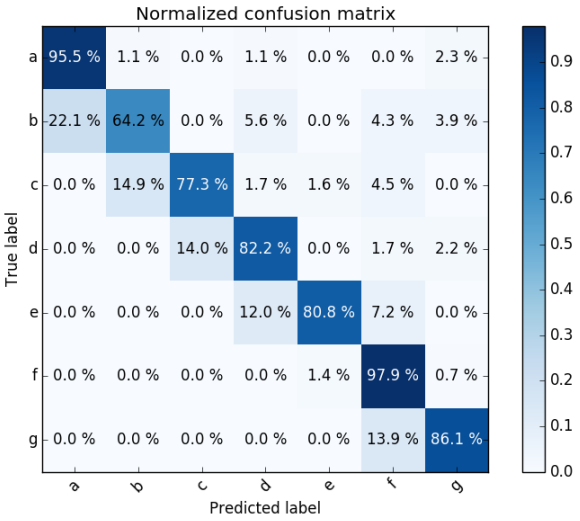

Figure. 2. Normalized Confusion Matrix. A row represents an instance of the actual class (i.e. an actual surgical step), whereas a column represents an instance of the predicted class (i.e. the predicted surgical step). Consequently, the values of the diagonal elements represent the degree of correctly predicted classes. The confusion is expressed by the false classified off-diagonal elements, since they are mistakenly confused with another class.

Unlike in the results of our former work [3] where we investigated a situation detection based on Random Forests, there is almost no confusion of the first surgical step "a" with other steps (cf. first row in Fig. 2). The overall prediction quality compared to our former work is improved, since the presented model based on DBN is able to utilize the knowledge derived from the workflow underlying the considered hip replacement surgery: Unreasonable sequences of surgical steps are prevented by low transition probabilities.

The few misclassifications observed happen predominantly during the switch from one surgical step to the next. They are caused by the DBN-inherent smoothing of observations at run-time (cf. next section).

CONCLUSION AND DISCUSSION

In the presented prediction of surgical steps, the inherent DBN filter mechanism is used for smoothing – i.e. while the model receives single feature vectors over time, only prior (and not future) time steps are considered for smoothing. This makes our algorithm able to classify on-line – whereas smoothing considering the whole sequence of actions in a dataset D at once is only possible offline, since in an on-line scenario of a real surgery the upcoming feature vectors would be unknown.

Besides the outlined benefits, a drawback of the DBN-inherent smoothing is that the model needs some time to recognize a change of surgical steps. I.e. there is a slight time delay in which steps in intermediate sections are confused. Considering the assistance function prior outlined, this delay is negligible, but offers room for further improvements.

Compared to our former results in [3], the quality of surgical step prediction is further improved – this is an important aspect for advanced assistance functions.

ACKNOWLEDGEMENT

The presented study is part of the project "KonsensOP" which is funded by the Federal Ministry of Education and Research (BMBF), Germany.

REFERENCES

[1] Patrick Philipp, Yvonne Fischer, Dirk Hempel, and Jürgen Beyerer "Framework for an Interactive Assistance in Diagnostic Processes Based on Probabilistic Modeling of Clinical Practice Guidelines" in Emerging Trends in Applications and Infrastructures for Computational Biology, Bioinformatics, and Systems Biology, Elsevier; 2016; 371-390.

[2] Florent Lalys and Pierre Jannin "Surgical process modelling: a review." in International Journal of Computer Assisted Radiology and Surgery (CARS); 2014; 9.3: 495-511.

[3] Luzie Schreiter, Patrick Philipp, Johannes Giehl, Yvonne Fischer, Jörg Raczkowsky, Markus Schwarz, Jürgen Beyerer, and Heinz Wörn "Situation Detection for an Interactive Assistance in Surgical Interventions Based on Random Forests" in Proceedings of International Journal of Computer Assisted Radiology and Surgery (CARS); 2016; 115-116.

[4] Tim Beyl, Luzie Schreiter, Philip Nicolai, Jörg Raczkowsky and Heinz Wörn "3D Perception Technologies for Surgical Operating Theatres", Studies in Health Technology and Informatics; 2016, 45–50.

[5] Advanced Realtime Tracking GmbH, Weilheim. Germany, Website: http://www.ar-tracking.com

[6] Andreas Bihlmaier, Tim Beyl, Philip Nicolai, Mirko Kunze, Julien Mintenbeck, Luzie Schreiter, Thorsten Brennecke, Jessica Hutzl, Jörg Raczkowsky, and Heinz Wörn "ROS-based Cognitive Surgical Robotics. Robot Operating System (ROS) - The Complete Reference", 2015, 1095–1106.

[7] Kevin Patrick Murphy "Dynamic Bayesian Networks: Representation, Inference and Learning", PhD thesis, UC Berkeley, 2002.

Surgeon's Assistant: A Touch-free navigation system

N. Kalavakonda[1], N. Aghdasi[1], B. Hannaford[1]

[1]*Department of Electrical Engineering, University of Washington*
nkalavak@uw.edu

INTRODUCTION

Surgeons review medical images and records pre- and intra operatively during procedures to place biopsy needles, tubes or other implants in precise locations. Currently the interaction with most of the complex systems rely on physical contact with interface devices, such as a mouse and keyboard, to view the Computed Tomography (CT) or Magnetic Resonance Imaging (MRI) slides. Given the sterile environment they work under, this process would result in contact with non-sterile devices. Such interactions have been found to spread infections [1]. In recent days, sterile interface devices, such as sealed touch screens, are also used for interaction with a machine. However, both these processes require the surgeon to step away from the operation table or communicate their needs with an operating room (OR) assistant. In addition to this being a time-consuming process, the surgeons are distracted by having to concentrate on the interaction. Previous research has shown that ineffective communication and lack of familiarity between teams lead to errors in the operating room [2]. It would hence be useful to have a mechanism which does not require as much effort but still performs this important task.

A comparison study was conducted by Microsoft Research to test if the deployment of voice controlled system or a gesture-controlled system was favored by surgeons in the operating room [3]. The research group used a Microsoft Kinect to identify the gestures while speech processing was used for voice control. Though the surgeons initially showed more interest in voice control, the study showed that gesture control was preferred for interaction with the display device.

In [4], researchers built a prototype for a gesture recognition system, Gestix, which worked on recognition of gestures using hand color segmentation. This model was tested during a neurosurgical brain biopsy at Washington Hospital Center. The dependence on only the color segmentation for hand tracking led to a number of false positives by the system. Another method commonly used for gesture recognition is fingertip tracking, such as Gestonurse [5] developed in Purdue University. The published results for the system also show that the gesture system that is purely dependent on color-based segmentation had higher false positive rate.

Taking into account the successes and failures of these methods, an improved system for gesture recognition of the surgeons is proposed in this paper. The surgeon's hand was detected using the combination of skin segmentation and Harr Cascade classifier [6]. Various gestures are determined by considering the number of fingers held up and their relative orientation to each other. This was successfully implemented and tested in an environment similar to that in an operating room. The method used to obtain the final results are described in the following sections. Figure 1 explains the architecture pipeline for the gesture recognition system.

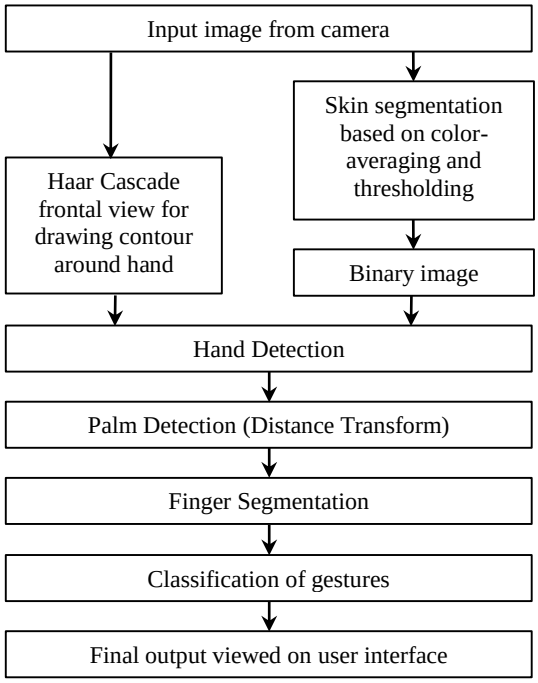

Figure. 1. Pipeline of the Gesture Recognition system

MATERIALS AND METHODS

Due to the variation of skin colors and lighting in the room, finding a fixed color threshold for all the cases is challenging. To overcome this, in the proposed system, users were asked to place their palm in a predefined area. There were seven small square boxes visualized on the screen, where the skin color pixels were accumulated. The RGB color were converted to HSV space since it is more robust to lighting condition. Then the average color was used to set the threshold in original image. The result from this step was a binary image where objects with color similar to skin were labeled foreground object and everything else was background. While using the system in an OR, it would be easier to segment the hand since surgeons could wear gloves of a distinct color, easing the process of segmentation. To improve the hand detection accuracy and to isolate the hand from other objects and body parts, a Haar cascade classifier was used. In this step, given an input image, the classifier detects the hand and creates a bounding box around it. Similar to the Haar

Cascade classifier for face detection, the Haar wavelet features were used to detect palm. The classifier was trained using images of different palms from the Sebastian Marcel Static Hand Posture Database [7].

In the next step, the palm was subtracted to help detect the fingers accurately. For achieving this, the center of the palm is detected by performing a distance transform [8] on the binary image of the hand. On finding the distance transform, the pixel with largest distance to the boundary is chosen as palm center. The radius of the palm is determined by considering the distance from the center to the first black pixel encountered in any direction. The radius measurement provides the size of the palm. The palm is subtracted from the binary image by choosing a radius which is slightly greater than the palm (1.2-1.3 times). The resulting contours are fingers of the user.

To make the system robust, a palm line is constructed, which disqualifies any contour below a certain line to be accounted for the number of fingers. The implementation of this step is important so that the arm is not included. Based on the number of fingers the user holds up and the spatial orientation of the fingers with respect to each other and to the palm center, various gestures to perform a set of actions were defined. The rule set includes four different gestures - manipulating the reconstructed skull to move to the left, to the right, zooming in and zooming out. Pointing a single finger to the left or right were mapped to move the skull in the respective direction. When the palm was held open, the skull would be zoomed in, and a closed palm would zoom out.

RESULTS

The experiment was performed by making use of the camera present on a Mac-Book Air'13. The lighting and background were maintained similar to that in an operation theater for the purpose of testing. The reconstructed skull was interfaced and manipulated using OpenGL. The time taken for initial calibration of skin color was approximately 30 seconds.

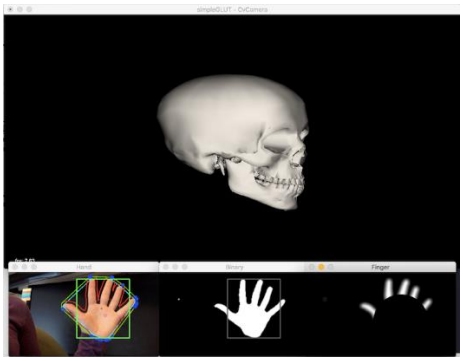

Figure. 2. User Interface with gesture for zoom

The final output obtained is shown in Figure 2. The hand and palm detection are shown at the bottom of the image. The gesture displayed zooms into the reconstructed skull. The program was tested in real-time and all the four gestures were recognized and translated as defined above. The preliminary tests had an accuracy for 90% of the test time. The performance of the system was also tested by rapidly changing the gestures to test response time. The gesture actions were recognized unerringly during the test runs but there existed a delay of few seconds at certain instances. This was a result of the lack of processing speed for real-time data in the laptop.

CONCLUSION AND DISCUSSION

The proposed system performed well in an environment set up to mimic the operating room, as well as in a cluttered environment. Since the system worked well with the harder case of working with skin color, it should be easy to port the work to meet the needs during a surgical procedure if the surgeon wears gloves of a distinct color. This would make the detection and segmentation of the hand less expensive. The user interface could also be modified to interact with individual scan slices. If this system is successfully implemented during a surgery, it would reduce the pressure on the surgeon and the surgical assistant with regard to the task of interacting with the scans. The proposed system has some limitations with respect to delay and data acquisition. We believe this could be improved by using a dedicated computer and a better camera for gesture recognition. Finally, using more training data could help identify additional gestures and implement a variety of well-defined modules to the system that would help a surgeon in the OR.

REFERENCES

[1] Schultz. M, et. al. “Bacterial contamination of computer keyboards in a teaching hospital,” Infect Control Hosp. Epidemiol, 4 (24) (2003), pp. 302–303

[2] Halverson, A.L., et. al. Communication failure in the operating room. Surgery 149, 3 (2010), 305–310.

[3] Helena M., et al. Voice or Gesture in the Operating Room. CHI 2015 Crossings, 773–780, 2015

[4] Wachs, J.P. “A Gesture-based Tool for Sterile Browsing of Radiology Images”. Journal of the American Medical Informatics Association (2008;15:321-323, DOI 10.1197/jamia.M24)

[5] Jacob. M. G, et. al. "Gestonurse: A Multimodal Robotic Scrub Nurse", 7th ACM/IEEE International Conference on Human-Robot Interaction (HRI), March 5-8, 2012

[6] “Cascade Classification”[Online]. Available: http://docs.opencv.org/2.4/modules/objdetect/doc/cascade_classification.html. OpenCV documentation. [Accessed Jun 3, 2016].

[7] Marcel, S. “Hand Posture Recognition in a Body-Face Centered Space”. Proceedings of the Conference of Human Factors in Computer Systems, 1999.

[8] Fisher, R., et. al, “Distance Transform”[Online]. Available: http://homepages.inf.ed.ac.uk/rbf/HIPR2/distance.htm. [Accessed Jun 5, 2016]

Hand-eye Calibration Using Instrument CAD Models in Robotic Assisted Minimally Invasive Surgery

Krittin Pachtrachai, Max Allan, Vijay Pawar, Stephen Hailes and Danail Stoyanov

Centre for Medical Image Computing (CMIC), University College London
krittin.pachtrachai.13@ucl.ac.uk, maximilian.allan.11@ucl.ac.uk, v.pawar@ucl.ac.uk, danail.stoyanov@ucl.ac.uk

INTRODUCTION

Robot-assisted minimally invasive surgery (RMIS) enables the remote control of surgical instruments with a high degree of safety and accuracy. RMIS is performed by using articulated surgical instruments, including a laparoscopic stereo camera inserted through keyhole access ports [1]. Accurate and real-time localisation of the surgical instruments in a camera reference is an important step towards developing new applications in robotic surgery such as automatic instrument motion control with visual servo and assisted instrument guidance with augmented reality. For such applications to work, the robot kinematics needs to be used to add robustness to visual tracking and this requires accurate hand-eye calibration in order to correctly overlay the information from camera to robot frame.

Hand-eye calibration is the estimation of the rigid transformation linking a camera reference frame and an end-effector frame of a robot. The conventional setup for the calibration is illustrated in Figure 1. The world coordinate frame $\mathbf{F}_{grid}$ is fixed at the calibration grid, while the robot coordinate frame $\mathbf{F}_{base}$ is at the base of the robot. Camera calibration and forward kinematics are applied to identify the rigid transformations ${}^{cam}\mathbf{T}_{grid}$ and ${}^{base}\mathbf{T}_{robot}$, respectively. In order to perform camera calibration, most existing hand-eye calibration methods involve the use of a known-dimensional object as a calibration target. Mostly used calibration objects are checkerboards or uniform grids with circle dots and their physical dimensions are priorly known. The principle behind this estimation is to identify a homography from which the pose of camera with respect to a calibration target known as extrinsic parameters can be extracted [3]. Although these calibration targets usually provide accurate data for hand-eye calibration, the use of these markers is time consuming and inconvenient in surgical applications. To handle this problem, structure-from-motion (SFM) approaches could be used to calibrate the hand-eye matrix without using any calibration target [4], however, anatomical features in surgery can deform which makes the problem ill-posed and in addition, the movement of surgical camera is confined by remote centre of motion which prevents the collection of sufficient viewpoints to provide accurate calibration.

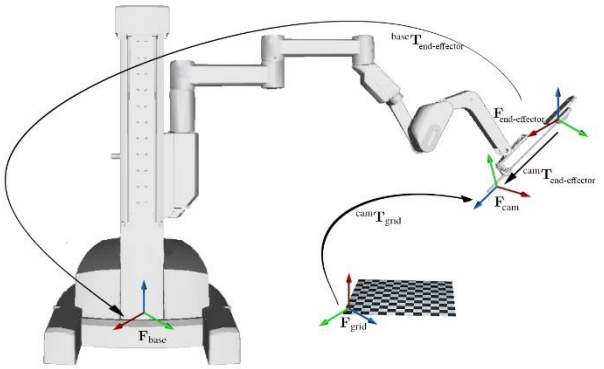

Figure 1. The conventional set-up for hand-eye calibration with a da Vinci Surgical Robot. Hand-eye calibration identifies the relative pose between camera frame and end-effector frame ${}^{cam}\mathbf{T}_{robot}$ [2].

Alternatively, surgical instruments can be used as calibration targets for hand-eye calibration. Their physical dimensions are priorly known and they also have greater range of motion than the camera which give an advantage over checkerboards and uniform grids. Many existing methods are proposed for instrument tracking application, using differents features such as color or local gradient from the target to align 3D model of the instrument with the image [5]. This paper introduces a new approach for hand-eye calibration which uses a surgical instrument as a calibration target. The instrument is tracked while it moves within a field of view of the camera. We use a 3D instrument tracking method in [5] and demonstrate through experiments that hand-eye calibration using surgical tool tracking achieves higher accuracy in rotation than using a conventional calibration object.

METHODS

Hand-eye calibration is to solve for $\mathbf{X} \in SE(3)$ in the following mathematical equation.

$$\mathbf{AX} = \mathbf{XB} \qquad (1)$$

In a conventional case, $\mathbf{A}$ and $\mathbf{B}$ are relative motion of camera and robot, but in our case where we use a surgical tool as a calibration target, we modify the relative transformations to be

$$\mathbf{A} = {}^{arm}\mathbf{T}_{base}(\tau)({}^{arm}\mathbf{T}_{base}(\tau'))^{-1} \qquad (2)$$

$$\mathbf{B} = {}^{tool}\mathbf{T}_{cam}(\tau)({}^{tool}\mathbf{T}_{cam}(\tau'))^{-1} \qquad (3)$$

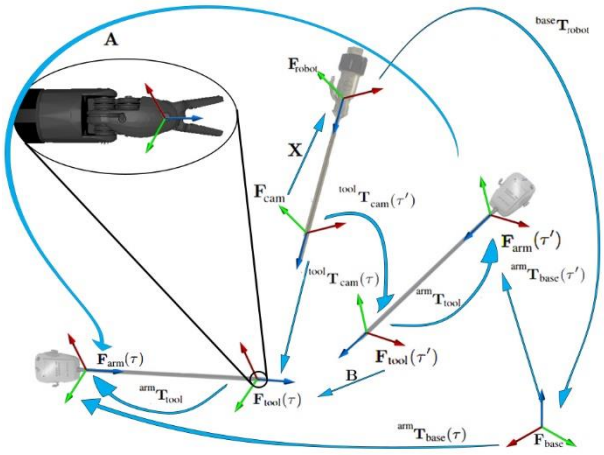

Figure 2. The schematic for a hand-eye calibration incorporating a tool tracking algorithm as mathematically represented in Eq. 2-3.

where τ and τ' are discrete parameters indicating that the two transformations with different poses as shown in Figure 2. During the capturing, the surgical tool is tracked using the method from [5] which tracks the instrument by minimising the joint cost between aligning 3D model of the instrument with color-based segmentation and a local optical flow point tracking. The optimiser uses gradient descent for the stereo camera to create stereo constraints and Kalman filter for temporal consistency in frame-to-frame tracking. Da Vinci kinematics data is used to create **A** in Eq. 2 while tracking data is used in Eq. 3. Since da Vinci kinematics are noisy, we introduce an additional constraint derived from the property of the adjoint transformation to the problem to compensate the inaccuracy and this allows the alternate optimisation between the estimations of rotation (Eq. 4) and translation components (Eq. 5).

$$\begin{bmatrix} a_0 - b_0 & -(\vec{a}-\vec{b})^T \\ \vec{a}-\vec{b} & [\vec{a}+\vec{b}]_\times + (a_0-b_0)\mathbf{I}_3 \\ 0 & -(\vec{v}_A - [\vec{t}]_\times \vec{\omega}_A - \vec{v}_B)^T \\ \vec{v}_A - [\vec{t}]_\times \vec{\omega}_A - \vec{v}_B & [\vec{v}_A - [\vec{t}]_\times \vec{\omega}_A + \vec{v}_B]_\times \end{bmatrix} \mathbf{q} = \vec{0} \quad (4)$$

$$[\vec{\omega}_A]_\times \vec{t} = \mathbf{R}\vec{v}_B - \vec{v}_A \quad (5)$$

where $\mathbf{q}$, $[a_0, \vec{a}]$ and $[b_0, \vec{b}]$ are quaternion representations of rotation components of ${}^{arm}\mathbf{T}_{tool}$, **A** and **B**, respectively, $\vec{v}_A, \vec{\omega}_A$ and $\vec{v}_B, \vec{\omega}_B$ are Lie algebra of **A** and **B** and $\vec{t}$ is the translation component of ${}^{arm}\mathbf{T}_{tool}$. The algorithm solves these two equations alternately until the solution converges. The solution ${}^{arm}\mathbf{T}_{tool}$ allows us to finally compute the hand-eye matrix **X**.

RESULTS

We evaluate the performance of the calibration by using the prediction method originally used in [6]. The experiment is performed by collecting 20 poses of a surgical tool from tracking data as well as the kinematic data, but only N poses are included into the calibration (N is run from 3 to 14, i.e. 2 to 13 motions).

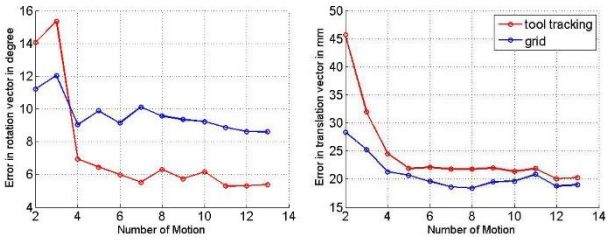

Figure 3. Comparison of calibration performance between using a standard grid and a surgical instrument as a calibration target.

This process is repeated 100 times to generate meaningful results. According to Figure 3, using a surgical tool as a calibration target has a clear improvement in rotation estimation. Although the conventional method still outperforms tool tracking method in translation estimation, the result from using tool tracking has a comparable error.

CONCLUSION

In this paper, we propose a hand-eye calibration method using an unconventional calibration target, i.e. a robotic surgical instrument [7], [8]. In RMIS using the da Vinci Surgical Robot where camera motion is confined to a small volume, capturing an image of checkerboard does not provide sufficient viewpoints for the calibration. On the other hand, a surgical instrument has wider range of motion and thus can provide wider range of poses for the calibration which allows the calibration to achieve higher accuracy. The result shows a clear improvement in rotation estimation and a comparable error in translation estimation, after several data are included. Moreover, apart from the improved calibration accuracy itself, the use of a surgical tool as a calibration target potentially allows online and real-time calibration. The approach is also more practical than using a conventional calibration target and introduces the possibility of automatic calibration in computer assisted interventions which will offer a simpler workflow for calibrations during surgical procedures [9], [10].

ACKNOWLEDGEMENT

We would like to thank Simon Di Maio and Mahdi Azizian at Intuitive Surgical, CA for providing us with CAD models of the instrument and the DVRK community for their support. The work was part funded by the EPSRC (EP/N013220/1, EP/N022750/1, EP/N027078/1, NS/A000027/1), The Wellcome Trust (WT101957, 201080/Z/16/Z) and the EU-Horizon 2020 project EndoVESPA (H2020-ICT-2015-688592).

REFERENCES

[1] L. R. Kavoussi *et al.*, "Comparison of robotic versus human laparoscopic camera control", in *J Urol.* 1995; 158(4): 2134-2136.

[2] Intuitive Surgical, Inc. ISI API User Guide, 2014.

[3] S. J. D. Prince, *Computer Vision Models, Learning and Inference*, 1st ed. UK: Cambridge University Press, 2012.

[4] J. Heller *et al.*, "Structure-from-motion based hand-eye calibration using L_∞ minimization", in *IEEE CVPR*, 2011, pp. 3497-3503.

[5] M. Allan *et al.*, "Image based surgical instrument pose estimation with multi-class labelling and optical flow", in *MICCAI*, 2015, pp. 331-338.

[6] K. Daniilidis, "Hand-eye calibration using dual quaternions", in *IJRR* 1999; 18(3): 286-298.

[7] F. Vasconcelos *et al.*, "Spatial calibration of a 2D/3D ultrasound using a tracked needle", in *IJCARS*, 2016; 11(6): 1091-1099.

[8] F. Vasconcelos *et al.*, "Similarity registration problems for 2D/3D ultrasound calibration", in *ECCV*, 2016 [Accepted]. Available: http://arxiv.org/abs/1608.00247.

[9] D. Stoyanov *et al.*, "Laparoscope self-calibration for robotic assisted minimally invasive surgery", in *MICCAI*, 2005, pp. 114-121.

[10] S. Thompson *et al.*, "Hand-eye calibration for rigid laparoscopes using an invariant point", in *IJCARS*, 2016; 11(6): 1071-1080.

Laser Doppler Based Sensing for Blood Vessel Detection with a Steerable Needle

Vani Virdyawan, Matthew Oldfield, and Ferdinando Rodriguez y Baena
Department of Mechanical Engineering, Imperial College London, UK
f.rodriguez@imperial.ac.uk

INTRODUCTION

In minimally invasive brain surgery, percutaneous interventions are commonly used, for example, in biopsies and deep brain stimulation implantations. During these procedures, puncturing blood vessels can be a life threatening complication. Unfortunately, imaging modalities such as MRI and X-ray cannot detect small blood vessels that are sub-millimetre in size or, in the case of Ultrasound, cannot penetrate the skull.

To avoid haemorrhage caused by puncturing blood vessels during procedures, investigations have been conducted on the deployment of a forward looking, laser-based sensor on needle tips [1], [2]. The laser signals are delivered and collected through optical fibres. These laser-based sensors can detect blood vessels by means of Doppler shift generated by the movement of the blood cells that they contain. Since the laser light is scattered randomly in the tissue, the exact position of the blood vessel cannot be determined. Fredriksson et. al. [3] developed a model in order to define the significant measurement depth covered by a laser Doppler probe. Their Doppler probe's measurement depth covered 0.39 mm in human grey matter [3].

Current percutaneous intervention procedures use a rigid needle. This means that, if there is an obstacle (e.g. a blood vessel) along the insertion path, the procedure needs to be interrupted. To address this limitation, current research has been directed towards the field of steerable needles. One such needle design, first demonstrated by Ko et. al in 2012 [4] and referred to as STING, is a multi-segment, flexible design which is inspired by the egg laying channel of certain insects. Each segment has a working channel that can be used to, for example, deliver drugs or insert an optical fibre for imaging or diagnostics. It is believed that, by embedding a laser Doppler probe in the STING needle, a blood vessel on its current insertion path can be detected beyond the measurement range identified in [3]. As there is no reported use of a forward-looking sensor in a steerable needle system, the measurement range of a laser Doppler probe needs to be characterised in order to investigate the feasibility of this approach in the STING device. Here, this is done by measuring the maximum depth and off-axis distance to a blood vessel phantom that can be detected by a suitable sensing probe. A commercial, laser Doppler, blood-flow monitoring system (OxyFlo^{TM} (Oxford Optronix, Abingdon, UK)) with bare-fibre type probe (NX-BF/F (Oxford Optronix, Abingdon, UK)) has been used for this purpose. Based on the sensing characterisation, the feasibility of deploying a laser Doppler probe in the STING needle is discussed.

MATERIALS AND METHODS

A tissue phantom that mimics the optical properties of human grey matter was used during the experiment. The phantom was made by adding 3 g/L of titanium dioxide (TiO_2) into 4.5% weight gelatine [5]. A capillary tube with an outer diameter of 0.9 mm and an inner diameter of 0.6 mm was used as a blood vessel phantom, while the blood surrogate was milk, with 1.5% fat content [6].

To test measurable depths below the gelatine surface, the tube was placed on a gradient inside the gelatine [7]. The maximum detection depth was investigated by scanning axially above the tube on the gelatine surface. Off-axis detection range was measured by moving the probe laterally across the tube's axis. The probe was held in a two degree of freedom precision linear stage (Figure 1). During the experiment, milk flow velocities were achieved using a syringe pump (Graseby 3200, Graseby Medical Ltd., UK).

The depth detection range was measured for three different flow velocities: 1 mm/s, 5 mm/s, and 10 mm/s, with 0.3 mm depth resolution, starting from 0.3 mm tube depth. The lateral measurements were done for 5 mm/s flow velocity, with 0.1 mm resolution at four different tube depths. The measurements in each case were done a minimum of 5 times.

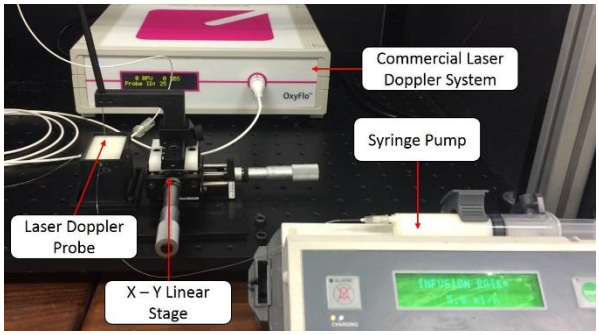

Figure 1. Experimental configuration for laser Doppler characterisation of vessel flow in a brain phantom

RESULTS

Figure 2 shows the signal strength of different flow velocities at variable depths. Figure 3 shows the off-axis signal strength of a flow at 5 mm/s at four depths when measured across the capillary tube. The measurement value is an arbitrary unit (AU) of perfusion value in the range of 0 – 5000 AU. Based on the background signal, the threshold value of a detected flow is 100 AU.

DISCUSSION AND CONCLUSION

Using a 100 AU perfusion value as a threshold, the maximum on-axis depth for the tube that can be detected

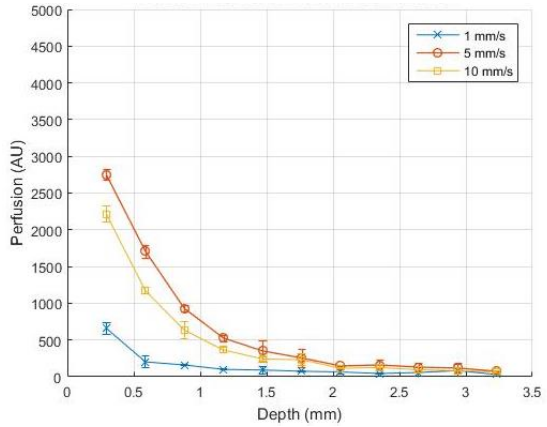

Figure 2. Means and standard deviations of signal strength against capillary depth for three different flow velocities

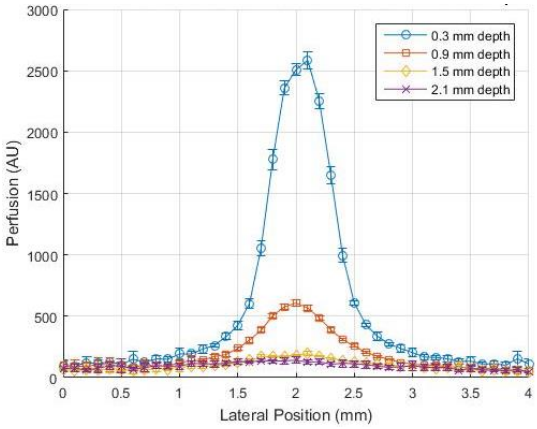

Figure 3. Means and standard deviations of signal strength when measured laterally across the capillary at different depths

at 5 mm/s is 2.1 mm. With the same flow velocity up to 0.9 mm depth, the measurement threshold is met up to a 1 mm off-axis position. Figure 4 shows the geometry of a 2.5 mm STING needle. The axial distance from the tip of a fibre to the tip of the needle is 0.67 mm, while the lateral distance is 0.88 mm. This value is deeper compared to [3], since in the latter, depth was determined by computing the cumulative signal contribution, which amounted to 63% of the total. Based on this geometry constraint and the characterisation of the probe for 5 mm/s flow rate, it is feasible to use the laser Doppler system in the STING needle.

The measurement value of the laser Doppler system is affected by both the concentration of the scattering particles and the flow velocity. Figure 2 shows that a higher flow velocity can be detected farther ahead compared to a lower velocity. Therefore, a vessel with lower flow velocity may not be detected before it is too close to the tip of the needle.

Due to a dependency on depth and flow velocity, it is not possible to determine the exact position of blood vessels with respect to the needle. However, laser Doppler sensing can be used as a detector to give a prediction about whether there is a vessel in front of the tip of the needle so that the STING's steering capability may be used. In order to avoid the vessel, it is also necessary to know its position and orientation with respect to the tip of the needle. Combining measurements from multiple segments may provide this information and will form the basis of future investigations. In addition, a dynamic re-planning method able to exploit these measurements for vessel avoidance will be investigated.

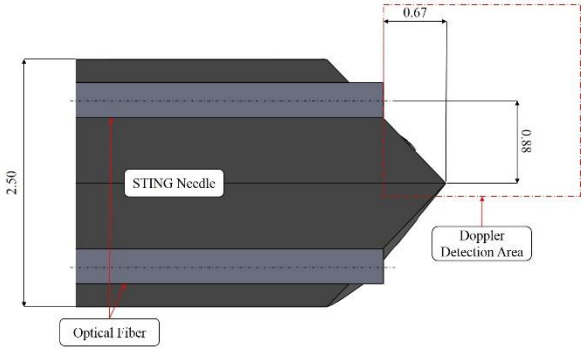

Figure 4. STING needle geometry and its constraint on the Doppler detection range in front of the optical fibre

ACKNOWLEDGMENT

This research was supported by the Indonesian Directorate General of Higher Education[1], the European Research Council under the European Union's Seventh Framework Programme (FP7/2007–2013) / ERC grant agreement no 258642-STING, and EPSRC. This project has also received funding from the European Union's Horizon 2020 research and innovation programme under grant agreement 688279. The authors are grateful to Michael Rau and Oxford Optronics for the loan of the equipment and advice relating to its use.

[1]Vani Virdyawan is a lecturer at Institut Teknologi Bandung, Indonesia, now pursuing a PhD Degree at Imperial College London.

REFERENCES

[1] Liang C-P, et. al. "Coherence-gated Doppler: a fiber sensor for precise localization of blood flow" Biomed. Opt. Express; 2013; 4(5): 760–71.

[2] Wardell K, et. al. "High-Resolution Laser Doppler Measurements of Microcirculation in the Deep Brain Structures: A Method for Potential Vessel Tracking" Stereotact. Funct. Neurosurg.;2016;1-9.

[3] Fredriksson I, et. al. "Measurement depth and volume in laser Doppler flowmetry" Microvasc. Res.; 2009; 78(1):4-13.

[4] Ko SY and F Rodriguez y Baena. "Toward a miniaturized needle steering system with path planning for obstacle avoidance" IEEE Trans. Biomed. Eng.; 2013; 60(4):910-7.

[5] Pogue BW, et. al. "Absorbed photodynamic dose from pulsed versus continuous wave light examined with tissue-simulating dosimeters" Appl. Opt.; 1997; 36(28): 7257–7269.

[6] Öberg PÅ. "Tissue motion - a disturbance in the laser-Doppler blood flow signal?" Technol. Health Care; 1999; 7(2-3): 185-92.

[7] Woolsey N et. al. "Surgical Navigation Probe Utilizing Optical Coherence Tomography and Laser Doppler"; Biomedical Optics; 2014 (Online).

Tactile sensor array integrating fiber Bragg grating transducers for biomechanical measurement

L.Massari[1], P.Saccomandi[2], F.Sorgini[1], E.Sinibaldi[3], G.Ciuti[1], A.Menciassi[1], P.Cappa[4], E.Schena[5], C.M.Oddo[1]

[1]*The BioRobotics Institute,Scuola Superiore Sant'Anna, Pisa, Italy*
[2]*Institute of Image-Guided Surgery (IHU), Strasbourg, France, S/c Ircad, STRASBOURG Cedex*
[3]*Center for Micro-BioRobotics @SSSA, Istituto Italiano di Tecnologia, Pontedera (PISA), Italy*
[4]*Department of Mechanical and Aereospace Engineering,'Sapienza' University of Rome, Italy*
[5]*Center for Integrated Research, University Campus Bio-Medico, Rome, Italy*
l.massari@sssup.it, c.oddo@sssup.it

INTRODUCTION

This paper presents the development and validation of an array of multi-axis tactile sensors that is intended to measure selected part of the components of torque and force vectors acting on the surface where the sensor is integrated. The developed tactile sensor is based on Fiber Bragg Grating (FBG) technology [1].

The proposed tactile sensor can be used to enhance robot-assisted surgical operations by encoding tool-tissue tactile interaction, which then can be displayed to the operator by means of a haptic or other interface on the master console. Furthermore, the sensor is ultra-soft, hence suitable for application in the field of smart textiles; for example, it can be integrated in a glove in order to sense both external forces and hand movements while preserving wearer's comfort [2]. Another main characteristics is the possibility to develop MR-compatible systems thanks to the FBG immunity to electromagnetic interference [3, 4].

The first section of this manuscript illustrates the FBG working principle, the developed sensing system and the experimental setup and protocols. Then experimental results are presented and discussed, and roadmaps for future works are envisaged.

MATERIALS AND METHODS

Transduction principle and sensor design

FBGs are sensitive to both strain and temperature, which are encoded in the temporal modulation of the spatial period of a grating patterned on the optical fiber. The readout of sensor information requires the injection of light from a spectrally broadband source into the fiber. Part of the injected light is transmitted and another narrow part of the spectrum, centered around the so-called Bragg wavelength (λ_B) is back-reflected (Figure 1); the principal wavelength of the reflected light is dependent on: (i) the grating period of the strain and (ii) the temperature to which the sensor is exposed. Hence, the Bragg wavelength λ_B is given by the expression:

$$\lambda_B = 2 \cdot n_{eff} \cdot \Lambda_B$$

where n_{eff} is the effective refraction index of the fiber core and Λ_B is the grating period. The response of FBG is defined both from the physical elongation of the sensor (and the corresponding change in the period) and the change in the fiber index due to photoelastic effect that arises from the thermal expansion of the fiber material. The present tactile sensor uses 12 FBGs in a single optical fiber (Figure 2), being embedded in a thin polymeric sheet to obtain a pad with a low thickness (1mm). An excessively small bending radius can lead to damage or even breakage in the optical fiber, therefore the path followed by the encapsulated fiber is designed accordingly. The encapsulation polymer is Dragon Skin (10 medium, Smooth-on, USA), which has appropriate mechanical properties since it is flexible, stretchable and is able to transmit deformations. Thanks to its characteristics, this sensing pad is able to measure several mechanical quantities (e.g. elongation, strain and pressure) along the whole surface. Furthermore, the pad may be embedded, attached or wrapped on a specific surface.

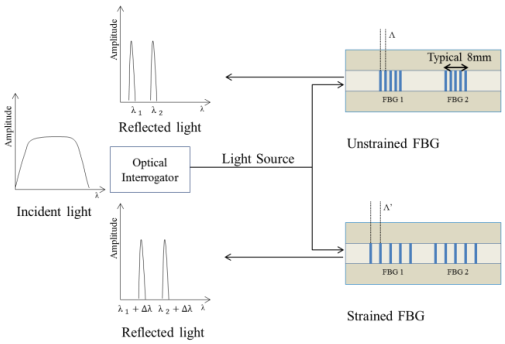

Figure 1 - FBG measurement architecture.

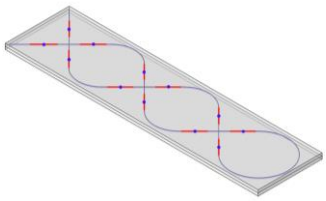

Figure 2-Rendering showing the optical fiber path in the encapsulation polymer, the positioning of the 12 FBG transducers (red lines) and the indentation sites for the experimental evaluation (blue dots).

Experimental setup and protocol

A quasi-static calibration process was performed to establish the relationship between the applied force and the sensor output. Figure 3 shows the experimental setup for this aim. A testing machine (Instron, 5900

Series, Figure 3B) was used to apply known values of force on the sensor surface. A cylindrical probe with diameter of 5 mm (Figure 3A-1) was used to apply deformation to the surface of the array (Figure 3A-2). The Instron was used to move the indenter along the Z-axis with constant speed of $0.1\,mm \cdot s^{-1}$. During the indentation experiments, the probe was applied in 12 selected sites of the sensor surface (Figure 2). Multiple runs (N=6) were performed to evaluate repeatability with load stimulation range up to 1 N, 2 N and 3 N (see Figure 5 for related results). No temperature variations occurred during the experiments, anyway a dummy FBG sensor could be integrated in the future in the final device, for compensating the possible occurrence of temperature variations in operational conditions.

Two stages were used to translate the sensor along the two other axes, X and Y. The output of each FBGs was measured by an optical spectrum interrogator (sm125, Micron Optics), and recorded by PC with the dedicated software.

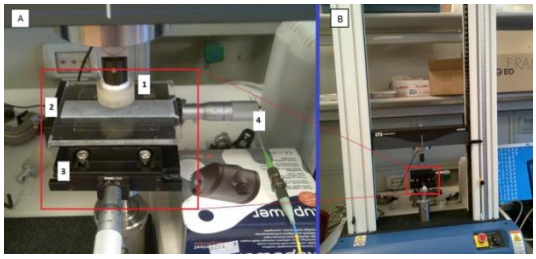

Figure 3-Experimental Setup: (A1) cylindrical indenter, (A2) sensor array integrating FBG, (A3) Y-translational stage, (A4) X-translational stage, (B) Testing machine.

RESULTS

The variation of the wavelength was dependent on the applied force. From an examination of Figure 4, where paradigmatic time histories of the applied force and sensor output are reported, it emerges that the indentation force F_Z was tracked by the transducers with a consistent variation of the wavelength.This variation was highly repeatable (±1% fitting variation) and monotonic. Figure 5 displays the wavelength variation as a function of the applied force, providing evidence of linearity between these two physical quantities (0.040 nm/N sensitivity).

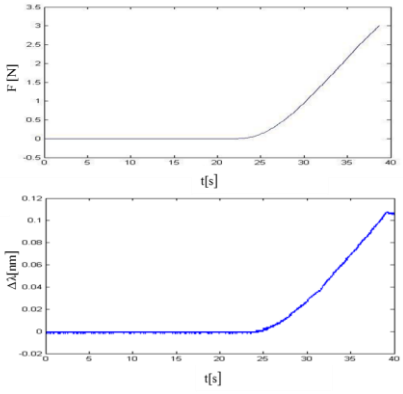

Figure 4 - The upper plot shows indentation force Fz as a function of time. The plot below displays wavelength variation as a function of time.

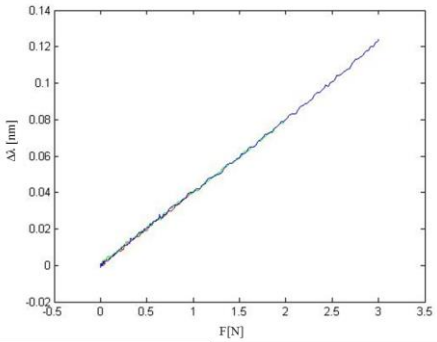

Figure 5- Repeatable monotonic modulation of wavelength as a function of the normal indentation force F_Z. The trends with stimulation up to 1 N,2 N and 3N are shown in the plot.

DISCUSSION AND CONCLUSION

This extended abstract deals with the presentation and the design of a tactile sensor array integrating FBG transducers for biomechanical measurements in several application scenarios. Due to the known immunity to electromagnetic interference, the chosen technology allows the use of such tactile sensor in MR environment, that will be tested in future studies. Furthermore, unlike traditional sensing elements, increasing the number of FBGs will not lead to a huge wiring encumbrance since a single optical fiber (or a few fibers) can convey information from multiple transducers.

The obtained results are promising and give encouraging perspectives for this prototype. Future investigations will target a more accurate fabrication process, the elaboration of a FEM model of mechanotransduction, and the experimental evaluation within real application scenarios such as with surgical robotics instruments.

ACKNOWLEDGEMENT

This study was supported in part by the Tuscany Region of Italy with theIMEROS project (FAS-SALUTE call, CUP D66D16000120002) and in part by the European Commission with the FUTURA project (FP7-ICT-Challenge 2 call, GA 611963).

REFERENCES

[1] C. Massaroni, P. Saccomandi, and E. Schena, "Medical Smart Textiles Based on Fiber Optic Technology: An Overview," *Journal of functional biomaterials*, vol. 6, pp. 204-221, 2015.

[2] A. F. da Silva, A. F. Goncalves, P. M. Mendes, and J. H. Correia, "FBG sensing glove for monitoring hand posture," *Sensors Journal, IEEE*, vol. 11, pp. 2442-2448, 2011.

[3] A. Grillet, D. Kinet, J. Witt, M. Schukar, K. Krebber, F. Pirotte, *et al.*, "Optical fiber sensors embedded into medical textiles for healthcare monitoring," *Sensors Journal, IEEE*, vol. 8, pp. 1215-1222, 2008.

[4] P. Saccomandi, C. M. Oddo, L. Zollo, D. Formica, R. A. Romeo, C. Massaroni, *et al.*, "Feedforward Neural Network for Force Coding of an MRI-Compatible Tactile Sensor Array Based on Fiber Bragg Grating," *Journal of Sensors*, vol. 2015, pp. 1-9, 2015.

Sonopill: A Platform for Gastrointestinal Disease Diagnosis and Therapeutics

G. Cummins[1], H. Lay[2], B.F. Cox[3], V. Seetohul[1], Y. Qiu[1], F. Stewart[4], J. Faerber[1], V. Mitrakos[1], M. Al Rawhani[1], J. Beeley[1], D.E. Watson[1], R. Poltarjonoks[1], C. Démoré[2], I. Nathke[4], R.J.C. Steele[3], D.Cumming[2], M.P.Y. Desmulliez[1], S. Cochran[2]

[1]*School of Engineering and Physical Sciences, Heriot-Watt University, Edinburgh, UK*
[2]*School of Engineering, University of Glasgow, Glasgow, UK*
[3]*School of Medicine, University of Dundee, Dundee, UK*
[4]*School of Life Sciences, University of Dundee, Dundee, UK*

G.Cummins@hw.ac.uk

INTRODUCTION

Gastrointestinal (GI) disease is recognised as a significant public health issue due to the growing number of patients diagnosed with colorectal cancer, coeliac disease and inflammatory bowel conditions such as Crohnôs disease. Endoscopy or colonoscopy is often used to image the GI tract to confirm diagnosis. However, while early detection is vital in cases of cancer as it increases the likelihood of survival, colonoscopy can induce discomfort in patients, reducing their willingness to undergo the procedure, delaying detection and treatment. Another disadvantage is that significant parts of the small bowel cannot be easily viewed as standard endoscopic imaging is limited to the upper GI tract and colonoscopy to the terminal ileum and below

More than one million patients have benefitted from capsule endoscopy (CE) since it emerged as a diagnostic tool over 10 years ago [1]. However, as shown in Table I, many of the commercially available CE tools utilise only visual imaging, limiting inspection to the mucosal surface. There is therefore room for innovation, with one route being the introduction of additional modalities so that the full potential of CE can be realised [2].

Ultrasound diagnosis and therapy are important goals of the Sonopill programme through integration in a capsule of the same physical volume as that used in video CE. Secondary modalities being developed for further integration are based on pressure, pH, temperature and chemical sensors. This development is being supported by pre-clinical work to demonstrate the complementary nature of multimodal imaging by ultrasonic and optical means in translational studies. The integration of these capabilities brings challenges and opportunities in a range of areas such as ultrasound device, sensor and systems design, microengineering, packaging and positioning and localisation as well as identifying routes to translation into clinical practice. This paper discusses some of these challenges and provides a brief overview of the work done to date.

MATERIALS AND METHODS

As shown in Figure 1, the Sonopill programme principally aims to achieve two demonstrator devices, ERIC (Epithelial Research Imaging Capsule) and CAIT (Capsule for Autonomous Imaging and Therapy), both intended to exceed the capabilities of existing capsules.

ERIC is a diagnostic capsule for imaging and sensing along and below the mucosal surface of the GI tract. Ultrasound is one of the main diagnostic imaging modalities, working in conjunction with visual imaging. It is safe and works in real time and is therefore already incorporated many endoscopic tools with miniaturised devices to fit within small volumes [3]ï[5]. It is also inexpensive to produce transducers, a vital factor for

Table I: Comparison between some commercially available capsule endoscopes and Sonopill

Brand	**Medtronic**			**Endo-capsule**		**Medimetrics**	**Sonopill**	
Model	SMARTpill	ESO2	COLON2	EC1	EC1-S10	Intellicap	**ERIC**	**CAIT**
Length (mm)	26	26	31.5	26	26	26.7	**30**	**30**
Diameter (mm)	13	11	11	11	11	13	**10**	**10**
Imaging (mm)	N/A	CMOS Image Sensor				N/A	**CMOS Image Sensor, High resolution ultrasound**	
Drug Delivery	No	No	No	No	No	Yes	**No**	**Yes**
Sensors	Pressure, pH, Temperature					pH	**Capability for pH, pressure, chemical, temperature**	

disposable devices such as CEs. However, its key ability is that it can image beneath the surface of the tissue, complementing visual imaging and improving early diagnosis of submucosal neoplasms amongst others.

Ultrasound can also act as a therapeutic treatment, either through direct tissue ablation using high intensity focussed ultrasound or through sonoporation to increase cell permeability for improved drug uptake [6]. These technologies, as well as other therapeutic methods, are being investigated for incorporation into CAIT.

The development of ERIC and CAIT makes the related challenges of positioning and localisation, already encountered by other CEs, even more acute. Therapeutic capsules will require accurate knowledge of the location of treatment sites detected by ERIC as well as the ability to resist the peristaltic forces of the gut that might otherwise move it during treatment. The ability to reorient the capsule would also improve diagnosis, allowing sites of interest to be investigated carefully and repeatedly. The development of the positioning system faces multiple challenges including the need to withstand the corrosive environment of the stomach to get to the small bowel and enhanced miniaturisation to allow sufficient space for imaging and therapeutic payloads while still being able to generate sufficient motive forces.

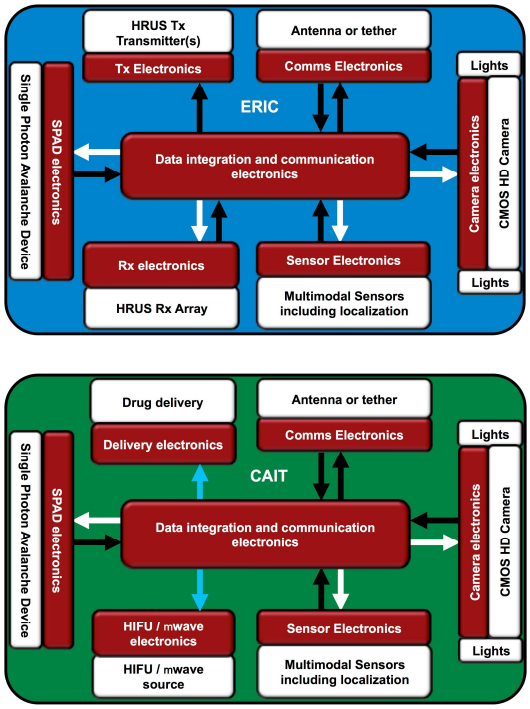

Fig. 1: ERIC (top) and CAIT (bottom)

Wireless communications is another challenge. Preliminary investigation of integrated antenna approaches has shown promise, but low efficiency [7] compared with imaging needs (~ 1 MB per frame). To mitigate this, as well as power consumption concerns, accelerometers will be integrated into the final design to allow the active components to be shut-down during slow movement and to complete data transmissions.

RESULTS

Currently the Sonopill programme has developed several reduced functionality, tethered ñpathfinderò pills to allow various sensing and therapeutic modalities and other systems such as communications to be independently tested before integration into the more functionally complex ERIC and CAIT demonstrators. These simpler pills will be used for translational studies *in vivo* in the near future.

CONCLUSION AND DISCUSSION

Reported cases of GI disease are growing worldwide and CE is increasingly used as a means of diagnosis. However, it is an immature technology in many realisations, open to further innovation and integration to provide new diagnostic and therapeutic tools as well as new avenues of research. In the Sonopill programme, ultrasound imaging and other clinically useful sensing modalities are being integrated into ERIC and new therapeutic methods are being investigated for CAIT. However, challenges such as positioning and localisation will need to be overcome to fully realise the goal of autonomous, steerable, wireless CE.

REFERENCES

[1] G. Iddan, G. Meron, A. Glukhovsky, and P. Swain, ñWireless capsule endoscopy,ò *Nature*, vol. 405, no. May, pp. 417ï418, 2000.

[2] A. Koulaouzidis, D. K. Iakovidis, A. Karargyris, and E. Rondonotti, ñWireless endoscopy in 2020: Will it still be a capsule?,ò *World J. Gastroenterol.*, vol. 21, no. 17, pp. 5119ï5130, 2015.

[3] T. L. Szabo, *Diagnostic Ultrasound Imaging*. Academic Press, 2004.

[4] J. Correia, ñFinal Report Summary - TROY (Endoscope Capsule using Ultrasound Technology),ò 2009.

[5] J. H. Lee, G. Traverso, C. M. Schoellhammer, D. Blankschtein, R. Langer, K. E. Thomenius, D. S. Boning, and B. W. Anthony, ñTowards wireless capsule endoscopic ultrasound (WCEU),ò in *2014 IEEE International Ultrasonics Symposium*, 2014, pp. 734ï737.

[6] A. Melzer, S. Cochran, P. Prentice, M. P. MacDonald, Z. Wang, and A. Cuschieri, ñThe importance of physics to progress in medical treatment,ò *Lancet*, vol. 379, no. 9825, pp. 1534ï1543, 2012.

[7] A. Kiourti, K. A. Psathas, and K. S. Nikita, ñImplantable and ingestible medical devices with wireless telemetry functionalities: A review of current status and challenges,ò *Bioelectromagnetics*, vol. 35, no. 1, pp. 1ï15, Jan. 2014.

Feature extraction-based automated camera motion for surgical endoscopy support

Renáta Elek[1*], Dénes Ákos Nagy[1,2], Imre J. Rudas[1], Tamás Haidegger[1,2]

[1]*Antal Bejczy Center for Intelligent Robotics, Óbuda University, Budapest, Hungary*

[2]*Austrian Center for Medical Innovation and Technology (ACMIT), Wiener Neustadt, Austria*
renata.elek@irob.uni-obuda.hu

INTRODUCTION

The wide acceptance of minimally invasive surgeries in the medical practice further contributed to crowding the operating room, since an additional personal is typically required to hold the endoscope. This problem was recognized early by the community, and several companies developed camera handling platforms. Intuitive Surgical's da Vinci surgical system is such an example, while other solutions focused solely on camera handling, including AESOP (from Computer Motion) or FreeHand (previously EndoAssist) from Prosurgics. These systems are mostly tele-operated, and do not adapt to the changes in the operational field, causing constant need for manual readjustment of the camera position [1-2].

Visual servoing is a robot control technique based on the visual sensor information, which determines the robot's trajectory. It is possible to track surgical instruments, or compensate motions automatically with visual servoing to improve the ergonomics in the OR during laparoscopic surgery. The method presented here targets to handle minor readjustments caused by the patients' physiological movements, and by the shifting of internal organs during the operation. The current algorithm employs known feature-extraction methods, yet, despite our efforts, the algorithm is implicitly not able to target major camera movement just by visually following the laparoscopic tools [3-4].

MATERIALS AND METHODS

The aim was to create a visual servoing based tracking method which is easily adapting to the continually changing environment and gives universal solution to the camera handling automation problem. Our method was based on the Speeded-Up Robust Features (SURF) feature extraction computer vision algorithm. It is a scale-invariant algorithm, and has good computational time performance [5].

SURF's main weaknesses are that it is not adapting well to changes in lightning or to the 3D rotations of the targeted object. To overcome these problems, we propose the constant update of the template, extracted from recent camera frames, therefore utilizing the algorithm's built-in tolerance for minor distortions. The problem with this approach is that the constant updates of the template causes the inclusion of more and more "outside" features, causing the template to gradually crawl off the target object. This behavior makes the algorithm not suitable to instrument tracking, since when the targeted scene is rapidly moving, and is small compared to the search image, we can see the template updating to outside regions really fast.

Based on these findings, we propose the algorithm to be used primarily for the tracking of physiological movements in the surgical field. In this case, the algorithm adapts to soft tissue deformation by template updates, which is of great benefit. Since SURF focuses on a significantly larger area than what the manipulators take up on the surgical image, the feature points found on the instruments will be simply discarded. There is also no need for previously recorded templates, the surgeon can just select the current view, and the algorithm will initiate that Region Of Interest (ROI) as the first template. After that, on every batch of ten frames, the program searches for a new template: this template will be the best matching with the last template, and the program validates it with the object's area. This way, the algorithm can solve the rotation problem, and filter out fake objects. (See in Fig. 3.) With this new template, we employ SURF again, and again on. If the program can't find an object or it is invalid, it asks for a new template. On every frame, where the program found good match, it will calculate the recent object position and the optimal position (which is the center of the frame) difference, which gives the error vector for visual servoing. We used it as motion input for the robotic endoscope holder robot manipulation. The program also calculates the zoom value from the areas. In this way the camera holder robot can track the chosen template. You can find the algorithm flowsheet in Fig. 1. For this method, we used the OpenCV 2.4.9 library. Our implementation is available online (irob.uni-obuda.hu) upon request.

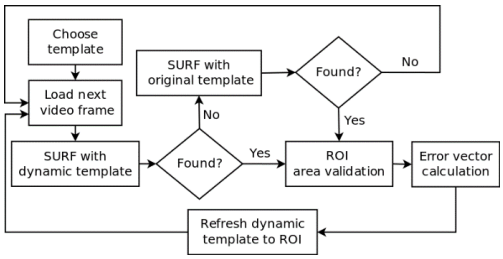

Figure 1. *Algorithm flowsheet. At the start of the algorithm, we choose the template for SURF and on every video frame, the program refreshes this to the ROI. If the object is lost, the program tries to match with the original and the last dynamic template.*

RESULTS

For the experimental trials, we used a phantom environment, originally created for radical prostatectomy. It was placed in a surgical box trainer, developed by our colleagues at the Antal Bejczy Center for Intelligent Robotics. The CALap was also employed, which is a robotic endoscope holder arm that was created in our lab. According to the original setup, we wanted to track surgical instruments, therefore used the easily recognizable parts of the mechanical structure. We found that our method was underperforming during instrument tracking tasks: the template was too small, and the algorithm could not recognize enough features to keep the template on the manipulator; furthermore the background is very complex, therefore providing too many false matches for the SURF. It makes the problem even more complicated that during the instrument tracking, there is constant 3D instrument movement, which SURF cannot handle sufficiently. We tested this task with 3 persons during laparoscopic training. As a consequence, the otherwise stable algorithm relatively quickly loose the object in the more life-like environment, and find wrong objects on the background. Originally, constant update of the templates was implemented for targeting the 3D instrument movement, however we found that the other features from the background can pull the template away from the targeted manipulator (Fig. 2).

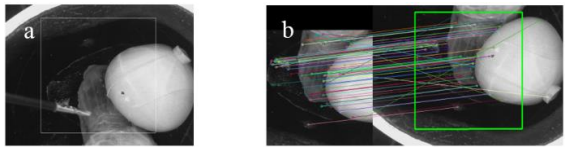

Figure 2. *Feature extraction-based instrument tracking. a) Surgical instrument template. b) The tracking algorithm moved the template from the instrument to a more feature-rich area on the background.*

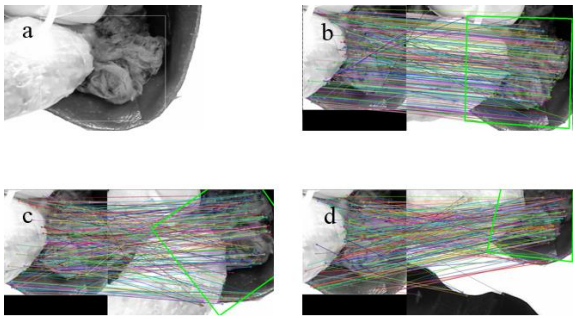

Figure 3. *Feature extraction-based background tracking for soft tissue motion compensation and camera stabilization. a) template for the SURF algorithm. First time the user choose the ROI (white square). b-d) The tracking algorithm worked well in the tasks (planar movement, rotation, distance changing).*

Due to the results of the template fixating on a region of the background, we expected that this behavior can be used sufficiently for tracking tissue motion. In order to test this approach, we selected a template—comparable to the whole image frame— and ran the algorithm expecting it to follow the tissue movement. The program kept the template on the targeted area in every trial, even when the surgical field was distorted, making it especially useful for stabilizing the camera and can keep the video feed on the targeted region, even if the surgical field is being constantly manipulated. The preliminary results shows that the laparoscopic robot can track this motions (covered planar movement, distance changing and multi-axis rotation) safely because of the fake object filtering. Some elements from the SURF can be seen as results in Fig. 3.

CONCLUSION AND DISCUSSION

We presented a feature extraction-based tracking method, aiming for surgical robotics interventions. Our method is based on the Speeded-Up Robust Features algorithm (SURF). Because of the algorithm's weaknesses, we refresh the template periodically. The method has been tested for instrument tracking and for dynamic movement compensation when soft tissue deformation occur. The algorithm failed to be sufficiently robust for instrument tracking, but is exceptionally capable for motion compensation in the surgical field. The algorithm runs on a regular PC, causing around 0.5 s latency. Future work could improve it significantly by using designated hardware for image processing, and running the template updates and the SURF algorithms as separate threads. Novel, alternative algorithms are also being investigated to replace SURF.

ACKNOWLEDGMENT

The research was supported by the Hungarian OTKA PD 116121 grant. Tamás Haidegger is a Bolyai Fellow of the Hungarian Academy of Sciences.

REFERENCES

[1] Cleary, K. et al.: "Image-guided interventions: technology review and clinical applications." *Annu. Rev. Biomed. Eng.*, no. 12., pp. 119–142., 2010.

[2] Pandya, A. et al. "A review of camera viewpoint automation in robotic and laparoscopic surgery." *Robotics*, vol. *3., no.* 3., pp. 310-329., 2014.

[3] Krupa, A. et al. "Combined image-based and depth visual servoing applied to robotized laparoscopic surgery." In *Intern. Conf.e on Int. Rob. & Sys.*, vol. 1., pp. 323-329., 2002.

[4] King, B. W. et al. "Towards an autonomous robot for camera control during laparoscopic surgery." *Jour. of Lapar. & Adv. Surg. Tech.*, vol. *23. no. 12.*, 1027-1030., 2013.

[5] Bay, H. et al. "Speeded-up robust features (SURF)."*Comp. vis. & ima. unders.* vol. 110., no 3., pp. 346-359., 2008.

Angle Detection and Measurement on Continuous and Deformable Medical Tools

F. Visentin, P. Fiorini

Department of Computer Science, University of Verona - Italy
francesco.visentin@univr.it

INTRODUCTION

The surgical field is under constant evolution by benefiting from the rapid technological advancement driven by the pursuit for early intervention, short recovery time, and minimally invasive therapy. This was also possible thanks to robotic-assisted surgery that has helped to enhance the surgeon's dexterity and manipulation abilities as well to improve safety and accuracy during the operation [1]. Today's new challenges consist in the development of novel tools that meet the demands of flexible access surgery. These tools should be able to operate through complex pathway, and be capable to adapt their shape according to the needs. Some devices for Minimal Invasive Surgery have been already developed following these new requirements and demonstrated good results [2]. Despite these, additional improvement should be achieved before the full deployment of such technology in medical applications. Among these, proprioceptive sensing is one of the most valuable.

In this paper we focus on the detection and measurements of bending angles that can occur over a continuum deformable device. Solutions have already been presented, but most of them need to include sensors in accurately pre-defined positions. Our approach, on the contrary, does not require stiff components embedded directly into the device. Instead, it uses a stretchable smart skin, and bases its sensing capabilities on a tomographic imaging technique that allows having a distributed sensing independent of the underlying design. The method is still in its initial stage, but the results prove its feasibility and open new opportunities in this research field.

MATERIALS AND METHODS

Electrical Impedance Tomography (EIT) is a well-established technique [3,4] that is used to infer the internal structure of the studied domain by estimating its conductivity distribution. Since its initial development, the technique has been used in different application fields spanning from geophysical analysis to patient ventilation monitoring.

In a typical EIT application, electrical current is injected into the studied body, and voltage potentials are measured at its boundaries. The acquired values are then processed to reconstruct the domain resistivity map. Given an initial homogeneous map, it is possible to detect changes in the domain conductivity due to local variation (Figure 1).

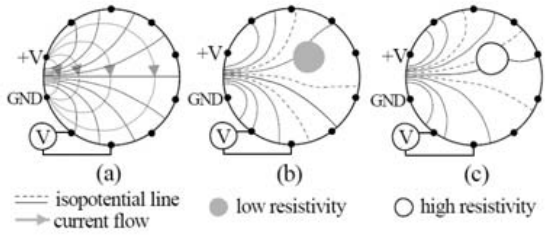

Figure. 1. Electrical Impedance Tomography changes due to local variation. (a) Reference measurements with iso-potential lines due to the current injection. (b) and (c) Changes in the iso-potential lines and measured voltage potential due to a change in resistivity.

SYSTEM DESCRIPTION

The system that we propose is a simplify version of a standard EIT device. We decided to develop our in-house system in order to be able to fully control its parameters both in the current injection phase, and in the possibility to choose the most appropriate measurement patterns. It consists of three main components: i) a current generator, ii) a channel selector, iii) and a computer used to perform the inverse problem solving. The channel selector circuit is designed to allow the control of which electrode acts as a current source, current sink (connected to ground), or none of the two (high impedance stage). An ATmega2560 microcontroller interfaced with Matlab controls the independent switches and is also used as data acquisition system. A customised version of EIDORS [5] is used to perform the inverse solving. At its current version, the system uses only 8 electrodes.

EXPERIMENTAL SETUP

A highly conductive stretchable textile – that changes its conductivity when stretched – was used as layer on which the EIT measurements were taken. The textile ($250x150mm^2$) was attached over a foam surface ($250x150x2mm^3$) that was placed over a dummy arm (diameter 30mm, total length 295mm) that can be bend between 0° and 90°. Using this experimental setup (Figure 2), we tested the capability of the sensing system to detect and measure different bending angles. Due to material stiffness of the foam media, and the structure of the dummy arm, we were able to test the effects of a single bending point.

For each of the measured angles, we performed a full cycle of EIT voltage acquisitions, and then the data was processed using Matlab.

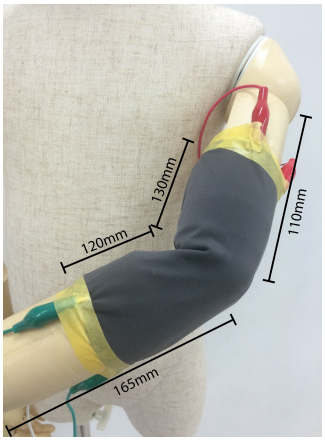

Figure 2. Experimental setup. The sensor was placed over a dummy arm that can bend and keep in position. We tested the capabilities of the sensing system to distinguish between different angles.

RESULTS

We tested the system by varying the bending angle from 0° to 90° with incremental steps of 15° each. For every configuration, we reconstruct the conductivity map associated to the inverse EIT problem, and then extract the region of interest (ROI) defined as the area formed by the pixel having intensity greater or equal to the 75% of the map maximum value. The number of pixel inside the region was used as measure of the angle. To maintain consistency among the results, we first run a series of simulation to better identify the parameter to use in the inverse problem solving, then we used the same parameters in every configurations. Figure 3 shows the results of selected angles.

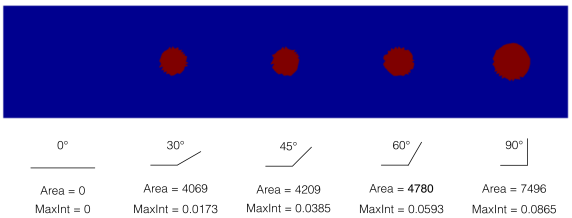

Figure 3. Results obtained on a single bending area. For each angle the region of interest (ROI) was extracted by considering the pixel having intensity greater or equal to 75% of the image maximum value. Area of the ROI, and the maximum intensity value of the image are also reported.

As the results suggest, with the increase of the bending angle, the area of region of interest increases. A similar trend can also be identified when the maximum intensity value is considered. These results can be explained with the fact that wider angles generate a stronger push of the underlying structure towards the conductive textile. As a consequence, the conductive textile stretches and thus changes its conductivity in the area where the push occurs.

It is possible to derive a simple rule to identify angles according to the extracted measurements. Due to limitations related to the conductivity map reconstruction – it can detect changes that have area wider than 10% of the domain width – we could not provide good values for the polynomial fit in the lower extreme. Results of the fit are presented in Figure 4.

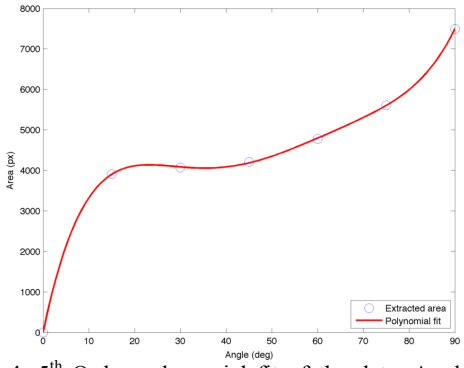

Figure 4. 5th Order polynomial fit of the data. Angle lower than 15° do not provide reliable value due to a limitation of the conductivity map reconstruction algorithm.

CONCLUSION AND DISCUSSION

We presented a novel method to detect and measure bending angle over bendable devices. The method used is based on a tomographic technique known as Electrical Impedance Tomography. One of the most important features of the use of such technique is that sensing capabilities are continuous in space, without the need to place stiff components within the sensing area.

As results suggest, by comparing a reference measurement with the ones acquired in later stages, it is possible to detect the region where an event – such bending – occurs. With a proper tuning of the system over the device, it is possible to derive the value of the bending angle as a measure of the size of the detected region. Future works include a better characterization of the measurements, and the increase of electrodes numbers to obtain better spatial resolution.

REFERENCES

[1] Vitiello, V.; Su-Lin Lee; Cundy, T.P.; Guang-Zhong Yang, "Emerging Robotic Platforms for Minimally Invasive Surgery," Biomedical Engineering, IEEE Reviews in, vol.6, no., pp.111,126, 2013.

[2] I. De Falco, M. Cianchetti, A. Menciassi "STIFF-FLOP surgical manipulator: design and preliminary motion evaluation" 4th Joint WorkShop on Computer/Robot Assisted Surgery (CRAS), October 14-16, 2014. Genoa, Italy.

[3] R. P. Henderson and J. G. Webster. An Impedance Camera for Spatially Specific Measurements of the Thorax. *IEEE Transactions on Biomedical Engineering*, vol. BME-25, no. 3, pp. 250-254, May 1978.

[4] Lytle, R. and Dines, K. An impedance camera: A system for determining the spatial variation of electrical conductivity. Technical report, Lawrence Livermore Laboratory, University of California, Livermore California. Report UCRL-52413.

[5] Adler A, Lionheart WR. Uses and abuses of EIDORS: an extensible software base for EIT. Physiol Meas. 2006 May, 27(5) S25-42.

A Novel Inflatable and Flexible Endoscope for Inherently Safe Minimally Invasive Examination

Agostino Stilli[1], Helge A Wurdemann[2] and Kaspar Althoefer[3]

[1]*Department of Informatics, King's College London*

agostino.stilli@kcl.ac.uk

[2]*Department of Mechanical Engineering, University College London*

[3]*School of Electronic Engineering & Computer Science, Queen Mary University of London*

INTRODUCTION

The use of flexible endoscopes (or flexible scopes), introduced into the human body through natural orifices, such as mouth, urethra, or anus, or through small incisions in the skin, allow obtaining and examining visual images of internal soft tissue. In today's medical interventions, these instruments are made of a sequence of rigid and/or semi-flexible links and joints [1], [2]. The operating handle includes either a manual or robotic tendon-based control system to steer and manoeuvre the endoscope tip around organs and, at the same time, to keep a safe distance between the scope and the internal anatomy. These robotic tools typically are made to exhibit a certain flexibility (adapting the endoscopes shape to the anatomy to a certain extent), but also have sufficient stiffness (to be pushed forward through narrow openings towards a desired target without bending excessively) – the stiffness of standard endoscopes cannot be controlled.

A different solution is proposed by Ginsberg et al. in [3], where the flexibility of the probe gradually varies throughout its length due to the changing in the material of the outer tube. In this case the level of compliance of the device can be regulated by means of compressing and extending a specific coil attached to the tip of the probe. Another approach is described in [4], where a flexible laparoscopic camera is able to switch between being rigid and compliant using vacuum pressure.

In this paper, we present our work towards the realisation of an inherently safe, soft, tendon-driven inflatable endoscope. The proposed design has been inspired by our previous work on soft inflatable devices described in [5], [6]. A tendon-based driven actuation was chosen because it minimises the encumbrance of the actuation means, and allowing to place the actuators outside the articulated structure and, in turn, considerably. Hence, this type of actuation ensures miniaturisation of the whole system, decreasing the structure's diameter to a minimum which makes our proposed device suitable for minimally invasive interventions. The proposed system is able to intrinsically vary its structural stiffness level allowing to have a high compliancy during insertion and investigation procedures and a firm pose when a stable.

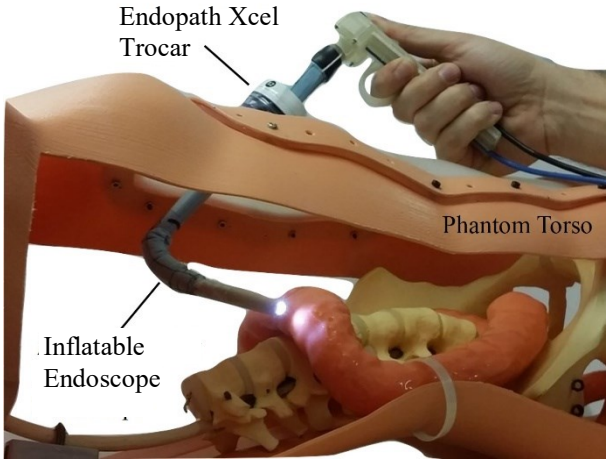

Fig. 1 The new antagonistically actuated endoscope accessing a 1:1 scale phantom of the abdominal cavity through a standard trocar port (12 mm diameter).

camera image at the site of interest is needed. The presented prototype has a diameter at the tip of 11.8 mm, hence, it is suitable to be inserted through a 12 mm trocar port.

MATERIALS AND METHODS

We have created a concept design for a novel inexpensive flexible and steerable soft endoscope (see Fig. 1). The design is inspired and based on our previous work presented in [4] [5]: The soft endoscope actuation principle is based on a combination of pneumatic and tendon-driven actuation. Pneumatic air pressure is used to inflate an air-tight extensible bladder which is fitted inside a non-stretchable fabric sleeve. The outer sleeve limits the inflation of the inner bladder allowing stiffness adjustment by the means of pressure regulation. A number of tendons are fixed to the scope's tip and guided along the length of the manipulator. This actuation means provides steering capability to the system exerting a longitudinal pulling force. When all tendons are pulled simultaneously and the pressure inside the bladder set, both actuation principle are working antagonistically and, hence, the stiffness of the endoscope is increased.

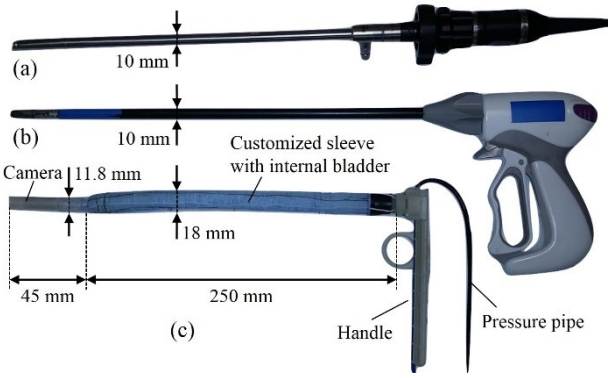

Fig. 2 Comparison of surgical instruments: (a) standard rigid endoscopic camera, (b) laparoscopic instrument, and (c) our new antagonistically actuated endoscope.

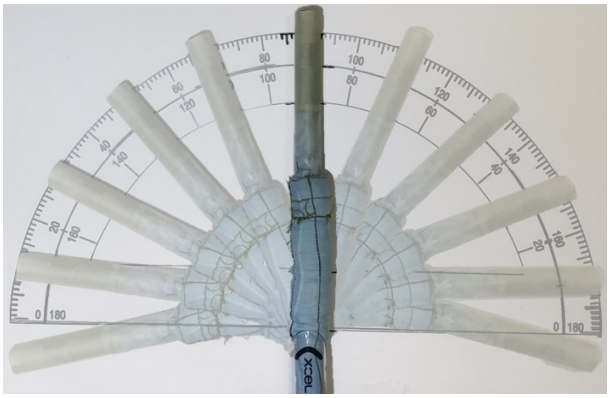

Fig. 2 Bending behaviour of the flexible endoscope in one plane actuated by a single tendon after the insertion through a 12 mm diameter trocar port.

The prototype of the flexible endoscope in Fig. 2(c) is composed of five main elements:

1. A customized sleeve machine-sewn in the shape of a cylinder with a length of 250 mm and a diameter of 18 mm, composed of two layers of polyester fabric;
2. An air-tight bladder made of flexible material (latex) fitted inside the sleeve and pressurised through a 4 mm diameter pressure pipe;
3. Four nylon tendons, 90° spaced apart along the perimeter of the sleeve and attached on one side to the base of the housing structure of the camera and on the other side with four individual sliders. The tendons have been embedded between the two layers of the fabric that composes the outer sleeve;
4. A commercially available endoscopic USB camera with a diameter of 8.5 mm and a length of 45 mm (Flylinktech® USB Endoscope);
5. A 3D printed ergonomic handle to hold the endoscope with a manual control system of four tendon sliders.

RESULTS

The inflatable endoscope proposed in this paper is composed of a single air chamber and a set of four tendons connected to the base of the camera integrated at the tip of the endoscope. Since the four tendons are arranged in the periphery of the central axis of our manipulator with a radial displacement of 90°, the movements of the scope are decoupled along the axis of the Cartesian space allowing intuitive manoeuvring. Figure 3 shows a number of experimental results demonstrating different bending angles: These sequences of body poses were achieved pulling a single tendon successively in two opposing directions keeping the pressure constant at 0.2 bar. The behaviour of the manipulator depends on the constraint posed by the trocar port that is rigid.

DISCUSSION

In this paper, a novel design for a flexible and steerable endoscope was presented and explored. The capability of the system to adjust its compliance by means of an antagonistic actuation principle (tendon-based and pressure actuation) leads to inherently safe contact with delicate soft tissue inside the human body. The novel flexible endoscope is able to elongate, bend around objects and increase stiffness to provide a stable camera view to the user. The squeezability of the manipulator body allows the scope to be easily inserted through narrow openings that are smaller than the actual diameter of the pressurised manipulator. In this manner, the novel flexible endoscope can be inserted through standard trocar ports without limiting its dexterity.
In future works, we will replace the current USB camera with a smaller endoscopic camera with a length. Further, we will explore how to enhance the manual control system for this endoscope combining tendon and pressure actuation.

REFERENCES

[1] P. J. Schuler, M. Scheithauer, N. Rotter, J. Veit, U. Duvvuri, and T. K. Hoffmann, “A single-port operator-controlled flexible endoscope system for endoscopic skull base surgery,” HNO, vol. 63, no. 3, pp. 189–194, 2015.

[2] A. Degani, H. Choset, A. Wolf, and M. A. Zenati, “Highly articulated robotic probe for minimally invasive surgery,” Proc. - IEEE Int. Conf. Robot. Autom. vol. 2006, pp. 4167–4172, 2006.

[3] G.G. Ginsberg, “Colonoscopy with the variable stiffness colonoscope”, Endoscopy, vol. 58, no. 4, pp. 545–552, 2003.

[4] A. Jiang, K. Althoefer, P. Dasgupta, and T. Nanayakkara, “The Core Snake, the variable stiffness laparoscopic camera,” in The Hamlyn Symposium on Medical Robotics, London, United Kingdom, 2013.

[5] A. Stilli, H. A. Wurdemann, and K. Althoefer, “Shrinkable, stiffness-controllable soft manipulator based on a bio-inspired antagonistic actuation principle,” in IEEE International Conference on Intelligent Robots and Systems, pp. 2476–2481, 2014.

[6] F. Maghooa, A. Stilli, Y. Noh, K. Althoefer, and H. A. Wurdemann, “Tendon and pressure actuation for a bio-inspired manipulator based on an antagonistic principle,” Robotics and Automation, IEEE International Conference on. pp. 2556–2561, 2015.

Cooperative Control with Distal Manipulation for Fetoscopic Laser Photocoagulation

G Dwyer[1], C Bergeles[2], F Chadebecq[1], V Pawar[3], E. Vander Poorten[4], S Ourselin[2], J Deprest[5], P De Coppi[6], T Vercauteren[2], D Stoyanov[1]

[1]Surgical Robot Vision Group, CMIC, University College London (UCL), [2]Translational Imaging Group, CMIC, UCL, [3]TouchLab, UCL, [4]Dept. Mechanical Engineering, KU Leuven, [5] University Hospital Leuven, [6]Institute of Child Health, UCL

george.dwyer.14@ucl.ac.uk

INTRODUCTION

Fetoscopic Laser Photocoagulation (FLP) is a minimally invasive fetal intervention used to treat Twin-Twin Transfusion Syndrome (TTTS)[1]. TTTS is a placental defect that causes an imbalance in the blood flow between fetuses, which can result in death or severe impairments. During the TTTS procedure, the surgeon manually manipulates a rigid (either straight or curved) fetoscope in order to observe the placenta and selectively coagulate vessels to sever the flow of shared blood supply. The process requires for the surgeon to manually scan the surface of the placenta to determine which vessels need to be coagulated in order to ablate vascular joins. This is technically difficult because the fetoscope must be kept approximately 10 mm from the placenta to deliver appropriate laser power for coagulating vessels while refraining from physical contact with the placenta which can lead to complications. The procedure can possibly be improved by increasing the dexterity and stability of the fetoscope by actuating the tip of the instrument and enhancing the stability of the instrument by an active robotic arm which assists the manipulation of the fetoscope. This could also assist in techniques to map the placenta as the position and orientation of the endoscope is known[2], [3].

Continuum mechanisms have been used in surgical robotics in order to potentially facilitate smaller diameter instruments and larger number of degrees of freedom (DOF). However, these mechanisms are often applied to single port surgery, intravascular or neurosurgery, where the mechanism is fixed outside the body (proximal to the surgeon) and controls all the movement from within (distal to the surgeon). In comparison, more established articulated mechanisms such as the Da Vinci surgical robot utilise both proximal and distal motion from the parallel linkage and wrist joints separately. This approach results in seven active DOF, four proximal and three distal (one of which being the end effector). While continuum robots, such as concentric tube robots [4], [5], have demonstrated over six DOF, they often have a comparatively small workspace and low pose accuracy. Even though small profile mechanisms have been presented using concentric tube robots coupled with a passive proximal arm for single port prostate surgery[6], the comanipulation of the device was not fully explored. The concentric tube robot was inserted through an endoscope with a working channel allowing the endoscope to be manipulated with the passive arm and the robot to be manipulated relative to the endoscope.

This paper presents the mechanism design and control of a two DOF concentric tube robot combined with the coupling to a seven degree of freedom robotic arm constrained to a remote centre of motion. The combination of the two actuation mechanisms allows the end-effector to be positioned with five degrees of freedom. The mechanism was designed to be compact and attachable to the proximal robotic arm. A cooperative control scheme is designed and implemented allowing the position of the camera to be controlled by the operator while the orientation of the tip is automatically controlled to remain perpendicular to the desired imaging plane.

METHODS

Instrument Design: The distal actuation mechanism was designed to be compact and easily attached to the proximal actuation mechanism. The mechanism provides two DOF to manipulate the axial rotation and translation of the nitinol tube. Both DOF are actuated from the back of the mechanism through a lead screw for the tube translation and a square shaft for the tube rotation following a similar design presented by Burgner *et. al.* [7]. A carriage is used to transmit torque from the motors to the nitinol tube as shown in 1a. The carriage contains the lead screw nut and a gear with a square 10 mm bore constrained in place with two rotational bearings either side. A linear bearing to provide the interface between the gear and square shaft is printed using wear resistant filament (iglide Tribo-Filament, Igus). The use of the carriage allows the inner tube to be easily swapped without dismantling the mechanism. The inner tube is fixed to a spur gear and two rotational bearings positioned either side of the gear. This is held in the carriage by fixing both bearings in place. The mechanism housing and carriage were 3d printed using PLA on a Ultimaker 2 and the inner tube couple using tough resin on a Formlabs 1+.

The instrument was then assembled with a steel outer tube with an inner and outer diameter of 1.8mm and 2.4mm respectively, and a nitinol inner tube, 1.4mm and 1.59. Dynamixel MX-28 motors (Robotis Inc., USA) are attached to the lead screw and square shaft at the back of the mechanism shown in 1b.

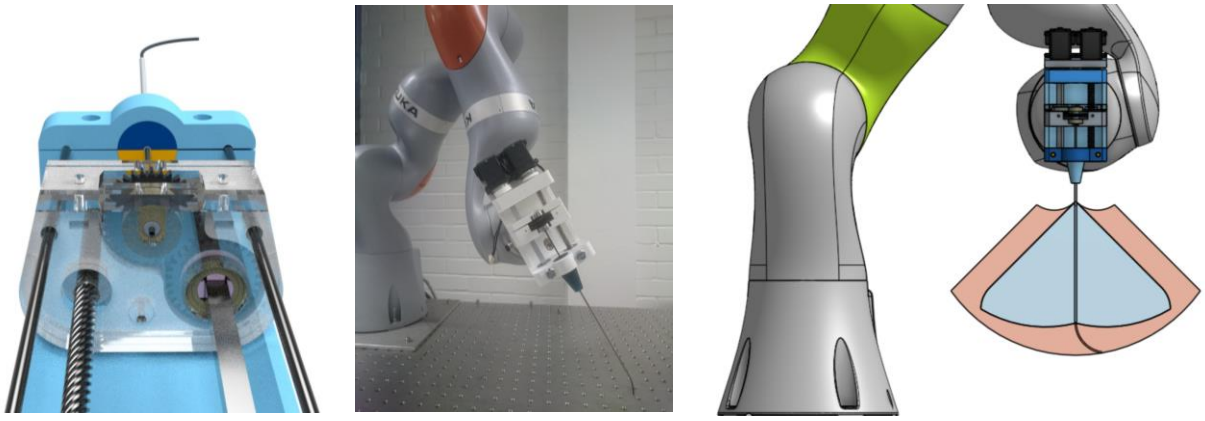

Figure 1: a) CAD render of the distal mechanism and workings of the carriage. b) The assembled mechanism coupled to a KUKA iiwa robot arm operating as the proximal co-manipulator. c) The reachable (red) and orientated (blue) workspace of the instrument

Instrument Control: The principle of this mechanism relies on the bending stiffness of the outer straight tube to be significantly larger than the stiffness of the inner tube, causing the shape of the inner tube to conform to the shape of the outer. This allows the overall shape of the instrument to be assumed as the shape of the outer tube and then from the tip of the outer tube an arc with the curvature of the inner tube, k, length extruded from the outer tube, l and bending plane given by the orientation of the tube, φ. With the length and orientation given by the motor encoder values. This can be represented as:

$$^{Shaft}T_{Tip} = T_{RotZ}(\varphi)\, T_{trans}\left(\frac{1-\cos(kl)}{k}, 0, \frac{\sin(kl)}{k}\right) T_{RotY}(kl) \quad (1)$$

Where $T_{RotZ}(\varphi)$ is a transform containing a rotation around the Z axis of angle φ and $T_{trans}(x, y, z)$ is a transform containing a translation along the X, Y and Z axis respectively.

Proximal Co-Manipulation: An articulated arm (KUKA LBR iiwa 7 R800) is used for the proximal manipulation of the instrument. The arm is a seven DOF arm with torque sensors on each joint. Minimally invasive surgery requires the instruments used to be constrained to a remote centre of motion (RCM) due to the small incisions used to access the inner anatomy through a port. A RCM constrains the motion to four DOF, translation, r, and rotations along the instrument shaft (Z axis), and extrinsic rotations of the X and Y axes. However, as the distal actuation mechanism provides continuous rotation along the z axis, the z axis rotation is restricted. From the RCM, the transform of the tip of the instrument shaft, in this case the outer tube, can be shown as:

$$^{RCM}T_{Shaft} = T_{RotZ}(\alpha) T_{RotY}(\beta) T_{RotZ}(-\alpha) T_{trans}(0, 0, r) \quad (2)$$

The KUKA direct servo application programming interface (API) provides the external force applied to the flange of the arm, after calibrating the weight of the tool attached. With the coordinate frame in the same orientation as T_{RCM} the x, y and z axis forces are mapped to incrementing the desired x, y and z position.

The desired position can then be mapped to α, β and r through:

$$\alpha = \tan^{-1}\left(\frac{y}{x}\right),\ r = \sqrt{x^2 + y^2 + z^2},\ \beta = \cos^{-1}\left(\frac{z}{r}\right) \quad (3)$$

A manually tuned PID controller is then implemented to minimise the external force on each axis by manipulating position of the arm. In order to keep a consistent orientation, the distal actuation mechanism is constrained to a certain position according to the current position of the instrument shaft. Firstly, the orientation of the tube, φ, that aligns the bending plane of the tube perpendicular to the desired imaging plane; and secondly, length of the tube extended, l, must be found to achieve the perpendicular constraint. The orientation of the tube can be found by finding the difference between T_{RCM} and T_{Shaft} around the z axis. While the length the can be found by finding the angle between the RCM z axis and the instrument shaft axis, θ.

$$\varphi = \alpha,\ \theta = \beta,\ l = \frac{\theta}{k} \quad (4)$$

As these constraints are resolved using the current position they are evaluated at the same frequency as the cooperative controller (avg 200Hz) to ensure any error in the tip orientation remains as low as possible.

RESULTS

The workspace of the presented instrument was calculated through simulation. The limits applied to each of the kinematic variables were:

$$\alpha \in [0, 2\pi], \beta \in \left[0, \frac{\pi}{4}\right], r \in [0, 140],$$
$$\varphi \in [0, 2\pi], l \in [0, 50]$$

Two workspaces were calculated, the reachable workspace and the orientated workspace, which is the workspace in which the device can adhere to the perpendicular constraint, eq. 4. This resulted in workspaces of 5607678.9 mm^3 and 2377427.2 mm^3 for the reachable and orientated workspace respectively. The orientated workspace allows a planar surface to be scanned with the area of a circle with a diameter of 218.5 mm.

DISCUSSION

We have developed a new concentric tube robot design for fetoscopic procedures. The mechanism has a small diameter of 2.4mm in order to minimise entry access trauma. Our device, while still preliminary, has the advantage of being mounted onto a compliant robotic arm that can sense interaction forces. The control system for this robot is developed to allow improved fetoscopic surgery that can observe and ablate placental vasculature to ensure complete and accurate photocoagulation that severs the TTTS condition. In our future work we would like to extend this platform to include visual servo methods using both ultrasound and fetoscopic information as well as more advanced co-manipulation control.

ACKNOWLEDGEMENT

This work was supported through an Innovative Engineering for Health award by Wellcome Trust [WT101957]; Engineering and Physical Sciences Research Council (EPSRC) [NS/A000027/1] and the EPSRC- funded UCL Centre for Doctoral Training in Medical Imaging (EP/L016478/1).

REFERENCES

[1] F. Slaghekke, E. Lopriore, L. Lewi, J. M. Middeldorp, E. W. Van Zwet, A. Weingertner, F. J. Klumper, P. Dekoninck, R. Devlieger, M. D. Kilby, M. A. Rustico, J. Deprest, R. Favre, and D. Oepkes, "Fetoscopic laser coagulation of the vascular equator versus selective coagulation for twin-to-twin transfusion syndrome : an open-label randomised controlled trial," *Lancet*, vol. 383, no. 9935, pp. 2144–2151, 2014.

[2] P. Daga, F. Chadebecq, D. Shakir, L. C. Garcia-Peraza Herrera, M. Tella, G. Dwyer, A. L. David, J. Deprest, D. Stoyanov, T. Vercauteren, and S. Ourselin, "Real-time mosaicing of fetoscopic videos using SIFT," *SPIE Med. Imaging Proc.*, vol. 9786, pp. 1–7, 2015.

[3] M. Tella, P. Daga, F. Chadebecq, S. Thompson, D. I. Shakir, G. Dwyer, W. Ruwan, J. Deprest, D. Stoyanov, T. Vercauteren, and S. Ourselin, "A combined EM and visual tracking probabilistic model for robust mosaicking of fetoscopic videos," *IEEE Proc. 7th Int. Work. Biomed. Image Regist.*, 2016.

[4] R. J. Webster, J. M. Romano, and N. J. Cowan, "Mechanics of Precurved-Tube Continuum Robots," *IEEE Trans. Robot.*, vol. 25, no. 1, pp. 67–78, Feb. 2009.

[5] P. E. Dupont, J. Lock, B. Itkowitz, and E. Butler, "Design and Control of Concentric-Tube Robots," *IEEE Trans. Robot.*, vol. 26, no. 2, pp. 209–225, Apr. 2010.

[6] R. J. Hendrick, S. D. Herrell, and R. J. Webster, "A multi-arm hand-held robotic system for transurethral laser Prostate surgery," in *IEEE International Conference on Robotics and Automation (ICRA)*, 2014, pp. 2850–2855.

[7] J. Burgner, P. J. Swaney, R. a. Lathrop, K. D. Weaver, and R. J. Webster, "Debulking From Within: A Robotic Steerable Cannula for Intracerebral Hemorrhage Evacuation," *IEEE Trans. Biomed. Eng.*, vol. 60, no. 9, pp. 2567–2575, Sep. 2013.

Continuum Manipulators Mechanics, A Comparative Study of Three Methods for Surgery Applications

S.M.Hadi Sadati[1], S. Elnaz Naghibi[2], Ali Shiva[1], Kaspar Althoefer[2], T. Nanayakkara[1]

[1]*Department of Informatics, King's College London, UK.*

[2]*Department of Material and Mechanical Engineering Queen Mary, University of London, UK.*
seyedmohammadhadi.sadati@kcl.ac.uk

INTRODUCTION

Control and optimization of continuum manipulators with compound structure is a controversial subject. Different kinematic and dynamic modeling approaches have been presented and tested in previous research with advantageous and limiting features in different which can be categorized into three groups: 1) Lumped model elements using Lagrangian demonstration, which includes a number of rigid-link pieces combined with springs and dampers. 2) Cosserat rod model, as used in [1] which leads to a boundary value problem. 3) Approximate solutions on the basis of identification of the system with a polynomial or series based shape functions [2] which construct a setup-specific model. The approximate solutions, appropriate for control purposes, are more precise and increase the performance but do not account for the structural characteristics, while the lumped model elements and Cosserat rod model suffer from heavy calculations despite there being suitable for design and optimization. In most of these methods, numerical inaccuracy and singularities in deriving the inverse kinematics are inevitable. Additionally, force control is essential especially in medical and surgery applications. In this paper, a comparative study of three main proposed methods of such manipulators is presented. Lumped system, continuous constant curvature and shape function identification based modeling methods are derived in a unified mathematical framework and investigated in simulation and experiments to clarify their advantageous in different applications.

MATERIALS AND METHODS

The spatial orientation of a continuum manipulator can be derived based on system kinematics. This can be used as the system control model by predicting the geometrical relation between input lengths and output orientation; however, a more precise model should consider mechanical properties of the manipulator as well. These models can be addressed in three main groups.

- Equivalent Lumped Model:

A continuum manipulator can be assumed as a highly articulated rigid link system where spring-damper supported spherical joints connect an infinite number of rigid plates together. Denavit-Hartenberg method is used to describe the system kinematics. TMT method which is a vector form of Lagrange equation of motion can be used to simplify the derivation process as in. We used an automatic algorithm based on this method as in [3] to simulate a four-rigid-disk lumped model of an STIFF-FLOP manipulator [4]. The model can capture the transient behavior of the manipulator with high accuracy and good performance. This model can be used for control design purpose and provides some structural information that can be used for design optimization.

- Constant curvature Model:

As the most common used model, the manipulator is considered as a continuous constant curvature curve as in [4]. Here, a geometric map (f_G) and a structural specific map (f_S) describe the system mechanics. f_G maps curvature parameters to curve tip position. It can be found from constant curvature assumptions using a set of transformations. This map suffers from inherent singularity for the straight position. f_S maps input parameters space for hydraulic and tendon driven models or input pressures (p) for pneumatic actuators to curvature parameters space. Despite the tendon driven manipulators, for pneumatic actuators, a second step is needed to map pressure inputs to actuator length. For pneumatic braided extensible actuators two analytical solutions are presented based on the principle of virtual work. The most famous model which is used by Trivedi for the first time for continuum manipulators. The principle of virtual energy for a chamber is $w_{C,\lambda} + w_{G,\lambda} = 0$, where w_C is the chamber body deformation energy, w_G is the air pressure work, $\lambda = l/l0$, which is considered as the only system state, is the axial deformation rate, l_l and l_d are the module axis initial and deformed length. This can be solved for $p = f_S^{-1}(q)$. Trivedi presentation of this formula in his paper is not correct. For a dense threaded chamber as in most actuators of this type where $\gamma \approx \pi/2$ and chamber deformation does not change γ significantly, the thread helix radius does not change significantly ($r_c \approx r_{c0}$) and the relation simplifies. Sadati recently used a new method called geometry deformation inspired by Rivlin with the same assumption as Trivedi [1]. He only constrains the outer diameter of the chamber to the thread deformed diameter and does not constrain the chamber surface slip motion w.r.t thread which is a source of some errors in Trivedi's model [1]. Here we present a third very simple model. We assume a dense thread constrains the chamber inner body. So the internal area of the actuator preserves. The outer radius of the chamber shrinks as the actuator extends. A homogeneous incompressible cylinder undergoing axial elongation with axial deformation ratio λ, experiences radial and circumferential deformation

with deformation rate $1/\sqrt{\lambda}$ to satisfy incompressibility criteria. The Neo-Hookean model suggests the deformation energy of body becomes $w_S = Ea_{t0}l_0(\lambda^2 + 2/\lambda - 3)/6$, where a_{t0} is the initial chamber thickness area. A comparison between the results of these methods for one actuator from STIFF-FLOP manipulator is presented in Fig. 1. The figure shows a small difference in Trivedi and simple model and their good accuracy in predicting an STIFF-FLOP actuator chamber. Sadati model behaves differently and shows less accuracy here. f_S need to be derived by considering body deformation energy virtual work too. A simple solution for body deformation energy (w_S) can be found according to Euler-Bernoulli beam theory. A more accurate but more complex solution is presented by Sadati in [4]. This method predicts the cross-sectional deformation mechanics too. The model has an average of 12% error. A simple solution for manipulators with body shell, i.e. STIFF-FLOP, can be found by assuming the braids on the inner surface of the chambers.

Constant curvature assumption results in big errors for systems with a relatively high external load. Mahvash used constant curvature assumption for geometric map of an eccentric tube catheter and then used a modifying map to model the static force effects [5]. Here we present a similar solution to using Castigliano's method for continuum manipulators. The constant curvature model has an average of 40% error, while this is reduced to 30% for the modified version.

- Identification Based Model

The static and dynamic behavior of a continuum manipulator can be approximated with experiment based identification of an assumed shape function constants [2]. The model by Godage assumes to be separated to a time-dependent vector term ($\gamma(t)$) and a shape defining matrix term ($\Psi(\epsilon)$) as a function of geometrical variables (s) which is a parameter describing the curve axis length. The model is considered to be of the form of a Taylor series with a finite number of terms with shape dependent term as its time-independent coefficients and time-dependent base shape function. Choice of the shape function and time-dependent function can be based on observation, guessed solution or completely arbitrary. They should satisfy boundary and initial conditions and the Taylor Series converges by increasing the number of terms. Here we introduce a simpler series each of which with eight coefficients to be determined based on experimental results and using Least Square Value optimization. Simulation results show this method is fast both in parameter identification and in simulation and gives the most accurate results in predicting the static behavior of the manipulator which makes it a perfect choice for control purposes (Fig. 2). However, the model does not any give structural information which is necessary for design optimization. Besides the complexity of the series solution make any further analytical analysis such as dynamic modeling and controller design and stability analysis a hard task.

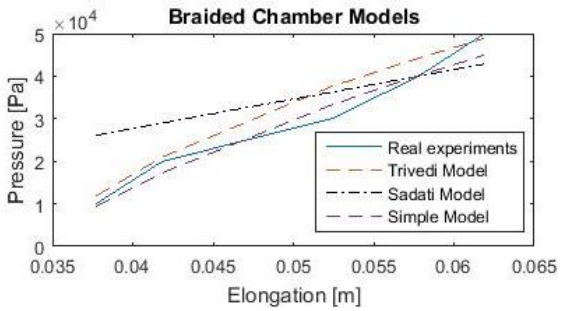

Fig. 1. Comparison of modelling methods for a STIFF-FLOP pneumatic braided extensor actuator.

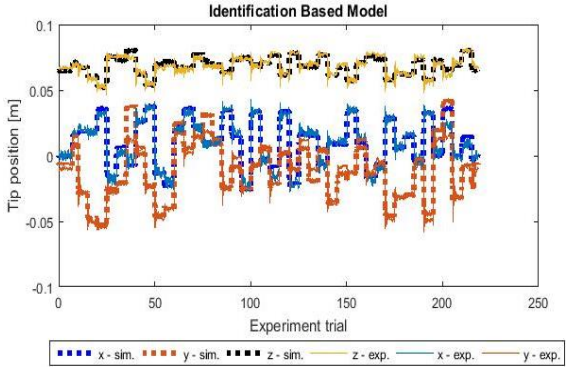

Fig. 2. Identification based modelling of a STIFF-FLOP arm manipulator section. ¾ of the data points are used for training and the rest for verification.

CONCLUSION AND DISCUSSION

Lumped system model, constant curvature model, and identification based model are derived and implemented for an STIFF-FLOP arm continuum manipulator section. Our study shows the advantageous of identification based model in terms of accuracy and performance, while dynamic behavior prediction and control method implementation are easier with lumped system model. Different constant curvature models based on the principle of virtual work shows less accuracy but the good incorporation of structural characteristics which makes them suitable for design optimization purposes.

REFERENCES

[1] D. Trivedi, et. al., "Model-based shape estimation for soft robotic manipulators: The planar case," J. of Mech. and Robotics, vol. 6, no. 2, p. 021005, 2014.

[2] I. S. Godage, et. al., "Shape function-based kinematics and dynamics for variable length continuum robotic arms," IEEE ICRA, 2011.

[3] S. Sadati, et. al., "An Automatic Algorithm to Derive Linear Vector Form of Lagrangian Equation of Motion with Collision and Constraint," Procedia Computer Science, vol. 76, pp. 217–222, 2015.

[4] S. M. H. Sadati, et. al., "A Geometry Deformation Model for Compound Continuum Manipulators with External Loading," IEEE ICRA, 2016.

[5] M. Mahvash, et. al., "Stiffness control of a continuum manipulator in contact with a soft environment," IEEE IROS, 2010, pp. 863–870.

Implementation of an analytical magnetic model for medical robots design

E.S. Barjuei[1], J. Li[1,2], G. Ciuti[1], Y. Hao[3], P. Zhang[3], Q. Shi[3], A. Menciassi[1], Q. Huang[2,3] and P. Dario[1,2]

[1]*The Biorobotics Institute, Scuola Superiore Sant'Anna, Italy*
[2]*Beijing Innovation Center for Intelligent Robots and Systems, Beijing Institute of Technology, China*
[3]*Intelligent Robotics Institute, School of Mechatronical Engineering, Beijing Institute of Technology, China*
erfan.shojaei@sssup.it

INTRODUCTION

Nowadays, a large amount of medical robots exploit magnetic field sources as the main actuation and navigation mean. Magnetic locomotion represents a promising alternative to conventional actuation approaches (*e.g.*, electric and pneumatic) as it avoids for direct electrical contacts; moreover, steady / strong linkage and controlled navigation between objects, in absence of mechanical and rigid connections, can be considered as the most significant challenge but also benefit of using magnetic fields in medical applications.
Several research groups are working on implementing accurate models for the design of magnetically-driven robots; therefore, advanced developments of medical devices will be expected in the near future [1].
Two different magnetic-based approaches can be followed, *i.e.* use of permanent or electromagnetic sources. The main benefit of a permanent magnet over electromagnet is that the first does not need electrical current to generate its magnetic field and a dedicated, often bulky and heavy, cooling system. Moreover a permanent magnet is smaller in size with respect to an electromagnet source with the same magnetic field density produced [2].
Accurate and robust magnetic models are mandatory for the design and development of magnetically-driven medical robots and a large amount of works have been carried out in the field of magnetic modeling and analysis up to now [3].

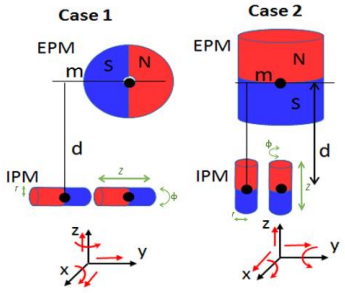

Fig. 1. Typical working scenarios for magnetically-driven medical robots. *d* is the EPM-IPM distance, *m* is the linear mismatch along *y*. DOFs for each configuration are shown using red arrows.

The aim of this paper is to provide a ready and easy-to-use implementation of an accurate and reliable analytical magnetic model able to derive magnetic forces and torques acting on a medical robot (with an internal permanent magnet -IPM- embedded) through an external permanent magnetic source. Two of the most common operating scenarios are illustrated in Fig.1, where two configurations of external permanent magnets (EPMs) and IPMs are presented. Besides, the allowed degrees-of-freedom (DOFs) for the IPMs, due to the motion of the EPMs, are shown accordingly. Both configurations of Fig. 1 can be followed for the design and development of medical robots, such as magnetically-driven endoscopic robotic capsules where an IPM, embedded onto the device, is robotically-driven by an EPM [1].

MATERIALS AND METHODS

An analytical magnetic model has been implemented and it describes the magnetic field as well as the forces and torques among permanent magnets. According to the work in [3], the magnetic force and toque equations are based on a current model methodology. Magnetic force, which is exerted on the IPM by the external magnetic field, is represented as follows:

$$\vec{F} = M \int_{z_1}^{z_2} \int_0^{2\pi} \left[cos\emptyset B_z \vec{x} + sin\emptyset B_z \vec{y} + \left(-sin\emptyset B_y - cos\emptyset B_x \right) \vec{z} \right] R d\emptyset' dz' \quad (1)$$

whereas, the magnetic torque can be written as follows:

$$\vec{T} = M \int_{z_1}^{z_2} \int_0^{2\pi} -\left(r_y sin\emptyset B_y + r_y cos\emptyset B_x + r_z sin\emptyset B_z \right) \vec{x} + \left(r_x sin\emptyset B_y + r_y cos\emptyset B_x + r_z cos\emptyset B_z \right) \vec{y} + \left(r_x sin\emptyset B_z + r_y cos\emptyset B_z \right) \vec{z} R d\emptyset' dz' \quad (2)$$

In Eqs.(1) and (2), for the IPM, M represents the magnetization magnitude, R is the radius, $r\ (r_x, r_y, r_z)$ is the position vector from the torque calculation point to the integration point in the IPM, $\emptyset$ is the standard polar coordinate and z_1 and z_2 represent the dimensional parameters.
A comparison analysis for evaluating the accuracy of the model in terms of magnetic flux density ($\vec{B}$), magnetic force ($\vec{F}$) and magnetic torque ($\vec{T}$) through analytical and numerical (*i.e.*, Finite Element Method - FEM) methods has been performed. The analysis for $\vec{B}$ is to compare the results of a set of measuring points along different axes of a radially magnetized cylinder (*e.g.*, EPM in Fig.1 case 1) and axially magnetized cylinder (*e.g.*, IPMs in Fig. 1 case 1 and 2 and EPM in case 2). Measuring points are distributed along *x*, *y* and *z* axes of the radially magnetized EPM and *x*, *z* axes of axially magnetized IPM, with a discrete incremental step of 25 mm (see Fig. 2). The parameters for this test are reported in Table 1 and labelled as EPM1 and IPM1.

The analysis for $\vec{F}$ and $\vec{T}$ is to compare the results where the EPM and IPM are configured as illustrated in Fig. 1. For those tests, parameters are reported in Table 1 and labelled as EPM2 and IPM2.
Data have been specifically set only for testing purposes. Average and maximum errors for the comparison analysis are computed for $\vec{B}$, $\vec{F}$ and $\vec{T}$.

Table. 1. Parameters for IPM and EPM.

Parameters	M (kA/m)	Length (mm)	R (mm)
EPM1	1114	80	Outer: 45, Inner: 7
IPM1	1154	25	25
EPM2	430	80	45
IPM2	800	12	3

It is worth mentioning that the proposed model can be used for the realization of different magnetically-driven robots with the same design concepts of Fig. 1 (axially and diametrically magnetized cylindrical magnets).

RESULTS

The results for magnetic flux density are illustrated in Fig. 2, where Bmx, Bmy, Bmz are the results from the derived model along the *x*, *y*, *z* axes (shown in Fig. 1, case 1). Similarly, Bcx, Bcy, Bcz are the results from the FEM method along the *x*, *y*, *z* axes. For IPM, *y* component was not calculated because of the symmetrical feature of the magnetic field (same of x component). The average and maximum errors for each axis of the magnets, between the analytical model and FEM method, are reported in the table of Fig. 2 , where EBX1 and EBZ1 are the errors along the *x* and *z* axes respectively, whereas EBX2, EBY2 and EBZ2 are the errors along *x*, *y* and *z* axes respectively (Fig. 1, case 1).

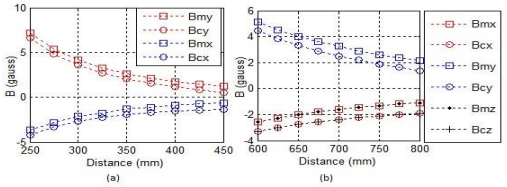

	EBY1	EBX1	EBX2	EBZ2	EBY2
Average	0.61	0.62	0.77	0.77	0.72
Maximum	0.74	0.76	0.83	0.83	0.78

Fig.2. Magnetic flux density ($\vec{B}$) comparison analysis between analytical and numerical data. Average and maximum errors for $\vec{B}$ (unit: gauss) are reported in the table.

Fig. 3 (a) illustrates the forces with different distances along axis *z* (with mismatch along y axis of 0 mm) in case 1 of Fig. 1. Fig.3 (b) shows the forces and torques with different mismatches along y (with EPM-IPM distance of 0.1m and distance along x axis of 0 mm) in case 1 of Fig. 1. F_{cy}, F_{cy}, F_{cz} and T_{cx} are forces and torques obtained from FEM method and F_{mx}, F_{my}, F_{mz} and T_{mx} are forces and torques obtained from the analytical model. Fig.4 (a) represents the forces with different distances along axis z (with mismatch along y axis of 0 mm) in case 2 of Fig. 1. Fig.4 (b) demonstrates the forces and torques with different mismatches along y axis (with EPM-IPM distance of 0.08m and distance along x axis of 0 mm) in case 2 of Fig. 1. F_{cx}, F_{cy}, F_{cz} and T_{cx} are forces and torques obtained from FEM method and F_{mx}, F_{my}, F_{mz} and T_{mx} are forces and torques obtained from the analytical model.

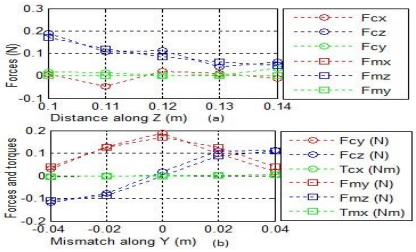

Fig.3. Force analysis in different configurations of axially magnetized IPM and radially magnetized EPM.

To exemplify the results in more details, the errors as average and maximum values for calculated forces and torques are also reported in the table of Fig. 4, where $err_{F_{z1}}$ is the force error of Fig.4 (a), and $err_{F_{y2}}$, $err_{F_{z2}}$, $err_{T_{x2}}$ are the errors for forces and torques of Fig.4 (b).

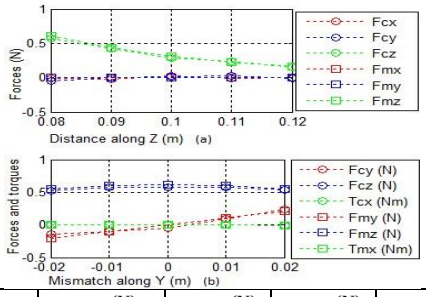

	$err_{F_{z1}}$(N)	$err_{F_{y2}}$ (N)	$err_{F_{z2}}$ (N)	$err_{T_{x2}}$ (Nm)
Average	0.0199	0.0306	0.0223	2.3e-4
Maximum	0.043	0.0622	0.04	5.0e-4

Fig.4. Force analysis at different configurations of axially magnetized IPM and axially magnetized EPM. Average and maximum errors for force and torque are reported in the table.

The obtained results shown that the analytical magnetic model, in terms of $\vec{B}$, $\vec{F}$, $\vec{T}$, and the FEM method matched with a maximum error 0.0622 N.

CONCLUSION AND DISCUSSION

In this work an analytical magnetic model for calculating forces and torques generated by EPMs and IPMs in two different configurations has been developed and validated with a numerical FEM method. The results show that the analytical model represents a suitable and reliable tool for the design of magnetically-driven medical robots.

ACKNOWLEDGEMENT

This work was partially supported by the EU EndoVESPA project in ICT 24 - 2015 (Grant Agreement No. 688592) and performed in part within a joint research collaboration between the Scuola Superiore Sant'Anna and the Beijing Institute of Technology.

REFERENCES

[1] L. Sliker, G. Ciuti, M. Rentschler, and A. Menciassi, "Magnetically driven medical devices: a review," *Expert review of medical devices*, 2015.

[2] D. Jiles, *Introduction to magnetism and magnetic materials*. CRC press, 2015.

[3] E. P. Furlani, *Permanent magnet and electromechanical devices: materials, analysis, and applications*. Academic press, 2001.

Haptic Guidance Schemes for Robot-Assisted Minimal Invasive Fetal Surgery

C. Gruijthuijsen[1], A. Javaux[1], A. Devreker[1], T. Vercauteren[2],
S. Ourselin[2], D. Stoyanov [3], J. Deprest[4], D. Reynaerts[1], E. Vander Poorten[1]

***Abstract*— The GIFT-Surg Project (*Image-Guided Intrauterine Minimally Invasive Fetal Diagnosis and Therapy*) is a Wellcome Trust/EPSRC funded project that started in July 2014 and that runs until June 2022. The project focuses on advancing the state of clinical practice in fetal surgery by developing novel technology that could potentially assist the surgeon during diagnosis and therapy of a number of serious fetal conditions. Treatment at an early gestational stage is believed to influence the chance for a positive outcome of the conditions that are addressed by GIFT-Surg. However, early treatment also means that the structures in scope are smaller and that these structures are more fragile. Consequently, the project aims to develop technology that allows displaying greater levels of precision and dexterity. This abstract sketches a number of guidance schemes geared at offering the right amount of assistance and precision necessary to accomplish the surgical task successfully. A detailed analysis of the problem and tracking experiments have been conducted to extract the requirements for the envisioned stabilisation system. Based on this information, the argumentation for using a high-bandwidth back-drivable comanipulation robot is provided. Next, a number of interesting guidance schemes are presented. Through experiments with surgeons, the appropriateness of at least some of these schemes has already been demonstrated.**

I. Introduction

The surgical skills required are quite demanding for conducting Minimal Invasive Surgeries (MIS) during fetal therapeutic interventions. The surgeon inserts his instrument through an incision on the womb in order to access the inside of the uterus and manipulates the surgical tool with high precision and dexterity in order to execute the necessary therapeutic steps [1]. Another difficulty of MIS interventions is the limited vision. The surgeon is only provided with a 2D image of the inside of the uterus and an ultrasound scan, and thus must reconstruct mentally the 3D scene [1]. If the instrument handling could be facilitated, the current mental load of the surgeon could be alleviated. This is one of the potential benefits of introducing a robotic system in a comanipulation set-up, i.e. having both the surgeon and the device manipulating the instrument in synergy. The design of such a system must satisfy some requirements in order to be integrated in the operating room. These were carefully studied. Some aspects are described in later sections.

Research funded by Wellcome Trust and EPSRC, project GIFT-Surg

[1]KU Leuven, Department of Mechanical Engineering, Leuven, Belgium allan.javaux@kuleuven.be

[2]Department of Medical Physics & Biomedical Engineering, University College London, London, United Kingdom

[3]Department of Computer Sciences, University College London, London, United Kingdom

[4] University College London Hospitals, London, United Kingdom; University Hospital Leuven, Leuven, Belgium

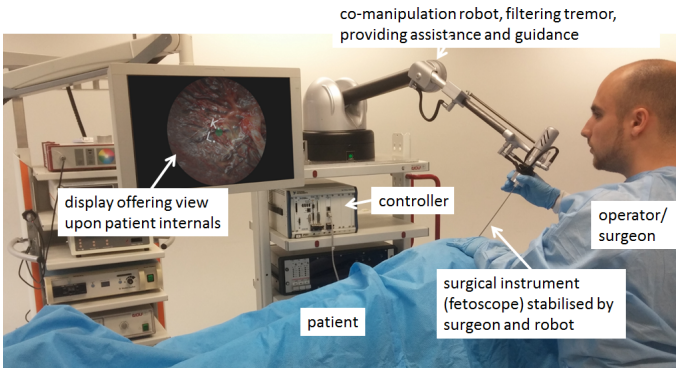

Fig. 1. A possible layout for robot assisted fetal surgery via comanipulation.

II. Materials and Methods

A. Envisioned system layout

We have been tracking the surgical tool's position during clinic interventions treating the TTTS (Twin-to-Twin Transfusion Syndrome) fetal disorder. This data has provided us with an estimate of the required workspace for instrument handling, as seen in Fig.2, and thus giving design guidelines for the robotic device. A possible set-up could be as represented in Fig.1. The surgeon holds the surgical tool attached to a stabilizing robot. The robotic device and its hardware are positioned aside leaving enough room for the rest of the staff, e.g. space is required for an ultrasound operator who scans continuously the inside of the uterus. The different components are described hereafter.

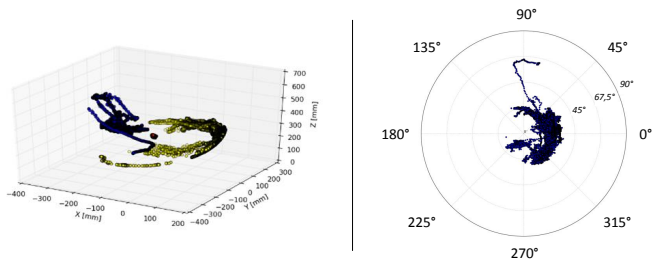

Fig. 2. Example workspace occupancy of a TTTS therapeutic intervention.

B. Hardware setup

A crucial requirement for the robotic system is back-drivability. This is necessary as the surgeon will not accept being restrained in his/her motion. Additionally, it was found that a force in the order of 20N had to be delivered. After a survey of the commercially availabe haptic devices, the Virtuose6D (Haption S.A., Laval, France) was chosen as it best meets the requirements in terms of workspace and payload. Experiments were done with an in-house built flexible fetoscope, based on [2], which is equipped with a chip-on-tip camera, a light source, a therapeutic laser and a distance sensor.

C. Software Architecture

The software system that was implemented to monitor and steer all the components combined the middleware frameworks ROS and OROCOS. They allow the communication between hardware and software process while respecting real-time requirements. A user-friendly Qt GUI was developed to combine different guidance schemes on-the-fly.

III. Haptic Guidance

Following guidance schemes have been implemented.

A. Maintaining pivot point

The incision provides a natural moving pivot point through which the instrument always passes. In consequence, the local stresses applied on the surrounding tissue may be quite large and depend on the surgeon's manoeuvres. An assistive device may help reduce the stress level e.g. by imposing a fixed pivot point at a strategic location as such relaxing the neighbouring tissue (Fig.3)

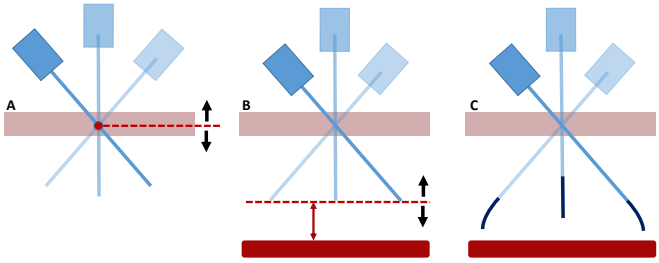

Fig. 3. Different guidance schemes were implemented, some of which are *a)* maintaining pivot point, *b)* keeping distance to surface, *c)* maintaining orientation of tip.

B. Keeping distance to surface

Another haptic guidance scheme helps the surgeon to maintain a constant distance to a certain surface. For certain tasks such as ablation it is important to maintain such distance as it would help to control the ablation process and additionally embeds a certain safety features helping indirectly to avoid contact with such sensible tissue (Fig.3). For treating TTTS [3] the distance to the placenta is to be controlled and contact between the laser fiber and the placenta could cause irrepairable damage.

C. Maintaining orientation with respect to surface

With a flexible actuated endoscope, it becomes possible to orient the tip of the instrument while in a specific pose. However, leaving this task to the surgeon could increase his/her mental load. Considering the set-up explained previously, a control scheme capable of maintaining a desired orientation w.r.t. a known surface was developed. For a given surface normal the distal instrument DoF and the stabilizer's joints are coordinately controlled to maintain perpendicularity to the surface.

D. Tremor filtering

In order to improve surgical precision, tremor could be cancelled out. This can be done fairly easy by introducing virtual damping. The damping will dampen out the surgeon and/or instrument motion.

IV. Experiments

Different experiments were conducted. The haptic schemes were first tested in virtual reality with a dummy tool. Once the parameters were tuned, the tool was integrated. The results were successful. Fig.4 shows how the controller maintains the orientation of the tip always perpendicular to a flat placenta phantom.

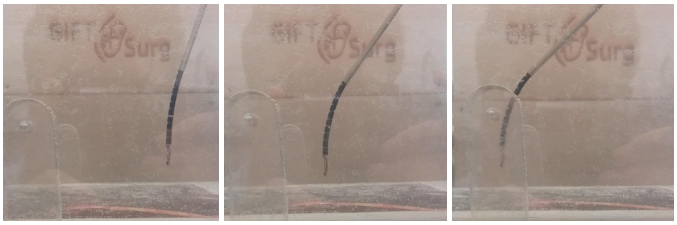

Fig. 4. Coordinated comanipulation control. The images nicely show how the tip can be controlled to be perpendicular to the placental surface regardless of the instrument pose.

V. Conclusion

This abstract introduces a comanipulation setup that has been designed for enhancing the controllability of miniature active fetoscopes. The system was integrated and offers various assistance schemes that can be switched on-the-fly. Some first experiments already showed the potential of the set-up. The system is ready for more extensive experiments with clinicians.

References

[1] Z. Lin, M. Uemura, M. Zecca, S. Sessa, and H. e. a. Ishii, "Objective skill evaluation for laparoscopic training based on motion analysis," *IEEE Trans. on Biomedical Eng.*, vol. 60, no. 4, pp. 977–85, 2013.

[2] A. Devreker, B. Rosa, A. Desjardins, E. Alles, L. Garcia-Peraza, E. Maneas, D. Stoyanov, T. Vercauteren, A. David, J. Deprest, S. Ourselin, D. Reynaerts, and E. Vander Poorten, "Fluidic actuation for intra-operative in situ imaging," in *Intelligent Robots and Systems, 2015. (IROS 2015). Proceedings. 2015 IEEE/RSJ International Conference on*, 2015, p. accepted for publication.

[3] C. Gruijthuijsen, A. Javaux, G. Borghesan, T. Vercauteren, D. Stoyanov, S. Ourselin, J. Perret, D. Reynaerts, and E. Vander Poorten, "Haptic guidance in comanipulated laser surgery for fetal disorders," in *Actuator*, 2016.

A Real-Time Collision Avoidance Simulation Software Tool for a Multi-Robot, Unstructured and Time-Variant Scenario

D.M. De Micheli[1], M. Curti[1], A. Diodato[2], G. Ciuti[2], A. Menciassi[2]

[1]*S.M. - Scienzia Machinale Srl, Pisa, Italy*
[2]*The BioRobotics Institute, Scuola Superiore Sant'Anna, Pisa Italy*
dmdemicheli@smrobotica.it

INTRODUCTION

Collision avoidance is mandatory when manipulators operate in an unstructured environment. The problem can be addressed in many ways, however knowledge of the involved geometries and of their mutual distance is necessary in order to plan and/or adjust manipulator trajectories [1]. In order to achieve a reliable motion planning, a collision avoidance strategy is necessary [2].
A collision avoidance strategy, based on an on-line collision simulator, will be developed within the framework of the FUTURA project. The FUTURA project (Focused Ultrasound Therapy Using Robotic Approaches – www.futuraproject.eu) proposes a robotic-assisted platform for flexible non-invasive HIFU therapy. In the FUTURA computer-integrated surgical scenario, geometric shapes may be either known or unknown; this latter case being represented by (at least) the patient and the surgeon(s). Information about a-priori unknown geometry is collected from additional devices (*e.g.*, Kinect sensor) and, combined with the a-priori knowledge of other structured geometries, lead to an accurate 3D reconstruction of the robotic scenario; this is crucial for planning a surgical task in a safe and reliable manner. It allows to position the manipulators into the surgical environment in complete freedom and safety, by leaving to the operator extended possibilities of movements. Moreover, the possibility to simulate movements of the robots, in addition to the actual ones, provides the operator with a further wide freedom of movement and action; with the 3D reconstruction the future trajectories, selected among all possible movements of the system, will reach the desired position avoiding collisions between robots and operators, both in structured and unstructured environments.
The on-line collision simulator, representing one of the primary module for the implementation of a reliable collision avoidance strategy, has been developed and tested. It is worth noting that the presented simulator, tested in the FUTURA project framework, can be applied in a wide range of robotic-integrated scenarios.

MATERIALS AND METHODS

Design requirements of the collision simulator are:

I. **reliability**: the 3D environmental reconstruction is accurate and no failures are acceptable;
II. **safety**: provides the possibility to detect not only the collisions between the objects of the scene, but also dangerous proximity;
III. **low computation cost**: since the trajectories have to be planned in *real-time*, the 3D reconstruction is able to provide rapid responses both for the actual situation onto the scene as well as for next possible movements.

In a first step, the development of the on-line collision simulator was implemented by using Blender platform (Figure 1); it represents a suite for 3D applications, especially useful for rapid prototyping. In addition to the modelling environment, the Bullet Physics engine module, already included in the distribution of Blender, has been exploited for distances and collisions calculations.

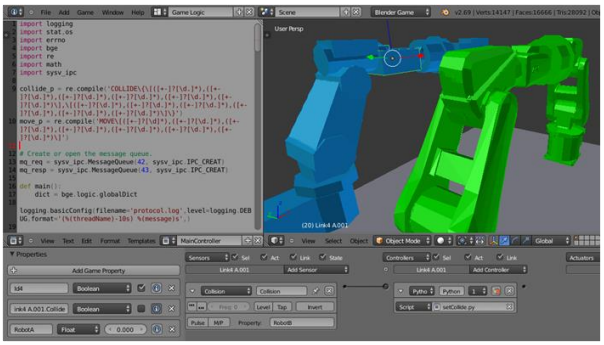

Figure. 1. Blender development suite (www.blender.org)

Once validated the approach and with the aim of improving the performances of the system, direct programming in the Bullet Physics engine has been preferred, delegating, when necessary, visualization of the simulated scene to a simple open source viewer (Ogre3D - Figure 2). In addition, the use of Bullet Physics engine guarantees a multi-platform compatibility: by using a client-server approach, applications written in different programming languages can be interfaced with the collision avoidance simulator through a simple dedicated interface (*e.g.*, socket applications).
The implemented software allows the 3D reconstructed scene to be dynamically adapted by embedding, removing or changing geometries. The objects captured by the Kinect sensor are processed and the information are integrated inside the simulator, allowing for a full representation of the current real scene.
To reduce as much as possible the computational cost, a-priori known objects, *e.g.* robots links, were re-modelled

with a simplified geometry. In particular, the simplified model envelops the real model of the manipulator links by creating a safety region around the model itself [3].

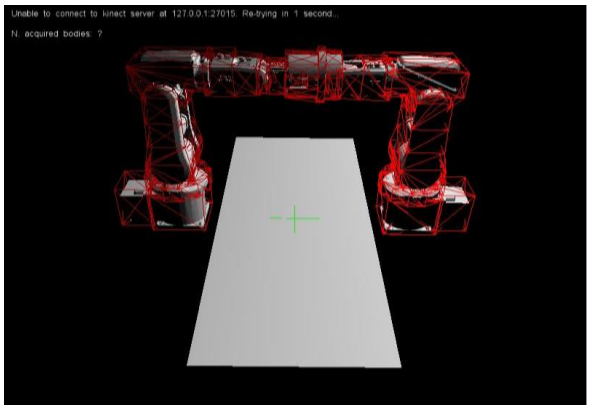

Figure. 2. The Ogre render window (www.ogre3d.org)

The developed simulator allows pre-loading in the scene of all the fixed objects, in particular the robots and the operatory table, including the kinematics parameters for accurate motion.
A simulation for estimating the computational cost of the different implementations (*i.e.*, Blender, Bullet Physics + Ogre and Bullet Physics only) has been performed calculating the average time with different numbers of triangles for the complex scene represented in Fig. 2.

RESULTS

In order to compare the performance of the three presented solutions (Blender, Bullet + Ogre3D, Bullet only) multiple randomized simulations were performed. In particular, the average computational time needed for the collision detection analysis was used as the measurement reference; this is an estimation of the average time needed by the algorithm to calculate the distances between all the objects in the scene in a new pose for the two robots and for the unstructured objects. As expected the times increase with the increasing of the total number of triangles occurring in the scene. Below is the table that reports the comparison between the average computation time for the three solutions and the percentage variation between the Blender-based method and the other two solutions (Table1).

Table. 1. Comparison analisys for the three implemented solutions.

	Low poly (100 trg)	**Med poly (200 trg)**	**High poly (300 trg)**
Blender	1.1 ms	1.8 ms	3.9 ms
Bullet P. + Ogre3D	0.6 ms (-45%)	1.2 ms (-33%)	3.3 ms (-15%)
Bullet P.	0.3 ms (-70%)	0.9 ms (-50%)	3.1 ms (-20%)

CONCLUSION AND DISCUSSION

An on-line collision avoidance simulator was developed for fulfilling a wide set of applications, involving motion planning and control in an only partially structured environment, as in robot-assisted surgery.
The proposed software has been developed using state-of-the-art software libraries and dedicated algorithms [4]. CAD re-modelling has been studied and applied with the aim to optimize mesh and computational time complexity. A computation time lower than 0.9 ms has been achieved using a suitable simplified manipulator geometry (*i.e.*, less than 200 triangles in total). The manipulator geometry used for calculating distances between objects is depicted as red cages in Fig. 2.
It is worth mentioning that the developed collision avoidance simulator can be also used as an open framework for implementing and validating novel collision avoidance strategies.
Since very often the developed software tool runs on the same machine together with the client application, in order to achieve cleaner (and even faster) transmission of the complex data structures involved, a shared-memory communication protocol may be a valid alternative to be implemented in next software revisions, replacing the TCP/IP based protocol.

AKNOLEDGEMENTS

The research leading to these results has received funding from the European Community's Seventh Framework Programme (FP7/2007-2013) under grant agreement num. 611963 (FUTURA Project).

REFERENCES

[1] B. Siciliano and O. Khatib, Springer handbook of robotics: Springer Science & Business Media, 2008.
[2] L. E. Kavraki and S. M. LaValle, "Motion planning," in Springer handbook of robotics, ed: Springer, 2008, pp. 109-131.
[3] J. Thompson, B. Berbank-Green, N. Cusworth (2007). Game design course: principles, practice, and techniques. John Wiley and Sons. p.144.
[4] Gilbert, E.G.; Johnson, D.W.; Keerthi, S.S., "A fast procedure for computing the distance between complex objects in three-dimensional space," in Robotics and Automation, IEEE Journal of, vol.4, no.2, pp.193-203, Apr 1988.

Development of a Haptic Simulator for the Training of Surgeons in Knee Physical Exam Skills

Y. Chen, S.A. Bowyer, J.W. Giles

Mechatronics in Medicine Laboratory, Department of Mechanical Engineering
Imperial College London
Joshua.Giles@imperial.ac.uk

INTRODUCTION

Mechanical analysis and haptic simulation are widely used in training tools for surgeons to provide an improved understanding of the kinetic and kinematic environment. One important and difficult skill for a surgeon to perfect is how to accurately and effectively assess a patient's joint (e.g. knee) using physical exam techniques. This could be significantly improved using a haptic training simulator developed around a biomechanical model that mimics the joint's properties for both healthy and clinically relevant injury conditions.

Coles et al. [1] reviewed the development of haptic technologies for medical training and found that simulators had been applied to a range of clinical environments. Lin et al. [2] developed a surgical training simulator with visual and haptic feedback to learn bone-sawing skills, and achieved this by combining the Omega.6 (Force Dimension, Nyon, Switzerland) with 6 degrees of freedom (DOF) and 3 DOF feedback, with a computational method that predicted feedback forces. In work previously unrelated to haptic training, complex computational models of the human knee have been developed and used as a tool for biomechanical research. Delp et al. [3] built an open-source software platform named OpenSim (Stanford University, California, USA) for musculoskeletal modelling and analysis, as well as a knee model with a single rotation axis. Based on this, Xu et al. [4] improved the model by considering all DOF and the geometry and properties of the knee ligaments.

Taking the complex mechanical characteristics of the knee joint into consideration, this work aims to combine the previously demonstrated training capabilities of haptic devices in surgery with a high fidelity online computational knee model for physical exams including the anterior drawer and pivot shift tests that are used to evaluate joint stability. This work presents the development of the haptic knee environment, which is the critical first step in creating a robotics-based physical exam haptic trainer.

MATERIALS AND METHODS

In order to simulate the diagnosis process, the knee haptic training simulator is composed of three parts (Figure 1): the computational knee model to simulate the mechanical state, a haptic device to interface with the surgeon, and a control program to integrate these two tasks. The physical simulator is composed of an anatomical knee model in which the tibia is directly connected to a haptic device and the femur is fixed to the ground; however, the physical articulation between the bones and all simulated soft tissues (e.g. ligaments) have been resected to ensure the physical model does not produce any force. The surgeon interacts with the simulator by grasping the tibia model, in the same way they would grasp a patient's leg during a clinical exam, and applying displacements to it to perform specific exam techniques. The haptic device obtains the 6 DOF pose of the knee during these exam motions, sends this to the computational knee model, after which the forces are calculated and fed back to the surgeon through the haptic device.

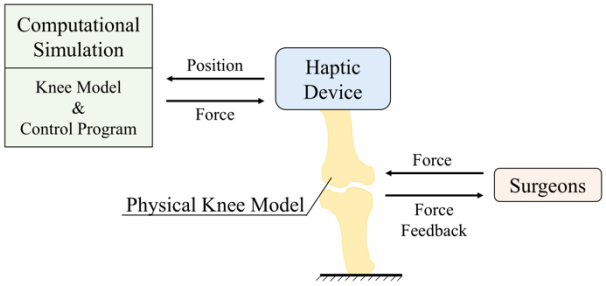

Fig. 1 Composition and work procedure of the knee haptic training simulator.

To provide physiologically accurate haptic feedback and achieve an acceptable haptic control rate, the primary focus of this research was to adapt and assess a knee model based on that presented by Xu et al. (2015). This OpenSim musculoskeletal knee model (Figure 2) considers the knee joint with 4 DOF: extension, adduction, rotation and mediolateral translation; and contains three bones: the femur, the tibia, and the patella. Knee physical exams are conducted with patients in a relaxed position, thus, the knee muscles are lax and can be considered to have a negligible tone load. The primary sources of load are the tibial gravity force and the four knee ligaments: anterior cruciate ligament (ACL), posterior cruciate ligament (PCL), medial collateral ligament (MCL) and lateral collateral ligament (LCL). To replicate the knee's ligamentous anatomy with high fidelity, the model simulates these four ligaments using ten discrete bundles with unique lines of action, attachments and stiffness values.

The surgeon's interaction with this computational knee model is defined by a virtual three DOF actuator whose point of application corresponds to the standard clinician

hand placement, approximately 10 cm distal to the knee joint. To determine the haptic force that should be felt by a surgeon while interacting with the training simulator, the current position of the haptic device is transformed to the OpenSim knee model coordinate system and fed into an inverse dynamics analysis that solves for the haptic force. To produce high haptic performance, a multi-threaded program was created, based on the workflow in Figure 1, to independently acquire data and run the computational simulation. The model's physiological accuracy and runtime performance were then assessed.

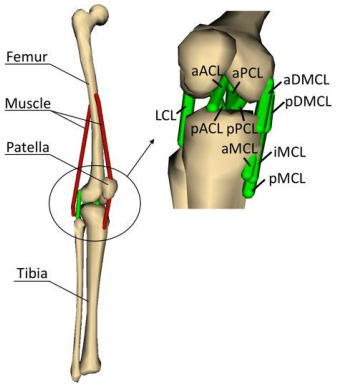

Fig. 2 OpenSim knee model with bones, muscles & ligaments.

The computational model was assessed using a clinical stability test in which simulated translations were input to the model (two conditions: healthy & PCL deficient knee) and the resulting haptic force was computed using an inverse dynamic analysis. Subsequently, the healthy knee forces were input to a forward dynamics analysis that calculated the resulting poses. These data allow the model's physiologic accuracy to be qualitatively assessed by comparing the resulting forces to clinical knowledge while the algorithm could be quantitatively assessed by comparing the input and output translations.

RESULTS

With the same applied translations for both states, smaller haptic forces were calculated for the injured conditions in comparison to the healthy knee state, which matches clinical findings (Figure 3). Table 1 shows the poses used to produce the force represented by the solid line in Figure 3 and the poses that result from feeding these forces back to a forward dynamics analysis. The resulting poses achieved an accuracy within 0.1º.

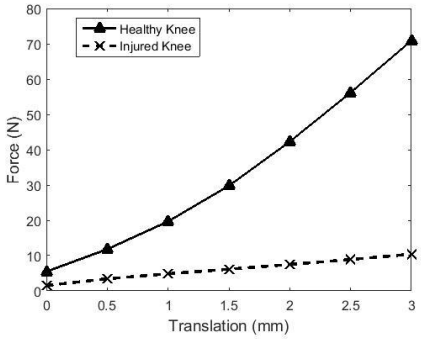

Fig. 3 Force results from inverse analysis of knee translations in models with healthy and injured ligaments.

Tab. 1 The knee model's designed poses and pose results from forward analysis of the inverse analysis force results.

Trials	Designed Poses			
	Extension(º)	Rotation(º)	Adduction(º)	Tz(m)
#1	0	0	0	0
#2	0	0	0	0.0005
#3	0	0	0	0.0010
#4	0	0	0	0.0015
#5	0	0	0	0.0020
#6	0	0	0	0.0025
#7	0	0	0	0.0030
Trials	Pose Results			
	Extension(º)	Rotation(º)	Adduction(º)	Tz(m)
#1	0.021	-0.121	0.035	0.0002
#2	0.021	-0.120	0.034	0.0007
#3	0.021	-0.118	0.033	0.0012
#4	0.021	-0.116	0.031	0.0016
#5	0.021	-0.115	0.030	0.0021
#6	0.021	-0.113	0.029	0.0026
#7	0.021	-0.110	0.028	0.0031

The computational time of the inverse dynamics analysis trials was measured because this is the most important factor affecting the simulator's haptic performance (i.e. feel). The average runtime across all trials was 188ms, which only changed slightly after optimizing the algorithm's iteration and convergence conditions.

DISCUSSION

The haptic model for a physical exam training simulator developed here was found to produce realistic haptic forces that could aid a surgeon in learning how to accurately discern the differences between knee injuries. However, the model's computational time was unacceptably long (188ms) which would result in a low control rate and poor haptic feel. This delay is attributable to OpenSim's use of an iterative optimization procedure that is critical during dynamic simulations; however, because physical exams are quasi-static, a simpler analysis can be adopted. Furthermore, the current model constrains anterior/posterior movement, which is need for some ligament tests. Therefore, in the future, a full 6 DOF mathematical knee model optimized for faster computation will be developed and validated against the OpenSim model presented in this paper.

REFERENCES

[1] T.R. Coles, D. Meglan and N.W. John. "The role of haptics in medical training simulators: A survey of the state of the art." IEEE Transactions on Haptics; 2011; 4(1):51-66.

[2] Y. Lin, X. Wang, F. Wu, et al. "Development and validation of a surgical training simulator with haptic feedback for learning bone-sawing skill." Journal of biomedical informatics; 2014; 48:122-129.

[3] S.L. Delp, F.C. Anderson, A.S. Arnold, et al. "OpenSim: Open-source software to create and analyse dynamic simulations of movement." IEEE Transactions on Biomedical Engineering; 2007; 54(11):1940-1950.

[4] H. Xu, D. Bloswick and A. Merryweather. "An improved OpenSim gait model with multiple DOF knee joint and knee ligaments." Computer Methods in Biomechanics and Biomedical Engineering; 2015; 18(11): 1217-1224.

A 2 Degrees-of-Freedom Planar Remote Center of Motion Mechanism for Minimally Invasive Surgery Manipulators

S. Nisar, T. Endo, F. Matsuno

Department of Mechanical Engineering & Science,
Graduate School of Engineering, Kyoto University
nisar.sajid.78v@st.kyoto-u.ac.jp

INTRODUCTION

Due to easier construction and inherent safety features, planar Remote Center of Motion (RCM) mechanisms, such as the double-parallelogram based RCM mechanisms (Fig. 1), have been highly popular for Minimally Invasive Surgery (MIS) manipulator designs [1]. However, these mechanisms can only provide one DoF - pitch - by virtue of the mechanism itself. Another important DoF for surgical purposes – translation - is generally implemented using some *external means* such as cable-pulleys [2-3] or actuators mounted over the distal-end of a manipulator [4-5]. This has negative affects over the performance of a manipulator.

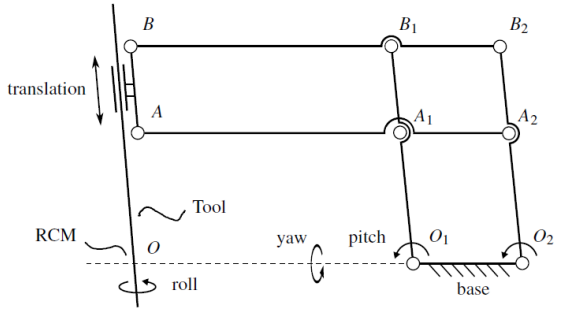

Figure. 1. A double parallelogram 1 DoF planar remote center of motion (RCM) mechanism

To solve this limitation of 1 DoF planar RCM mechanisms, we propose a new RCM mechanism capable of generating 2 DoFs – pitch and translation – through its mechanism design. The proposed mechanism offers pitch and translation DoFs without emloying any afore-mentioned *external means* and, therefore, offers several advantages.

MATERIALS AND METHODS

MIS requires four DoFs at the incision point, namely pitch, yaw, roll and translation. In the existing planar RCM mechanisms, implementation of pitch, yaw and roll is relatively easier. However, the implementation of translation DoF using *external means* is challenging due to higher force and torque requirements. In some cases, the use of *external means* results in increased size and weight of the distal-end of a manipulator.

To achieve pitch and translation DoFs by virtue of the mechanism design, we propose a new 2 DoF RCM mechanism as shown in Fig. 2. M_1 and M_2 are the two actuators to generate pitch (θ) and translation (R) DoFs.

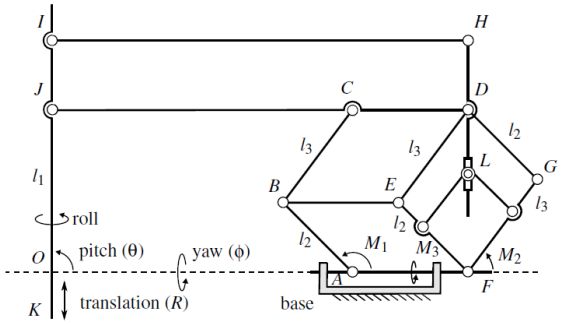

Figure. 2. The proposed 2 DoF Planar Remote Center of Motion (RCM) Mechanism

When both actuators have same direction of rotation, mechanism generates pitch motion. Whereas, when both act in opposite direction, translation DoF is achieved. Point O represents the remote center of motion. Joint L is a passive prismatic joint with all other joints being rotary. In the proposed mechanism, yaw (ϕ) can be achieved by tilting the mechanism along it base axis (link AF). Given the low torque and resolution requirements, roll can be easily achieved using *external means* mentioned earlier.

The pitch (θ), translation (R) and yaw (ϕ) can be expressed in forward kinematic equations as,

$$\theta = \tan^{-1}\left(\frac{l_2\sin(q_1)+l_3\sin(q_2)}{l_2\cos(q_1)+l_3\cos(q_2)}\right), \quad (1)$$

$$R = l_1 - \sqrt{l_2^2 + 2l_2l_3\cos(q_1-q_2)+l_3^2}\,, \quad (2)$$

$$\phi = q_3\,. \quad (3)$$

Here, l_1,l_2, l_3 represent the lenghts of links JK,AB, BC respectively and q_1 , q_2 , q_3 are the joint variables corresponding to M_1, M_2 and M_3. Similarly, the relation of tip translational and rotational velocities to the joint velocities is given by,

$$\begin{bmatrix}\dot{R}\\ \dot{\theta}\\ \dot{\phi}\end{bmatrix} = J(q)\begin{bmatrix}\dot{q}_1\\ \dot{q}_2\\ \dot{q}_3\end{bmatrix}, \quad J(q) = \begin{bmatrix}\frac{A}{\sqrt{E}} & \frac{B}{\sqrt{E}} & 0\\ \frac{C}{\sqrt{E}} & \frac{D}{\sqrt{E}} & 0\\ 0 & 0 & 1\end{bmatrix}, \quad (4)$$

where, $J(q)$ is the Jacobean matrix with elements,

$$A = -l_2 l_3 \sin(q_1 - q_2),\ B = l_2 l_3 \sin(q_1 - q_2),$$
$$C = l_2 l_3 \cos(q_1 - q_2) + (l_2)^2,\ D = l_2 l_3 \cos(q_1 - q_2) + (l_3)^2,$$
$$E = (l_2 \cos q_1 + l_3 \cos q_2)^2 + (l_2 \sin q_1 + l_3 \sin q_2)^2.$$

Using the Jacobean matrix, the mechanism is analyzed for singularities by solving $\det J(q)$ for zero. This results in,

$$\{(q_1, q_2) | q_1 = q_2, q_1 = q_2 \pm \pi\}, \qquad (5)$$

which means when link AB and BC become aligned with each other, the mechanism will attain a singular configuration.

RESULTS

Kinematic simulation with arbitrary link lengths and joint variables demonstrate that the mechanism is able to maintain remote center of motion. Figure 3 shows the end-effector position traversing between $45° - 135°$ in the pitch direction.

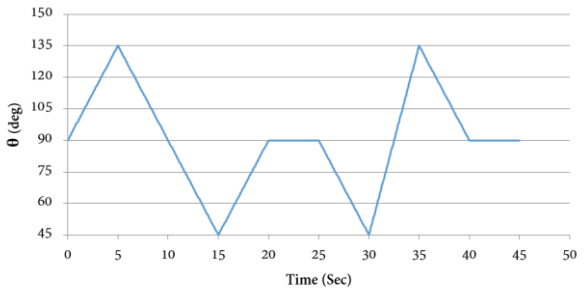

Figure. 3. End-effector position for the pitch movement while the mechanism maintains RCM

Moreover, to achieve maximum kinematic performance an optimal configuration (resulting maximum manipulability) of the mechanism is determined. Solving $\det J(q)$ shows that the mechanism attains optimal configuration when $q_1 = q_2 + \pi/2$. Geometrically, this corresponds to the mechanism configurations when link AB and BC become perpendicular to each other.

Then, we generated the mechanism workspace for variables $q_1 = [\pi/4, \pi]$, $q_2 = [0, 3\pi/4]$ and $q_3 = [-\pi/4, \pi/4]$ and compared it graphically with the required workspace as shown in Fig. 4.

CONCLUSION AND DISCUSSION

To overcome the limitations of traditional planar RCM mechanisms, a new 2 DoF RCM mechanism is proposed. The mechanism offers mechanical RCM and achieves the two most important DoFs from surgical view point – pitch and translation - by virtue of its mechanical design. Contrary to an existing design [6], this mechanism has no downward protruding link, thus minimizing the risk of any unwanted interference with the surgical scene. The mechanism can generate the workspace required for MIS procedures. Due to absence

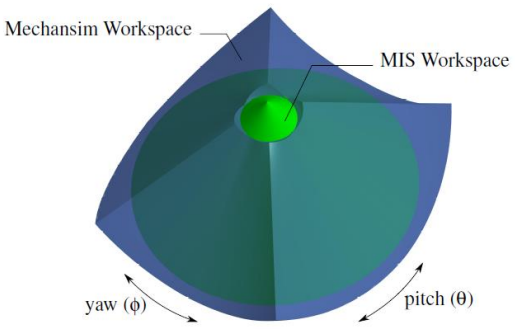

Figure. 4. Mechanism workspace (outer volume, $\theta = [45°, 135°]$, $\phi = [-47.5°, 47.5°]$) comparison with the MIS workspace (inner volume). Depth of 3D region corresponds to the translation ($R = 200\ mm$) DoF.

of *external means* to achieve translation DoF, a manipulator built upon such a mechanism will have a compact and lighter distal-end. This can be highly useful for surgical applications demanding operation in confined and narrow spaces or multiple manipulators operating in close vicinity. As the pitch and translation actuators can be easily installed at the base of manipulator, bigger and high-powered actuators can be used to achieve the critical DoFs without affecting the size and performance of a manipulator.

As a next step, the mechanism will be optimized to maximize its kinematic performance and a prototype will be developed.

REFERENCES

[1] Zong G, Pei X, Yu J, Bi S. Classification and type synthesis of 1-DOF remote center of motion mechanisms. Mechanism and Machine Theory. 2008 Dec 31;43(12):1585-95.

[2] Devengenzo RL, Solomon TR, Cooper TG, inventors; Intuitive Surgical Operations, Inc., assignee. Cable tensioning in a robotic surgical system. United States patent US 9,050,119. 2015 Jun 9.

[3] Hannaford B, Rosen J, Friedman DW, King H, Roan P, Cheng L, Glozman D, Ma J, Kosari SN, White L. Raven-II: an open platform for surgical robotics research. IEEE Transactions on Biomedical Engineering. 2013 Apr;60(4):954-9.

[4] Hassan T, Hameed A, Nisar S, Kamal N, Hasan O. Al-Zahrawi: A Telesurgical Robotic System for Minimal Invasive Surgery. IEEE Systems Journal, 2014;PP(99):1-11.

[5] van den Bedem LJ. Realization of a demonstrator slave for robotic minimally invasive surgery/door Linda Jacoba Martina van den Bedem. Department of Mechanical Engineering. Doctoral degree Technische Universiteit Eindhoven. 2010:199.

[6] Gijbels A, Vander P. EB, Stalmans P, Van Brussel H, Reynaerts D: Design of a teleoperated robotic system for retinal surgery. In 2014 IEEE International Conference on Robotics and Automation (ICRA) 2014 May:2357-2363.